



UNIVERSIDADE FEDERAL DE SANTA CATARINA
CENTRO TECNOLÓGICO
PROGRAMA DE PÓS-GRADUAÇÃO EM ENGENHARIA QUÍMICA

Heloisa Ramlow

**POLYSILAZANE-DERIVED ELECTROSPUN SiCN FIBER MATS:
CHARACTERIZATION AND APPLICATION IN ELECTROMAGNETIC FIELD
SHIELDING AND ELECTROCHEMICAL ENERGY STORAGE**

Florianópolis
2022

Heloisa Ramlow

**POLYSILAZANE-DERIVED ELECTROSPUN SiCN FIBER MATS:
CHARACTERIZATION AND APPLICATION IN ELECTROMAGNETIC FIELD
SHIELDING AND ELECTROCHEMICAL ENERGY STORAGE**

Tese submetida ao Programa de Pós-graduação
em Engenharia Química da Universidade
Federal de Santa Catarina para a obtenção do
título de Doutor em Engenharia Química

Orientador: Prof. Dr. Ricardo Machado

Coorientadores: Prof.^a Dr.^a Cintia Marangoni e
Dr. Günter Motz

Florianópolis

2022

Ficha de identificação da obra elaborada pelo autor, através do Programa de Geração Automática da Biblioteca Universitária da UFSC.

Ramlow, Heloisa

Polysilazane-derived electrospun SiCN fiber mats: characterization and application in electromagnetic field shielding and electrochemical energy storage / Heloisa Ramlow; orientador, Ricardo Antonio Francisco Machado, coorientador, Cintia Marangoni, coorientador, Günter Motz, 2022.

187 p.

Tese (doutorado) - Universidade Federal de Santa Catarina, Centro Tecnológico, Programa de Pós-Graduação em Engenharia Química, Florianópolis, 2022.

Inclui referências.

1. Engenharia Química. 2. Electrostatic spinning. 3. Non oxide ceramics. 4. Polymer-derived ceramic. 5. Pre ceramic polymer. I. Machado, Ricardo Antonio Francisco. II. Marangoni, Cintia. III. Motz, Günter IV. Universidade Federal de Santa Catarina. Programa de Pós-Graduação em Engenharia Química. V. Título.

Heloisa Ramlow

Polysilazane-derived electrospun SiCN fiber mats: characterization and application in electromagnetic field shielding and electrochemical energy storage

O presente trabalho em nível de doutorado foi avaliado e aprovado por banca examinadora composta pelos seguintes membros:

Prof. Fabrício Luiz Faita, Dr.
Universidade Federal do Rio Grande do Sul

Prof.^a Letícia da Costa, Dr.^a
Universidade Federal de Santa Catarina

Prof. Luiz Fernando Belchior Ribeiro, Dr.
Universidade Federal de Santa Catarina

Certificamos que esta é a **versão original e final** do trabalho de conclusão que foi julgado adequado para obtenção do título de doutor em Engenharia Química.

Coordenação do Programa de Pós-Graduação

Prof. Ricardo Antonio Francisco Machado, Dr.
Orientador

Florianópolis, 2022.

To my beloved family who always trusted in my decisions.

To my grandfather, in loving memory.

To my love who always understood me even when I couldn't.

For their endless love, support and encouragement.

ACKNOWLEDGMENT

First and foremost, I would like to praise and thank God, who has granted me countless blessings, knowledge, and opportunities during my life journey.

I would like to thank my supervisors Prof. Dr. Ricardo Machado, Prof.^a Dr.^a Cintia Marangoni, Dr. Günter Motz and Prof. Dr. Gurpreet Singh for trusting in my work and for always pushing me to new limits during this work period.

I am grateful for the awesome colleagues and friends of the Polymerization Process and Control Laboratory, Electromagnetism and Electromagnetic Compatibility Laboratory, Laboratory of Electrical Materials (Federal University of Santa Catarina, Brazil), Sensors and Materials Laboratory (National Institute for Space Research, Brazil), the group of Ceramic Precursors (University of Bayreuth, Germany) and the group of Nanoscience and Engineering Laboratory (Kansas State University, USA) for the friendship, help and collaboration.

I acknowledge the Graduate Program in Chemical Engineering (Federal University of Santa Catarina), CAPES, CNPq and DAAD for the financial support.

A special feeling of gratitude to my loving parents, Sara and Jorge, my brother Franz, my grandmother Ruth, my uncles Graciela and Carlos and my little cousin Vitor who have always loved me unconditionally and whose good examples have taught me to work hard for the things that I aspire to achieve. I have to mention in special my grandfather, Servino. Although he could not see my final steps on this path, without his efforts I could not have had the optimum conditions to succeed in my academic career. Last but not least, I appreciate my boyfriend Henrique, who has always encouraged me to pursue my dreams, for his understanding and incentives for the accomplishment of this work.

ABSTRACT

In this work, the manufacturing of polysilazane-based fiber mats via electrospinning was investigated based on the gaps provided by a literature review. First, the electrospinning of polysilazane was optimized with a statistical approach to obtain thinner fibers. The reduction in Berry's number from 94 to 22 indicated the positive effect of adding organic polymer on the polysilazane chains to obtain homogeneous fibers. Fractional factorial design and Box-Behnken design enabled the establishment of the relationship between fiber diameter and operating parameters of electrospinning. The morphology of the fibers was analyzed by electron microscopy. After optimization, polysilazane and polysilazane/polyacrylonitrile fibers with a diameter of $1.79 \pm 0.26 \mu\text{m}$ and $0.57 \pm 0.04 \mu\text{m}$ were manufactured, respectively. The polymer to ceramic evolution at high temperature was evaluated by Fourier-transform infrared spectroscopy and thermal analyses. After pyrolysis, SiCN and SiCN/C fibers showed a diameter of $1.37 \pm 0.19 \mu\text{m}$ and $0.15 \pm 0.02 \mu\text{m}$. The composition and structure of the materials were investigated by X-ray photoelectron spectroscopy, energy-dispersive X-ray spectroscopy, Raman spectroscopy, X-ray diffraction, and ^{29}Si solid-state nuclear magnetic resonance spectroscopy. The electrospinning of polysilazane led to a higher degree of carbon ordering and improved oxidation resistance up to $600 \text{ }^\circ\text{C}$ in SiCN/C fiber mats compared to oligosilazane-derived SiCN/C. The fiber mats containing polysilazane were tested in advanced applications. The C/SiCN fiber mats were pyrolyzed at $800 \text{ }^\circ\text{C}$ and exhibited enhanced electromagnetic reflection loss from 0.1 MHz to 4.5 GHz compared to carbon, including more than 80% electromagnetic field shielding of the 5G C-band attributed to appropriate electrical conductivity, high degree of carbon disorder, and presence of heterogeneous microstructure forming interfacial polarization. In Ku-band shielding (from 12.4 to 18 GHz), the SiCN/C fibers showed higher permittivity ($\epsilon' = 5.8$ and $\epsilon'' = 2.1$) compared to SiCN ($\epsilon' = 3.2$ and $\epsilon'' = 0.15$) at 16.9 GHz. Moreover, the electromagnetic field absorption was increased by $\sim 179\%$ with the addition of carbon in the SiCN matrix. The influence of the atmosphere when electrospinning polysilazane was also evaluated. In lithium-ion battery, the SiCN/C electrode electrospun in air showed the highest charge capacity of $773 \text{ mA}\cdot\text{h}\cdot\text{g}^{-1}$ due to higher oxygen content, while the SiCN/C electrospun in nitrogen demonstrated stable cycling with a charge capacity of $299 \text{ mA}\cdot\text{h}\cdot\text{g}^{-1}$ at $50 \text{ mA}\cdot\text{g}^{-1}$ due to enhanced free carbon content. These capacities are higher than SiCN and carbon electrodes, suggesting that hybrid materials were prepared with the synergetic contribution of SiCN as a pathway for Li^+ transfer, and carbon, which improved the electronic conductivity and provided more active sites for Li^+ ions. This work proved the advantages of using polymer-derived ceramics shaped via electrospinning by controlling the composition, molecular structure and morphology. Moreover, the applications of SiCN fiber mats will inspire future work in the field of advanced ceramics.

Keywords: Electrostatic spinning. Non-oxide ceramics. Polymer-derived ceramic. Pre-ceramic polymer.

RESUMO

Neste trabalho, a fabricação de tecidos fibrosos por meio da eletrofiação de polissilazano foi investigada com base nas lacunas fornecidas por uma revisão da literatura. Primeiramente, a eletrofiação do polissilazano foi otimizada com uma abordagem estatística para a obtenção de fibras mais finas. A redução do número de Berry de 94 para 22 indicou o efeito positivo da adição de polímero orgânico nas cadeias do polissilazano para obter fibras homogêneas. O projeto fatorial fracionado e o projeto Box-Behnken permitiram o estabelecimento da relação entre o diâmetro das fibras e os parâmetros operacionais da eletrofiação. A morfologia das fibras foi analisada por microscopia eletrônica. Após a otimização, foram fabricadas fibras de polissilazano e polissilazano/poliacrilonitrila com diâmetro de $1,79 \pm 0,26 \mu\text{m}$ e $0,57 \pm 0,04 \mu\text{m}$, respectivamente. A evolução do polímero para cerâmica a alta temperatura foi avaliada por espectroscopia de infravermelho de Fourier e análises térmicas. Após pirólise, as fibras SiCN e SiCN/C apresentaram um diâmetro de $1,37 \pm 0,19 \mu\text{m}$ e $0,15 \pm 0,02 \mu\text{m}$. A composição e estrutura dos materiais foram investigadas por espectroscopia de fotoelétrons excitados por raios X, espectroscopia de raios X por dispersão em energia, espectroscopia Raman, difração de raios X e ^{29}Si espectroscopia de ressonância magnética nuclear de estado sólido. A eletrofiação do polissilazano levou a um maior grau de ordenação do carbono e melhorou a resistência à oxidação até $600 \text{ }^\circ\text{C}$ em tecidos fibrosos SiCN/C em comparação com SiCN/C derivado de oligossilazano. Os tecidos fibrosos contendo polissilazano foram testados em aplicações avançadas. Os tecidos fibrosos C/SiCN foram pirolisados a $800 \text{ }^\circ\text{C}$ e exibiram perda por reflexão eletromagnética aumentada de 0,1 MHz a 4,5 GHz em comparação com o carbono, incluindo mais de 80% de blindagem do campo eletromagnético da banda C 5G atribuída à condutividade elétrica apropriada, alto grau de desordem de carbono e presença de microestrutura heterogênea formando uma polarização interfacial. Na blindagem da banda K_u (12,4 a 18 GHz), as fibras SiCN/C apresentaram maior permissividade ($\epsilon'=5,8$ e $\epsilon''=2,1$) em comparação com SiCN ($\epsilon'=3,2$ e $\epsilon''=0,15$) a 16,9 GHz. Além disso, a absorção do campo eletromagnético foi aumentada em $\sim 179\%$ com a adição de carbono na matriz de SiCN. Também foi avaliada a influência da atmosfera de eletrofiação do polissilazano. Na bateria de íons de lítio, o eletrodo SiCN/C eletrofiado em ar apresentou a maior capacidade de carga de $773 \text{ mA}\cdot\text{h}\cdot\text{g}^{-1}$ devido ao maior conteúdo de oxigênio, enquanto o SiCN/C eletrofiado em nitrogênio demonstrou ciclos estáveis com uma capacidade de carga de $299 \text{ mA}\cdot\text{h}\cdot\text{g}^{-1}$ a $50 \text{ mA}\cdot\text{g}^{-1}$ devido ao maior conteúdo de carbono livre. Estas capacidades são mais altas do que eletrodos de SiCN e de carbono, sugerindo que materiais híbridos foram preparados com a contribuição sinérgica do SiCN como um caminho para a transferência de Li^+ , e carbono, que melhorou a condutividade eletrônica e forneceu locais mais ativos para íons Li^+ . Este trabalho provou as vantagens de utilizar cerâmicas derivadas de polímeros moldadas por eletrofiação, controlando a composição, a estrutura molecular e a morfologia. Além disso, as aplicações dos tapetes fibrosos de SiCN inspirarão o trabalho futuro no campo de cerâmicas avançadas.

Palavras-chave: Cerâmica derivada de polímeros. Cerâmica não-óxida. Fiação eletrostática. Polímero pré-cerâmico.

RESUMO EXPANDIDO

TECIDO FIBROSO ELETROFIADO DE SiCN DERIVADO DE POLISILAZANO: CARACTERIZAÇÃO E APLICAÇÃO EM BLINDAGEM DE CAMPOS ELECTROMAGNÉTICOS E ARMAZENAMENTO DE ENERGIA ELETROQUÍMICA

Introdução

Os polímeros pré-cerâmicos (*Preceramic Polymers* – PCPs) à base de silício têm sido intensamente estudados há mais de 50 anos para produzir fibras cerâmicas, revestimentos, espumas, nanocompósitos e outros. Estes precursores representam sistemas inorgânicos/organometálicos que produzem cerâmicas derivadas de polímeros (*Polymer-derived Ceramics* – PDCs) com composição química ajustada e uma organização nanoestrutural bem definida por meio do tratamento térmico adequado em atmosfera protetora. Em comparação com as cerâmicas tradicionais utilizando tecnologia de pó, os principais benefícios dos PDCs incluem maior controle de pureza/composição, redução significativa da temperatura de processamento, possibilidade de produzir materiais multicomponentes e híbridos (orgânico-inorgânicos) e alta versatilidade em termos de processabilidade.

Os campos de aplicação dos PDCs têm sido ampliados significativamente pelas recentes atividades de pesquisa e desenvolvimento utilizando a técnica de eletrofiação. Esta técnica de moldagem pode oferecer o desenvolvimento de materiais multifuncionais com uma microestrutura inovadora que atendem a vários objetivos por meio de uma estrutura. Entretanto, a eletrofiação também apresenta novos desafios em termos de controle de processo, uma vez que requer a adição de um auxiliar de fiação para a fabricação de fibras homogêneas contínuas.

Os tapetes fibrosos/fibras de PDCs moldados por eletrofiação têm sido investigados em aplicações avançadas. Os metais são os materiais típicos de revestimento para bloquear a propagação da radiação de um campo eletromagnético. Porém a alta densidade, a fácil corrosão e o difícil processamento limitam sua ampla aplicação. Portanto, o desenvolvimento de novos materiais para blindagem de campo eletromagnético que possuem baixa densidade, flexibilidade e alta eficiência é um campo de pesquisa promissor. Atualmente, os eletrodos de

carbono são utilizados em baterias de íons de lítio devido a seu baixo custo, apesar de sua baixa capacidade. Estudos recentes investigaram cerâmicas à base de silício preparadas via processo PDC como eletrodos potenciais para baterias, porém a maioria está baseada em SiOC utilizando o método pasta-moldagem (*slurry-casting*), o que, no entanto, pode aumentar o peso total da bateria. Alguns progressos têm sido feitos com PDCs moldados por eletrofição para produzir tapetes fibrosos sem suporte, mas pesquisas adicionais são necessárias. Fibras cerâmicas eletrofiadas a partir de PCPs à base de silício seguido pelo tratamento térmico adequado são promissores para o desenvolvimento de materiais que demonstram as propriedades desejadas na blindagem do campo eletromagnético e no armazenamento de energia eletroquímica.

Objetivo

Este trabalho tem como objetivo preparar tapetes fibrosos/fibras de cerâmica a partir de PCPs à base de silício, utilizando o polissilazano como um dos principais precursores e a eletrofição como a técnica de moldagem para aplicações avançadas, incluindo a blindagem do campo eletromagnético e o armazenamento de energia eletroquímica.

Metodologia

A primeira etapa do trabalho envolveu a revisão do estado-da-arte sobre PDCs moldados por eletrofição conforme base de dados disponíveis. Dessa forma foram identificadas as lacunas da literatura e os tópicos que necessitam maior pesquisa para a eletrofição dos PCPs e produção dos respectivos PDCs. Iniciou-se pela investigação do comportamento reológico das soluções poliméricas e otimização estatística dos parâmetros operacionais da eletrofição para produção de fibras mais finas como a segunda etapa da pesquisa. Primeiramente preparou-se o polissilazano a partir do oligosilazano por meio do processo de cura seletivo. Soluções de polissilazano e polissilazano + poliácridonitrila foram preparadas em diferentes concentrações de polímero adicionando o agente de cura dicumila peróxido e os solventes dimetilformamida e tetrahidrofurano. As soluções foram eletrofiadas em ambiente inerte (N_2) e a solução que produziu fibras homogêneas contínuas foi escolhida para os testes posteriores. Um projeto fatorial fracionário foi implementado para selecionar os

três fatores mais significativos que afetam o diâmetro das fibras. Em seguida, um modelo de superfície de resposta foi desenvolvido utilizando o projeto Box-Behnken para obter uma relação quantitativa entre os parâmetros operacionais e o diâmetro da fibra. Na terceira etapa, a influência da molécula de silazano (oligosilazano e polissilazano) na microestrutura da fibra foi investigada em termos de resistência à termo-oxidação. Foram preparadas soluções contendo 60 wt.% ou 30 wt.% de silazano acrescido de poliacrilonitrila, que foram eletrofiadas em ambiente inerte (N_2) e pirolisados a 1000 °C em atmosfera inerte (N_2) para produzir tapetes fibrosos SiCN/carbono. A perda por reflexão eletromagnética na banda C 5G dos tapetes fibrosos carbono/SiCN e carbono foi investigada na quarta etapa deste trabalho utilizando um analisador de redes vetoriais de 1-porta de 0,1 MHz a 4,5 GHz. Soluções de poliacrilonitrila e poliacrilonitrila + polissilazano (7:3 wt.%) foram eletrofiadas em ambiente inerte (N_2) e pirolisadas a 800 °C, 1000 °C ou 1200 °C em atmosfera inerte (N_2). Como análise complementar, a condutividade elétrica de corrente contínua também foi avaliada pelo método de sonda de quatro pontos. As propriedades de absorção eletromagnética foram estudadas na quinta etapa. Soluções de polissilazano e polissilazano + poliacrilonitrila (3:2 wt.%) foram eletrofiadas em ambiente inerte (N_2). Os tapetes fibrosos foram pirolisados a 1200 °C em atmosfera inerte (N_2), macerados e as fibras foram misturadas com silicone para produzir amostras com diferentes espessuras. Os parâmetros de dispersão e perdas por reflexão foram avaliados em um analisador de redes vetoriais de 2-portas com ondas guiadas por banda K_u (12,4-18 GHz) e o método Nicolson-Ross-Weir. Também foram conduzidas simulações computacionais para avaliar o comportamento de seção transversal do radar em uma placa plana composta pelo material desenvolvido. Na sexta etapa os tapetes fibrosos foram utilizados como eletrodos de bateria de íons de lítio. Soluções contendo polissilazano ou polissilazano + poliacrilonitrila (3:2 wt.% e 3:7 wt.%) foram eletrofiadas em ambiente inerte (N_2) ou em ar, seguido pela pirólise a 1200 °C em atmosfera inerte (N_2). O eletrodo foi perfurado do tapete fibroso no diâmetro de 6,35 mm e montado em uma bateria de célula tipo moeda LIR-2032.

Resultados

A revisão do estado-da-arte sobre PDCs moldados por eletrofiação possibilitou a seleção das principais estratégias para obter fibras utilizando PCPs incluindo as propriedades

da solução, parâmetros operacionais, condições ambientais, procedimentos de cura e pirólise, e as aplicações e propriedades dos tapetes fibrosos/fibras eletrofiadas.

A redução do número de Berry de 94 para 22 indicou o efeito positivo da adição de polímero orgânico nas cadeias do polissilazano para obter fibras mais finas. Após a aplicação da abordagem estatística, os modelos foram utilizados para encontrar os parâmetros operacionais da eletrofiação que produzem fibras mais finas. Para o polissilazano, a taxa de alimentação de solução mostrou um efeito positivo, enquanto que para o polissilazano + poliacrilonitrila uma interação entre a taxa de alimentação e a distância entre ponta da agulha e coletor foi o fator mais significativo, com um efeito positivo. Sob parâmetros operacionais otimizados, foram fabricadas fibras de polissilazano com diâmetro de $1,79 \pm 0,26 \mu\text{m}$ e fibras de polissilazano/poliacrilonitrila com diâmetro de $0,57 \pm 0,04 \mu\text{m}$. Embora o polissilazano apresente uma estrutura complexa para ser eletrofiado, os modelos propostos foram validados experimentalmente no nível de significância desejado de 95%.

Em comparação com o oligossilazano, o polissilazano promoveu a elasticidade das fibras durante a eletrofiação atribuído a uma cadeia molecular mais homogênea e com maior massa molecular. As análises FTIR-ATR, XRD, Raman e $^{29}\text{Si-NMR}$ confirmaram a transformação de polissilazano e poliacrilonitrila para respectivamente SiCN e carbono. As medições XPS mostraram que o sistema oligossilazano + poliacrilonitrila aumentou a concentração de oxigênio e carbono na cerâmica final devido aos locais reativos Si-H, o que também reduziu a perda de massa durante a pirólise devido a reações de cura entre ambos os componentes. No entanto, o uso do polissilazano no sistema levou a um maior grau de ordenação do carbono e melhorou a resistência à oxidação a $600 \text{ }^\circ\text{C}$. Ao utilizar o oligossilazano, a separação de fases reduziu o efeito protetor proporcionado pela fase SiN_4 resistente à oxidação, devido à formação de regiões desprotegidas de carbono.

A condutividade elétrica dos tapetes fibrosos de carbono/SiCN variou entre $0,0028 \text{ S}\cdot\text{cm}^{-1}$ a $0,0120 \text{ S}\cdot\text{cm}^{-1}$ quando a temperatura de pirólise aumentou de $800 \text{ }^\circ\text{C}$ para $1200 \text{ }^\circ\text{C}$. O carbono/SiCN melhorou significativamente a perda por reflexão eletromagnética em comparação com o carbono puro. Particularmente, o tapete fibroso carbono/SiCN pirolizado a $800 \text{ }^\circ\text{C}$ exibiu uma ampla largura de banda de $0,1 \text{ MHz}$ a $4,5 \text{ GHz}$ com perda de reflexão menor do que -7 dB , incluindo mais de 80% de blindagem da banda C 5G. Esta dissipação de energia foi atribuída à condutividade elétrica moderada, alto grau de desordem de carbono como

confirmado por análises de Raman e XRD, e presença de uma microestrutura heterogênea formando polarização interfacial.

Em 16,9 GHz, as fibras SiCN/carbono apresentaram maior permissividade elétrica relativa complexa ($\epsilon' = 5,8$ e $\epsilon'' = 2,1$) em comparação com SiCN ($\epsilon' = 3,2$ e $\epsilon'' = 0,15$). A absorção eletromagnética foi aumentada em $\sim 179\%$ com a adição de carbono na matriz de SiCN. As simulações computacionais apresentaram o melhor efeito protetivo do SiCN/carbono contra o campo eletromagnético em comparação com o SiCN. A capacidade favorável de absorção de microondas foi atribuída a três aspectos, incluindo o aumento da perda por condução derivada da condutividade do carbono livre, perda por polarização dipolo e interfacial gerada por defeitos, e perda por reflexão múltipla aumentada por uma rede hierárquica formada a partir das fibras eletrofiadas. Além disso, a adição do precursor de carbono representou uma redução de peso de 17% para as fibras de SiCN/carbono em comparação com as fibras de SiCN, conforme medido por picnometria de hélio.

A microscopia eletrônica mostrou que as fibras eletrofiadas em ambiente inerte (N_2) são mais finas do que as amostras eletrofiadas convencionalmente em ar devido a uma descarga do jato de solução pelas moléculas de água presente no ar, reduzindo o alongamento do jato. As análises XPS confirmaram que as fibras eletrofiadas em ar incorporaram uma maior quantidade de oxigênio. A maior capacidade de carga de $773 \text{ mA}\cdot\text{h}\cdot\text{g}^{-1}$ a $50 \text{ mA}\cdot\text{g}^{-1}$ foi obtida com o tapete fibroso SiCN/carbono eletrofiado em ar. O oxigênio aumentou a capacidade devido a seu alto caráter para atrair íons Li^+ , porém uma histerese de tensão foi observada. O tapete SiCN/carbono eletrofiado em nitrogênio demonstrou capacidade estável de $299 \text{ mA}\cdot\text{h}\cdot\text{g}^{-1}$ devido ao aumento do conteúdo de carbono livre. Estas capacidades são maiores do que eletrodos SiCN e carbono processados em condições similares atribuído aos efeitos sinérgicos entre SiCN atuando como um caminho para a transferência de Li^+ , e carbono melhorando a condutividade elétrica e com mais locais ativos para íons Li^+ . Após 100 ciclos, o eletrodo SiCN/carbono eletrofiado em atmosfera inerte apresentou até 98% da capacidade inicial, uma vez que retornou ao ciclo de corrente mais baixa, mostrando uma melhor estabilidade e menores perdas de capacidade.

Conclusões

Os resultados obtidos na primeira etapa mostraram que os PDCs moldados por eletrofiação têm sido cada vez mais estudados como materiais cerâmicos em aplicações avançadas. Na segunda etapa, a investigação da morfologia e da otimização estatística apresentaram resultados favoráveis para adequar a arquitetura das fibras, estabelecendo efetivamente uma base para estudos adicionais, nos quais o escopo está relacionado com a qualidade morfológica dos tapetes fibrosos/fibras eletrofiados de PCPs. O projeto de cerâmicas com propriedades feitas sob medida pode ser convenientemente ajustado por meio da manipulação da conformação molecular do precursor conforme investigado na terceira etapa. Devido à sua estabilidade a altas temperaturas e resistência à oxidação, o SiCN/carbono produzido neste trabalho pode ser usado como suporte catalítico. A quarta etapa demonstrou que o tapete flexível carbono/SiCN pode ser empregado como um novo material leve para proteção contra interferência eletromagnética. O ajuste da temperatura de pirólise e a adição de polissilazano variou o nível de defeitos presentes na estrutura do carbono e assim alterou a condutividade elétrica e as propriedades de blindagem eletromagnética dos tapetes fibrosos. Também a quinta etapa corroborou que as fibras SiCN/carbono são potenciais para serem usadas como materiais leves para aplicações de absorção eletromagnética sob ambientes agressivos. O desempenho eletroquímico dos eletrodos SiCN/carbono pode ser melhorado por meio da atmosfera de eletrofiação para controlar a estrutura e composição do material, como demonstrado na sexta etapa. Conclui-se que este trabalho mostrou que materiais à base de polissilazano podem ser preparados por eletrofiação convencional usando diferentes estratégias que estão disponíveis para serem totalmente exploradas, ou seja, adição de precursor orgânico, cura seletiva do oligossilazano e controle da atmosfera de eletrofiação, para adequar a microestrutura e composição final da cerâmica para aplicações avançadas.

Palavras-chave: Cerâmica derivada de polímeros. Cerâmica não-óxida. Fiação eletrostática. Polímero pré-cerâmico.

LIST OF FIGURES

Figure 3.1 – Green fiber diameter of Si-based PCP fibers manufactured through electrospinning and melt-spinning. The diameter of polysilane, polysilazane, and polysilsesquioxane fibers available in the literature was considered [1,2,11–20,3,21–30,4,31–40,5,41–50,6,51–60,7,61–70,8,71–77,9,10] (the x-axis has no variation).....	23
Figure 3.2 – Number of publications about ‘PDCs and fibers’ and ‘PDCs and electrospinning’ until 2021 (stand: 11/22/2021). The queries correspond to ‘PCPs, PDCs, and fibers’: ‘preceramic polymers’ OR ‘polymer-derived ceramics’ OR ‘PDCs’ AND ‘fibers’; ‘PCPs, PDCs, and melt-spinning’: ‘preceramic polymers’ OR ‘polymer-derived ceramics’ OR ‘PDCs’ AND ‘melt-spinning’; and ‘PCPs, PDCs, and electrospinning’: ‘preceramic polymers’ OR ‘polymer-derived ceramics’ OR ‘PDCs’ AND ‘electrospinning’ (database: Scopus).....	24
Figure 3.3 – Schematic diagram of the electrospinning process	25
Figure 3.4 – Schematic depiction of the manufacturing of PDC fibers/fibrous mats through electrospinning and thermal treatment	26
Figure 3.5 – Ceramic fiber diameter as a function of the polymer concentration of the main PCPs available in the literature (PCS, PUS, MK, and H44) [45,47–49,51–54,58–60,62–65,67–71,78,80,101,117–139].....	29
Figure 3.6 – Properties of e-PDC fibers regarding voltage/tip to collector distance ratio and feed rate with a) polymer concentration and b) ceramic fiber diameter [46–49,52,67,69–72,78,118,120–129,133,135,138,139,145–149].....	33
Figure 3.7 – Applications of electrospun ceramic fibers from Si-based preceramic polymers	38
Figure 4.1 – Electrospinnability results of HTTS according to polymer concentration (12.50 kV positive voltage, -12.50 kV negative voltage, 2 ml·h ⁻¹ feed rate, 18.50 cm tip-to-collector distance, and 0.8 mm needle diameter)	63
Figure 4.2 – Electrospinnability results of HTTS_PAN according to polymer concentration (10.00 kV positive voltage, -10.00 kV negative voltage, 1 ml·h ⁻¹ feed rate, 18.50 cm tip-to-collector distance, and 0.8 mm needle diameter)	64
Figure 4.3 – a) Surface tension, b) conductivity, c) viscoelasticity behavior of HTTS solutions, and d) viscoelasticity behavior of HTTS_PAN solutions	65

Figure 4.4 – Correlation of Berry’s number with solution concentration according to the morphology of a) HTTS and b) HTTS_PAN	66
Figure 4.5 – HTTS and HTTS_PAN concentration <i>versus</i> reduced viscosity	67
Figure 4.6 – Surface responses according to Box-Behnken design for a) HTTS_60 at 19.5 cm as tip-to-collector distance, +12.50 kV as positive voltage, and 0.8 mm as needle diameter; and b) HTTS_PAN_17.5 at 23.5 cm as tip-to-collector distance, -10.00kV as negative voltage, and 0.8 mm as needle diameter	71
Figure 4.7 – Fibers resulting from optimization of a) HTTS_60 and b) HTTS_PAN_17.5	73
Figure 5.1 – Scheme presenting the general preparation of C-rich SiCN fiber mats	84
Figure 5.2 – a) Viscosity as a function of shear rate and b) conductivity and surface tension of the solutions.....	86
Figure 5.3 – SEM images showing mean fiber diameter, respective histogram, and sample photo of a) HTT1800_PAN, b) HTT1800_PAN_1000, c) HTTS_PAN, d) HTTS_PAN_1000, e) PAN_HTT1800, f) PAN_HTT1800_1000, g) PAN_HTTTS, and h) PAN_HTTTS_1000	87
Figure 5.4 – Curves of a) TGA and b) DSC of as-spun fiber mats pyrolyzed in nitrogen atmosphere.....	88
Figure 5.5 – a) FTIR-ATR spectra of as-spun samples, b) FTIR-ATR spectra of pyrolyzed samples, c) XRD patterns, and d) Raman spectra	89
Figure 5.6 – Solid-state ²⁹ Si-NMR of samples heat-treated at 1000 °C in nitrogen atmosphere	91
Figure 5.7 – High-resolution XPS spectra of the (a) HTT1800_PAN_1000, (b) HTTS_PAN_1000, (c) PAN_HTT1800_1000 and (d) PAN_HTTTS_1000 fiber mats	93
Figure 5.8 – Ternary SiCN phase diagram of C-rich SiCN fiber mats. Hydrogen and oxygen were neglected.....	94
Figure 5.9 – Curves of a) TGA and b) DSC of C-rich SiCN fiber mats for thermo-oxidation resistance evaluation (heating rate: 5 °C·min ⁻¹ ; atmosphere: synthetic air).....	95
Figure 5.10 – SEM images containing respective histogram, mean fiber diameter, and sample photo after thermo-oxidation test at 600 °C for 1 h of a) HTT1800_PAN_1000, b) HTTS_PAN_1000, c) PAN_HTT1800_1000, and d) PAN_HTTTS_1000	97
Figure 5.11 – High-resolution XPS spectra of oxidized HTTS_PAN_1000 fiber mats	97

Figure 6.1 – Fabrication of C/SiCN nanofiber mats via precursor approach and electrospinning technique.....	106
Figure 6.2 – Diagram of DC electrical conductivity and S_{11} scattering parameter analyses.	108
Figure 6.3 – Properties of PAN:HTTS (7:3 wt.% and 13 wt.% polymer concentration) and PAN solutions (10 wt.% polymer concentration). The viscosity is presented according to shear rate, solution appearance, respective electrical conductivity (in $\mu\text{S cm}^{-1}$), and surface tension (in mN m^{-1}).....	110
Figure 6.4 – As-spun and pyrolyzed electrospun PAN:HTTS (7:3 wt.%) and PAN mats with corresponding mean fiber diameter (\emptyset) and sample photo	111
Figure 6.5 – TGA and DSC thermograms of PAN:HTTS (7:3 wt.%) and PAN.....	112
Figure 6.6 – FTIR-ATR spectra of as-spun and pyrolyzed (a) PAN:HTTS and (b) PAN samples	113
Figure 6.7 – Weight content of C and C/Si ratio for pyrolyzed PAN:HTTS samples based on EDS results	114
Figure 6.8 – (a) XRD spectra, (b) first-order Raman spectra and (c) second-order Raman spectra of PAN:HTTS and PAN pyrolyzed at different temperatures.....	115
Figure 6.9 – Electromagnetic characterization of PAN:HTTS and PAN pyrolyzed at different temperatures highlighted in the 5G C-band. (a) absorption coefficient $A(\omega)$, (b) reflection shielding effectiveness SER, and (c) reflection loss RL. The photo inset shows the flexibility of the PAN:HTTS/800 °C sample. The flexibility of the mats was very similar, i.e. the addition of SiCN into the carbon did not change the flexibility because it is present in a low content and is well distributed throughout the carbon matrix	118
Figure 6.10 – (a) VSWR in 5G C-band and (b) DC electrical conductivity of PAN:HTTS and PAN pyrolyzed at different temperatures	119
Figure 6.11 – Schematic illustration of EM field shielding mechanisms based on the C/SiCN nanofiber mat.....	122
Figure 7.1 – Schematic diagram of preparing SiCN and SiCN/C samples to be tested for microwave absorption and EMF shielding.....	134
Figure 7.2 – Images of the N5230C-PNA-L VNA and accessories for electromagnetic measurements in K_u -band guided wave testing. (a) Equipment overview, (b) picture of samples, (c) picture of the coaxial cable connected at the coaxial to waveguide transition. Two metal	

panels are shown, the offset plate, which is cast in rectangular form with the dimensions for guided K_u -band testing (10.16 mm high by 22.86 mm wide) and the metal panel, (d) exploded view of the experimental setup for reflection loss testing, and (e) exploded view of the setup applied for NRW testing.....	134
Figure 7.3 – (a) Curves of TGA and DSC, (b) FTIR-ATR spectra, and TEM images with respective SAED and elemental composition according to EDS results of (c) SiCN and (d) SiCN/C fibers	137
Figure 7.4 – Solid-state Si-NMR of SiCN and SiCN/C fibers	139
Figure 7.5 – (a) XRD patterns and (b) Raman spectra of SiCN and SiCN/C fibers	139
Figure 7.6 – SE absorption of (a) SiCN and (b) SiCN/C fibers in K_u -band (include experimental error range)	140
Figure 7.7 – (a) Real (ϵ_r'), (b) imaginary (ϵ_r'') components of the complex permittivity obtained experimentally by the NRW method (include experimental error range) and (c) Cole-Cole curves of SiCN and SiCN/C fibers (4.5 mm) in the K_u -band frequency range.....	142
Figure 7.8 – Tangent of electrical losses of SiCN and SiCN/C fibers (4.5 mm) obtained experimentally by the NRW method in the K_u -band frequency range.....	143
Figure 7.9 – Reflection loss of (a) SiCN and (b) SiCN/C fibers in K_u -band (include experimental error range)	144
Figure 7.10 – Computational results of RCS scattering study in free space. a) Numerical computation of the far-field spectral diagram of radiation scattering RCS from SiCN/C at the frequency of 12.4 GHz, b) 15.2 GHz, and c) 18.0 GHz. d) Computational setup illustration for the far-field spectral diagram of radiation scattering.....	146
Figure 7.11 – Radiation diagram according to observation angle (θ) from -90° to 90° of SiCN and SiCN/C at the frequency of 18 GHz	147
Figure 8.1 – Schematic diagram of the experimental process of this work including (a) precursor solution preparation, (b) electrospinning in air or protective atmosphere (nitrogen), (c) preparation of as-spun fiber mats for pyrolysis, (d) pyrolyzed fiber mats, and (e) punching of fiber mat electrode	157
Figure 8.2 – SEM images, respective fiber diameter (Φ) and histogram of pyrolyzed fiber mats electrospun in air (SiCN-40C-a and SiCN-70C-a) or protective atmosphere (SiCN-40C-i and SiCN-70C-i)	159

Figure 8.3 – SEM images, respective fiber diameter (Φ) and histogram of pyrolyzed SiCN fiber mat electrospun in inert atmosphere and carbon fiber mat electrospun in air.....	159
Figure 8.4 – Voltage profiles with 1 st and 2 nd charge-discharge cycles of the (a-d) SiCN-40C-a, SiCN-40C-i, SiCN-70C-a, and SiCN-70C-i fiber mat electrodes.....	160
Figure 8.5 – Voltage profiles with 1 st and 2 nd charge-discharge cycles of the (a) SiCN and (b) carbon fiber mat electrodes.....	161
Figure 8.6 – XPS spectra of the fiber mat electrodes.....	163
Figure 8.7 – High-resolution XPS spectra of the (a) SiCN-40C-a, (b) SiCN-40C-i, (c) SiCN-70C-a, and (d) SiCN-70C-i fiber mats.....	164
Figure 8.8 – High-resolution XPS spectra of the (a) SiCN and (b) carbon fiber mats.....	164
Figure 8.9 – Differential capacity (Q) and V (voltage) curves of the (a-d) SiCN-40C-a, SiCN-40C-i, SiCN-70C-a, and SiCN-70C-i electrodes.....	168
Figure 8.10 – Differential capacity (Q) and V (voltage) curves of the (a) SiCN and (b) carbon electrodes.....	168
Figure 8.11 – Long-term stability and rate capability data of the SiCN-C for 100 cycles at different current densities. The cells were subjected to symmetric cycling at current densities of 50, 100, 200, 400, 600, and 800 mA g ⁻¹ for 10 cycles each followed by a current density of 50 mA g ⁻¹ for 40 cycles.....	170
Figure 8.12 – Long-term stability and rate capability data of the SiCN and carbon for 100 cycles at different current densities. The cells were subjected to symmetric cycling at current densities of 50, 100, 200, 400, 600, and 800 mA g ⁻¹ for 10 cycles each followed by a current density of 50 mA g ⁻¹ for 40 cycles.....	171

LIST OF TABLES

Table 3.1 – Electromagnetic field shielding performance of e-PDC materials.....	39
Table 3.2 – Energy storage performance of reported e-PDC materials.....	41
Table 3.3 – Authors’ contributions to Chapter 3	46
Table 4.1 – HTTS and HTTS_PAN solutions used to investigate the electrospinnability of the preceramic precursor	58
Table 4.2 – Experimental levels of independent factors	61
Table 4.3 – ANOVA according to Box-Behnken design (A is positive voltage in kV, B is negative voltage in kV, C is feed rate in $\text{ml}\cdot\text{h}^{-1}$, D is tip-to-collector distance in cm, and E is needle diameter in mm)	69
Table 4.4 – Comparison of electrospun preceramic polymers electrospun with/without organic polymer (¹ pyrolysed to ceramic)	75
Table 4.5 – Authors’ contributions to Chapter 4	76
Table 5.1 – Solutions’ characteristics and operating conditions of electrospinning according to samples containing oligosilazane or polysilazane	83
Table 5.2 – Absorption bands and respectively height intensity according to FTIR-ATR spectra of C-rich SiCN fiber mats.....	90
Table 5.3 – Raman features of C-rich SiCN fiber mats.....	91
Table 5.4 – Elemental compositions of C-rich SiCN fiber mats according to XPS analyses ..	92
Table 5.5 – Authors’ contributions to Chapter 5	99
Table 6.1 – FTIR peak assignments of as-spun and pyrolyzed PAN:HTTS and PAN samples	113
Table 6.2 – Raman peak assignments with corresponding full width at half maximum (FWHM) of pyrolyzed PAN:HTTS and PAN samples	117
Table 6.3 – Authors’ contributions to Chapter 6	124
Table 7.1 – Details of solution characteristics and operating conditions of electrospinning for manufacturing SiCN and SiCN/C fibers	133
Table 7.2 – Authors’ contributions to Chapter 7	148
Table 8.1 – Denomination of the samples investigated in this work.....	157
Table 8.2 – Elemental composition by XPS analyses	163

Table 8.3 – Charge and discharge capacities with respective Coulombic efficiency of 1 st and 2 nd cycles of fiber mat electrodes	165
Table 8.4 – Authors’ contributions to Chapter 8	174

LIST OF ABBREVIATIONS

AIPSZ	Polyaluminasilazane
ANOVA	Analysis of variance
ATR	Attenuated total reflection
BSU	Basic structural unit
CNTs	Carbon nanotubes
CVD	Chemical vapor deposition
D4Vi	Tetramethyltetravinylcyclotetrasiloxane
DC	Direct current
DCP	Dicumyl peroxide
DMF	N,N-Dimethylformamide
DSC	Differential scanning calorimetry
DTDS	1,3-Divinyltetramethyldisiloxane
EDS	Energy-dispersive X-ray spectroscopy
EM	Electromagnetic
EMF	Electromagnetic field
FTIR	Fourier transform infrared spectroscopy
FWHM	Full width at half maximum
H44	Polymethylphenylsilsequioxane
HTT1800	Oligosilazane
HTTS	Polysilazane
LIB	Lithium-ion battery
MK	Polymethylsilsequioxane
MWCNT	Multiwall carbon nanotubes
NMR	Nuclear magnetic resonance
NRW	Nicolson-Ross-Weir
PACS	Polyaluminocarbosilane
PAN	Polyacrylonitrile
PBSZ	Polyborosilazane
PCL	Polycaprolactone
PCP	Preceramic polymer
PCS	Polycarbosilane
PDC	Polymer-derived ceramic
PEO	Polyethyleneoxide
PHMS	Polyhydromethylsiloxane
PhSSQZ	Phenylsilsequiazane
PMMA	Poly(methyl methacrylate)
PPS	Polyphenylsilane
PS	Polystyrene
PUS	Polyureasilazane
PVP	Polyvinylpyrrolidone
RCS	Radar cross-section
RSN	Phenyl-siloxane
SAED	Selected electron area diffraction
SE	Shielding effectiveness

SEI	Solid electrolyte interphase
SEM	Scanning electron microscopy
TBAF	Tetra-n-butylammonium fluoride
TEM	Transmission electron microscopy
TEOS	Tetraethyl orthosilicate
TGA	Thermogravimetric analysis
THF	Tetrahydrofuran
TDSB	Tris(methyldichlorosilylethyl)borane
TPTS	1,3,5-Trivinyl-1,1,3,5,5-pentamethyltrisiloxane
TTCS	1,3,5,7-Tetramethyl-1,3,5,7-tetravinylcyclotetrasiloxane
VSWR	Voltage standing-wave ratio
XPS	X-ray photoelectron spectroscopy
XRD	X-ray diffraction

TABLE OF CONTENTS

1	INTRODUCTION	17
1.1	AIM OF THE WORK	18
1.2	STRUCTURE OF THE THESIS	18
1.3	REFERENCES	19
2	METHODOLOGICAL SEQUENCE FLOWCHART	21
3	Electrospun ceramic fibers from Si-based preceramic polymers¹	22
3.1	INTRODUCTION	22
3.2	ELECTROSPINNING.....	24
3.3	PRECERAMIC POLYMERS e-SPINNABILITY.....	26
3.3.1	Solution properties	27
3.3.1.1	<i>Polymer properties</i>	27
3.3.1.2	<i>Solvent properties</i>	30
3.3.2	Process parameters.....	32
3.3.3	Environmental conditions	33
3.4	PDC ELECTROSPUN FIBERS.....	34
3.4.1	Crosslinking	34
3.4.2	Ceramization.....	35
3.5	PROPERTIES AND APPLICATIONS OF e-PDC FIBERS	37
3.5.1	Electromagnetic field shielding	38
3.5.2	Supercapacitor and lithium-ion battery electrodes.....	40
3.5.3	Filtration membrane in harsh environments and gas sensing	42
3.5.4	Other properties and possible applications.....	43
3.6	FINAL REMARKS AND FUTURE PROSPECTS	45
3.7	ACKNOWLEDGEMENTS.....	45

3.8	AUTHORS' CONTRIBUTIONS	46
3.9	REFERENCES	46
4	Statistical optimization of polysilazane-derived ceramic: electrospinning with and without organic polymer as a spinning aid for manufacturing thinner fibers²	56
4.1	INTRODUCTION	56
4.2	EXPERIMENTAL	57
4.3	RESULTS AND DISCUSSION	61
4.3.1	Electrospinnability	61
4.3.2	Screening design of HTTS_60 and HTTS_PAN_17.5 solutions	67
4.3.3	Optimization of HTTS_60 and HTTS_PAN_17.5 solutions	68
4.3.4	Model validation	73
4.4	CONCLUSIONS	74
4.5	ACKNOWLEDGMENTS	76
4.6	AUTHORS' CONTRIBUTIONS	76
4.7	REFERENCES	76
5	Thermo-oxidative resistance of C-rich SiCN fiber mats influenced by selective crosslinking of oligosilazane³	81
5.1	INTRODUCTION	81
5.2	EXPERIMENTAL	83
5.3	RESULTS AND DISCUSSION	85
5.4	CONCLUSIONS	97
5.5	ACKNOWLEDGMENTS	98
5.6	AUTHORS' CONTRIBUTIONS	98
5.7	REFERENCES	99
6	Lightweight and flexible nanostructured C/SiCN nanofiber mat for electromagnetic reflection shielding of 5G C-band frequencies⁴	103
6.1	INTRODUCTION	103

6.2	EXPERIMENTAL.....	105
6.3	RESULTS AND DISCUSSION.....	109
6.4	CONCLUSIONS	122
6.5	ACKNOWLEDGMENTS	123
6.6	AUTHORS' CONTRIBUTIONS.....	123
6.7	REFERENCES	124
7	Lightweight SiCN/C fibers for microwave absorption and electromagnetic field shielding in Ku-band⁵	131
7.1	INTRODUCTION	131
7.2	EXPERIMENTAL.....	133
7.3	RESULTS AND DISCUSSION.....	136
7.4	CONCLUSIONS	147
7.5	ACKNOWLEDGEMENTS.....	148
7.6	AUTHORS' CONTRIBUTIONS	148
7.7	REFERENCES	148
8	Electrochemical performance of SiCN fiber mat electrodes for lithium-ion battery: electrospinning polysilazane in air or protective atmosphere⁶	154
8.1	INTRODUCTION	154
8.2	EXPERIMENTAL.....	156
8.3	RESULTS AND DISCUSSION.....	158
8.4	CONCLUSIONS	172
8.5	ACKNOWLEDGEMENTS.....	173
8.6	AUTHORS' CONTRIBUTIONS.....	174
8.7	REFERENCES	174
9	CONCLUSIONS.....	179
10	OUTLOOK.....	181

1 INTRODUCTION

Preceramic polymers (PCPs) have been intensively studied for more than 50 years to produce Si-based ceramic fibers, coatings, foams, nanocomposites and others [1]. These precursors represent inorganic/organometallic systems that provide polymer-derived ceramics (PDCs) with tailored chemical composition and a closely defined nanostructural organization by proper thermal treatment in a protective atmosphere [2]. Compared to traditional ceramics using powder technology, major benefits of PDCs rely on higher purity/composition control, significant reduction of the processing temperature, the possibility to produce multi-component and hybrid (organic-inorganic) materials, and high versatility in terms of processability [3]. The PDC route includes often four steps through the thermochemical conversion of PCPs: shaping (to produce a particular form), crosslinking (to obtain a thermoset polymer and avoid melting during pyrolysis), pyrolysis (to obtain an amorphous ceramic), and optionally annealing (to crystallize the amorphous ceramic) [4]. Properties, such as chemical and thermal stability, solubility, rheological behavior, and optical characteristics of PCPs, and the composition of final PDCs are strongly influenced by the backbone structure and the side groups, which is also critical to crosslinking and polymer to ceramic transformation [5].

The application fields of PDCs have been extended significantly by recent research and development activities using the electrospinning technique since the works of Sarkar *et al.* [6] and Shin *et al.* [7] in 2008. Shaping of PCPs by electrospinning offers innovative microstructure and mainly design possibilities for the manufacturing of multifunctional materials addressing several mission objectives with only one structure [8]. However, electrospinning also poses new challenges in terms of process control, since it requires the addition of a spinning aid to manufacturing homogeneous fibers. Despite the ongoing discovery of electrospun PDCs has shown outstanding results, research on electrospinning Si-based PCPs to produce advanced PDC fiber mats/fibers is still in the beginning. Exciting possibilities are emerging in the development of PDCs fiber mats/fibers including more studies on the intimate relationships between molecular architecture and microstructure and properties of the ceramic materials resulting from electrospun preceramic polymers and the application expansion of PDCs that are currently on the rise. With each new development, a greater understanding of the complex relationships between specific modifications and the changes they bring about is achieved.

Electrospun PDC fiber mats/fibers have been investigated in advanced applications. For the traditional electromagnetic field shielding material, metals are usually coated around electric equipment to block radiation propagation, however, the heavyweight, easy corrosion and difficult processing limit their broad application. Therefore, the development of new electromagnetic field shielding materials with light weight, flexibility and high shielding efficiency is a research hotspot. Currently, carbon electrodes are used in lithium-ion batteries (LIBs) due to their low price, despite low capacity. Recent studies have investigated Si-based ceramics prepared via the PDC route as potential LIB electrodes, mostly based on SiOC and using the slurry-casting method, which, however, increases the overall weight. Some progress has been made regarding PDCs shaped through electrospinning to produce freestanding fiber mats, but additional research is required. The development of electrospun ceramic fibers from Si-based PCPs that demonstrate desired properties in electromagnetic field shielding and electrochemical energy storage is promising.

1.1 AIM OF THE WORK

This work aims to prepare ceramic fiber mats/fibers from Si-based preceramic polymers while using polysilazane as one of the main precursors and electrospinning as the shaping technique for advanced applications including electromagnetic field shielding and electrochemical energy storage.

1.2 STRUCTURE OF THE THESIS

This thesis is divided into several Chapters, whose key points are provided hereafter.

In the current Chapter 1, a general contextualization is displayed alongside the aim of this work.

Chapter 2 is supposed to show the methodological sequence flowchart of this work by providing a picture overview of the separate steps in sequential order.

Chapter 3 is intended to provide an overview of the state of the art of electrospun ceramic fibers from Si-based preceramic polymers to visualize the big picture where this thesis is framed. In this review, the different strategies to prepare ceramic fibers via electrospinning, including preceramic polymer e-spinnability and polymer-to-ceramic transformation, are discussed. Subsequently, the properties and applications of e-PDC fibers are demonstrated.

Chapters 4, 5, 6, 7 and 8 consist of the experimental results achieved during this Ph.D. work. In Chapter 4, the electrospinning of polysilazane-derived ceramic with and without organic polymer as a spinning aid was optimized using a statistical approach to manufacturing thinner fibers. Chapter 5 describes the influence of selective crosslinking of oligosilazane on electrospinning and thermo-oxidative resistance of SiCN/C fiber mats. In Chapter 6, the potentiality in electromagnetic reflection loss in 5G C-band and modification of electrical conductivity of C/SiCN fiber mats are demonstrated. The microwave absorption and electromagnetic field shielding properties of SiCN/C fibers in the K_u-band were investigated in Chapter 7. Chapter 8 reports the influence of electrospinning polysilazane in air or protective atmosphere and the electrochemical performance of SiCN and SiCN/C fiber mat electrodes for lithium-ion batteries.

Chapter 9 presents a summary of the main conclusions from this Ph.D. work, putting into perspective the contributions derived from it. Moreover, the interconnection between the papers that originated from this work is evidenced as well.

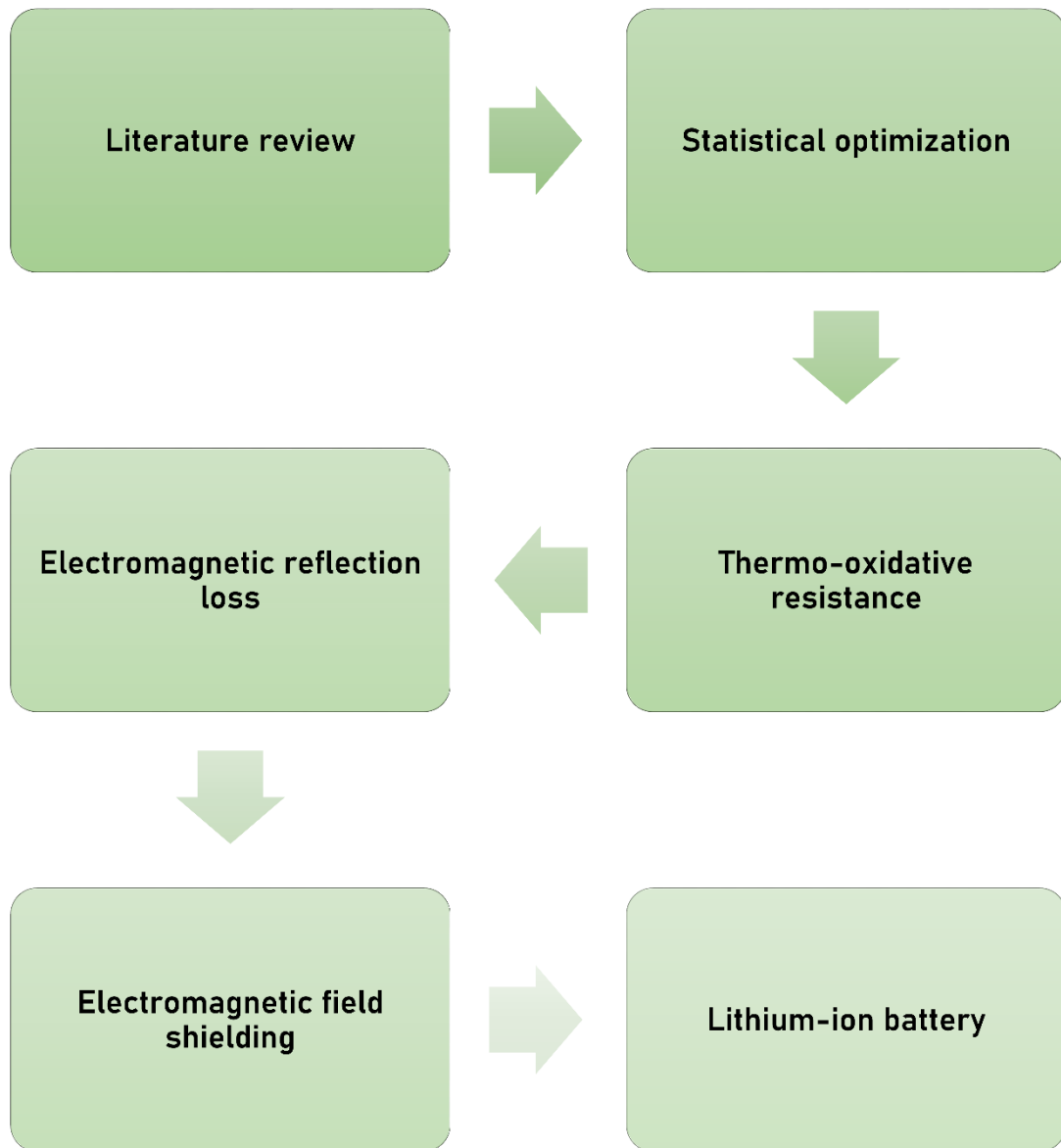
Chapter 10 extrapolates the horizon of possibilities for future works related to this topic, discussing some outlooks and remnant gaps in this matter.

1.3 REFERENCES

- [1] Q. Wen, Z. Yu, R. Riedel, The fate and role of in situ formed carbon in polymer-derived ceramics, *Prog. Mater. Sci.* 109 (2020) 100623. <https://doi.org/10.1016/j.pmatsci.2019.100623>.
- [2] P. Colombo, G. Mera, R. Riedel, G.D. Sorarù, Polymer-derived ceramics: 40 years of research and innovation in advanced ceramics, *J. Am. Ceram. Soc.* 93 (2010) 1805–1837. <https://doi.org/10.1002/9783527631971.ch07>.
- [3] A. Lale, M. Schmidt, M.D. Mallmann, A.V.A. Bezerra, E.D. Acosta, R.A.F. Machado, U.B. Demirci, S. Bernard, Polymer-derived ceramics with engineered mesoporosity: from design to application in catalysis, *Surf. Coatings Technol.* 350 (2018) 569–586. <https://doi.org/10.1016/j.surfcoat.2018.07.061>.
- [4] D. Hotza, R.K. Nishihora, R.A.F. Machado, P. Geffroy, T. Chartier, S. Bernard, Tape casting of preceramic polymers toward advanced ceramics: a review, *Int. J. Ceram. Eng. Sci.* 1 (2019) 21–41. <https://doi.org/10.1002/ces2.10009>.
- [5] G. Barroso, Q. Li, R.K. Bordia, G. Motz, Polymeric and ceramic silicon-based coatings - a review, *J. Mater. Chem. A* 7 (2019) 1936–1963. <https://doi.org/10.1039/c8ta09054h>.
- [6] S. Sarker, A. Chunder, W. Fei, L. An, L. Zhai, Superhydrophobic mats of polymer-derived ceramic fibers, *J. Am. Ceram. Soc.* 91 (2008) 2751–2755. <https://doi.org/10.1111/j.1551-2916.2008.02500.x>.
- [7] D.G. Shin, D.H. Riu, H.E. Kim, Web-type silicon carbide fibers prepared by the electrospinning of polycarbosilanes, *J. Ceram. Process. Res.* 9 (2008) 209–214.

- [8] G. Mera, M. Gallei, S. Bernard, E. Ionescu, Ceramic nanocomposites from tailor-made preceramic polymers, *Nanomaterials*. 5 (2015) 468–540. <https://doi.org/10.3390/nano5020468>.

2 METHODOLOGICAL SEQUENCE FLOWCHART



3 ELECTROSPUN CERAMIC FIBERS FROM Si-BASED PRECERAMIC POLYMERS¹

This chapter aims to provide a literature review on the manufacturing of ceramic fibers from Si-based preceramic polymers via electrospinning. This chapter brings the description of the electrospinning technique, the main strategies to achieve fibers by this method using preceramic polymers, crosslinking and pyrolysis procedures, and the applications and properties of Si-based electrospun mats/fibers.

3.1 INTRODUCTION

The Si-based PCPs are inorganic/organometallic systems that provide polymer-derived ceramics (PDCs) with tailored chemical composition and a closely defined nanostructure organization by proper thermal treatments in controlled atmospheres [1]. The technology of PDCs is based on the conversion of suitable molecular PCPs into ceramics through a series of thermally or chemically-induced processes. First, thermoset polymers are formed by crosslinking reactions and then converted into a ceramic due to eliminating non-crosslinkable organic groups [2–4].

Due to the simplified shaping process and lower temperatures (from about 800 °C), high aspect ratio ceramic structures are more straightforward to produce from PCPs [5]. In contrast to oxide ceramics, ceramic fibers manufactured from PCPs may broaden the properties and applications of these advanced materials. Features such as high tensile strength, creep resistance, and oxidation resistance has boosted the research on ceramic fibers derived from PCPs [6–8].

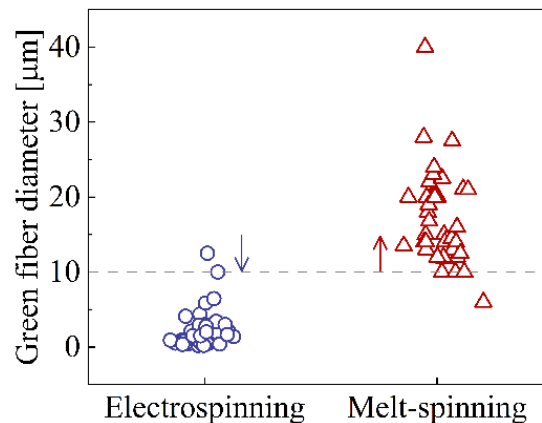
Currently, two main manufacturing approaches exist to obtain PCP fibers, known as indirect and direct. In the indirect approach, the ceramic fibers are obtained by coating available template fibers. In chemical vapor deposition (CVD), the gas phase of ceramics is deposited on carrier fibers, while in the relic process, absorbent organic fiber materials are saturated with salt solutions or sols followed by burn off of the organic [9]. Contrariwise, the inorganic precursors are directly shaped as fibers using polymer-like processing techniques in the direct approach. In the preceramic polymer route, the spinning dope consists of either a solution of an inorganic

¹Based on a paper to be submitted for publication.

polymer, which can be spun via electrospinning or meltable PCPs using melt-spinning. In the so-called solution process, soluble salts are used in the spinning dopes, while in the sol/gel process, colloidal inorganic components are used as precursors, which can be converted into ceramics during a ceramization step. In the slurry process, coarse ceramic particles are added to salt or sol-based spinning dopes to reduce the shrinkage during ceramization and increase ceramic yield.

Electrospinning and melt-spinning are the most used to produce PCP fibers. The most remarkable difference between these polymer processing techniques lies in the diameter of the fibers, electrospinning commonly renders fibers with a diameter below 10 μm , while melt-spinning yields higher-sized fiber diameter (Figure 3.1).

Figure 3.1 – Green fiber diameter of Si-based PCP fibers manufactured through electrospinning and melt-spinning. The diameter of polysilane, polysilazane, and polysilsesquioxane fibers available in the literature was considered [1,2,11–20,3,21–30,4,31–40,5,41–50,6,51–60,7,61–70,8,71–77,9,10] (the x-axis has no variation)

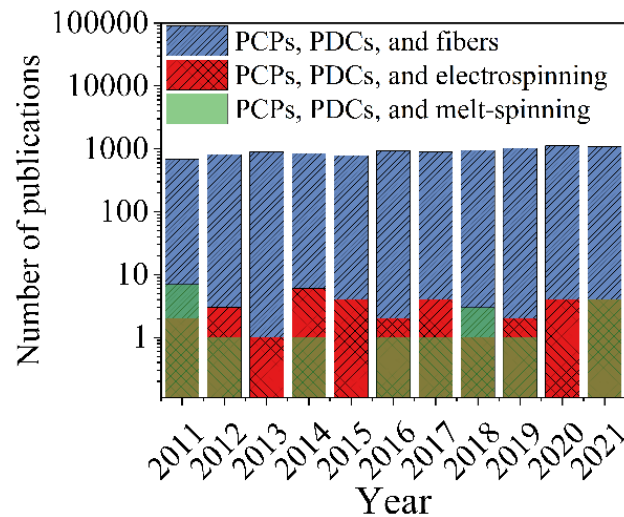


Melt-spinning is currently preferred to manufacture PCP fibers [29,87]. Nevertheless, the stringent rheological requirements limit the minimum fiber size above the microscale range ($>10 \mu\text{m}$) [88]. Electrospinning generally produces fibrous mats onto static or rotating drum collectors, whereas melt spinning produces fibers onto winders. The e-spinning approach has proven to be a suitable shaping method for several Si-based PCPs, and the processing of fibers by combining the PDC route with electrospinning, hereafter called e-PDC fibers, has gained attention over the past decade (Figure 3.2). Nevertheless, research on e-PDCs is still scarce when compared to the number of publications on PDC fibers.

The present work aims to seize the background, organize and provide a better understanding of electrospinning requirements, and fiber morphologies, establishing generalizations and guidelines in PCPs e-spinnability and morphology control, including

thermal treatment, applications, properties, and further research prospects in PDC fibers.

Figure 3.2 – Number of publications about ‘PDCs and fibers’ and ‘PDCs and electrospinning’ until 2021 (stand: 11/22/2021). The queries correspond to ‘PCPs, PDCs, and fibers’: ‘preceramic polymers’ OR ‘polymer-derived ceramics’ OR ‘PDCs’ AND ‘fibers’; ‘PCPs, PDCs, and melt-spinning’: ‘preceramic polymers’ OR ‘polymer-derived ceramics’ OR ‘PDCs’ AND ‘melt-spinning’; and ‘PCPs, PDCs, and electrospinning’: ‘preceramic polymers’ OR ‘polymer-derived ceramics’ OR ‘PDCs’ AND ‘electrospinning’ (database: Scopus)

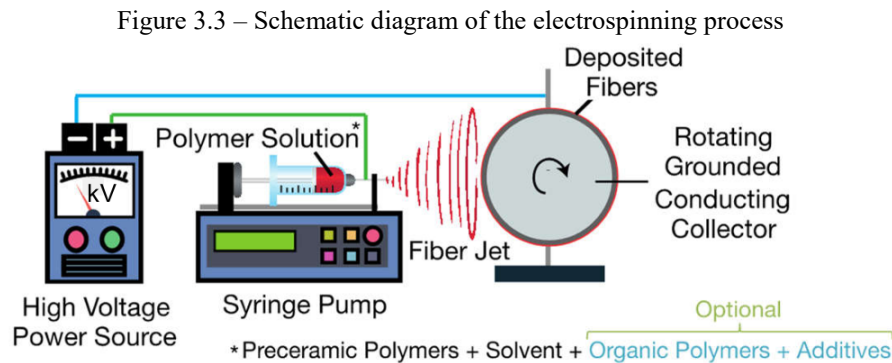


3.2 ELECTROSPINNING

Electrospinning, or still electrostatic spinning or e-spinning, is a standard process to manufacture non-woven mats, i.e., thin fibers between micrometer to nanometer dimensions. Typically, an electrostatic force attracts an extruded polymer solution from a capillary spinneret to a suitable conductive collector [89]. The basic experimental setup consists of an extruder with a capillary spinneret, a high voltage supply, and a collector (Figure 3.3). The electrostatic charge of a solution drop held at the tip of the fine capillary overcomes the drop surface tension when a sufficiently high electric field is applied, causing the liquid ejection from the tip to the collector, resulting in the formation of drops or fibers, electrospinning or electrospinning, depending on process parameters. The syringe dosing pump with a control feed rate normally varies typically from 0.1 to 5 ml·h⁻¹; the provided voltage supply must be able to generate a potential difference up to 30 kV; and the collector body consists of a conductor assembly, which can be static or rotating.

Organic polymers are undoubtedly the most used to produce electrospun fibers (e-fibers) [90]. Electrospinning-shaped ceramic fibers have been composed of simple oxides (alumina [91], silica [92], titania [93], and zirconia [94]) and complex oxides [95] (such as

CaCu₃Ti₄O₁₂ and Li_{1.6}Al_{0.6}MnO₄) since the initial reports in 2002 and 2003 [96]. Electrospun non-oxide ceramics have also shown a promising development since the pioneering work in 2005 on boron carbide/carbon fibers from a polynorbornenyldecaborane [97]. Remarkably, the e-spinning of Si-based PCPs has presented an increasing interest in the fabrication of advanced ceramics since the works of Sarkar *et al.* [98] and Shin *et al.* [62] in 2008.



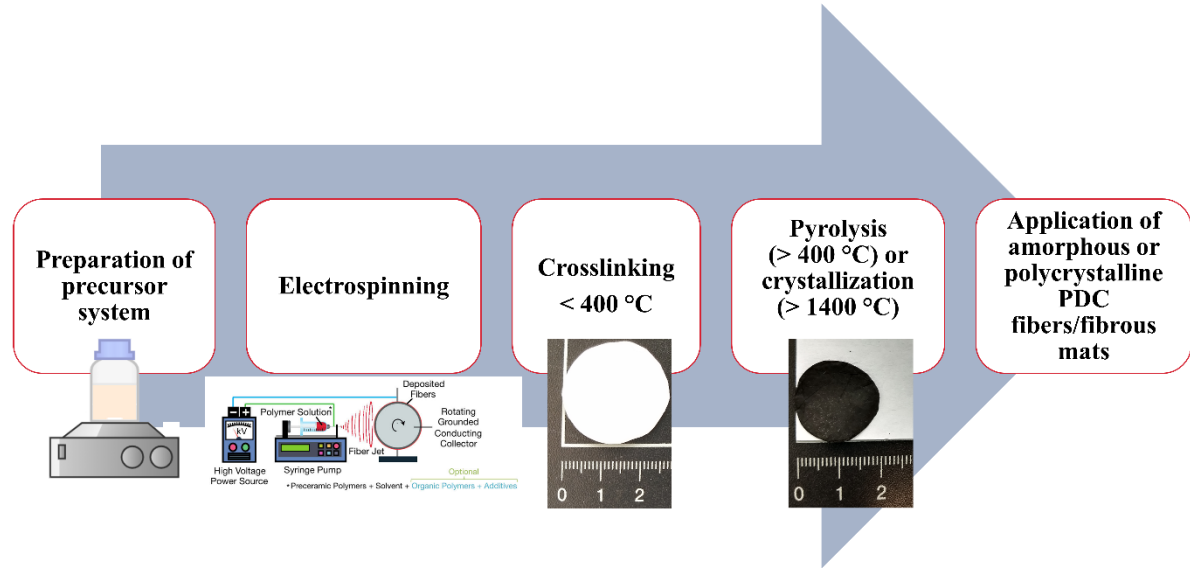
Nowadays, thin fibers (<1 μm) can be obtained through different techniques such as electrospinning, melt blowing, self-assembly, sonochemical synthesis, and template-based synthesis. Emerging techniques have also been applied, such as solution blow spinning, centrifugal jet spinning, CO₂ laser supersonic drawing, electrohydrodynamic direct writing, and plasma-induced synthesis [99]. Among those shaping-processing routes, electrospinning stands out, mainly due to its simplicity and versatility in producing thin fibers with controllable morphology from various polymers, including Si-based PCPs.

Among ceramic spinning processes, electrospinning has the advantage of producing thin fibers from PCPs ranging from nano- to micrometers by adjusting the process parameters [100]. Lower fiber diameters result in enhanced fiber strength for the same material due to the reduction of possible defects generated during the manufacturing process. Furthermore, thin e-fibers present a higher specific surface area, which broadens their application. First, the precursor system is usually prepared with the addition of PCP, an organic polymer, solvent, and other additives, and the solution is electrospun with the appropriate operating parameters. The electrospun fibers are then crosslinked and pyrolyzed with the possibility of crystallization to obtain amorphous or polycrystalline PDC fibers (Figure 3.4).

Through electrospinning and thermal treatment, PDC fibers can be produced with a diameter from 10 nm to 2 μm [84], 700 to 1400 times smaller than fibers fabricated by melt-spinning. For example, the diameter of silicon carbonitride (SiCN) fibers could achieve 50 nm

in electrospinning [101], whereas values of up to 35 μm are reported for melt-spinning [102]. Furthermore, silicon carbide (SiC) fibers derived from polycarbosilane (PCS) presented diameters of 10 nm when obtained by electrospinning [84], 14 μm by melt-spinning [6], 100 μm by dry spinning [103], and 1800 μm by dry-wet spinning [104].

Figure 3.4 – Schematic depiction of the manufacturing of PDC fibers/fibrous mats through electrospinning and thermal treatment



Although electrospinning is a mature technique, e-PDCs published research is incipient. The spinning of PCPs is only slightly referred to in the most cited review on PDCs [1]. Most of the reviews available on PDCs deal with only a subset of PCPs and ceramics fibers, e.g., polysilazanes, to produce SiCN-based ceramic fibers [105–107].

3.3 PRECERAMIC POLYMERS e-SPINNABILITY

The term e-spinnability, i.e., electrospinnability, was coined to indicate polymer solutions suitable to electrospun allowing the production of homogenous fibers at different diameter scales, classified as microfibers (1 μm to 1 mm), ultrafine/submicrofibers (100 nm to 1000 nm), and nanofibers (<100 nm). The resultant morphologies from electrospun PCPs range from single droplets (electrospraying) to seamless uniform fibers, with beads-on-string structures as a transition between both. This shape depends on the solution properties, process parameters, and environmental conditions that control the properties of the electrified jet during electrospinning. The e-spinnability can be categorized as excellent when no droplets and beads-

on-string are observed in the collector and fibers, the latter known as seamless fibers. The factors are divided hereafter into three categories: solution properties, process parameters, and environmental conditions.

3.3.1 Solution properties

The interplay among the solvent, precursors, and concentration determines the properties of the solution. The PCPs are typically used in a blend with organic polymers, the latter component as an additive to meet the e-spinnability conditions to fulfill the process.

3.3.1.1 Polymer properties

To get seamless fibers is not a straightforward task; e-fibers manufacture requires a sufficient amount of chain entanglements in the polymer solution, which prevents the electrospun jet from breaking up, resulting in a steady formation of fibers. These entanglements mainly depend on the polymer molecular weight and the solution concentration [108]. When increasing the polymer concentration, the polymer chain entanglements strengthen, and the chain mobility declines, hardening the jet extension and reducing the disruptions during jet flying, thus favoring the formation of large-diameter fibers [109]. Therefore, the fiber diameter is proportional to the entanglement density [110]. Contrariwise, a low molecular weight polymer or low concentration solution produces electrospaying, droplets formation instead of fibers [83,111].

The main electrospinning challenge of PCPs is the entanglements mentioned above, which can be related to rheological requirements. Commercially available PCPs are composed of cyclic or linear units with a complex structure and low molecular weight, making the electrospinning procedure extremely difficult. For this reason, most of the current works on e-PDCs are based on the mixture of PCPs with high molecular weight organic polymers, which provides the required viscoelasticity. Despite the improved manufacturability, organic polymers may compromise mechanical stability by generating undesirable macropores within the fibers during the pyrolysis step.

Most of the works dealing with preceramic (silicon-based) and organic (carbon-based) polymer blends employed a concentration of 75 wt.% PCP and 25 wt.% organic polymers. Organic polymers mostly employed are polyvinylpyrrolidone (PVP), poly(methyl

methacrylate) (PMMA), polystyrene (PS), polyacrylonitrile (PAN), polycaprolactone (PCL), and polyethyleneoxide (PEO). The organic polymer used as an e-spinnability agent is chosen based on the inorganic-organic polymer blend compatibility with the solvent and its commercial availability. These polymers are also offered in several viscosity grades and a wide range of molecular weight and molecular structure.

PVP is largely used as e-spinning agent for polyureasilazane (PUS), polymethylphenylsilsesquioxane (H44) and polymethylsilsesquioxane (MK). PVP binds these PCPs exceptionally well, a feature attributed to the polar character of these polymers. Furthermore, all the above-mentioned polymers solubilize in N,N-dimethylformamide (DMF), acetone, ethanol, and isopropanol.

Another broadly used polymer is PMMA, reported as a sacrificial template for coaxial electrospinning due to its immiscibility with PCS/DMF/toluene solution but good solubility in DMF/toluene solvent. PMMA decomposition with negligible residues at around 400 °C and excellent e-spinnability make this e-spinning agent suitable for PCP blends [56]. As PMMA, the addition of PS into phenylsilsesquiazane (PhSSQZ)/DMF solution aided the formation of bead-free fibers through electrospinning by increasing the chain entanglements and viscosity [81].

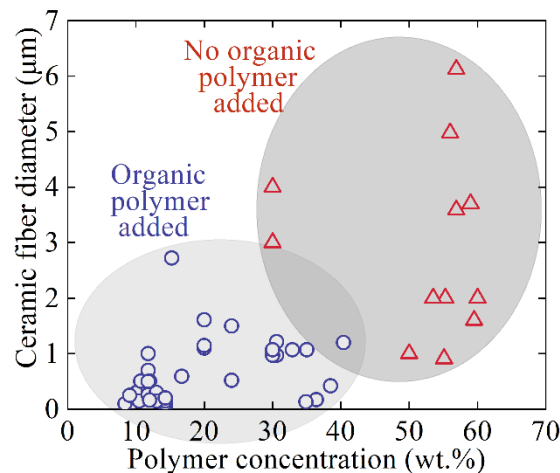
As previously mentioned, PAN, PCL, and PEO are used to improve PCPs e-spinnability, but less than PS and PMMA, which is attributed to their cost and availability. The former polymers are considered high quality, and the latter are commonly used as porous formers or as a template for burnout, even in conventional ceramics manufacture [112,113]. Nevertheless, PAN, PCL, PEO, and PCPs mixtures enhance the e-spinnability of the blend. For instance, the addition of PEO into polyaluminasilazane (AlPSZ)/chloroform/DMF solution improved the e-spinnability through hydrogen bonding, which increased the chain overlap of the polymers [98].

The diameter and morphology of e-fibers derived from PCPs are dependent on the polymer concentration and the nature of the solvent. In the case of blends, the diameter depends on both preceramic and organic polymer concentration. For example, electrospun PUS/PMMA/acetone fibers are slightly larger and more varied in size than PUS/PS/DMF fibers [69], since PMMA is more viscous than PS [114]. The diameter of SiC e-fibers derived from PUS/PVP/ethanol increased comparatively 2400%, just by using threefold PUS (from 12 to 36 wt.%), as previously discussed, this attributed to higher chain entanglements [65]. The fiber diameter can be diminished by lowering the viscosity of the spinning solution. However, this

approach to control the fiber size corresponds to an equilibrium condition and cannot diminish indefinitely since lower viscosities induce bead formation or hinder fiber formation [115]. In addition to organic polymers, other additives such as crosslinking agents, surfactants, and conductivity modifiers have been reported to aid in controlling the fibers' size, also serving as e-spinnability agents.

Although the use of organic polymers and additives seems to be a common practice in the electrospinning of PDCs, some studies reporting the use of pure PCPs can be found in the literature. In general, PCPs electrospun without the aid of an organic result in larger ceramic fibers due to the required higher polymer concentration (Figure 3.5). For instance, the addition of PAN to polysilazane reduced fiber diameter from 1.79 μm to 0.57 μm due to a decrease in the degree of polymer chain entanglement i.e. more relaxation of the ceramic precursor molecular chains [116]. The viscosity of the precursor solution is usually proportional to the concentration and molecular weight of the spinning solution. Higher viscosity increases the chain entanglement among the polymer chains in the Taylor cone at the point of disruption, resulting in a pronounced effect on the electrospinning process. The chain entanglements of the polymer solution overcome the surface tension and ultimately result in uniform beadless electrospun fibers.

Figure 3.5 – Ceramic fiber diameter as a function of the polymer concentration of the main PCPs available in the literature (PCS, PUS, MK, and H44) [45,47–49,51–54,58–60,62–65,67–71,78,80,101,117–139]



Ribeiro *et al.* observed different polymer solution regimes (diluted, semi-diluted, and concentrated) for the resulting morphology of e-spun polysilazane synthesized by selective crosslinking of oligosilazane (spherical particles, beaded fibers, and seamless fibers) [72]. This transition was observed when the PCP concentration was increased from 50 to 65 wt.% of

polysilazane in tetrahydrofuran (THF). Furthermore, the rheological investigation showed that a pronounced shear-thinning behavior appeared for samples with polymer concentrations higher than 60 wt.% attributed to the polymer chain alignment in the applied shear stress direction and the switch of diluted to a semi-diluted regime in the range of 50 to 60 wt.% of polysilazane concentration.

To produce e-PDC fibers from pure PCS is a difficult task for its low molecular weight, commonly lower than $2000 \text{ g}\cdot\text{mol}^{-1}$ [139]. Electrospun PCS without spinning additives has been previously reported [51,58,59,133]. However, the manufacturing window is challenging to achieve concerning the resultant morphology and the sensitive production parameters. When employing a $0.9 \text{ g}\cdot\text{L}^{-1}$ PCS concentration in DMF/toluene solution, large beads are found within the fibers, even when changing the electrospinning conditions [132]. A weak entanglement network of the polymer solution does not stabilize the charged jet, generating drops and fibers with beads [109]. By varying the PCS solution to $1.1 \text{ g}\cdot\text{L}^{-1}$, homogeneous fibers can be obtained, whereas, for $1.2 \text{ g}\cdot\text{L}^{-1}$ concentration, the solution was unspinnable.

3.3.1.2 Solvent properties

Beyond the rheological properties of the polymeric solution, the properties of the solvent and its interaction with the polymer also play an essential role in optimizing the electrospinning process [140]. The solvent can also support the control over the fibers' size and morphology, as they can be used to adjust the properties of the polymer solution and process parameters [105]. In general, the solvent might meet some basic requirements: to solubilize the polymer; and have a moderate boiling point, which provides an idea about their volatility [89]. PCPs are usually modified to add functionalities and to promote manufacturability and, after this modification, the precursor is required to remain soluble in the solvent. To accurately electrospun PCPs, suspension stability is required to produce homogeneous fibers when present any insoluble material within the solution. The solvents used for this purpose are conventionally DMF, chloroform, xylene, ethanol, acetone, and THF. Within the electric field, the fiber jet from a high conductive solution is subjected to greater tensile forces, reducing the diameter of the fibers [141]. The Rayleigh equation, which relates the rate at which a viscous fluid thread is broken up into droplets, states that solvents with low surface tension produce smooth fibers, while solvents with high surface tension result in fluid thread breakup (instability), thus, impeding the fibers formation or promoting defects. Thus, the diameter of the fibers can be

reduced by decreasing the solution surface tension, diminishing the viscosity, increasing the solution dielectric constant, or the electrical conductivity [142,143].

DMF is often used as an additive in the solvent system to prepare organic polymer fibers, and this is also a common practice in the electrospinning of PCPs. DMF influenced the fibers' mat formation, fiber-size reduction, uniformity, and elimination of beads in PCS e-fibers [62]. The reduction of fiber diameter with DMF due to higher dielectric constant is also reported in the electrospinning of AIPSZ precursor [98]. The diameter of the SiOC e-fibers derived from H44/PVP/DMF is smaller than those formed from MK/PVP/isopropanol [71]. Despite that DMF possesses higher surface tension, the smaller diameter is determined by its higher dielectric constant when compared to isopropanol.

The mixture of solvents is typically focused on controlling the dielectric constant and surface tension of the polymeric solutions. By adjusting the solvent properties, Luo *et al.* (2011) produced different fiber morphologies starting with the same polymeric precursor. Continuous smooth fibers with circular cross-sections were produced from MK in acetone; seamless fibers were produced from MK in a binary solvent system prepared by mixing methyl acetate and cyclohexanone at 1:1 volume ratio; short discontinuous fibers were produced from MK in methanol [82]. Therefore, the resultant morphology is related to the properties of each solvent: methanol has a much higher dielectric constant and lower surface tension values than acetone, methyl acetate, and cyclohexanone. The solvent properties resulted in different dynamic effects on the fluid jet of electrospinning. The high dielectric constant of methanol produced bending instabilities due to the available free charge in the solution.

The removal of the solvent is a crucial part of the electrospinning process since the presence of residual solvent modifies the polymer properties, in particular, acting as a plasticizer. If the solvent is insufficiently volatile, the solvent cannot be removed during electrospinning, causing fibers to become fused when in contact. For a highly volatile solvent, the spinneret might become blocked by the accumulation of dry material. The amount of solvent is adjusted to achieve the equilibrium between the described scenarios and reach a suitable spinning solution viscosity.

The evaporation rate of the solvent is related to the solution viscosity, charge density, ambient, and jet diameter. The solvent evaporation rate is not uniform and directly depends on the surface area [144]. Solvents with different evaporation rates induce phase separation, generating nanostructures on the e-fiber surfaces. The electrospinning of AIPSZ precursor solubilized in chloroform/DMF solution resulted in surface roughness [98]. Nevertheless, e-

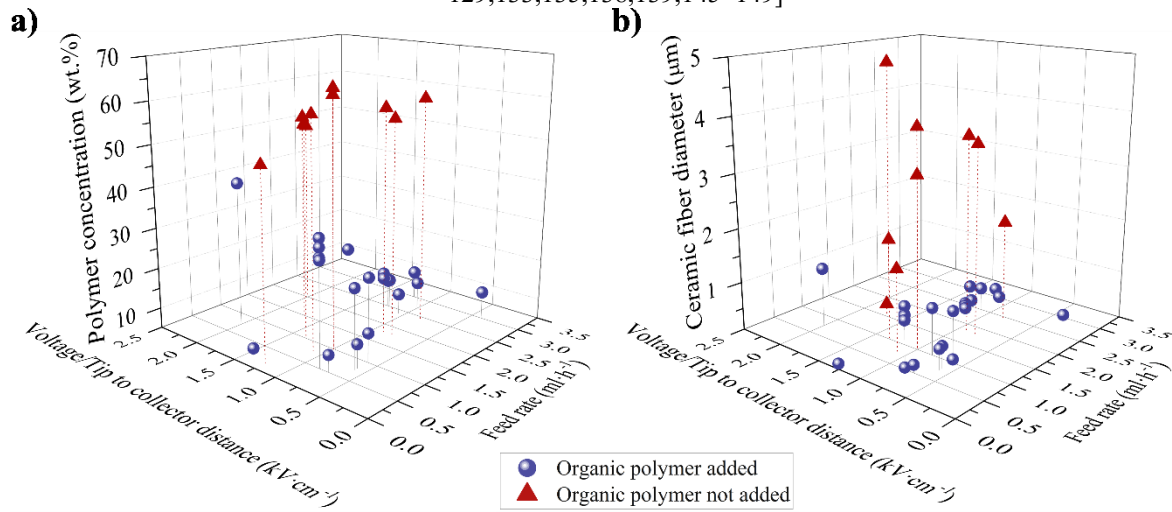
spinnability is primarily determined by polymer concentration [71]. The solvent system and the molecular weight of the PCP independently affected the e-fiber aspect ratio [82].

3.3.2 Process parameters

Electric field strength, tip-to-collector distance, feed rate, and orifice diameter of the nozzle are the typical electrospinning process parameters. The electric field strength can be manipulated by changing the applied voltage or adjusting the distance between the tip and the collector. During electrospinning of PCS, PUS, MK, and H44 with an organic polymer, a higher polymer concentration requires a higher voltage/tip to collector distance ratio and lower feed rate (Figure 3.6a). Nevertheless, this trend is not followed for electrospun PCPs without an organic polymer; a ratio of $\sim 1 \text{ kV}\cdot\text{cm}^{-1}$ and $\sim 1\text{-}2 \text{ ml}\cdot\text{h}^{-1}$ as feed rate are often the chosen process parameters. In general, for several organic polymers, higher values of applied voltage increase the electrostatic repulsive forces on the ejected jet and therefore decrease the fiber diameter; whereas, a low feed rate reduces fiber diameter [90]. When considering the ceramic fiber diameter, the influence of voltage/tip to collector distance ratio is difficult to foresee for PCPs blended with an organic polymer; however, a lower feed rate leads to thinner fibers (Figure 3.6b). A higher voltage/tip-to-collector distance ratio contributes to thinner PCPs' fibers, whereas feed rate does not show a clear tendency. The critical values of electric field strength, tip to collector distance, and feed rate vary from PCP to PCP. An interaction between process parameters of PCPs' electrospinning cannot be neglected as well.

Despite the fundamental relevance of process parameters in electrospinning, they are somehow neglected and little explored in the electrospun PCPs field. These parameters are optimized through a trial-error approach of heightened factors, barely mentioned in the e-PDCs literature. Only one work studied the voltage as a parameter, which ranged from 10-70 kV. As expected, the diameter of SiC e-fibers derived from PCS was smaller when increasing the applied voltage during the electrospinning [51]. Therefore, other factors widely studied in the electrospinning of organic polymers are expected to be applied to the PCPs field in the same way.

Figure 3.6 – Properties of e-PDC fibers regarding voltage/tip to collector distance ratio and feed rate with a) polymer concentration and b) ceramic fiber diameter [46–49,52,67,69–72,78,118,120–129,133,135,138,139,145–149]



3.3.3 Environmental conditions

The environmental conditions in electrospinning include temperature, humidity, local atmosphere flow, atmospheric composition, and pressure. Constant temperature ensures the reproducibility of the electrospun PCPs due to constant viscosity. Small changes in temperature, pressure and relative humidity can have a significant effect on the e-PDC. It is also important to point out that some PCPs are sensitive to moisture. For example, polycobaltsilazane is electrospun in an argon atmosphere to control the effects of moisture and oxygen during electrospinning [74]. Furthermore, incorporating oxygen during electrospinning can result in different physical and chemical characteristics of the e-PDCs, such as observed with electrospun fibers from organic polymers [150].

Controlling the humidity is one of the simplest ways to modify the surface of electrospun fibers regarding pore frequency and size (diameter and depth) through the nonsolvent-induced phase separation method; water forms droplets on the surface, producing pores. The humidity is typically controlled in a protected atmosphere inside a closed chamber. For high relative humidity, above 70% in the electrospinning chamber, water worked as entrapment for the solvent leading to macropores formation on the PCS fiber surface [139]. This effect has been observed in DMF and acetone/DMF solvents, which are miscible in water, resulting in macropores on the electrospun fibers [133].

3.4 PDC ELECTROSPUN FIBERS

Controlled thermal treatment of electrospun PCPs provides ceramic fibers with nanostructures strongly influenced by the chemistry and architecture of the precursors and the parameters used for their pyrolysis (heating rate, reactive or inert atmosphere, and dwelling time). This section discusses the post-electrospinning processes of SiC, SiOC, and other PDCs, dividing into crosslinking and ceramization. Electrospun fibers of PCPs without further pyrolysis are also reported in the literature [73,100,151]. In these cases, the volume change of the organic polymer during ceramization could cause internal stresses, leading to a collapse of the structure of the e-fibers.

3.4.1 Crosslinking

Crosslinking is essential for maintaining the fibrous structure, avoiding fibers' melting and loss of shape during high-temperature treatment. During crosslinking, the PCP fibers are converted into organic/inorganic materials at low temperatures. This transformation prevents the loss of low molecular weight components of the PCPs and fragmentation processes during ceramization and consequently leads to high ceramic yields [152]. Incorporating suitable functional groups (e.g., Si-H, Si-OH, or Si-vinyl functionalities) enables the formation of a thermoset via condensation or addition that occurs spontaneously [1].

The crosslinking of PCP fibers is based on catalyst-assisted and thermal techniques. Typically, the PCP fibers are crosslinked in air at 210 °C for 2 h. The addition of a crosslinking catalyst is usually necessary to maintain the fiber shape during the polymer-to-ceramic transformation. There are various crosslinking catalyst agents reported in the literature: aluminum acetylacetonate [134], azobisisobutironitrile [72], dibutyltin dilaurate [70,71,126,127], dicumyl peroxide [153], palladium acetylacetonate [154], platinum divinyltetramethyldisiloxane [155], tin acetate [128], zinc acetylacetonate hydrate [135], and zirconium acetylacetonate [71,127,129]. The non-addition of a catalyst may increase the curing time of the e-fibers [130]. Furthermore, spontaneous crosslinking may occur in air during electrospinning; the extent of crosslinking strongly affects the rheological behavior of the PCP, and therefore it has to be carefully controlled.

Alternative crosslinking methods of PCP e-fibers include photo-curing and e-beam irradiation. During electrospinning of acrylate-grafted PCS/xylene/acetone mixed with a photo-

initiator, 400 W UV-light lamp illuminated directly onto the jet traveling from the syringe to the aluminum foil collector [78]. This induced photo-crosslinking by polymerizing the acrylate group on acrylate-grafted PCS. Polycarbomethylsilane was cured under a 254 nm wavelength UV lamp for 24 h [88]. The electrospun PCS mat was crosslinked by electron beam irradiation up to 10 MHz in an argon atmosphere and set on a water-cooled stainless-steel bed to prevent the temperature from rising [149]. This crosslinking resulted in the formation of the Si-Si bond from Si-H and Si-CH₃. The e-beam crosslinked PCS mat was thermodynamically more stable than the PCS mat without crosslinking. The e-fibers cured by electron beam irradiation showed lower oxygen content in a nitrogen atmosphere and 1% oxygen because the crosslinking reaction mainly occurred between Si-C bonds [56]. Crosslinking in air at low temperatures is mostly the chosen method; however, oxidative crosslinking of PCS leads to SiC materials with oxygen contents [152].

3.4.2 Ceramization

After obtaining the green non-woven mat by crosslinking, the polymer-to-ceramic transformation continues with pyrolysis (~400-1400 °C), where amorphous ceramic fibers are manufactured, or crystallization/annealing (~1000-2000 °C), where crystalline ceramic fibers are manufactured. Typically, the crosslinked PCP fibers are pyrolyzed/crystallized in argon at 1000-1400 °C for 2 h. The microstructure and the composition of the e-PDC depend on the precursor and the parameters of thermal treatment, which are inherent to PDC technology.

The e-PDC fibers are usually circular at the cross-section, but other morphologies are reported, such as ribbon-like [135], wrinkle-like [156], bamboo-like [69], and luffa-like [157]. The e-PDC fibers are mostly ultrafine/submicron and microfine/micro, while nanofibers are scarce, even though the electrospinning process is indicated for this purpose. The e-PDC fiber with the smallest diameter was reported with SiC derived from PCS/PS/chloroform solution through the technique of concentric electrospinning [84]. However, Liu *et al.* did not mention the stability-uniformity of the obtained mat.

The ceramization of e-PDC fibers involves different mass losses according to the reaction mechanisms of each PDC class [152]. After crosslinking, the thermogravimetric analysis of polysilborazane fibers was divided into three stages from 30 to 2000 °C [158]. In the first stage, from room temperature to 500 °C, the fibers have about 5% mass loss due to the release of oligomers. The largest mass loss caused by the formation of CH₄ and H₂ during

polymer-to-ceramic transformation occurred in the second stage (500-860 °C). A slight mass loss was observed in the third stage (860-1000 °C), but from 1000 to 1500 °C, a total 12% mass loss was detected. The principal loss between 1500-1700 °C was caused by silicon nitride reaction with carbon to form silicon carbide and nitrogen and crystallization of the amorphous SiBCN fibers. The final mass loss of 5% (1800-2000 °C) was accounted for by the decomposition of silicon nitride into silicon and nitrogen.

The diameter of SiC e-fibers derived from polyaluminocarbosilane (PACS) decreased by 22.2% when heating temperature from 100 °C to 1400 °C [146]. The reduction of fiber diameter with increased pyrolysis temperature occurs due to volume shrinkage and density variation inherent to PDC technology caused by the gas release of products. When the thermal treatment is properly conducted, the e-PDC fibers may relieve stress smoothly due to a suitable shape with small dimensions. For example, SiC/hafnium carbide [52] and SiOC [129] e-fibers were manufactured after pyrolysis with a reduction of, respectively, 86.6% and 87.0% in diameter.

In the ceramization step, the organic polymer is converted into nanocrystalline graphite, while PCP is transformed into PDC. The SiC e-PDCs derived from PCS are the most studied material in this area, attributed to their versatility in several applications. The ceramization temperature and time influence the application of the e-PDC. High pyrolysis temperatures (>1200 °C) applied to SiC derived from PCS/PCL caused high conductivity due to the formation of nanocrystalline graphite and increased crystallization degree; consequently, an impedance mismatch with free space led to a decline in the performance of electromagnetic (EM) field absorption [138]. The dwelling time may be specifically evaluated according to PCP; otherwise, for a too long time, the e-fibers can become brittle, starting to decompose [76].

The manufacture of nanocrystalline SiC was conducted by combining conventional annealing and spark plasma sintering. After pyrolysis at 1150 °C, amorphous SiC was additionally annealed using the spark plasma sintering method at 1600 °C for 1 h under vacuum [48]. As a result, 3C-SiC e-fibers with a cubic structure were obtained. The final annealing step was performed in air at 700 °C for 1 h to remove the rest of the carbon.

SiOC e-fibers are also extensively investigated in electrospinning followed by a thermal treatment approach. The SiOC/titanium dioxide e-fibers with wrinkle-like surfaces were produced by electrospinning Ti-modified polyhydromethylsiloxane [156]. The wrinkle-like surface is related to the evaporation of the solvent, decomposition of the organic polymer, and the anisotropic volume shrinkage during pyrolysis. The fibers exhibited amorphous silicon

and titanium oxycarbide glass phase at 1000 °C, separated into cristobalite-SiO₂, brookite-titanium dioxide, and a trace of titanium carbide nanocrystals at 1300 °C.

Other ceramic systems, including SiCN, are also investigated in manufacturing electrospun ceramic fibers from Si-based PCPs. Electrospun PUS/PVP fibers were pyrolyzed by microwave heating to prepare SiCNO fibers, reducing thus heating time and energy consumption compared to conventional pyrolysis [80]. The microwave-assisted pyrolysis with a temperature ranging from 600-1400 °C showed favorable morphology stability of the SiCNO fibers; however, e-PDCs obtained at 1400 °C showed the highest specific superficial area with an amorphous mesoporous morphology. A higher degree of graphitization under lower temperature microwave-assisted pyrolysis was also proved.

Most of the electrospun PCP fibers are pyrolyzed with no further crystallization process. However, some studies reported crystalline e-PDC fibers. Electrospun fibers derived from PACS showed an amorphous structure at 1200 °C, a crystallization character at 1400 °C, and an increase in crystallization at 1600 °C [146]. The annealing at 1800 °C increased the SiC crystal by 1400% compared to 1300 °C; however, the pyrolysis at 1800 °C formed pores on the surface of SiC fibers due to oxygen evaporation generated during thermal curing [6]. Similar behavior was observed with the pyrolysis of UV-cured acrylate-grafted PCS electrospun mats at 1100 °C, which resulted in uniform fibers [78]. However, further heating (1500 °C), produces undesirable holes in the fiber, and the content of carbon and oxygen decreases due to the decomposition of the SiO_xC_y phase.

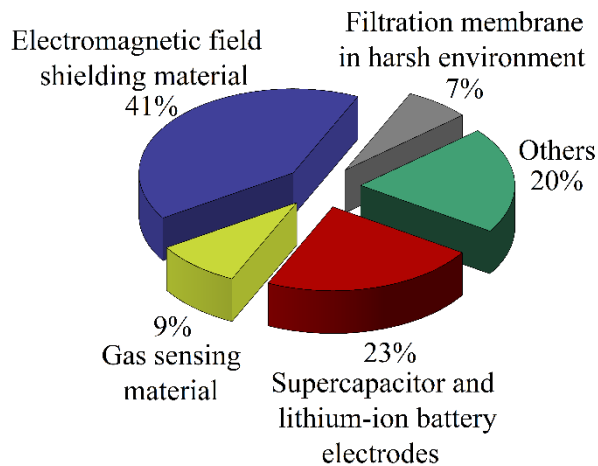
3.5 PROPERTIES AND APPLICATIONS OF e-PDC FIBERS

Electrospinning of PCPs offers a versatile and controllable approach to producing nanosized ceramic fibers that other methods cannot achieve. Well-designed synthesis of the precursors, materials processing, and characterization play a key role in producing e-PDCs with desired properties. Usually, e-PDCs are black-colored due to the generated free carbon from the decomposition of the PCP. Integrating other functional materials into the polymeric fibers introduces additional functionality and structure to the final ceramic fibers, providing new applications. The characteristics of e-PDCs can be thus varied by adding suitable fillers or modifying the process parameters. Adding some functionalities to the PDC fibers by including specific compounds confer them electrical, magnetic, or catalytic properties [105]. Fibers

produced by electrospinning combined with the PDC route present several potential applications.

The current state-of-the-art shows that most of the publications are focused on developing the e-PDC rather than its practical application. Nevertheless, for large-scale e-PDCs' application, the starting material should be cheap and readily available, and the synthesis should be straightforward. The most studied applications of e-PDCs include EM field shielding, supercapacitor and lithium-ion battery electrodes, gas sensing, and filtration membrane in a harsh environment (Figure 3.7). The applications and properties of e-PDCs are discussed hereafter. Due to the high applicability of e-PDCs to EM field shielding and energy storage, the performance of these applications is detailed.

Figure 3.7 – Applications of electrospun ceramic fibers from Si-based preceramic polymers



3.5.1 Electromagnetic field shielding

The growing popularity of handheld and wearable devices aggravates the hidden and harmful EM radiation on a large scale, directly affecting public health and the regular operation of electronic and telecommunication devices [117,118,159,160]. Therefore, exploring EM shielding materials with strong absorption, wide shielding bandwidth, small thickness, and lightweight using e-PDCs has recently received attention. These are mainly composed of the PCS/PVP or PCS/PCL systems (Table 3.1). The performance in EM-interference shielding is related to the precursor, addition of fillers, electrospinning procedure, and thermal treatment.

Table 3.1 – Electromagnetic field shielding performance of e-PDC materials

Material	Precursor	Ceramic fiber diameter (nm)	Minimum reflection loss	Effective absorption bandwidth (GHz)	Reference
SiC	PCS/PVP	200	-61 dB at 10.56 GHz	7.04	[161]
SiC	PCS/PVP	100	-41 dB at 11 GHz	5	[41]
SiC	PCS/PVP	150	-57.8 dB at 14.6 GHz	5.5	[138]
SiC	PCS/PVP	200	-19.4 dB at 5.84 GHz	14.8	[84]
SiC	PCS/PVP	150	-36 dB at 6.8 GHz	4.1	[80]
SiC	PCS/PCL/Zr(acac) ₄	330	-18.9 dB at X band	N/A	[79]
SiC/C	PCS/PVP	150	-57.8 dB at 14.8 GHz	7.3	[83]
SiC/C coated with nickel	PCS/PVP	300	-32.3 dB at 4.3 GHz	4.5	[78]
SiC/CNTs	PCS/PCL/CNTs	700	-61 dB at 12.3 GHz	2.9	[137]
SiC/Fe	PCS/PCL/Fe ₃ O ₄	10000	-46.3 dB at 6.4 GHz	5.6	[52]
SiC/Fe	PCS/PCL/Fe(acac) ₃	500	-49 dB at 8.6 GHz	7.2	[86]
SiC/Fe ₃ Si	PCS/PCL/Fe(acac) ₃	1000	-22.5 dB at 16.5 GHz	8.5	[49]
SiC/Fe ₃ Si/C	PCS/PVP/Fe(acac) ₃	230	-46.1 at 12.8 GHz	11.5	[162]
SiC fibrous aerogel	PCS/PVP	600	-21.4 dB at 10.5 GHz	2.5	[147]
SiC/graphite	PCS/PVP	300-500	-22 dB at 16.8 GHz	4.7	[81]
SiC/HfC	PCS/PCL/Hf(acac) ₄	260	-33.9 dB at 12.8 GHz	7.4	[48]
SiC/Si ₃ N ₄	PCS/PVP	100-500	-57.8 dB at 14.6 GHz	6.4	[82]
SiBCN	PBSZ	300	-56.9 dB at 10.56 GHz	3.45	[163]
C-SiCN	HTTS/PAN	420	-7 dB at 3.3 GHz	0.5	[111]
SiCN/Fe	HTT1800/PVP/Fe(acac) ₃	250	-47.6 dB at 14.6 GHz	4.3	[164]
Fe-doped SiCN	HTT1800/PVP/Fe ₂ O ₃ nanoparticles	500	-22.7 dB at 14.4 GHz	4.5	[113]

Table 3.1 – Electromagnetic field shielding performance of e-PDC materials (continuation)

Material	Precursor	Ceramic fiber diameter (nm)	Minimum reflection loss	Effective absorption bandwidth	Reference
SiCN	PCS/PVP	100-300	-54.2 dB at 17.8 GHz	4	[166]
SiCN	HTT1800/PVP	350	-31.1 dB at 11 GHz	4.6	[167]
SiCN	PCS/PVP	50-650	-53.1 dB at 11 GHz	5.6	[100]

The abbreviations correspond to PBSZ: polyborosilazane, Zr(acac)₄: zirconium acetylacetonate, CNTs: carbon nanotubes, HTTS: polysilazane, HTT1800: oligosilazane, Hf(acac)₄: hafnium acetylacetonate, and Fe(acac)₃: ferric acetylacetonate.

In this way, the EM absorption properties of e-PDCs are provided by the addition of a compound that takes up a photon's energy and transforms EM energy into the internal energy of the absorber. For example, the addition of iron into SiC e-fibers increased the permittivity and the permeability for microwave absorption by acting as catalyst sites to facilitate the growth of 100 nm SiOC nanowires on the surface of the hybrid fibers after pyrolysis [57].

The e-PDCs may form an interconnected network providing more conductive paths to improve the EM absorption property [168]. The performance of e-PDCs in EM absorption also appears from the interfacial polarization caused by large quantities of heterogeneous interfaces formed among phases, which accumulate free electrons, inducing interfacial dipoles [118]. As an example, SiC e-fibers, constituted mainly of abundant SiC nanocrystallites, a small quantity of turbostratic graphite on fibers surface and randomly distributed amorphous SiO_xC_y phase, showed excellent dielectric and EM absorption properties, which were tuned by adjusting the mass ratio of the organic polymer in the precursor solution [138]. The defect density of graphite structure increases with higher PCS concentration and determines impedance matching between SiC fibers and free space. A higher PCS mass ratio than 10 wt.% decreases the EM absorption of SiC fibers due to multi-reflection among SiC fibers gradually weakening the incident EM field.

3.5.2 Supercapacitor and lithium-ion battery electrodes

Nowadays, there is an increasing demand for optimizing the efficiency of energy design of several devices. In this way, supercapacitors and lithium-ion batteries are being developed for energy storage applications as backup power and high-surge demand

applications. Electrospun fibrous mats are attractive to be used as electrodes due to their operation at high charge/discharge rates without the addition of polymer binders and conductive compounds [128]. SiBCN electrospun fibers showed almost 7 times higher electrochemical capacity than SiBCN powder ceramics as anode materials for lithium-ion batteries after 30 cycles [158]. The manufacture of e-PDC electrodes is based on various systems of PCP and organic polymer. However, it is focused on SiOC ceramics (Table 3.2). The differences in energy storage are also related to the precursor, addition of fillers, electrospinning procedure, and thermal treatment.

Table 3.2 – Energy storage performance of reported e-PDC materials

Material	Precursor	Ceramic fiber diameter (nm)	Performance	Reference
SiBCN	TDSB	470	Electrical charge capacity: $348 \text{ mA}\cdot\text{h}\cdot\text{g}^{-1}$ (after 30 cycles at $80 \text{ mA}\cdot\text{g}^{-1}$)	[158]
Carbon-rich SiOC	DTDS/PVP and TPTS/PVP	1000 and 200	Electrical charge capacity: $700 \text{ mA}\cdot\text{h}\cdot\text{g}^{-1}$ (after 100 cycles at $100 \text{ mA}\cdot\text{g}^{-1}$) (DTDS) Capacitance: $30 \text{ F}\cdot\text{g}^{-1}$ (after 5000 cycles) (TPTS)	[117]
SiOC	SiOC particles derived from PCS and TTCS/PAN	190	Electrical charge capacity: $595 \text{ mA}\cdot\text{h}\cdot\text{g}^{-1}$ (after 200 cycles at $200 \text{ mA}\cdot\text{g}^{-1}$)	[72]
SiOC	PHMS/D4Vi/PVP	2000	Electrical charge capacity: $686 \text{ mA}\cdot\text{h}\cdot\text{g}^{-1}$ (after 500 cycles at $50 \text{ mA}\cdot\text{g}^{-1}$)	[118]
SiOC	MK, H44 or RSN/PVP	1000 (MK and H44), 2000 (RSN)	Capacitance: $50 \text{ F}\cdot\text{g}^{-1}$ (after 2000 cycles) Electrical charge capacity: $350 \text{ mA}\cdot\text{h}\cdot\text{g}^{-1}$ for H44-derived SiOC (after 50 cycles at $100 \text{ mA}\cdot\text{g}^{-1}$)	[70]
SiOC	H44/PVP/tin acetate	960	Electrical charge capacity: $400\text{-}509 \text{ mA}\cdot\text{h}\cdot\text{g}^{-1}$ (after 100 cycles at $70 \text{ mA}\cdot\text{g}^{-1}$)	[89]

Table 3.2 – Energy storage performance of reported e-PDC materials (continuation)

Material	Precursor	Ceramic fiber diameter (nm)	Performance	Reference
SiOC	H44	4976	Capacitance: 135 F·g ⁻¹	[97]
SiOC	TTCS/PAN	300	Electrical discharge capacity: 669 mA·h·g ⁻¹ (after 80 cycles at 50 mA·g ⁻¹)	[170]
SiOC	PPS/PAN	130	Capacitance: 165 F·g ⁻¹	[171]
SiOC	PHMS/PAN	100-250	Capacitance: 126.86 F·g ⁻¹	[172]
SiOC	PUS/PAN	163	N/A	[61]
SiOC	PCS/PS	500-1500	N/A	[173]
SiON and SiOC	PPS/PAN	84	Capacitance: 107.6 F·g ⁻¹	[174]

The abbreviations correspond to TDSB: tris(methyldichlorosilylethyl)borane, DTDS: 1,3-divinyltetramethyldisiloxane, TPTS: 1,3,5-trivinyl-1,1,3,5,5-pentamethyltrisiloxane, TTCS: 1,3,5,7-tetramethyl-1,3,5,7-tetravinylcyclotetrasiloxane, PHMS: polyhydromethylsiloxane, D4Vi: tetramethyltetravinylcyclotetrasiloxane, RSN: phenyl-siloxane, and PPS: polyphenylsilane.

Continuous SiOC e-fibers with tin nanoparticles were tested for lithium-ion batteries [128]. The hybrid electrodes showed very high initial reversible capacities (840-994 mA·h·g⁻¹) at 35 mA·g⁻¹ and retained 280-310 mA·h·g⁻¹ at 350 mA·g⁻¹. After 100 cycles at 70 mA·g⁻¹, the hybrid fibers maintained 400-509 mA·h·g⁻¹. Compared to the literature, the e-mats presented a high first cycle reversible capacity due to the mass of Sn/SiOC fiber mat without binder or conductive additives, which contributed to the lithium insertion, the presence of metallic tin, and the high conductivity of the continuous fiber network. A higher concentration of tin decreased the conductivity of the e-PDCs by removing the conductive carbon phase since a higher amount of carbon and a higher graphitization degree promote higher conductivity and stable electrochemical performance. Low concentration of tin aided in the crosslinking of the PCP, the reduction of electrochemically inactive silicon carbide domains within the e-fibers, and the formation of metallic tin clusters, which contributed to a higher Li⁺ insertion in the first cycles.

3.5.3 Filtration membrane in harsh environments and gas sensing

Water pollution is one of the current global challenges, and the development of e-PDC membranes for remediation of harsh solutions is reported in the literature as promissory

technology to aid in tackling this environmental concern. Due to their superior mechanical and functional characteristics, increasing demands for harsh environment applications have triggered intensive research on non-oxide ceramics, such as SiC, Si₃N₄, SiBN, and SiCN [133]. For example, the SiC and SiOC e-fibers were stable after applying to sulfuric acid, potassium hydroxide, and sodium hydroxide solutions, pointing to the potential use in complex media [54,56,123,124]. The SiOC membranes doped with palladium showed excellent chemical resistance, thermal stability at high temperatures, high emulsion separation efficiency, and highly cohesive force, which further extended their potential applications for intelligent filters and small droplets transferor [124]. The authors obtained a high hydrophobic e-PDC membrane (water contact angle > 135°). Fibrous ceramic membranes achieve higher permeation than those produced from powder particles because ceramic membranes constructed with thin fibers lead to interconnected pores, high porosity, low tortuosity, and high surface area. Moreover, oxide-type ceramic membrane performance is limited in harsh environments [175].

Gas sensors, which can detect the presence and various concentrations of a specific gas in the ambient atmosphere, play a crucial role in many applications, such as environmental monitoring and industries, and have been studied with e-PDCs. For instance, the SiBNC e-mat was studied as a scaffold by depositing tin oxide nanowires with the CVD process, enhancing conductivity and specific surface area with even smaller pore sizes [115]. The gas sensing of SnO₂@SiBNC e-mat was further tested by measuring the change in resistivity when the structure was exposed to ethanol, showing a direct and reversible response-recovery performance. The properties of e-PDC fibers in gas sensing are attributed to the more effective active sites generated by the hierarchically interconnected macro-mesoporous structure, facilitating thus the gas diffusion [47].

3.5.4 Other properties and possible applications

The manufacturing of e-PDCs may find several other applications, such as conductors, dye absorbers, fibrous aerogels, pollutant removers, photochromic devices, thermal insulators, and photocatalysts. Moreover, some properties such as porosity, hierarchical structure, and hydrophobicity are evaluated in e-PDCs.

The porosity can be engineered in electrospun PCPs controlling through the nonsolvent-induced phase separation method. Surface pore formation is believed to result from water vapor condensing on the fiber surface and spinodal decomposition, causing phase

separation. The hollow structure is formed due to skin formation on a micron-scale on the polymer fiber, trapping the solvent that evaporates and diffuses through the outer layer leaving behind voids within the fiber. For example, a significant influence of solvent in porosity was observed when electrospinning PCS, suggesting an ideal concentration of a solvent mixture [139]. Xylene dissolved PS, acetone enhanced the e-spinnability of PCS solution, and DMF originated the pore formation on the fiber surface due to vapor-induced phase separation. Since DMF is nonsolvent for PCS, DMF might be expelled out to the fiber surface when PCS jets are elongated and stretched to form a fiber shape during electrospinning. The porosity formed during electrospinning enables several applications such as filtration, absorption, membrane supports, separation membranes, lightweight structural materials, porous bioimplants, sensors, etc. [176].

Hierarchically structured e-mats were studied using the PDC route for improving some properties, such as strength and toughness. The existence of nanostructures on the fiber surface may partially improve the functional efficiency of the original matrix, especially for catalysis, filtration, and separation applications. Macro, meso, and microporous SiC e-fibers were prepared by adjusting the spinning solution's PCS concentration and solvent composition [139]. The SiOC e-fibers with the hierarchical structure were synthesized using cobalt acetate as the catalyst precursor, which generated nanowires at 1300 °C [129]. Hierarchically structured fiber mats possessed a ~231% higher specific surface area than a sample produced without the cobalt catalyst.

The superhydrophobicity requires not only low surface energy but also hierarchical surface roughness. The e-fibers themselves naturally provide one level of roughness because of the small fiber size. On the other hand, the dry skin model describes the faster evaporation of the solvent on the surface than in the core of the liquid jet during electrospinning, leading to the formation of a dry polymer skin around the still liquid core, resulting in surface roughness. When the solvent in the core evaporates, the core shrinks to cause the dry polymer skin to collapse to wrap the core, wrinkling the surface [98]. Superhydrophobic SiC e-fibers with a water contact angle of 149.05° were reported due to their rough surface and functional groups such as C-C and C=C on the surface [123]. The pyrolysis temperature at 1200 °C of SiC e-fibers increased their hydrophobic behavior.

3.6 FINAL REMARKS AND FUTURE PROSPECTS

The manufacturing of Si-based ceramic electrospun fibers offers excellent control of their mechanical and chemical properties by manipulating the composition and physical properties of the precursor and the parameters of electrospinning. Merely 1D PDC fibers or their 2D PDC non-woven mats can be formed via electrospinning. The major limitation of electrospinning is that the process requires high molecular weight PCPs and high viscosity solutions. Otherwise, there arises an inability to spin. Therefore, further studies on rheology and the appropriate solvent/curing conditions that provide the minimum ratio of polymer chain entanglements for electrospinning are required.

During the electrospinning of PCPs, several parameters need to be tightly controlled to obtain high-quality, reproducible results. These include solution properties, process parameters, curing temperatures, and environmental conditions. Different crosslinking/curing and ceramization processes provide e-PDCs with various nanostructures. Crosslinking PCP fibers by photo-curing/electron beam concomitant to electrospinning in inert conditions seems to be an easy method to obtain ceramic fibers with less contamination of oxygen. The fabrication of fibers with controlled nanosized structures and more functionalities will be the goal of future research.

The preparation of electrospun ceramic fibers may significantly increase their performance in the existing products and open the doors to new applications. Thanks to the combination of PDC processing and electrospinning, high yield of fiber production with desired properties such as high specific surface area, high porosity, high hydrophobicity, mechanical properties, thermal stability, or with the desired functionalization via modification of precursor with suitable metals is also possible. Thus far, there is still plenty of room for developing electrospun fibers for several applications. The combination of well-designed chemical synthesis, materials processing, and characterization will offer numerous opportunities for new PDCs. Proper understanding and new avenues of PDC fibers introduced in this review will hopefully shed light on forthcoming electrospun ceramic fiber products.

3.7 ACKNOWLEDGEMENTS

This study was financed in part by the Coordenação de Aperfeiçoamento de Pessoal de Nível Superior - Brasil (CAPES) - Finance Code 001. The authors thank CAPES and

Deutscher Akademischer Austauschdienst (DAAD) for supporting this work within the project PROBRAL (Grant n° 88887.368756/2019-00).

3.8 AUTHORS' CONTRIBUTIONS

The paper is mainly based on the work of the first author and author of this thesis Heloisa Ramlow. This work was conducted in collaboration with the group of Ceramic Precursors (University of Bayreuth, Germany). The precise contributions of each author are listed below (Table 3.3).

Table 3.3 – Authors' contributions to Chapter 3

Author	Contribution
Ramlow, H.	Conceptualized the work, wrote the manuscript
Awin, E. W.	Helped in the scientific evaluation and editing of the manuscript
González, S. Y. G.	Gave conceptual and scientific advice, helped in the scientific evaluation and editing of the manuscript
Schafföner, S.	Gave conceptual and scientific advice, helped in the scientific evaluation and editing of the manuscript
Motz, G.	Gave conceptual and scientific advice, helped in the scientific evaluation and editing of the manuscript
Machado, R.	Gave conceptual and scientific advice, helped in the scientific evaluation and editing of the manuscript

3.9 REFERENCES

- [1] J. Hong, Y. Ko, K.Y. Cho, D.G. Shin, P. Singh, D.H. Riu, In situ generation of graphene network in silicon carbide fibers: Role of iodine and carbon monoxide, *Carbon* N. Y. 158 (2020) 110–120. <https://doi.org/10.1016/j.carbon.2019.11.053>.
- [2] J. Hong, K.Y. Cho, D.G. Shin, J. Il Kim, S.T. Oh, D.H. Riu, Low-temperature chemical vapour curing using iodine for fabrication of continuous silicon carbide fibres from low-molecular-weight polycarbosilane, *J. Mater. Chem. A*. 2 (2014) 2781–2793. <https://doi.org/10.1039/c3ta13727a>.
- [3] S.M. Dong, G. Chollon, C. Labrugère, M. Lahaye, A. Guette, J.L. Bruneel, M. Couzi, R. Naslain, D.L. Jiang, Characterization of nearly stoichiometric SiC ceramic fibres, *J. Mater. Sci.* 36 (2001) 2371–2381. <https://doi.org/10.1023/A:1017988827616>.
- [4] K. Kita, M. Narisawa, A. Nakahira, H. Mabuchi, M. Itoh, M. Sugimoto, M. Yoshikawa,

- High-temperature pyrolysis of ceramic fibers derived from polycarbosilane-polymethylhydrosiloxane polymer blends with porous structures, *J. Mater. Sci.* 45 (2010) 139–145. <https://doi.org/10.1007/s10853-009-3905-x>.
- [5] Z. Su, M. Tang, Z. Wang, L. Zhang, L. Chen, Processing of silicon carbide fibers from polycarbosilane with polypropylene as the additive, *J. Am. Ceram. Soc.* 93 (2010) 679–685. <https://doi.org/10.1111/j.1551-2916.2009.03457.x>.
- [6] A. Tazi Hemida, R. Pailler, R. Naslain, J.P. Pillot, M. Birot, J. Dunogues, Continuous SiC-based model monofilaments with a low free carbon content: Part II from the pyrolysis of a novel copolymer precursor, *J. Mater. Sci.* 32 (1997) 2367–2372. <https://doi.org/10.1023/a:1018596821898>.
- [7] A. Idesaki, M. Narisawa, K. Okamura, M. Sugimoto, S. Tanaka, Y. Morita, T. Seguchi, M. Itoh, Fine SiC fiber synthesized from organosilicon polymers: relationship between spinning temperature and melt viscosity of precursor polymers, *J. Mater. Sci.* 36 (2001) 5565–5569. <https://doi.org/10.1023/A:1012549228826>.
- [8] M. Takeda, A. Saeki, J.I. Sakamoto, Y. Imai, H. Ichikawa, Properties of polycarbosilane-derived silicon carbide fibers with various C/Si compositions, *Compos. Sci. Technol.* 59 (1999) 787–792. [https://doi.org/10.1016/S0266-3538\(99\)00009-3](https://doi.org/10.1016/S0266-3538(99)00009-3).
- [9] Y.J. Joo, K.Y. Cho, C.J. Kim, Effect of pyrolysis temperature on heat-generating behavior and morphology of SiC fiber mats, *J. Ceram. Process. Res.* 20 (2019) 563–569. <https://doi.org/10.36410/jcpr.2019.20.5.563>.
- [10] K. Kita, M. Narisawa, A. Nakahira, H. Mabuchi, M. Sugimoto, M. Yoshikawa, Synthesis and properties of ceramic fibers from polycarbosilane/ polymethylphenylsiloxane polymer blends, *J. Mater. Sci.* 45 (2010) 3397–3404. <https://doi.org/10.1007/s10853-010-4346-2>.
- [11] J. Lipowitz, Structure and properties of ceramic fibers prepared from organosilicon polymers, *J. Inorg. Organomet. Polym.* 1 (1991) 277–297. <https://doi.org/10.1007/BF00702494>.
- [12] T.E. Kim, K.E. Khishigbayar, K.Y. Cho, Effect of heating rate on the properties of silicon carbide fiber with chemical-vapor-cured polycarbosilane fiber, *J. Adv. Ceram.* 6 (2017) 59–66. <https://doi.org/10.1007/s40145-017-0218-4>.
- [13] M. Takeda, Y. Imai, H. Ichikawa, N. Kasai, T. Seguchi, K. Okamura, Thermal stability of SiC fiber prepared by an irradiation-curing process, *Compos. Sci. Technol.* 59 (1999) 793–799. [https://doi.org/10.1016/s0266-3538\(99\)00010-x](https://doi.org/10.1016/s0266-3538(99)00010-x).
- [14] Y. Li, J. Gao, Preparation of silicon nitride ceramic fibers from polycarbosilane fibers by γ -ray irradiation curing, *Mater. Lett.* 110 (2013) 102–104. <https://doi.org/10.1016/j.matlet.2013.07.127>.
- [15] X. Dong, C. Guo, X. Liu, C. Gu, P. Wu, W. Lin, Y. Lu, Z. Su, Z. Yu, A. Liu, Processing, characterization and properties of novel gradient Si₃N₄/SiC fibers derived from polycarbosilanes, *J. Eur. Ceram. Soc.* 39 (2019) 3613–3619. <https://doi.org/10.1016/j.jeurceramsoc.2019.05.028>.
- [16] Z. Xie, S. Cao, J. Wang, X. Yan, S. Bernard, P. Miele, Engineering of silicon-based ceramic fibers: Novel SiTaC(O) ceramic fibers prepared from polytantalosilane, *Mater. Sci. Eng. A.* 527 (2010) 7086–7091. <https://doi.org/10.1016/j.msea.2010.07.087>.
- [17] C. Shao, Y. Zhu, X. Shang, H. Wang, High temperature resistant SiC fibres derived from novel boron containing polycarbosilane, *Mater. Res. Innov.* 18 (2014) S4892–S4895. <https://doi.org/10.1179/1432891714Z.000000000879>.
- [18] H. Zhang, M. Ge, H. Zhang, W. Kong, S. Yu, W. Zhang, Oxidation resistance and thermal stability of the SiC-ZrB₂ composite ceramic fibers, *J. Am. Ceram. Soc.* 104 (2021) 1633–1640. <https://doi.org/10.1111/jace.17554>.

- [19] X. Lv, S. Yu, M. Ge, Y. Tian, W. Zhang, Synthesis and microstructure of continuous composite ceramic fibres of ZrC/ZrB₂-SiC derived from polymeric precursors, *Ceram. Int.* 42 (2016) 9299–9303. <https://doi.org/10.1016/j.ceramint.2016.02.112>.
- [20] X. Hu, C. Shao, J. Wang, H. Wang, J. Cheng, Effects of residual radicals on compositional and structural stability of silicon nitride fibers, *J. Eur. Ceram. Soc.* 37 (2017) 4497–4503. <https://doi.org/10.1016/j.jeurceramsoc.2017.06.035>.
- [21] Y. Yu, Y. Guo, X. Cheng, Y. Zhang, Preparation of TiO₂/SiO₂ composite fiber by thermal decomposition of polycarbosilane-tetrabutyl titanate hybrid precursor, *J. Mater. Chem.* 19 (2009) 5637–5642. <https://doi.org/10.1039/b905860e>.
- [22] Y.-C. Song, Y. Hasegawa, S.-J. Yang, M. Sato, Ceramic fibres from polymer precursor containing Si-O-Ti bonds, *J. Mater. Sci.* 23 (1988) 1911–1920. <https://doi.org/10.1007/bf01115750>.
- [23] Y. Yu, X. Tang, X. Li, Characterization and microstructural evolution of SiC(OAl) fibers to SiC(Al) fibers derived from aluminum-containing polycarbosilane, *Compos. Sci. Technol.* 68 (2008) 1697–1703. <https://doi.org/10.1016/j.compscitech.2008.02.010>.
- [24] Y. Yu, J. Tai, X. Tang, Y. Guo, M. Tang, X. Li, Continuous Si-C-O-Al fiber derived from aluminum-containing polycarbosilane precursor, *Compos. Part A Appl. Sci. Manuf.* 39 (2008) 1101–1105. <https://doi.org/10.1016/j.compositesa.2008.04.008>.
- [25] D. Mocaer, R. Pailler, R. Naslain, C. Richard, J.P. Pillot, J. Dunogues, O. Delverdier, M. Monthieux, Si-C-N ceramics with a high microstructural stability elaborated from the pyrolysis of new polycarbosilazane precursors - Part III Effect of pyrolysis conditions on the nature and properties of oxygen-cured derived monofilaments, *J. Mater. Sci.* 28 (1993) 2639–2653. <https://doi.org/10.1007/BF00356198>.
- [26] A. Viard, H. Kurz, A. Lale, L. Heymann, B. Weber, S. Bernard, M. Knauer, G. Motz, Superparamagnetic silicon carbonitride ceramic fibers through in situ generation of iron silicide nanoparticles during pyrolysis of an iron-modified polysilazane, *Appl. Mater. Interfaces.* 13 (2021) 8745–8753. <https://doi.org/10.1021/acsami.0c20885>.
- [27] L. Yong, P. Shuai, C. Yongjie, Z. Chenyu, C. Kangzhuang, T.H.H. Elagib, H. Keqing, Z. Hui, Y. Muhuo, Influence of silicon sources on structures and properties of polyborosilazane precursor derived SiBNC ceramic fiber, *Ceram. Int.* 44 (2018) 21381–21385. <https://doi.org/10.1016/j.ceramint.2018.08.194>.
- [28] Y. Tang, J. Wang, X. Li, Z. Xie, H. Wang, W. Li, X. Wang, Polymer-derived SiBN fiber for high-temperature structural/functional applications, *Chem. - A Eur. J.* 16 (2010) 6458–6462. <https://doi.org/10.1002/chem.200902974>.
- [29] Y. Liu, K. Chen, S. Peng, Y. Cui, K. Han, M. Yu, H. Zhang, Synthesis and pyrolysis mechanism of a novel polymeric precursor for SiBN ternary ceramic fibers, *Ceram. Int.* 45 (2019) 20172–20177. <https://doi.org/10.1016/j.ceramint.2019.06.286>.
- [30] W. Li, J. Wang, Z. Xie, H. Wang, Y. Tang, Preparation of hollow Si-B-N ceramic fibers by partial curing and pyrolysis of polyborosilazane fibers, *Mater. Lett.* 78 (2012) 1–3. <https://doi.org/10.1016/j.matlet.2012.02.068>.
- [31] Y. Peng, K. Han, X. Zhao, M. Yu, Large-scale preparation of SiBN ceramic fibres from a single source precursor, *Ceram. Int.* 40 (2014) 4797–4804. <https://doi.org/10.1016/j.ceramint.2013.09.027>.
- [32] Y. Liu, S. Peng, Y. Cui, X. Chang, C. Zhang, X. Huang, K. Han, M. Yu, Fabrication and properties of precursor-derived SiBN ternary ceramic fibers, *Mater. Des.* 128 (2017) 150–156. <https://doi.org/10.1016/j.matdes.2017.05.018>.
- [33] X. Ji, C. Shao, H. Wang, J. Wang, J. Cheng, X. Long, T. Mao, A simple and efficient method for the synthesis of SiBNC ceramics with different Si/B atomic ratios, *Ceram. Int.* 43 (2017) 7469–7476. <https://doi.org/10.1016/j.ceramint.2017.03.022>.

- [34] C. Zhang, Y. Liu, Y. Cui, M. Jiang, K. Han, H. Zhang, M. Yu, Synthesis and characterization of a novel preceramic polymer for SiBNC ceramic fibers, *Fibers Polym.* 19 (2018) 956–964. <https://doi.org/10.1007/s12221-018-1104-6>.
- [35] W.H. Li, J. Wang, Z.F. Xie, H. Wang, A novel polyborosilazane for high-temperature amorphous Si-B-N-C ceramic fibres, *Ceram. Int.* 38 (2012) 6321–6326. <https://doi.org/10.1016/j.ceramint.2012.05.001>.
- [36] L. Gottardo, S. Bernard, C. Gervais, K. Inzenhofer, G. Motz, M. Weinmann, C. Balan, P. Miele, Chemistry, structure and processability of boron-modified polysilazanes as tailored precursors of ceramic fibers, *J. Mater. Chem.* 22 (2012) 7739–7750. <https://doi.org/10.1039/c2jm15919h>.
- [37] Y. Tang, J. Wang, X. Li, Z. Xie, H. Wang, Y. Wang, One-pot synthesis of novel polyborosilazane to SiBNC fibres, *Inorg. Chem. Commun.* 12 (2009) 602–604. <https://doi.org/10.1016/j.inoche.2009.04.032>.
- [38] S. Bernard, M. Weinmann, P. Gerstel, P. Miele, F. Aldinger, Boron-modified polysilazane as a novel single-source precursor for SiBCN ceramic fibers: synthesis, melt-spinning, curing and ceramic conversion, *J. Mater. Chem.* 15 (2005) 289–299. <https://doi.org/10.1039/b408295h>.
- [39] S. Bernard, S. Duperrier, D. Cornu, P. Miele, M. Weinmann, C. Balan, F. Aldinger, Chemical tailoring of single-source molecular and polymeric precursors for the preparation of ceramic fibers, *J. Optoelectron. Adv. Mater.* 8 (2006) 648–653.
- [40] M. Narisawa, Y. Satoh, R. Sumimoto, T. Kamegawa, H. Yamashita, Synthesis of SiOC base fibers from silicone resin with low carbon content and control of surface functionality by metal chloride treatment in vapor, *Mater. Sci. Forum.* 658 (2010) 400–403. <https://doi.org/10.4028/www.scientific.net/MSF.658.400>.
- [41] X. Li, J. Wei, B. Chen, Y. Wang, C. Jiang, H. Zhang, M. Qiao, Effective electromagnetic wave absorption and photoluminescence performances of flexible SiC nanowires membrane, *Ceram. Int.* 47 (2021) 17615–17626. <https://doi.org/10.1016/j.ceramint.2021.03.080>.
- [42] B. Yao, B. Lu, Q. Huang, Z.R. Huang, Q. Yuan, The preparation of SiC ultrafine fibers containing low amount of oxygen by the electrospinning and pyrolysis of vinyl-modified polycarbosilane, *Ceram. Int.* 46 (2020) 9894–9900. <https://doi.org/10.1016/j.ceramint.2019.12.265>.
- [43] N. Wu, B. Wang, C. Han, Q. Tian, C. Wu, X. Zhang, L. Sun, Y. Wang, Pt-decorated hierarchical SiC nanofibers constructed by intertwined SiC nanorods for high-temperature ammonia gas sensing, *J. Mater. Chem. C.* 7 (2019) 7299–7307. <https://doi.org/10.1039/c9tc01330j>.
- [44] V.B. Platonov, M.N. Rumyantseva, A.S. Frolov, A.D. Yapryntsev, A.M. Gaskov, High-temperature resistive gas sensors based on ZnO/SiC nanocomposites, *Beilstein J. Nanotechnol.* 10 (2019) 1537–1547. <https://doi.org/10.3762/bjnano.10.151>.
- [45] Q. Tian, N. Wu, B. Wang, Y. Wang, Fabrication of hollow SiC ultrafine fibers by single-nozzle electrospinning for high-temperature thermal insulation application, *Mater. Lett.* 239 (2019) 109–112. <https://doi.org/10.1016/j.matlet.2018.12.077>.
- [46] N. Wu, S. Ju, Y. Wang, D. Chen, Fabrication of Ni@SiC composite nanofibers by electrospinning and autocatalytic electroless plating techniques, *Results Phys.* 12 (2019) 853–858. <https://doi.org/10.1016/j.rinp.2018.12.051>.
- [47] Masripah, A. Zulys, J. Setiawan, Synthesis of silicon carbide fiber as semiconductor substrate for betavoltaic cell, *J. Phys. Conf. Ser.* 1025 (2018) 1–7. <https://doi.org/10.1088/1742-6596/1025/1/012129>.
- [48] Y. Hou, L. Cheng, Y. Zhang, Y. Yang, C. Deng, Z. Yang, Q. Chen, X. Du, C. Zhao, L.

- Zheng, Enhanced flexibility and microwave absorption properties of HfC/SiC nanofiber mats, *ACS Appl. Mater. Interfaces*. 10 (2018) 29876–29883. <https://doi.org/10.1021/acsami.8b07980>.
- [49] Y. Hou, Y. Zhang, X. Du, Y. Yang, C. Deng, Z. Yang, L. Zheng, L. Cheng, Flexible Fe₃Si/SiC ultrathin hybrid fiber mats with designable microwave absorption performance, *RSC Adv.* 8 (2018) 33574–33582. <https://doi.org/10.1039/c8ra06941g>.
- [50] N. Wu, L.Y. Wan, Y.-D. Wang, K. Frank, Electrospun silicon oxycarbide ultrafine fibers derived from polycarbosilane, *J. Inorg. Mater.* 33 (2018) 357–362. <https://doi.org/10.15541/jim20170153>.
- [51] Y. Liu, Y. Liu, W.C. Choi, S. Chae, J. Lee, B.-S. Kim, M. Park, H.Y. Kim, Highly flexible, erosion resistant and nitrogen doped hollow SiC fibrous mats for high temperature thermal insulators, *J. Mater. Chem. A*. 5 (2017) 2664–2672. <https://doi.org/10.1039/c6ta09475a>.
- [52] Y. Hou, L. Cheng, Y. Zhang, Y. Yang, C. Deng, Z. Yang, Q. Chen, P. Wang, L. Zheng, Electrospinning of Fe/SiC hybrid fibers for highly efficient microwave absorption, *ACS Appl. Mater. Interfaces*. 9 (2017) 7265–7271. <https://doi.org/10.1021/acsami.6b15721>.
- [53] Y. Yu, Y. Chen, X. Wu, Q. Fang, X. Wu, Flexible and hydrophobic silicon carbide fibrous mats prepared from polycarbosilane, *Kuei Suan Jen Hsueh Pao/Journal Chinese Ceram. Soc.* 42 (2014) 661–666. <https://doi.org/10.7521/j.issn.0454-5648.2014.05.17>.
- [54] T.-E. Kim, J.C. Bae, K.Y. Cho, Y.-G. Shul, C.Y. Kim, Fabrication of electrospun SiC fibers web/phenol resin composites for the application to high thermal conducting substrate, *J. Nanosci. Nanotechnol.* 13 (2013) 3307–3312. <https://doi.org/10.1166/jnn.2013.7264>.
- [55] J. Li, P. Cao, Y. Tan, L. Zhang, Effect of the addition of TEOS on the SiC fibers fabricated by electrospinning, *J. Adv. Ceram.* 2 (2013) 242–245. <https://doi.org/10.1007/s40145-013-0066-9>.
- [56] S.H. Choi, D.Y. Youn, S.M. Jo, S.G. Oh, I.D. Kim, Micelle-mediated synthesis of single-crystalline β (3C)-SiC fibers via emulsion electrospinning, *ACS Appl. Mater. Interfaces*. 3 (2011) 1385–1389. <https://doi.org/10.1021/am200171v>.
- [57] D.G. Shin, D.H. Riu, H.E. Kim, Web-type silicon carbide fibers prepared by the electrospinning of polycarbosilanes, *J. Ceram. Process. Res.* 9 (2008) 209–214.
- [58] Y. Liu, F. Gao, L. Wang, W. Yang, X. He, H. Hou, Fabrication of CdS-decorated mesoporous SiC hollow nanofibers for efficient visible-light-driven photocatalytic hydrogen production, *J. Mater. Sci. Mater. Electron.* 30 (2019) 1487–1495. <https://doi.org/10.1007/s10854-018-0419-9>.
- [59] H. Hou, C. Dong, L. Wang, F. Gao, G. Wei, J. Zheng, X. Cheng, B. Tang, W. Yang, Electrospinning graphite/SiC mesoporous hybrid fibers with tunable structures, *CrystEngComm*. 15 (2013) 2002–2008. <https://doi.org/10.1039/c3ce26862d>.
- [60] H. Hou, F. Gao, G. Wei, M. Wang, J. Zheng, B. Tang, W. Yang, Electrospinning 3C-SiC mesoporous fibers with high purities and well-controlled structures, *Cryst. Growth Des.* 12 (2012) 536–539. <https://doi.org/10.1021/cg201317b>.
- [61] P. Lu, Q. Huang, A. Mukherjee, Y. Lo Hsieh, SiCO-doped carbon fibers with unique dual superhydrophilicity/superoleophilicity and ductile and capacitance properties, *ACS Appl. Mater. Interfaces*. 2 (2010) 3738–3744. <https://doi.org/10.1021/am100918x>.
- [62] P. Lu, Q. Huang, A. Mukherjee, Y. Lo Hsieh, Synthesis of nickel nanoparticles supported on nanoporous silicon oxycarbide (SiCO) sheath-core fibers, *J. Phys. Chem. C*. 114 (2010) 11776–11782. <https://doi.org/10.1021/jp104605b>.
- [63] P. Lu, Q. Huang, A. Mukherjee, Y. Lo Hsieh, Effects of polymer matrices to the formation of silicon carbide (SiC) nanoporous fibers and nanowires under carbothermal

- reduction, *J. Mater. Chem.* 21 (2011) 1005–1012. <https://doi.org/10.1039/c0jm02543g>.
- [64] A. Guo, M. Roso, P. Colombo, J. Liu, M. Modesti, In situ carbon thermal reduction method for the production of electrospun metal/SiOC composite fibers, *J. Mater. Sci.* 50 (2015) 2735–2746. <https://doi.org/10.1007/s10853-015-8827-1>.
- [65] A. Guo, M. Roso, M. Modesti, J. Liu, P. Colombo, Pre-ceramic polymer-derived SiOC fibers by electrospinning, *J. Appl. Polym. Sci.* 131 (2014) 39836. <https://doi.org/10.1002/app.39836>.
- [66] L.F.B. Ribeiro, R.S. Cunha, A. de Noni, R.A.F. Machado, G. Motz, S.Y.G. González, Flexible and porous nonwoven SiCN ceramic material via electrospinning of an optimized silazane solution, *Adv. Eng. Mater.* 2100321 (2021) 1–7. <https://doi.org/10.1002/adem.202100321>.
- [67] S.A. Smith, B.P. Williams, Y.L. Joo, Effect of polymer and ceramic morphology on the material and electrochemical properties of electrospun PAN/polymer derived ceramic composite nano fiber membranes for lithium ion battery separators, *J. Memb. Sci.* 526 (2017) 315–322. <https://doi.org/10.1016/j.memsci.2016.12.052>.
- [68] Q. Zhang, D. Jia, Z. Yang, X. Duan, Q. Chen, Y. Zhou, Synthesis of novel cobalt-containing polysilazane nanofibers with fluorescence by electrospinning, *Polymers (Basel)*. 8 (2016) 1–13. <https://doi.org/10.3390/polym8100350>.
- [69] K. Ge, L. Ye, W. Han, Y. Han, C. Xu, T. Zhao, Si(B)CN-doped carbon nanofibers with excellent oxidation resistance, *Mater. Lett.* 112 (2013) 124–128. <https://doi.org/10.1016/j.matlet.2013.08.122>.
- [70] S. Bin Mujib, R. Cuccato, S. Mukherjee, G. Franchin, P. Colombo, G. Singh, Electrospun SiOC ceramic fiber mats as freestanding electrodes for electrochemical energy storage applications, *Ceram. Int.* 46 (2020) 3565–3573. <https://doi.org/10.1016/j.ceramint.2019.10.074>.
- [71] Y. Wang, X. Pei, H. Li, X. Xu, L. He, Z. Huang, Q. Huang, Preparation of SiC ceramic fiber from a photosensitive polycarbosilane, *Ceram. Int.* 46 (2020) 28300–28307. <https://doi.org/10.1016/j.ceramint.2020.07.333>.
- [72] M. Ma, H. Wang, X. Li, K. Peng, L. Xiong, X. Du, Free-standing SiOC/nitrogen-doped carbon fibers with highly capacitive Li storage, *J. Eur. Ceram. Soc.* 40 (2020) 5238–5246. <https://doi.org/10.1016/j.ceramint.2020.11.031>.
- [73] Y. Liu, W. Yang, X. He, H. Hou, Tailored synthesis of amorphous SiCNO mesoporous fibers through combining a facile electrospinning process and microwave-assisted pyrolysis, *Ceram. Int.* 45 (2019) 8640–8645. <https://doi.org/10.1016/j.ceramint.2019.01.184>.
- [74] S.H. Koo, S.G. Lee, H. Bong, Y.J. Kwark, K. Cho, H.S. Lim, J.H. Cho, Robust multifunctional superhydrophobic organic-inorganic hybrid macroporous coatings and films, *Polymer (Guildf)*. 55 (2014) 2661–2666. <https://doi.org/10.1016/j.polymer.2014.03.046>.
- [75] C.J. Luo, E. Stride, S. Stoyanov, E. Pelan, M. Edirisinghe, Electrospinning short polymer micro-fibres with average aspect ratios in the range of 10–200, *J. Polym. Res.* 18 (2011) 2515–2522. <https://doi.org/10.1007/s10965-011-9667-6>.
- [76] M. Rose, E. Kockrick, I. Senkovska, S. Kaskel, High surface area carbide-derived carbon fibers produced by electrospinning of polycarbosilane precursors, *Carbon N. Y.* 48 (2010) 403–407. <https://doi.org/10.1016/j.carbon.2009.09.043>.
- [77] H.A. Liu, K.J. Balkus, Electrospinning of beta silicon carbide nanofibers, *Mater. Lett.* 63 (2009) 2361–2364. <https://doi.org/10.1016/j.matlet.2009.08.009>.
- [78] Y. Huo, Y. Tan, K. Zhao, Z. Lu, L. Zhong, Y. Tang, Enhanced electromagnetic wave absorption properties of Ni magnetic coating-functionalized SiC/C nanofibers

- synthesized by electrospinning and magnetron sputtering technology, *Chem. Phys. Lett.* 763 (2021) 138230. <https://doi.org/10.1016/j.cplett.2020.138230>.
- [79] Y. Hou, L. Cheng, Y. Zhang, X. Du, Y. Zhao, Z. Yang, High temperature electromagnetic interference shielding of lightweight and flexible ZrC/SiC nanofiber mats, *Chem. Eng. J.* 404 (2021) 126521. <https://doi.org/10.1016/j.cej.2020.126521>.
- [80] Y. Huo, K. Zhao, Z. Xu, Y. Tang, Electrospinning synthesis of SiC/Carbon hybrid nanofibers with satisfactory electromagnetic wave absorption performance, *J. Alloys Compd.* 815 (2020) 152458. <https://doi.org/10.1016/j.jallcom.2019.152458>.
- [81] P. Wang, L. Cheng, Y. Zhang, W. Yuan, H. Pan, H. Wu, Electrospinning of graphite/SiC hybrid nanowires with tunable dielectric and microwave absorption characteristics, *Compos. Part A Appl. Sci. Manuf.* 104 (2018) 68–80. <https://doi.org/10.1016/j.compositesa.2017.10.012>.
- [82] P. Wang, L. Cheng, Y. Zhang, L. Zhang, Flexible SiC/Si₃N₄ composite nanofibers with in situ embedded graphite for highly efficient electromagnetic wave absorption, *ACS Appl. Mater. Interfaces.* 9 (2017) 28844–28858. <https://doi.org/10.1021/acsami.7b05382>.
- [83] P. Wang, L. Cheng, L. Zhang, One-dimensional carbon/SiC nanocomposites with tunable dielectric and broadband electromagnetic wave absorption properties, *Carbon N. Y.* 125 (2017) 207–220. <https://doi.org/10.1016/j.carbon.2017.09.052>.
- [84] P. Wang, L. Cheng, Y. Zhang, H. Wu, Y. Hou, W. Yuan, L. Zheng, Flexible, hydrophobic SiC ceramic nanofibers used as high frequency electromagnetic wave absorbers, *Ceram. Int.* 43 (2017) 7424–7435. <https://doi.org/10.1016/j.ceramint.2017.03.001>.
- [85] N. Wu, L.Y. Wan, Y. Wang, F. Ko, Conversion of hydrophilic SiOC nanofibrous membrane to robust hydrophobic materials by introducing palladium, *Appl. Surf. Sci.* 425 (2017) 750–757. <https://doi.org/10.1016/j.apsusc.2017.07.098>.
- [86] Y. Hou, L. Cheng, Y. Zhang, Y. Yang, C. Deng, Z. Yang, Q. Chen, X. Du, L. Zheng, SiC nanofiber mat: a broad-band microwave absorber, and the alignment effect, *ACS Appl. Mater. Interfaces.* 9 (2017) 43072–43080. <https://doi.org/10.1021/acsami.7b13634>.
- [87] X. Dong, R. Liu, W. Dong, Z. Wang, A. Guo, J. Liu, C. Chen, Y. Jiang, Fabrication and properties of lightweight SiOC fiber-based assembly aerogels with hierarchical pore structure, *Ceram. Int.* 44 (2018) 22760–22766. <https://doi.org/10.1016/j.ceramint.2018.09.064>.
- [88] A. Guo, M. Roso, M. Modesti, E. Maire, J. Adrien, P. Colombo, Characterization of porosity, structure, and mechanical properties of electrospun SiOC fiber mats, *J. Mater. Sci.* 50 (2015) 4221–4231. <https://doi.org/10.1007/s10853-015-8973-5>.
- [89] A. Tolosa, M. Widmaier, B. Krüner, J.M. Griffin, V. Presser, Continuous silicon oxycarbide fiber mats with tin nanoparticles as a high capacity anode for lithium-ion batteries, *Sustain. Energy Fuels.* 2 (2018) 215–228. <https://doi.org/10.1039/c7se00431a>.
- [90] A. Guo, M. Roso, M. Modesti, J. Liu, P. Colombo, Hierarchically structured polymer-derived ceramic fibers by electrospinning and catalyst-assisted pyrolysis, *J. Eur. Ceram. Soc.* 34 (2014) 549–554. <https://doi.org/10.1016/j.jeurceramsoc.2013.08.025>.
- [91] B. Yao, B. Lu, Q. Huang, Z. Huang, Q. Yuan, The preparation of SiC ultrafine fibers containing low amount of oxygen by the electrospinning and pyrolysis of vinyl-modified polycarbosilane, *Ceram. Int.* 46 (2019) 9894–9900. <https://doi.org/10.1016/j.ceramint.2019.12.265>.
- [92] Y.J. Joo, C.J. Kim, K.Y. Cho, Facile synthesis and morphological study of Si-Zr-C-O fiber felts with high-thermal resistance, *Ceram. Int.* 45 (2019) 16008–16014.

- <https://doi.org/10.1016/j.ceramint.2019.05.112>.
- [93] B. Wang, L. Deng, L. Sun, Y. Lei, N. Wu, Y. Wang, Growth of TiO₂ nanostructures exposed {001} and {110} facets on SiC ultrafine fibers for enhanced gas sensing performance, *Sensors Actuators, B Chem.* 276 (2018) 57–64. <https://doi.org/10.1016/j.snb.2018.08.080>.
- [94] K.E. Khishigbayar, Y.J. Joo, K.Y. Cho, Microwave-assisted heating of electrospun SiC fiber mats, *J. Korean Ceram. Soc.* 54 (2017) 499–505. <https://doi.org/10.4191/kcers.2017.54.6.04>.
- [95] B. Wang, Y. Wang, Y. Lei, N. Wu, Y. Gou, C. Han, D. Fang, Hierarchically porous SiC ultrathin fibers mat with enhanced mass transport, amphipathic property and high-temperature erosion resistance, *J. Mater. Chem. A.* 2 (2014) 20873–20881. <https://doi.org/10.1039/c4ta04847d>.
- [96] A. Vashisth, S. Khatri, S.H. Hahn, W. Zhang, A.C.T. Van Duin, M. Naraghi, Mechanical size effects of amorphous polymer-derived ceramics at the nanoscale: Experiments and ReaxFF simulations, *Nanoscale.* 11 (2019) 7447–7456. <https://doi.org/10.1039/c9nr00958b>.
- [97] A. Tolosa, B. Krüner, N. Jäckel, M. Aslan, C. Vakifahmetoglu, V. Presser, Electrospinning and electro spraying of silicon oxycarbide-derived nanoporous carbon for supercapacitor electrodes, *J. Power Sources.* 313 (2016) 178–188. <https://doi.org/10.1016/j.jpowsour.2016.02.077>.
- [98] B. Zhang, Z. Tong, H. Yu, H. Xu, Z. Chen, X. Li, H. Ji, Flexible and high-temperature resistant ZrO₂/SiC-based nanofiber membranes for high temperature thermal insulation, *J. Alloys Compd.* 872 (2021) 159618. <https://doi.org/10.1016/j.jallcom.2021.159618>.
- [99] Y. Zhang, Y. Zhao, Q. Chen, Y. Hou, Q. Zhang, L. Cheng, L. Zheng, Flexible SiC-CNTs hybrid fiber mats for tunable and broadband microwave absorption, *Ceram. Int.* 47 (2021) 8123–8132. <https://doi.org/10.1016/j.ceramint.2020.11.167>.
- [100] P. Wang, L. Cheng, L. Zhang, Lightweight, flexible SiCN ceramic nanowires applied as effective microwave absorbers in high frequency, *Chem. Eng. J.* 338 (2018) 248–260. <https://doi.org/10.1016/j.cej.2017.12.008>.
- [101] P. Wang, L. Cheng, Y. Zhang, L. Zhang, Synthesis of SiC nanofibers with superior electromagnetic wave absorption performance by electrospinning, *J. Alloys Compd.* 716 (2017) 306–320. <https://doi.org/10.1016/j.jallcom.2017.05.059>.
- [102] B. Wang, Y. Wang, Y. Lei, N. Wu, Y. Gou, C. Han, Tailoring of porous structure in macromeso-microporous SiC ultrathin fibers via electrospinning combined with polymer-derived ceramics route, *Mater. Manuf. Process.* 31 (2016) 1357–1365. <https://doi.org/10.1080/10426914.2015.1090601>.
- [103] K. Asadi-Pakdel, R. Mehdiavaz Aghdam, M. Shahedi Asl, M.A. Faghihi Sani, Synthesis and morphology optimization of electrospun SiBNC nanofibers, *Ceram. Int.* 46 (2019) 6052–6059. <https://doi.org/10.1016/j.ceramint.2019.11.063>.
- [104] Y. Yu, Y. Chen, L. An, Flexible hydrophobic and lipophilic aluminum-doped silicon carbide fibrous mats synthesized by electrospinning polyaluminocarbosilane, *Int. J. Appl. Ceram. Technol.* 11 (2014) 699–705. <https://doi.org/10.1111/ijac.12081>.
- [105] Z. An, C. Ye, R. Zhang, P. Zhou, Flexible and recoverable SiC nanofiber aerogels for electromagnetic wave absorption, *Ceram. Int.* 45 (2019) 22793–22801. <https://doi.org/10.1016/j.ceramint.2019.07.321>.
- [106] J.S. Li, T.Y. Hsu, C.H. Peng, C.C. Hwang, K.T. Lu, T.F. Yeh, Synthesis and characterization of poly(carbomethylsilane) prepared by catalytic polymerization with titanocene dichloride as a catalyst, *Mater. Express.* 10 (2020) 2070–2079. <https://doi.org/10.1166/mex.2020.1842>.

- [107] P.H. Kang, J.P. Jeun, D.K. Seo, Y.C. Nho, Fabrication of SiC mat by radiation processing, *Radiat. Phys. Chem.* 78 (2009) 493–495. <https://doi.org/10.1016/j.radphyschem.2009.03.033>.
- [108] Y. Huo, K. Zhao, Z. Xu, F. Li, X. Zhao, Q. Meng, C. Tang, Y. Tang, Ultralight and superelastic polyvinyl alcohol/SiC nanofiber/reduced graphene oxide hybrid foams with excellent thermal insulation and microwave absorption properties, *Ceram. Int.* 47 (2021) 25986–25996. <https://doi.org/10.1016/j.ceramint.2021.06.004>.
- [109] Y. Huo, K. Zhao, M. Peng, F. Li, Z. Lu, Q. Meng, Y. Tang, Anchoring of SiC and Fe₃Si nanocrystallines in carbon nanofibers inducing interfacial polarization to promote microwave attenuation ability, *J. Alloys Compd.* 891 (2022) 162006. <https://doi.org/10.1016/j.jallcom.2021.162006>.
- [110] Q. Chen, D. Li, X. Liao, Z. Yang, D. Jia, Y. Zhou, R. Riedel, Polymer-derived lightweight SiBCN ceramic nanofibers with high microwave absorption performance, *ACS Appl. Mater. Interfaces.* 13 (2021) 34889–34898. <https://doi.org/10.1021/acsami.1c07912>.
- [111] H. Ramlow, C. Marangoni, G. Motz, R.A.F. Machado, Statistical optimization of polysilazane-derived ceramic: Electrospinning with and without organic polymer as a spinning aid for manufacturing thinner fibers, *Chem. Eng. J. Adv.* 9 (2022) 100220. <https://doi.org/10.1016/j.cej.2021.100220>.
- [112] Y. Feng, X. Guo, J. Lu, J. Liu, G. Wang, H. Gong, Enhanced electromagnetic wave absorption performance of SiCN(Fe) fibers by in-situ generated Fe₃Si and CNTs, *Ceram. Int.* 47 (2021) 19582–19594. <https://doi.org/10.1016/j.ceramint.2021.03.296>.
- [113] X. Guo, F. Xiao, J. Li, H. Zhang, Q. Hu, G. Li, H. Sun, Fe-doped SiCN composite fibers for electromagnetic waves absorption, *Ceram. Int.* 47 (2021) 1184–1190. <https://doi.org/10.1016/j.ceramint.2020.08.236>.
- [114] Z. Li, F. Ye, L. Cheng, P. Wang, C. Guo, M. Li, L. Zhang, Synthesis of Si-C-N aligned nanofibers with preeminent electromagnetic wave absorption in ultra-broad band, *J. Mater. Chem. C.* 9 (2021) 16966–16977. <https://doi.org/10.1039/d1tc03663g>.
- [115] F. Xiao, H. Sun, J. Li, X. Guo, H. Zhang, J. Lu, Z. Pan, J. Xu, Electrospinning preparation and electromagnetic wave absorption properties of SiCN fibers, *Ceram. Int.* 46 (2020) 12773–12781. <https://doi.org/10.1016/j.ceramint.2020.02.046>.
- [116] Q. Chen, D. Jia, B. Liang, Z. Yang, Y. Zhou, D. Li, R. Riedel, T. Zhang, C. Gao, Electrospinning of pure polymer-derived SiBCN nanofibers with high yield, *Ceram. Int.* 47 (2021) 10958–10964. <https://doi.org/10.1016/j.ceramint.2020.12.215>.
- [117] S. Bin Mujib, F. Ribot, C. Gervais, G. Singh, Self-supporting carbon-rich SiOC ceramic electrodes for lithium-ion batteries and aqueous supercapacitors, *RSC Adv.* 11 (2021) 35440–35454. <https://doi.org/10.1039/d1ra05968h>.
- [118] Z. Sang, X. Yan, L. Wen, D. Su, Z. Zhao, Y. Liu, H. Ji, J. Liang, S.X. Dou, A graphene-modified flexible SiOC ceramic cloth for high-performance lithium storage, *Energy Storage Mater.* 25 (2019) 876–884. <https://doi.org/10.1016/j.ensm.2019.11.014>.
- [119] Y. Li, Y. Hu, Y. Lu, S. Zhang, G. Xu, K. Fu, S. Li, C. Chen, L. Zhou, X. Xia, X. Zhang, One-dimensional SiOC/C composite nanofibers as binder-free anodes for lithium-ion batteries, *J. Power Sources.* 254 (2014) 33–38. <https://doi.org/10.1016/j.jpowsour.2013.12.044>.
- [120] B.H. Kim, K.S. Yang, H.G. Woo, Physical and electrochemical studies of polyphenylsilane-derived porous carbon nanofibers produced via electrospinning, *Electrochim. Acta.* 59 (2012) 202–206. <https://doi.org/10.1016/j.electacta.2011.10.057>.
- [121] B.H. Kim, K.S. Yang, H.G. Woo, K. Oshida, Supercapacitor performance of porous carbon nanofiber composites prepared by electrospinning polymethylhydrosiloxane

- (PMHS)/polyacrylonitrile (PAN) blend solutions, *Synth. Met.* 161 (2011) 1211–1216. <https://doi.org/10.1016/j.synthmet.2011.04.005>.
- [122] Y.E. Roginskaya, A.D. Shepelev, T.K. Tenchurin, E.D. Politova, B.A. Loginov, N. V. Kozlova, T.L. Kulova, A.M. Skundin, Synthesis and structure of composite fibers based on silicon and carbon obtained by electrospinning, *Russ. J. Phys. Chem. A.* 85 (2011) 2013–2019. <https://doi.org/10.1134/s0036024411110264>.
- [123] C.H. Kim, B.H. Kim, Effects of thermal treatment on the structural and capacitive properties of polyphenylsilane-derived porous carbon nanofibers, *Electrochim. Acta.* 117 (2014) 26–33. <https://doi.org/10.1016/j.electacta.2013.11.082>.
- [124] M.H. Al-Saleh, W.H. Saadeh, U. Sundararaj, EMI shielding effectiveness of carbon based nanostructured polymeric materials: A comparative study, *Carbon N. Y.* 60 (2013) 146–156. <https://doi.org/10.1016/j.carbon.2013.04.008>.

4 STATISTICAL OPTIMIZATION OF POLYSILAZANE-DERIVED CERAMIC: ELECTROSPINNING WITH AND WITHOUT ORGANIC POLYMER AS A SPINNING AID FOR MANUFACTURING THINNER FIBERS²

The manufacturing of electrospun mats from preceramic polymers is complex due to low and disperse molecular chain entanglements and a large number of operating parameters. Here, the electrospinning of polysilazane and polysilazane/PAN solutions was evaluated and optimized. The reduction in Berry's number from 94 to 22 indicated the positive effect of adding organic polymer on the polysilazane chains to obtain homogeneous fibers. A fractional factorial design was first implemented to screen out the three most significant factors affecting fiber diameter. Then, a response surface model was developed using the Box-Behnken design to obtain a quantitative relationship between operating parameters and fiber diameter. Finally, the models were used to find the optimal conditions that yield the thinnest fiber. For polysilazane, the feed rate showed a positive effect, while for polysilazane/PAN an interaction between the feed rate and the tip-to-collector distance was the most significant factor, with a positive effect. The verification of the models was accomplished through model validation.

4.1 INTRODUCTION

The manufacturing of electrospun PDC fibers with optimized design may significantly increase their performance in the existing products and/or open the doors to new applications. Statistical optimization has been proven to be a powerful tool for understanding the electrospinnability of various polymers [1–3]. The response surface methodology is a simple and efficient optimization method to construct an approximation model for describing the relationship between a response and a set of predictor variables [4]. Box-Behnken design is the most commonly used method employing response surface methodology and optimization processes [5,6], which is gathered to obtain maximum outputs from minimum inputs [7]. This method is derived from factorial design with an incomplete block in the shape of a box, where its internal structure is fixed by a wireframe composed under the edges of the box [8]. The Box-Behnken design provides a mathematical relationship between factors and the response that can

²Based on a paper published in the Chemical Engineering Journal Advances (DOI: 10.1016/j.ceja.2021.100220).

be fitted to a second-order polynomial model [9]. This methodology has been successfully adopted to optimize the diameter of electrospun fibers [10–12].

Although great advances have been made in preparing electrospun PDC fibers, the electrospinning of preceramic polymers is still conducted by trial and error. This methodology could be considered an elementary process in science to knowledge; however, it is necessary for a statistical investigation arising from a hypothesis being confronted with conflicting observations. Also, there is a lack of statistical evaluation of operating parameters affecting the electrospinning of preceramic polymers in previous studies. The requirements and guidelines of preceramic polymer electrospinnability may be established by systematically studying the electrospinning requirements of ceramic precursors. Preceramic polymers are composed of cyclic and/or linear units with complex structures and low molecular weight [13]. This characteristic challenges the electrospinning of these materials due to low molecular chain entanglements. Therefore, the available literature regarding the electrospinning of Si-based preceramic polymers is based on the use of spinning aids, i.e., organic polymers. The necessity to predict the electrospinnability conditions from properties assessment might offer a tool to control the manufacture and the material morphology. The present work aims to evaluate and optimize the electrospinning of polysilazane with and without organic polymer as a spinning aid using a statistical approach.

4.2 EXPERIMENTAL

The oligosilazane HTT1800 (commercially available as Durazane 1800, Merck KGaA, Germany) was selected as the polysilazane precursor. Tetra-*n* butylammonium fluoride (TBAF) (1 M in THF) (Sigma-Aldrich Co. LLC., Germany) was used as the catalyst, and calcium borohydride bis(tetrahydrofuran) ($\text{Ca}(\text{BH}_4)_2 \cdot 2\text{THF}$) (Sigma-Aldrich Co. LLC., Germany) was used as a reaction inhibitor. THF 99.5% (Fischer Chemical, USA) and DMF 99.5% (Fischer Chemical, USA) were used for synthesis and electrospinning experiments. PAN with a mass ponderal weight of 200 kDa (Polysciences, USA) was used as the organic polymer. Dicumyl peroxide (DCP) 98% (Sigma-Aldrich Co. LLC., Germany) was used as a curing initiator of polysilazane.

HTT1800 was first crosslinked via the reactions between N-H and Si-H groups available in the precursor to increase the molecular weight [14]. The implementation of this strategy should lead to tailored polysilazane with the required properties for the spinning

process. The tunable rheology of preceramic polymers pre-crosslinking is useful for electrospinning due to the increase of molecular chain entanglements, producing more uniform fibers with thinner diameters. Briefly, 50 g of the oligosilazane HTT1800 was dissolved under vigorous magnetic stirring in 140 mL of THF inside a glass flask. Then 0.25 wt.% of the catalyst TBAF concerning HTT1800 was added dropwise to the reaction. The reaction was carried out for 120 min and then stopped with an excess of the inhibitor calcium borohydride bis(tetrahydrofuran). The mixture was stirred for another 5 min, and afterward, the solution was filtered with a qualitative filter paper. Finally, the solvent was removed under vacuum, resulting in a colorless solid polysilazane (HTTS).

The solutions of HTTS were prepared with the desired amounts of polysilazane by entirely dissolving in THF:DMF 9:1 wt.% and 3 wt.% of DCP inside a laboratory glass bottle by magnetic stirring for 12 h at room temperature. PAN was dried at 110 °C for 24 h before use and then dissolved in DMF at 100 °C for 3 h. The solutions HTTS_PAN were prepared by dissolving the appropriate amount of HTTS in the solution inside a laboratory glass bottle to obtain a concentration of polysilazane: PAN equal to 3:2 wt.% and 3 wt.% of DCP followed by magnetic stirring for 12 h at room temperature. The electrospinnability of the solutions HTTS and HTTS_PAN was investigated according to different polymer concentrations (Table 4.1). A lab-scale electrospinning device with a parallel collector inside a glove box (to avoid the influence of environmental conditions on the process) was used to electrospun the solutions.

Table 4.1 – HTTS and HTTS_PAN solutions used to investigate the electrospinnability of the preceramic precursor

Sample	Total polymer concentration (wt.%)	Name
HTTS solution	45	HTTS_45
	50	HTTS_50
	55	HTTS_55
	60	HTTS_60
	65	HTTS_65
HTTS_PAN solution	7.5	HTTS_PAN_7.5
	10.0	HTTS_PAN_10
	12.5	HTTS_PAN_12.5
	15.0	HTTS_PAN_15.0
	17.5	HTTS_PAN_17.5

The selection of meaningful ranges for each operating parameter was defined based on preliminary experiments. The operating parameters selected were: positive voltage, negative

voltage, feed rate, tip-to-collector distance, and needle diameter, and center points were established. A positive voltage was applied to the electrode fastened on the electrospinning needle, whereas a negative voltage was applied to the electrode in contact with the collector. Needle diameters correspond to 27G (0.4 mm), 21G (0.8 mm), and 18G (1.2 mm).

The rheological properties of the solutions were determined using a MCR 702 rotational rheometer (Anton Paar, Austria) in parallel plate configuration according to calculation method DIN 53018 R2/3. The upper moving plate has a diameter of 25 mm and the lower Peltier plate was adjusted to the temperature of 28 °C, which was the same during electrospinning inside the glove box. Viscosity was measured at shear rates in a logarithmic ramp increased from 0.1 to 1000 s⁻¹. Sixty-five points were initially measured for 20 s gradually increased to 1s of measurement time. The reported viscosities are the averages of two replicates. The behavior of shear rate and shear stress diagrams was adjusted according to the power-law model. The power-law index (n), flow rate (Q), and needle radius (a) were employed to calculate the shear rate (γ) according to steady-state flow in a straight circular pipe (Equation 4.1) [15]. The needle radius was here considered since it is difficult to evaluate the elongational strain rate applied to fiber processing that would best apply to electrospinning.

$$\gamma = \frac{Q}{\pi \times a^3} \times \left(3 + \frac{1}{n} \right) \quad (4.1)$$

The viscosity of each solution was calculated according to the shear rate specific to the electrospinning process conducted in the average values of the operating parameters. The specific viscosity (η_{sp}) and the reduced viscosity (η_{red}) were subsequently determined. Specific viscosity expresses the incremental viscosity due to the presence of the polymer in the solution. Likewise, reduced viscosity is the ratio of the specific viscosity to the mass concentration of the polymer species. Intrinsic viscosity (η_{int}) was determined as an extrapolation of reduced viscosity measured for various concentrations to the polymer concentration equal to zero. Intrinsic viscosity was related to Berry's number to measure the degree of molecular chain entanglement of polymer in solution regarding polymer molecular weight, polymer concentration, and polymer/solvent solubility parameter. Berry's number (Be) was calculated by multiplying the intrinsic viscosity (η_{int}) by the polymer concentration (c) (Equation 4.2) [16].

$$Be = \eta_{int} \times c \quad (4.2)$$

The critical chain overlap concentration (c^*) marks the onset of significant polymer overlap in solution and was estimated to be inversely proportional to intrinsic viscosity (η_{int}) (Equation 4.3) [17,18].

$$c^* = \frac{1}{\eta_{int}} \quad (4.3)$$

Surface tension measurements were conducted through a hanging-drop approach ($\sim 4 \mu\text{L}$ per drop) using a DSA25E drop shape analyzer (Krüss, Germany). The conductivity of the solutions was measured by a conductivitymeter SevenCompact S230-Basic (Mettler Toledo, EUA) at room temperature. Three measurements were done and the average is given. A Zeiss Gemini Sigma 300 VP scanning electron microscope (SEM) with an acceleration voltage of 3 kV and magnification of $\times 1000$ (HTTS) and $\times 3000$ (HTTS_PAN) was used to observe the morphology of the electrospun mats. The samples were previously sputter-coated with gold (thickness of about 280 Å) using a sputtering device Sputter Coater 108auto (Cressington, England). The fiber diameter was evaluated from four different SEM images measuring randomly 100 fibers of each sample using open-source ImageJ software.

The statistical optimization of HTTS_60 and HTTS_PAN_17.5 solutions was conducted using a Design of Experiment approach. Statistica software (TIBCO Statistica, StatSoft Europe GmbH) was used to perform the experimental design and data manipulation. Independent factors were defined as the operating parameters such as positive voltage (from 9 to 15 kV), negative voltage (from -15 to -9 kV), feed rate (from 0.8 to 3.0 $\text{ml}\cdot\text{h}^{-1}$), tip-to-collector distance (from 13.5 to 23.5 cm), and needle diameter (from 0.4 to 1.2 mm). The mean diameter of electrospun fibers was defined as the dependent factor (response).

The ranges of the investigated factors were tested at three levels of each factor (Table 4.2). First, the screening using a fractional factorial $2^{(5-2)}$ design (resolution III) was conducted to identify the three factors with the higher effects on electrospinning. Subsequent experiments were used to define the levels of critical values previously identified, which resulted in better process performance. The employed Box-Behnken design was an incomplete three-level factorial design.

Table 4.2 – Experimental levels of independent factors

		Level (actual)			
	Factor	Unit	Lower (-1)	Center (0)	Upper (+1)
HTTS_60	Positive voltage (needle)	kV	10.00	12.50	15.00
	Negative voltage (collector)	kV	-10.00	-12.50	-15.00
	Feed rate	ml·h ⁻¹	1.0	2.0	3.0
	Tip-to-collector distance	cm	13.50	18.50	23.50
	Needle diameter	mm	0.4	0.8	1.2
HTTS_PAN_17.5	Positive voltage	kV	9.00	10.00	11.00
	Negative voltage	kV	-9.00	-10.00	-11.00
	Feed rate	ml·h ⁻¹	0.8	1.0	1.2
	Tip-to-collector distance	cm	13.50	18.50	23.50
	Needle diameter	mm	0.4	0.8	1.2

The most significant independent factors were mathematically related to fiber diameter by quadratic polynomial models. The quality of the proposed models was determined based on the coefficient of determination (R-sqr) and the adjusted coefficient of determination (R-adj). Analysis of variance (ANOVA) followed by Fisher's exact test was carried out by modeling the results of the Box-Behnken design, where the critical probability level (p-value) of 0.05 was considered to reflect the statistical significance of the parameters of the proposed model. The optimized critical values were predicted by response surface methodology. The experimental error was assumed to be random and was estimated through three replicates at the design center points. The pure error option was selected to analyze the experimental error. The experiments were performed randomly to avoid any systematic bias in the outcomes. The plots of the normal distribution of the residuals and the actual values *versus* predicted values were analyzed. Solutions prepared in the same batch were used for screening design and Box-Behnken design.

4.3 RESULTS AND DISCUSSION

4.3.1 Electrospinnability

Electrospinnability of HTTS and HTTS_PAN solutions was observed with an increase in polymer concentration by the transition from beads to fibers. Homogeneous fibers without

beads were observed with HTTS_60 (Figure 4.1) and HTTS_PAN_17.5 (Figure 4.2). The mean fiber diameter and the respective histogram for each concentration tested are also provided in the supplementary material. Under the same operating parameters, a larger fiber diameter was produced with HTTS_65. In contrast, the solution was unspinnable for concentrations >65wt.%, which can be attributed to high surface tension that prevented the fibers from being drawn out by the electrical force. The beads formation observed for both solutions was attributed to low polymer chain entanglements resulting from low extensional viscosity, as will be eventually corroborated with Be number.

The viscoelasticity of the solution was increased by adding more polymer once the surface tension and conductivity of the solutions did not differ/increase with increasing polymer concentration (Figure 4.3a and Figure 4.3b), which suppressed the Rayleigh instability during electrospinning. The molecular chain entanglement results from the polymer concentration and the molecular weight, which is linked to the solutions' viscosity. The relationship between polymer concentration and viscosity is highly dependent on the nature of the polymer, such as molecular structure and molecular weight, and the intermolecular interactions within the polymer solution, such as polymer-polymer and polymer-solvent. The samples showed a pseudoplastic rheological behavior with a shear-thinning ($n < 1$) due to the alignment of the polymer chains in the direction of the applied shear stress and reduction of the solution viscosity (Figure 4.3c and Figure 4.3d).

The profiles of shear stress *versus* shear rate for HTTS and HTTS_PAN solutions presented a good data adjustment according to the power-law model. The shear rate was calculated according to each obtained power-law index and further used to calculate the reduced viscosity. For HTTS_PAN solutions, when the polymer concentration was low (<12.5wt.%), the solution viscosity increased slightly by adding more polymer. As the polymer concentration increases (>15wt.%), the viscosity increases gradually until the concentration reaches a specific value, after which the viscosity increases considerably. On the other hand, the solution viscosity increased slightly by adding more polymer for HTTS solutions. Both solutions presented a good data fit for an exponential model. The relationship between the solution viscosity and the polymer concentration is highly dependent on the nature of the polymer: structure, polydispersity, molecular weight, and intermolecular interactions. Specifically, HTTS has a high polydispersity and a low molecular weight when compared to organic polymers [14]. Thus, the increase in HTTS concentration did not notably increase the reduced viscosity since small molecules of different sizes do not provide the entanglement necessary to enhance viscosity.

The intrinsic viscosity, representing the volume occupied by the swollen polymer in solution, resulted in $70 \text{ mL}\cdot\text{g}^{-1}$ for HTTS solutions and $109 \text{ mL}\cdot\text{g}^{-1}$ for HTTS_PAN solutions.

Figure 4.1 – Electrospinnability results of HTTS according to polymer concentration (12.50 kV positive voltage, -12.50 kV negative voltage, $2 \text{ ml}\cdot\text{h}^{-1}$ feed rate, 18.50 cm tip-to-collector distance, and 0.8 mm needle diameter)

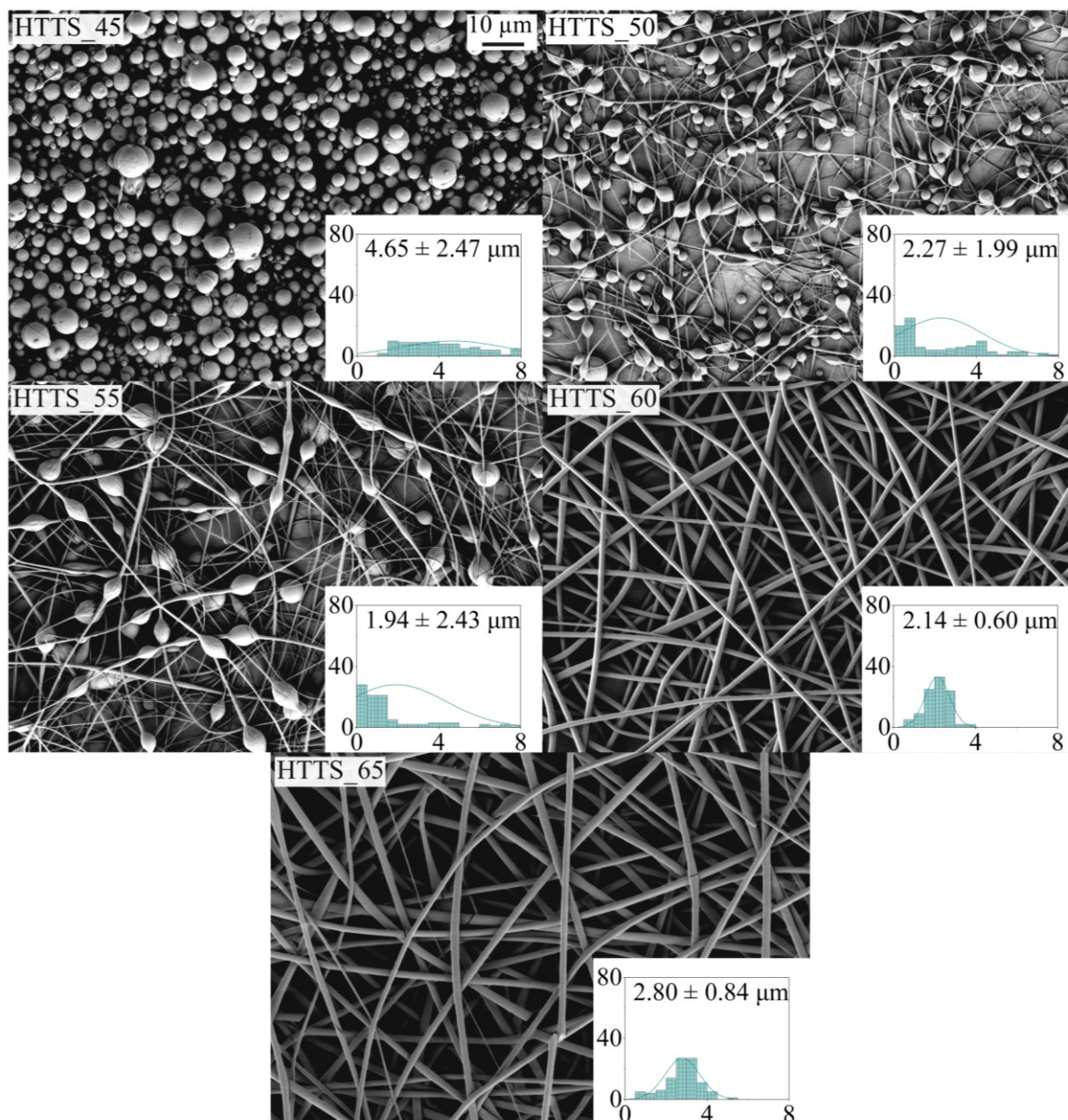


Figure 4.2 – Electrospinnability results of HTTS_PAN according to polymer concentration (10.00 kV positive voltage, -10.00 kV negative voltage, 1 ml·h⁻¹ feed rate, 18.50 cm tip-to-collector distance, and 0.8 mm needle diameter)

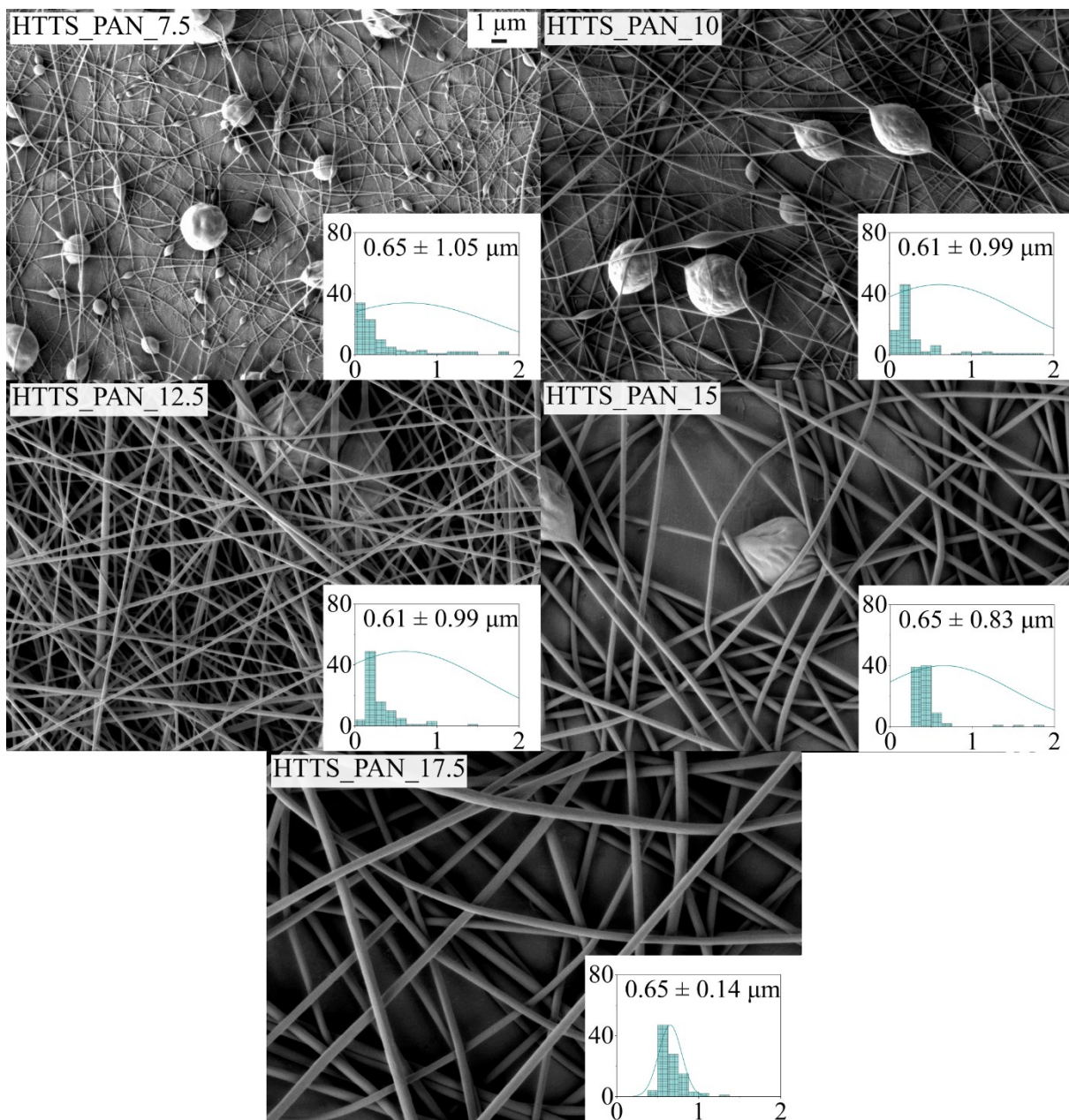
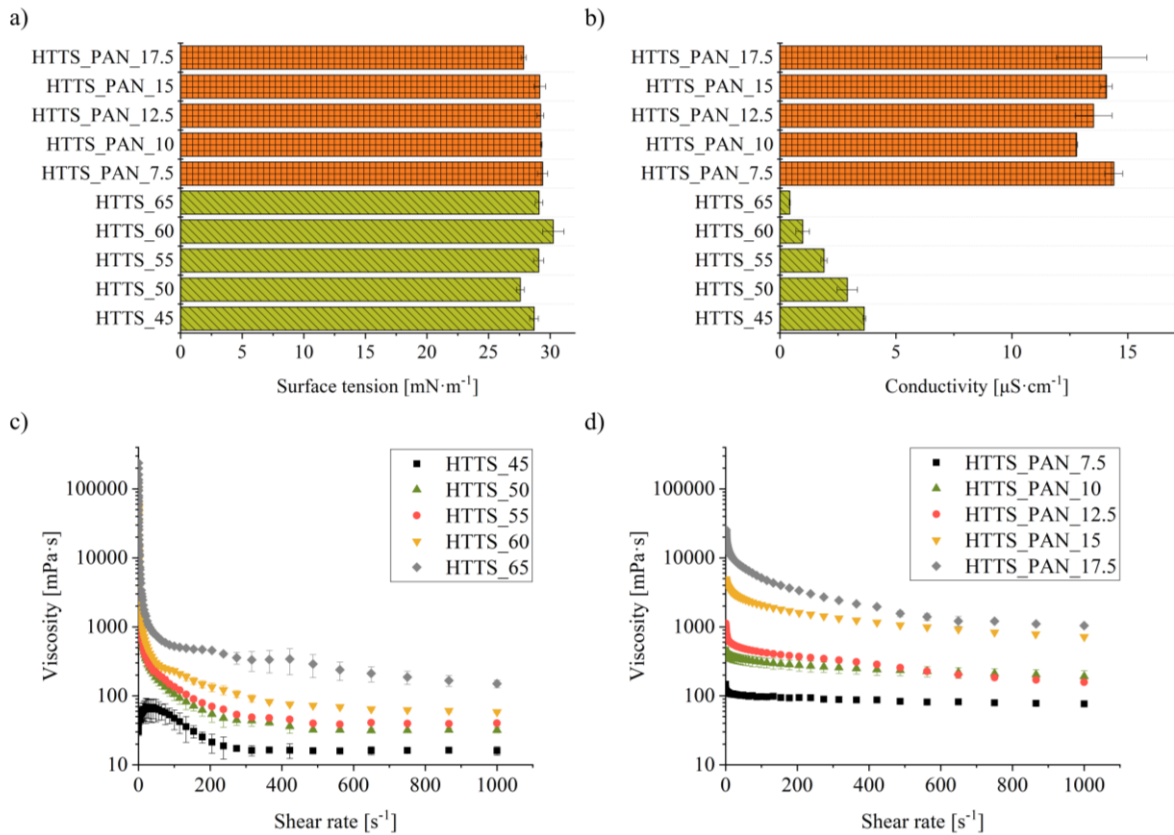


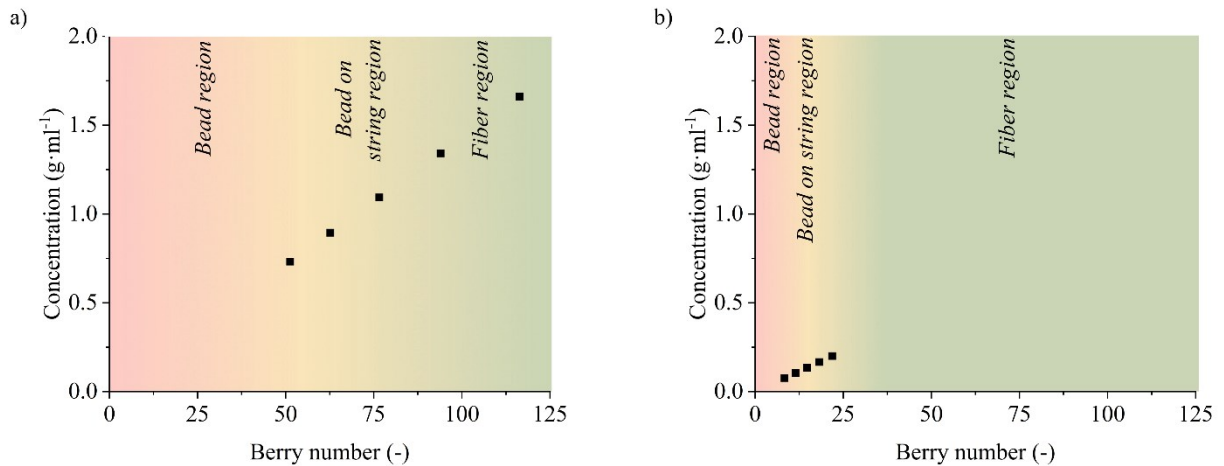
Figure 4.3 – a) Surface tension, b) conductivity, c) viscoelasticity behavior of HTTS solutions, and d) viscoelasticity behavior of HTTS_PAN solutions



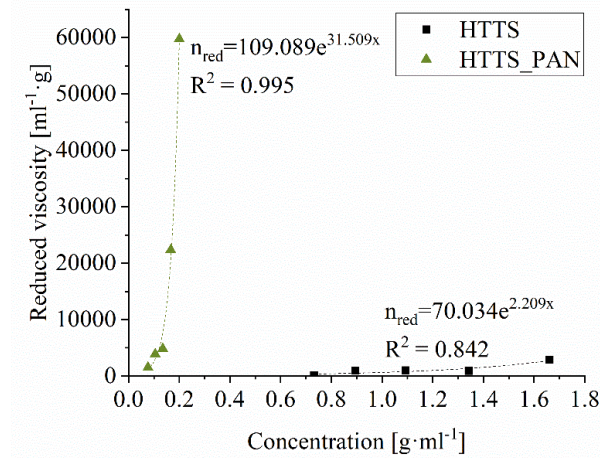
Berry's numbers ranged from 51 to 116 for HTTS solutions and 8 to 22 for HTTS_PAN solutions (Figure 4.4). Beads or beads on string were observed in HTTS and HTTS_PAN, respectively, with $Be < 94$ and $Be < 22$. The high-concentrated solution of the low molecular weight HTTS resulted in a reasonable Berry number exhibiting high viscosity; however, preceramic polymer chains could not form entanglements due to their short length [19]. Berry's number was related to the largest fiber diameter obtained with each concentration. For HTTS solutions, the fiber diameter increased by about 16% when Berry's number increased from 94 to 116 (HTTS_60 to HTTS_65). Homogeneous PAN fibers with $Be > 3.9$ [20] and $Be > 5$ [19] are observed in the literature; however, adding large amounts of polysilazane to the PAN solution raised requirements for the system to be electrospun, increasing Berry's number to 22. The electrospun fiber diameter was reduced by adding PAN to HTTS on the electrospun fiber diameter. This diameter reduction was explained by the reduction in Berry's number, i.e., degree of polymer chain entanglement, from 94 to 22. This result indicated the organic polymer's positive effect on the HTTS molecular chain entanglement in a solvent. The addition of PAN resulted in more relaxation for the HTTS molecular chains reducing the electrospun

fiber diameter. In diluted solutions, when $Be < 1$, the polymer molecules are sparsely distributed in the solution. Increasing concentration, i.e., Berry's number, some chains overlap, turning the unentangled semi-dilute regime with insufficient entanglement degree ($Be < 63$ for HTTS and $Be < 8$ for HTTS_PAN). As the concentration increases, chain entanglements induced by the larger occupied fraction of polymer molecules result in an entangled semi-dilute regime ($Be > 94$ for HTTS and $Be > 22$ HTTS_PAN). Moreover, the higher conductivity observed with HTTS_PAN solutions resulted in higher elongation forces and greater bending instability, contributing to thinner fibers.

Figure 4.4 – Correlation of Berry's number with solution concentration according to the morphology of a) HTTS and b) HTTS_PAN



The critical chain overlap concentration value (c^*) of HTTS_PAN solutions was about half of HTTS solutions ($0.009 \text{ g}\cdot\text{ml}^{-1}$ and $0.014 \text{ g}\cdot\text{ml}^{-1}$, respectively). This result indicates that molecular chains started to overlap with a lower concentration of polymer when PAN was added to the solution, anticipating the regime's transition from dilute to an entangled solution. HTTS is supposed to be trapped in the voids formed by the non-linear and complex structure of the PAN due to the presence of nitrile ($-\text{C}\equiv\text{N}$). The entanglement concentration was $1.34 \text{ g}\cdot\text{ml}^{-1}$ (HTTS) and $0.20 \text{ g}\cdot\text{ml}^{-1}$ (HTTS_PAN). The change in the slope of plot $c \cdot c^{*-1}$ versus relative viscosity also indicated the transition from unentangled to the entangled semi-dilute regime (Figure 4.5).

Figure 4.5 – HTTS and HTTS_PAN concentration *versus* reduced viscosity

4.3.2 Screening design of HTTS_60 and HTTS_PAN_17.5 solutions

The screening design was carried out to identify the factors that most influence the fiber diameter during electrospinning. Fibers of HTTS_60 ranging from 1.53 to 3.56 μm and fibers of HTTS_PAN_17.5 ranging from 0.50 to 0.88 μm were observed (SEM images not provided, please refer to the supplementary material of the published paper). Pareto charts demonstrate that the studied factors were statistically insignificant once all parameters presented $p\text{-value} > 0.05$. However, it was possible to identify the three key influence factors: feed rate, tip-to-collector-distance, and negative voltage for HTTS_60 and tip-to-collector-distance, feed rate, and positive voltage for HTTS_PAN_17.5. The needle diameter (0.4, 0.8, or 1.2 mm) was irrelevant for fiber diameter in solution electrospinning, compared to melt spinning of preceramic polymers [21]. Fluid velocity increased with a smaller needle diameter, resulting in different sizes of drops at the tip. The size and shape of the drop supported at the needle tip, i.e., Taylor cone during electrospinning, depended more on feed rate than needle diameter due to a mass balance between what was fed by the pump and what was ejected from the needle. When the applied potential reached the same critical value required to overcome the surface tension of the solution, a jet was ejected from the Taylor cone regardless of needle diameter. Higher voltage accelerated the stretching of the solution jet due to the greater Coulombic forces as well as a stronger electrostatic field. The negative voltage was the factor that least influenced the electrospinning of HTTS_PAN_17.5, possibly due to the already inherent high conductivity of this solution.

ANOVA results show that R-sqr was 0.72 for HTTS_60 and 0.86 for HTTS_PAN_17.5, whereas the lack of fit was insignificant, meaning that there is a random

variation around the fitted curve. These R-sqr are considered good values since most of the variability between predicted and experimental is due to pure error. Thus, quantitatively, the linear response models obtained by the low-resolution fractional factorial design analysis are not accurate enough to explore the design space without further experimentation. Nevertheless, this qualitative information was integral in choosing the variable ranges for the subsequent Box-Behnken design.

4.3.3 Optimization of HTTS_60 and HTTS_PAN_17.5 solutions

A Box-Behnken design was carried out to optimize the electrospinning process and obtain the thinner fiber diameter for HTTS_60 and HTTS_PAN_17.5. From the results of the screening design, a positive voltage of 12.50 kV, a needle diameter of 0.8 mm (HTTS_60), a negative voltage of -10.00 kV, and a needle diameter of 0.8 mm (HTTS_PAN_17.5) were controlled during the experiments. The obtained fibers of HTTS_60 ranged from 1.70 to 3.62 μm and of HTTS_PAN_17.5 from 0.58 to 0.85 μm .

The experimental data obtained from the Box-Behnken design was validated by ANOVA (Table 4.3). The F-values, sum of the squares, and p-values were the criteria to determine the significant factors. Significant parameters with a p-value < 0.05 were obtained, which shows the statistical significance at >95% confidence interval, indicating that the experimental data can adequately describe the proposed models obtained by response surface methodology [22]. For these parameters, the calculated F-value was higher than the tabulated one; therefore, it is valid with the 95% confidence level studied.

The model terms with p-value > 0.05 are insignificant; therefore, these terms were excluded from the model to enhance fitting [23]. For HTTS_60, the statistical analysis resulted in two models: one with no interaction and the other with two-way interactions. Although, as in the two-way interaction model, the misfit was significant (p=0.04), the model with no interaction was chosen since a good data adjustment was achieved (R-sqr=0.86) with most of the variability between predicted and experimental attributed to the pure error. The R-sqr value indicates the accuracy of the fitting of the model and a good correlation between predicted and experimental. According to ANOVA, feed rate and negative voltage were statistically significant to be included in the model since the p-value was respectively 0.014 and 0.004. The ANOVA table showed that the misfit was not significant (p=0.051), meaning that 5% of lack of fit is possible due to noise.

Table 4.3 – ANOVA according to Box-Behnken design (A is positive voltage in kV, B is negative voltage in kV, C is feed rate in $\text{ml}\cdot\text{h}^{-1}$, D is tip-to-collector distance in cm, and E is needle diameter in mm)

	Source	Sum of squares	df	Mean square	F-value	p-value
HTTS_60	<i>B (linear+quadratic)</i>	0.621	2	0.310	72.162	0.014
	<i>C (linear+quadratic)</i>	2.196	2	1.098	255.405	0.004
	D (linear +quadratic)	0.138	2	0.069	16.007	0.059
	Lack of fit	0.485	6	0.081	18.779	0.051
	Pure error	0.009	2	0.004	-	-
	Total	3.418	14	-	-	-
	R-sqr	0.86	-	-	-	-
	R-adj	0.75	-	-	-	-
HTTS_PAN_17.5	A (linear+quadratic)	0.0030	2	0.0015	6.4073	0.1350
	<i>C (linear+quadratic)</i>	0.0089	2	0.0044	19.0501	0.0499
	D (linear+quadratic)	0.0075	2	0.0037	15.9986	0.0588
	<i>AC (linear)</i>	0.0056	1	0.0056	24.1071	0.0391
	AD (linear)	0.0009	1	0.0009	3.8571	0.1885
	<i>CD (linear)</i>	0.0144	1	0.0144	61.7143	0.0158
	Lack of fit	0.0075	3	0.0025	10.6786	0.0868
	Pure error	0.0005	2	0.0002	-	-
	Total	0.0486	14	-	-	-
	R-sqr	0.84	-	-	-	-
R-adj	0.54	-	-	-	-	

For HTTS_PAN_17.5, the statistical analysis presented one model: two-way interactions (linear x linear). According to ANOVA, feed rate, tip-to-collector distance, an interaction between feed rate and positive voltage, and interaction between feed rate and tip-to-collector distance were statistically significant to be included in the model. The Pareto chart also showed these factors' significant influence on the electrospinning of the HTTS_PAN_17.5 solution. Also, an important result of this study was the observation that the interaction effects between feed rate and tip-to-collector distance are significant. In this case, to determine the optimum conditions in the process, these variables should not be analyzed in isolation because the effect of one depends on the level of the other; that is, it cannot change one factor without affecting the other. Likewise, higher F-values were observed for the most significant factors, for instance, 61.7143 for the interaction between feed rate and tip-to-collector distance, 24.1071 for the interaction between positive voltage and feed rate, and 19.0501 for feed rate; moreover, the misfit was insignificant ($p=0.0868$). Additionally, the overall predictability of the model and its statistical significance were expressed by the coefficient of determination (R-sqr).

Reasonably high values of R-sqr value were determined (R-sqr=0.86 for HTTS_60 and R-sqr=0.84 for HTTS_PAN_17.5), indicating the accuracy of the model fitting and good correlation between predicted and experimental values.

The gap between R-sqr and R-adj should be as small as possible and not exceed 0.2 [24]. This was observed for HTTS_60 (0.11) but not for HTTS_PAN_17.5 (0.3) due to the more complex solution involving low molecular weight polydispersive and high molecular weight polymers. The HTTS short chains are trapped between the long polymer chains of the organic polymer. Therefore, depending on the random structure formed during the electrospinning, different fibers are produced. Nonetheless, the mean square pure error was low, which shows that the variation is within the expected error. The low standard deviation showed that the quadratic model is the best option to represent the response.

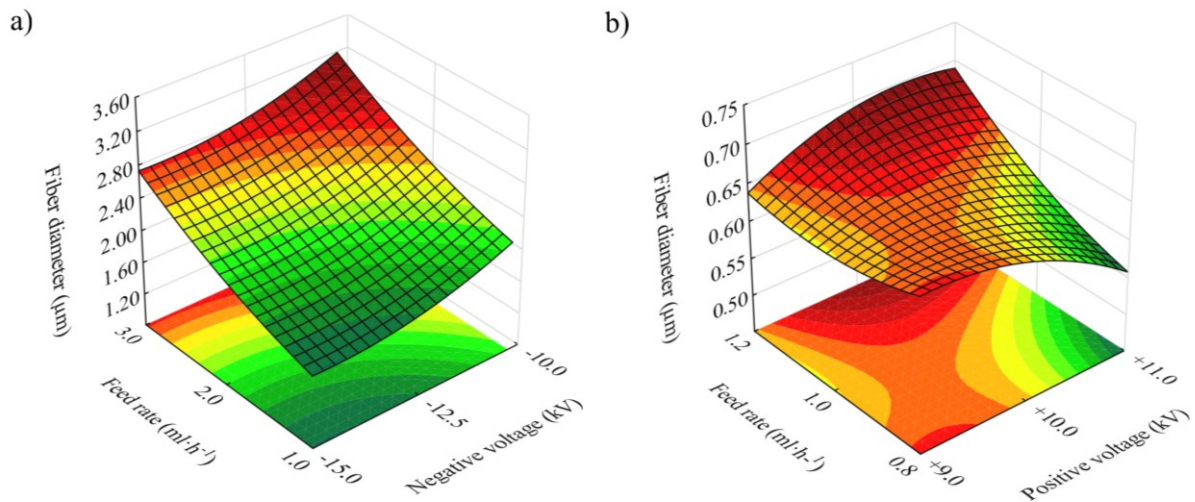
The graphical method was used to validate and characterize the nature of the distribution of the residuals of the models [23]. The verification of experimental results can be achieved by analyzing the plots from the model, such as actual *versus* predicted, normal probability of the residuals, and externally studentized residuals *versus* predicted. In this case, the ANOVA results were in good agreement with the normal probability plots. Data points reasonably overlap the straight line, meaning that the errors are normally distributed, i.e., all points are normally distributed around the straight line, showing the independence of the residuals. Furthermore, the normal distributions of the residuals indicated the accuracy of the assumptions and the independence of the residuals. So, the statistical analysis showed that the model could predict and optimize the process.

Three-dimensional response surfaces are important graphical plots to explain the interaction effects of the operating parameters on fiber diameter [22]. Also, the graphical interpretation of the models obtained for the mean diameter of electrospun fibers can be seen in the 3D graphics of the response surface. Interactions of variables and their value for a maximum response value are examined. The absence of interaction between the variables is observed if the shape is circular or parallel. On the other hand, an elliptical or curved shape indicates the presence of an interaction between the variables. The interactions of the independent variables in fiber diameter response are represented by two independent variables, the third of which was maintained at level 0 (central point value).

The critical values of optimized factors that result in thinner fibers for HTTS_60 are -14.6 kV, $1 \text{ ml} \cdot \text{h}^{-1}$, and 19.5 cm. The response surface was obtained at 19.5 cm as tip-to-collector distance (Figure 4.6a), which showed that the optimized fiber diameter value was located at a

low feed rate and negative voltage values. By elimination of insignificant variables, the electrospinning process was modeled by multiple regression. The critical values of optimized factors that result in thinner fibers for HTTS_PAN_17.5 are: +11.00 kV, 0.8 ml·h⁻¹, and 23.5 cm. At 23.5 cm as tip-to-collector distance, the response surface was obtained (Figure 4.6b).

Figure 4.6 – Surface responses according to Box-Behnken design for a) HTTS_60 at 19.5 cm as tip-to-collector distance, +12.50 kV as positive voltage, and 0.8 mm as needle diameter; and b) HTTS_PAN_17.5 at 23.5 cm as tip-to-collector distance, -10.00kV as negative voltage, and 0.8 mm as needle diameter



In contrast to HTTS_60, the HTTS_PAN_17.5 solution showed a transition of optimized critical values when decreasing the tip-to-collector distance from 23.5 cm to 21.5 cm, 18.5 cm, and 13.5 cm. This is related to the interaction effect of feed rate and tip-to-collector distance. The models are the same except for the last term, which represents the residual. The smallest fiber diameter was observed at 13.5 cm and 23.5 cm, i.e., low and high tip-to-collector distance. For low tip-to-collector distance, the fiber diameter decreased for a higher feed rate and lower positive voltage. In the case of high tip-to-collector distance, the fiber diameter decreased for a lower feed rate and higher positive voltage. Despite that both critical values resulted in similar predicted values, 23.5 cm was chosen as tip-to-collector distance due to the results of critical values given by the software. Moreover, higher tip-to-collector distance avoided fiber fusion during electrospinning due to the low volatility of DMF.

The feed rate showed an influence on the two systems of solutions studied in this work. For the ceramic precursor solution, the feed rate had the most significant effect. In contrast, for the organic polymer and ceramic precursor solution, an interaction between the feed rate and the tip-to-collector distance had the most significant effect. This result suggests that future work

on electrospinning of ceramic precursors may begin by varying the feed rate to improve the process and decrease the fiber diameter. In addition, the surface responses showed that a lower feed rate resulted in thinner fibers in high voltage module values.

The experimental relationship between fiber diameter and the operating parameters was correlated by the quadratic polynomial model [25]. The model in terms of coded variables for HTTS_60 is available (Equation 4.4), where d is fiber diameter (μm) and x and y are coded values of negative voltage and feed rate, respectively. It was seen that the feed rate was the most significant parameter. The model in terms of actual variables for HTTS_60 is also available (Equation 4.5), where d is fiber diameter (μm), NV is negative voltage (kV), and FR is feed rate ($\text{ml}\cdot\text{h}^{-1}$). The model explains 86% of the variance.

$$d = 2.21000 + 0.2575 \times x + 0.1563 \times x^2 + 0.5188 \times y + 0.1088 \times y^2 - 0.006 \quad (4.4)$$

$$d = 9.3473 + 0.7280 \times NV + 0.0250 \times NV^2 + 0.0838 \times FR + 0.1088 \times FR^2 - 2.5521 \quad (4.5)$$

The model in terms of coded variables for HTTS_PAN_17.5 is available (Equation 4.6), where d is fiber diameter (μm) and x , y and z are coded values of positive voltage, feed rate, and tip-to-collector distance, respectively. It was seen that an interaction between the feed rate and the tip-to-collector distance was the most significant parameter. The model in terms of actual variables for HTTS_PAN_17.5 is also available (Equation 4.7), where d is fiber diameter (μm), PV is positive voltage (kV), and FR is feed rate ($\text{ml}\cdot\text{h}^{-1}$). The model explains 84% of the variance.

$$d = 0.6533 + 0.0038 \times x - 0.0279 \times x^2 - 0.0313 \times y + 0.0171 \times y^2 + 0.0375 \times x \times y - 0.0150 \times x \times z + 0.06 \times y \times z - 0.0079 \quad (4.6)$$

$$d = 1.2073 + 0.4300 \times PV - 0.0279 \times PV^2 - 3.9954 \times FR + 0.4271 \times FR^2 + 0.1875 \times PV \times FR - 0.0030 \times PV \times TD + 0.0600 \times FR \times TD - 1.0828 \quad (4.7)$$

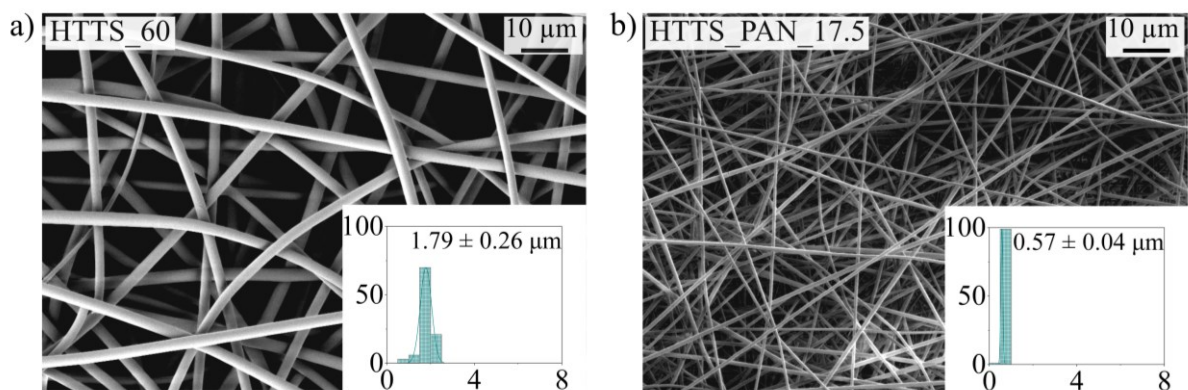
The predicted value of fiber diameter in the optimized conditions was $1.69 \pm 0.34 \mu\text{m}$ for HTTS_60 (deviation of prediction equal to 19.8%) and $0.56 \pm 0.10 \mu\text{m}$ for

HTTS_PAN_17.5 (deviation of prediction equal to 18.3%). As can be seen, the model shows good agreement with the experimental data and, therefore, can be considered for the determination of optimum conditions.

4.3.4 Model validation

The optimized factors, together with the central points were tested experimentally to validate the developed models. Homogeneous fibers with narrow distribution were obtained with a mean diameter of $1.79 \pm 0.26 \mu\text{m}$ for HTTS_60 (Figure 4.7a) and $0.57 \pm 0.04 \mu\text{m}$ for HTTS_PAN_17.5 (Figure 4.7b). These values are very close to the predicted values ($1.69 \pm 0.34 \mu\text{m}$ for HTTS_60 and $0.56 \pm 0.10 \mu\text{m}$ for HTTS_PAN_17.5). The errors between experimental and predicted values for fiber diameter were within 5.9% and 1.8%, respectively for HTTS_60 and HTTS_PAN_17.5, confirming the developed models. Interestingly, the electrospinning of preceramic polymers using PAN as a spinning aid resulted in fibers with an ultrathin diameter ranging from 0.1 to $0.66 \mu\text{m}$ as also observed in the present work [26–28]. It is highlighted that 46 experiments were required to model the electrospinning process of polysilazane with and without organic polymer instead of 486 if a full factorial design was employed. It is also worth noting that the models are only valid for the ranges of operating parameters employed here.

Figure 4.7 – Fibers resulting from optimization of a) HTTS_60 and b) HTTS_PAN_17.5



Although the electrospinning of preceramic polymers is common to be conducted with an organic polymer, some electrospun PDCs were developed to avoid defects by the decomposition of the spinning aid. The literature shows that electrospun preceramic polymer fibers usually have a larger diameter due to the requirement for higher precursor concentration,

as investigated here (Table 4.4). Additionally, the optimized operating parameters in the present work are relatively similar to some values reported in the literature. However, it should be noted that the experimental optimization through a Design of Experiments conducted in this work allowed finding the optimal points for the electrospinning of preceramic polymers, which had not yet been evaluated in the literature.

Although the addition of organic polymer can generate some defects such as pores after the pyrolysis of ceramic precursors, they provide the electrospinnability necessary to produce ultrathin fibers, thus increasing the surface area of the material. Furthermore, the organic polymer can be used to develop carbon-rich PDCs, which may broaden some material properties, such as electromagnetic shielding [29–31].

4.4 CONCLUSIONS

This work evaluated and optimized the electrospinning of polysilazane with and without organic polymer as a spinning aid using a statistical approach. Even though the ceramic precursor polysilazane presents a complex structure to be electrospun, mathematical models related to the most significant factors were developed at the desired significance level of 95%. A combination of the fractional factorial and Box-Behnken design was relatively accurate with high regression coefficients as well as a maximum 19.8% deviation of prediction. It provided the optimum conditions for polysilazane 60 wt.%: negative voltage (-14.6 kV), feed rate ($1 \text{ ml}\cdot\text{h}^{-1}$), and tip-to-collector distance (19.5 cm); and for polysilazane/organic polymer 17.5 wt.%: positive voltage (11.00 kV), feed rate ($0.8 \text{ ml}\cdot\text{h}^{-1}$), and tip-to-collector distance (23.5 cm). Under these optimal conditions, polysilazane fibers with a diameter of $1.79 \pm 0.26 \text{ }\mu\text{m}$ and polysilazane/polyacrylonitrile fibers with a diameter of $0.57 \pm 0.04 \text{ }\mu\text{m}$ were manufactured. The mathematical models can be used to predict the mean fiber diameter and its standard deviation as well as to optimize the assigned electrospinning parameters within the specified regions. The overall investigation of the morphology showed outstanding results to tailor the architecture of the fibers. This particular research work will effectively set up a foundation for further studies, in which the scope is related to the morphology quality of electrospun preceramic precursors.

Table 4.4 – Comparison of electrospun preceramic polymers electrospun with/without organic polymer (pyrolysed to ceramic)

Preceramic polymer	Organic polymer (wt.%)	Precursor concentration (g·ml ⁻¹)	Voltage (kV)	Feed rate (ml·h ⁻¹)	Tip-to-collector distance (cm)	Fiber diameter (μm)	Reference
Polymethylphenylsilsesquioxane	Free	0.6	28	1	21	4.874	[32]
	Polyvinylpyrrolidone (25)	N/A	28	1	21	1.640	[33]
	Polyvinylpyrrolidone (25)	N/A	10	0.5	12	1.610	[34,35]
	Polyvinylpyrrolidone (25)	0.32	10	0.5	12	1.022	[36]
Polycarbosilane	Free	1.5	20	1	20	4	[37]
	Free	1.25	12	2.4	15	2.000 ¹	[38]
	Free	1.3	20	0.1	18	2.200	[39]
	Free	0.2	20	2	10	2.100	[40]
Polysilazane	Polystyrene (25)	N/A	12	0.75	20	0.520	[41]
	Polycaprolactone (25)	0.15	25	2	N/A	0.723	[42]
	Polyvinylpyrrolidone (25)	0.1	6	3	15	0.500	[43]
	Free	1.33	27.1	1	19.5	1.790	This work
Polysilazane	Free	1.33	15	1.5	10	0.300	[44]
	Polyvinylpyrrolidone (34)	0.13	13	1	9	0.350-0.500 ¹	[45,46]
	Polyacrylonitrile (40)	0.12	21.0	0.8	23.5	0.570	This work

4.5 ACKNOWLEDGMENTS

The authors thank CAPES and Deutscher Akademischer Austauschdienst (DAAD) for supporting this work within the project PROBRAL (Grant n° 88887.368756/2019-00). This study was financed in part by the Coordenação de Aperfeiçoamento de Pessoal de Nível Superior - Brasil (CAPES) - Finance Code 001 and CNPq - Brasil (Grant n° 442149/2018-2).

4.6 AUTHORS' CONTRIBUTIONS

The paper is mainly based on the work of the first author and author of this thesis Heloisa Ramlow. This work was conducted in collaboration with the group of Ceramic Precursors (University of Bayreuth, Germany). The precise contributions of each author are listed below (Table 4.5).

Table 4.5 – Authors' contributions to Chapter 4

Author	Contribution
Ramlow, H.	Conceptualized the work, wrote the manuscript
Marangoni, C.	Gave conceptual and scientific advice, helped in the scientific evaluation and editing of the manuscript
Motz, G.	Gave conceptual and scientific advice, helped in the scientific evaluation and editing of the manuscript
Machado, R.	Gave conceptual and scientific advice, helped in the scientific evaluation and editing of the manuscript

4.7 REFERENCES

- [1] W.U. Arifeen, M. Kim, J. Choi, K. Yoo, R. Kurniawan, T.J. Ko, Optimization of porosity and tensile strength of electrospun polyacrylonitrile nanofibrous membranes, *Mater. Chem. Phys.* 229 (2019) 310–318. <https://doi.org/10.1016/j.matchemphys.2019.03.020>.
- [2] S. Demiroğlu Mustafafov, A.K. Mohanty, M. Misra, M.Ö. Seydibeyoğlu, Fabrication of conductive lignin/PAN carbon nanofiber with enhanced graphene for the modified electrode, *Carbon* N. Y. 147 (2019) 262–275. <https://doi.org/10.1016/j.carbon.2019.02.058>.
- [3] H. Wang, L. Kong, G.R. Ziegler, Aligned wet-electrospun starch fiber mats, *Food Hydrocoll.* 90 (2019) 113–117. <https://doi.org/10.1016/j.foodhyd.2018.12.008>.
- [4] A. Abbasi, M.M. Nasef, R. Faridi-Majidi, M. Etesami, M. Takeshi, E. Abouzari-Lotf,

- Highly flexible method for fabrication of poly(glycidyl methacrylate) grafted polyolefin nanofiber, *Radiat. Phys. Chem.* 151 (2018) 283–291. <https://doi.org/10.1016/j.radphyschem.2018.07.002>.
- [5] N.N.A. Malek, A.H. Jawad, K. Ismail, R. Razuan, Z.A. ALOthman, Fly ash modified magnetic chitosan-polyvinyl alcohol blend for reactive orange 16 dye removal: adsorption parametric optimization, *Int. J. Biol. Macromol.* 189 (2021) 464–476. <https://doi.org/10.1016/j.ijbiomac.2021.08.160>.
- [6] A.H. Jawad, A.S. Abdulhameed, M.A.K.M. Hanafiah, Z.A. ALOthman, M.R. Khan, S.N. Surip, Numerical desirability function for adsorption of methylene blue dye by sulfonated pomegranate peel biochar: Modeling, kinetic, isotherm, thermodynamic, and mechanism study, *Korean J. Chem. Eng.* 38 (2021) 1499–1509. <https://doi.org/10.1007/s11814-021-0801-9>.
- [7] A.H. Jawad, A.S. Abdulhameed, E. Kashi, Z.M. Yaseen, Z.A. ALOthman, M.R. Khan, Cross-linked chitosan-glyoxal/kaolin clay composite: parametric optimization for color removal and COD reduction of remazol brilliant blue R dye, *J. Polym. Environ.* 30 (2022) 164–178. <https://doi.org/10.1007/s10924-021-02188-1>.
- [8] P. Maneechakr, S. Karnjanakom, A combination of 2k factorial with Box-Behnken designs for FAME production via methanolysis of waste cooking palm oil over low-cost catalyst, *J. Environ. Chem. Eng.* 7 (2019) 103389. <https://doi.org/10.1016/j.jece.2019.103389>.
- [9] E. Bazrafshan, T.J. Al-Musawi, M.F. Silva, A.H. Panahi, M. Havangi, F.K. Mostafapur, Photocatalytic degradation of catechol using ZnO nanoparticles as catalyst: optimizing the experimental parameters using the Box-Behnken statistical methodology and kinetic studies, *Microchem. J.* 147 (2019) 643–653. <https://doi.org/10.1016/j.microc.2019.03.078>.
- [10] M. Yılmaz, A. Altan, Optimization of functionalized electrospun fibers for the development of colorimetric oxygen indicator as an intelligent food packaging system, *Food Packag. Shelf Life.* 28 (2021) 100651. <https://doi.org/10.1016/j.fpsl.2021.100651>.
- [11] C. Wang, Q. Zuo, L. Wang, B. Long, K.M. Salleh, N.I.S. Anuar, S. Zakaria, Diameter optimization of polyvinyl alcohol/sodium alginate fiber membranes using response surface methodology, *Mater. Chem. Phys.* 271 (2021) 124969. <https://doi.org/10.1016/j.matchemphys.2021.124969>.
- [12] R. Ekambaram, S. Saravanan, N. Selvam, S. Dharmalingam, Statistical optimization of novel acemannan polysaccharides assisted TiO₂ nanorods based nanofibers for skin cancer application, *Carbohydr. Polym. Technol. Appl.* 2 (2021) 100048. <https://doi.org/10.1016/j.carpta.2021.100048>.
- [13] A. Viard, P. Miele, S. Bernard, Polymer-derived ceramics route toward SiCN and SiBCN fibers: from chemistry of polycarbosilazanes to the design and characterization of ceramic fibers, *J. Ceram. Soc. Japan.* 124 (2016) 967–980. <https://doi.org/10.2109/jcersj2.16124>.
- [14] O. Flores, T. Schmalz, W. Krenkel, L. Heymann, G. Motz, Selective cross-linking of oligosilazanes to tailored meltable polysilazanes for the processing of ceramic SiCN fibres, *J. Mater. Chem. A.* 1 (2013) 15406–15415. <https://doi.org/10.1039/c3ta13254d>.
- [15] H.A. Barnes, *A Handbook of Elementary Rheology*, 1st ed., The University of Wales Institute of Non-Newtonian Fluid Mechanics, Penglais, Aberystwyth, Dyfed, Wales., 2000. <https://doi.org/10.1126/science.1201543>.
- [16] S. Zhang, B.T. Karaca, S.K. Vanoosten, E. Yuca, S. Mahalingam, M. Edirisinghe, C. Tamerler, Coupling infusion and gyration for the nanoscale assembly of functional polymer nanofibers integrated with genetically engineered proteins, *Macromol. Rapid*

- Commun. 36 (2015) 1322–1328. <https://doi.org/10.1002/marc.201500174>.
- [17] P. Gupta, C. Elkins, T.E. Long, G.L. Wilkes, Electrospinning of linear homopolymers of poly(methyl methacrylate): exploring relationships between fiber formation, viscosity, molecular weight and concentration in a good solvent, *Polymer (Guildf)*. 46 (2005) 4799–4810. <https://doi.org/10.1016/j.polymer.2005.04.021>.
- [18] O. Husain, W. Lau, M. Edirisinghe, M. Parhizkar, Investigating the particle to fibre transition threshold during electrohydrodynamic atomization of a polymer solution, *Mater. Sci. Eng. C*. 65 (2016) 240–250. <https://doi.org/10.1016/j.msec.2016.03.076>.
- [19] S. Basu, N. Gogoi, S. Sharma, M. Jassal, A.K. Agrawal, Role of elasticity in control of diameter of electrospun PAN nanofibers, *Fibers Polym.* 14 (2013) 950–956. <https://doi.org/10.1007/s12221-013-0950-5>.
- [20] K. Nasouri, A.M. Shoushtari, A. Kafrou, Investigation of polyacrylonitrile electrospun nanofibres morphology as a function of polymer concentration, viscosity and Berry number, *Micro Nano Lett.* 7 (2012) 423–426. <https://doi.org/10.1049/mnl.2012.0054>.
- [21] O. Flores, R.K. Bordia, S. Bernard, T. Uhlemann, W. Krenkel, G. Motz, Processing and characterization of large diameter ceramic SiCN monofilaments from commercial oligosilazanes, *RSC Adv.* 5 (2015) 107001–107011. <https://doi.org/10.1039/c5ra17300k>.
- [22] A. Reghioua, D. Barkat, A.H. Jawad, A.S. Abdulhameed, A.A. Al-Kahtani, Z.A. AlOthman, Parametric optimization by Box-Behnken design for synthesis of magnetic chitosan-benzil/ZnO/Fe₃O₄ nanocomposite and textile dye removal, *J. Environ. Chem. Eng.* 9 (2021) 105166. <https://doi.org/10.1016/j.jece.2021.105166>.
- [23] A.S. Abdulhameed, A.T. Mohammad, A.H. Jawad, Modeling and mechanism of reactive orange 16 dye adsorption by chitosan-glyoxal/tio₂ nanocomposite: application of response surface methodology, *Desalin. Water Treat.* 164 (2019) 346–360. <https://doi.org/10.5004/dwt.2019.24384>.
- [24] A. Czyski, J. Sznura, The application of Box-Behnken-Design in the optimization of HPLC separation of fluoroquinolones, *Sci. Rep.* 9 (2019) 1–10. <https://doi.org/10.1038/s41598-019-55761-z>.
- [25] A. Reghioua, D. Barkat, A.H. Jawad, A.S. Abdulhameed, S. Rangabhashiyam, M.R. Khan, Z.A. ALOthman, Magnetic chitosan-glutaraldehyde/zinc oxide/Fe₃O₄ nanocomposite: optimization and adsorptive mechanism of remazol brilliant blue R dye removal, *J. Polym. Environ.* 29 (2021) 3932–3947. <https://doi.org/10.1007/s10924-021-02160-z>.
- [26] S.A. Smith, B.P. Williams, Y.L. Joo, Effect of polymer and ceramic morphology on the material and electrochemical properties of electrospun PAN/polymer derived ceramic composite nano fiber membranes for lithium ion battery separators, *J. Memb. Sci.* 526 (2017) 315–322. <https://doi.org/10.1016/j.memsci.2016.12.052>.
- [27] Y. Li, Y. Hu, Y. Lu, S. Zhang, G. Xu, K. Fu, S. Li, C. Chen, L. Zhou, X. Xia, X. Zhang, One-dimensional SiOC/C composite nanofibers as binder-free anodes for lithium-ion batteries, *J. Power Sources.* 254 (2014) 33–38. <https://doi.org/10.1016/j.jpowsour.2013.12.044>.
- [28] M. Kamperman, L.T.J. Korley, B. Yau, K.M. Johansen, Y.L. Joo, U. Wiesner, Nanomanufacturing of continuous composite nanofibers with confinement-induced morphologies, *Polym. Chem.* 1 (2010) 1001–1004. <https://doi.org/10.1039/c0py00146e>.
- [29] J. Kaspar, M. Graczyk-Zajac, S. Choudhury, R. Riedel, Impact of the electrical conductivity on the lithium capacity of polymer-derived silicon oxycarbide (SiOC) ceramics, *Electrochim. Acta.* 216 (2016) 196–202. <https://doi.org/10.1016/j.electacta.2016.08.121>.

- [30] X. Long, C. Shao, J. Wang, Continuous SiCN fibers with interfacial SiC_xN_y phase as structural materials for electromagnetic absorbing applications, *ACS Appl. Mater. Interfaces*. 11 (2019) 22885–22894. <https://doi.org/10.1021/acsami.9b06819>.
- [31] Q. Wen, Z. Yu, R. Riedel, The fate and role of in situ formed carbon in polymer-derived ceramics, *Prog. Mater. Sci.* 109 (2020) 100623. <https://doi.org/10.1016/j.pmatsci.2019.100623>.
- [32] A. Tolosa, B. Krüner, N. Jäckel, M. Aslan, C. Vakifahmetoglu, V. Presser, Electrospinning and electrospraying of silicon oxycarbide-derived nanoporous carbon for supercapacitor electrodes, *J. Power Sources*. 313 (2016) 178–188. <https://doi.org/10.1016/j.jpowsour.2016.02.077>.
- [33] A. Tolosa, M. Widmaier, B. Krüner, J.M. Griffin, V. Presser, Continuous silicon oxycarbide fiber mats with tin nanoparticles as a high capacity anode for lithium-ion batteries, *Sustain. Energy Fuels*. 2 (2018) 215–228. <https://doi.org/10.1039/c7se00431a>.
- [34] A. Guo, M. Roso, M. Modesti, E. Maire, J. Adrien, P. Colombo, Characterization of porosity, structure, and mechanical properties of electrospun SiOC fiber mats, *J. Mater. Sci.* 50 (2015) 4221–4231. <https://doi.org/10.1007/s10853-015-8973-5>.
- [35] A. Guo, M. Roso, M. Modesti, J. Liu, P. Colombo, Preceramic polymer-derived SiOC fibers by electrospinning, *J. Appl. Polym. Sci.* 131 (2014) 39836. <https://doi.org/10.1002/app.39836>.
- [36] A. Guo, M. Roso, M. Modesti, J. Liu, P. Colombo, Hierarchically structured polymer-derived ceramic fibers by electrospinning and catalyst-assisted pyrolysis, *J. Eur. Ceram. Soc.* 34 (2014) 549–554. <https://doi.org/10.1016/j.jeurceramsoc.2013.08.025>.
- [37] J.S. Li, T.Y. Hsu, C.H. Peng, C.C. Hwang, K.T. Lu, T.F. Yeh, Synthesis and characterization of poly(carbomethylsilane) prepared by catalytic polymerization with titanocene dichloride as a catalyst, *Mater. Express*. 10 (2020) 2070–2079. <https://doi.org/10.1166/mex.2020.1842>.
- [38] Y. Wang, X. Pei, H. Li, X. Xu, L. He, Z. Huang, Q. Huang, Preparation of SiC ceramic fiber from a photosensitive polycarbosilane, *Ceram. Int.* 46 (2020) 28300–28307. <https://doi.org/10.1016/j.ceramint.2020.07.333>.
- [39] B. Yao, B. Lu, Q. Huang, Z.R. Huang, Q. Yuan, The preparation of SiC ultrafine fibers containing low amount of oxygen by the electrospinning and pyrolysis of vinyl-modified polycarbosilane, *Ceram. Int.* 46 (2020) 9894–9900. <https://doi.org/10.1016/j.ceramint.2019.12.265>.
- [40] Y. Yu, Y. Chen, X. Wu, Q. Fang, X. Wu, Flexible and hydrophobic silicon carbide fibrous mats prepared from polycarbosilane, *Kuei Suan Jen Hsueh Pao/Journal Chinese Ceram. Soc.* 42 (2014) 661–666. <https://doi.org/10.7521/j.issn.0454-5648.2014.05.17>.
- [41] N. Wu, B. Wang, C. Han, Q. Tian, C. Wu, X. Zhang, L. Sun, Y. Wang, Pt-decorated hierarchical SiC nanofibers constructed by intertwined SiC nanorods for high-temperature ammonia gas sensing, *J. Mater. Chem. C*. 7 (2019) 7299–7307. <https://doi.org/10.1039/c9tc01330j>.
- [42] Y. Hou, Y. Zhang, X. Du, Y. Yang, C. Deng, Z. Yang, L. Zheng, L. Cheng, Flexible Fe₃Si/SiC ultrathin hybrid fiber mats with designable microwave absorption performance, *RSC Adv.* 8 (2018) 33574–33582. <https://doi.org/10.1039/c8ra06941g>.
- [43] V.B. Platonov, M.N. Rumyantseva, A.S. Frolov, A.D. Yapryntsev, A.M. Gaskov, High-temperature resistive gas sensors based on ZnO/SiC nanocomposites, *Beilstein J. Nanotechnol.* 10 (2019) 1537–1547. <https://doi.org/10.3762/bjnano.10.151>.
- [44] Q. Chen, D. Li, X. Liao, Z. Yang, D. Jia, Y. Zhou, R. Riedel, Polymer-derived lightweight SiBCN ceramic nanofibers with high microwave absorption performance, *ACS Appl. Mater. Interfaces*. 13 (2021) 34889–34898.

- <https://doi.org/10.1021/acsami.1c07912>.
- [45] X. Guo, F. Xiao, J. Li, H. Zhang, Q. Hu, G. Li, H. Sun, Fe-doped SiCN composite fibers for electromagnetic waves absorption, *Ceram. Int.* 47 (2021) 1184–1190. <https://doi.org/10.1016/j.ceramint.2020.08.236>.
- [46] F. Xiao, H. Sun, J. Li, X. Guo, H. Zhang, J. Lu, Z. Pan, J. Xu, Electrospinning preparation and electromagnetic wave absorption properties of SiCN fibers, *Ceram. Int.* 46 (2020) 12773–12781. <https://doi.org/10.1016/j.ceramint.2020.02.046>.

5 THERMO-OXIDATIVE RESISTANCE OF C-RICH SiCN FIBER MATS INFLUENCED BY SELECTIVE CROSSLINKING OF OLIGOSILAZANE³

Here, C-rich SiCN fiber mats with thermo-oxidation resistance up to 600 °C were developed from electrospinning silazane and PAN with further pyrolysis. While PAN is used as a typical precursor of carbon, silazane-derived SiCN ceramic should lead to improved thermo-oxidation resistance. The influence of selective crosslinking of oligosilazane i.e. polysilazane on final ceramic was evaluated. Polysilazane promoted the stretchability of fibers during electrospinning assigned to a more homogeneous molecular chain compared to oligosilazane. FTIR-ATR, XRD, Raman and ²⁹Si-NMR analyses confirmed the transformation of polymer mats to C-rich SiCN mats. XPS measurements showed that blending of oligosilazane with PAN increased oxygen and carbon content in the final ceramic due to Si-H reactive sites. By combining oligosilazane and PAN, the weight loss during pyrolysis was reduced due to crosslinking reactions between both components. The tests demonstrated that depending on preceramic conformation, selective crosslinking of oligosilazane increased by ~10% the thermo-oxidative resistance. When using oligosilazane, the phase separation reduced the protective effect provided by the oxidation-resistant SiN₄ phase due to the formation of increased unprotected free carbon regions. Selective crosslinking of Si-based precursor before electrospinning led to a higher degree of carbon ordering and improved oxidation resistance.

5.1 INTRODUCTION

Carbon materials are well known as catalyst support due to their high porosity and excellent electron conductivity, however, the low stability in high-temperature and atmospheres containing oxygen are limiting factors [1,2]. The applications of carbon can be broadened when the surface area of the material is increased by using electrospinning [3]. While increasing surface area leads to improved catalytic activity, the challenges of avoiding thermo-oxidative issues also increase. To solve this problem, different alternatives have been investigated such as Si(B)CN-doped carbon nanofibers prepared through the PDC process [4].

PDCs have been developed to fulfill the growing demand for lightweight and thermo-

³Based on a paper to be submitted for publication.

oxidative resistant materials and for precise control over their composition and microstructure as well as their shaping as specific forms [5–12]. Coating carbon fibers with preceramic polysilazane with further pyrolysis is also one solution to increase the high-temperature stability and resistance to oxidation [13]. However, this can lead to cracks in the ceramic layer facilitating the access of oxygen to carbon, and sacrificing the material stability as the oxidative resistance was only guaranteed up to 500 °C.

A viable solution would be to ensure homogeneity between the phases by combining carbon precursors and preceramic polymers. The so-called C-rich PDCs represent an excellent alternative to get benefit from the properties of the two phases. By combining polysilazane-derived ceramic and carbon in one single system and using electrospinning as shaping, C-rich SiCN with increased surface area can be developed as materials for catalyst supports in a thermo-oxidative environment.

The development of C-rich PDCs follows three strategies: i) synthesis of preceramic polymers with a high content of suitable organic groups; ii) addition of carbon powder to a preceramic polymer, and iii) use of carbon precursors in combination with preceramic polymers. Carbon-rich ceramics can be defined as materials in which the content of carbon is exceeding 20 wt.% [14], and are normally derived from the substituents bonded at silicon in the preceramic polymer [15]. In the electrospinning of preceramic polymers, the use of carbon precursors is common due to the affordable electrospinnability provided by the organic polymer. The investigation of C-rich SiCN fiber mats as thermo-oxidative resistant materials is still incipient.

The chemical and physical properties of PDCs depend on the initial molecular arrangement of polymer precursor and processing conditions [14,16–18]. Specifically, the precipitation of carbon depends on the molecular structure of the preceramic polymer [19], and thus, the thermo-oxidative resistance properties of the PDCs can be modified [20].

This work aims to study the influence of selective crosslinking of oligosilazane on the thermo-oxidative resistance of C-rich SiCN electrospun fiber mats. The effect of employing oligosilazane or polysilazane in electrospinning and pyrolysis was evaluated. As-spun silazane/PAN fiber mats were obtained, which transformed to C-rich SiCN fiber mats after pyrolysis. The contribution of this work is also to investigate how the structure of the PDC fiber mat behaves in terms of oxidation resistance in high-temperature to explore new applications. Thermo-oxidation resistance experiments were conducted in air up to 600 °C and the influence

of free carbon and SiCN microstructure was discussed. The potential of C-rich SiCN fiber mats as catalyst support with thermo-oxidation resistance has not been discovered yet.

5.2 EXPERIMENTAL

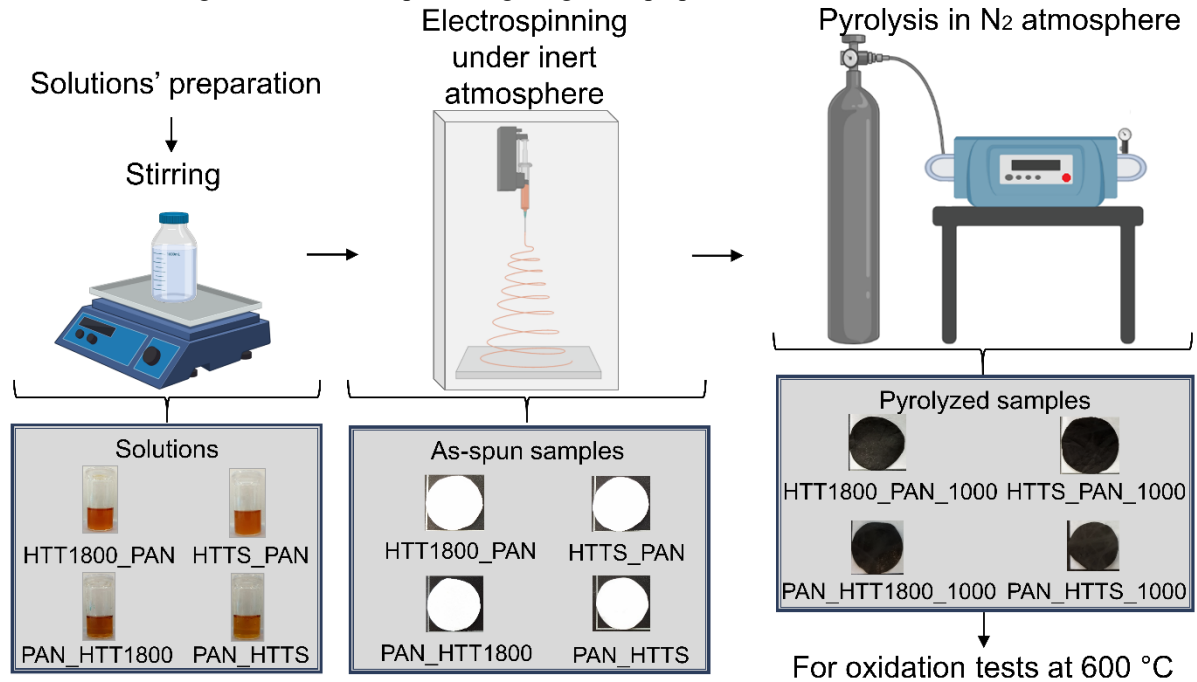
Polysilazane was prepared by selective crosslinking of oligosilazane (HTT1800) to obtain solid polysilazane (HTTS) [20]. Different solutions were prepared inside a laboratory glass bottle by first stirring PAN in DMF at 100 °C for 3 h. After cooling to room temperature, oligosilazane or polysilazane and 3 wt.% DCP in relation to silazane were added and stirred for 12 h at room temperature. The solutions were electrospun in nitrogen atmosphere using a lab-scale electrospinning device. The needle diameter corresponded to 21G (0.8 mm). The concentrations were established based on the electrospinnability of each solution defined according to preliminary experiments (Table 5.1). The samples were denoted as HTT1800_PAN and PAN_HTT1800 for oligosilazane, and HTTS_PAN and PAN_HTTS for polysilazane.

Table 5.1 – Solutions' characteristics and operating conditions of electrospinning according to samples containing oligosilazane or polysilazane

Name	Solutions' characteristics			Operating conditions of electrospinning		
	Polymer concentration in DMF (wt.%)	Oligosilazane: PAN ratio (wt.%)	Polysilazane :PAN ratio (wt.%)	Voltage (kV)	Need rate (ml·h ⁻¹)	Tip-to-collector-distance (cm)
HTT1800_PAN	17.5	3:2	-	21	0.8	23.5
HTTS_PAN	17.5	-	3:2	21	0.8	23.5
PAN_HTT1800	15	3:7	-	21	0.2	23.5
PAN_HTTS	13	-	3:7	21	0.2	23.5

The polymer mats were pyrolyzed in nitrogen atmosphere from 20 to 1000 °C (5 °C·min⁻¹), kept at 1000 °C for 1 h, and allowed to cool naturally to room temperature. Ultimately, C-rich SiCN fiber mats were obtained and denoted as HTT1800_PAN_1000, HTTS_PAN_1000, PAN_HTT1800_1000, and PAN_HTTS_1000. The scheme of the experiments is presented (Figure 5.1).

Figure 5.1 – Scheme presenting the general preparation of C-rich SiCN fiber mats



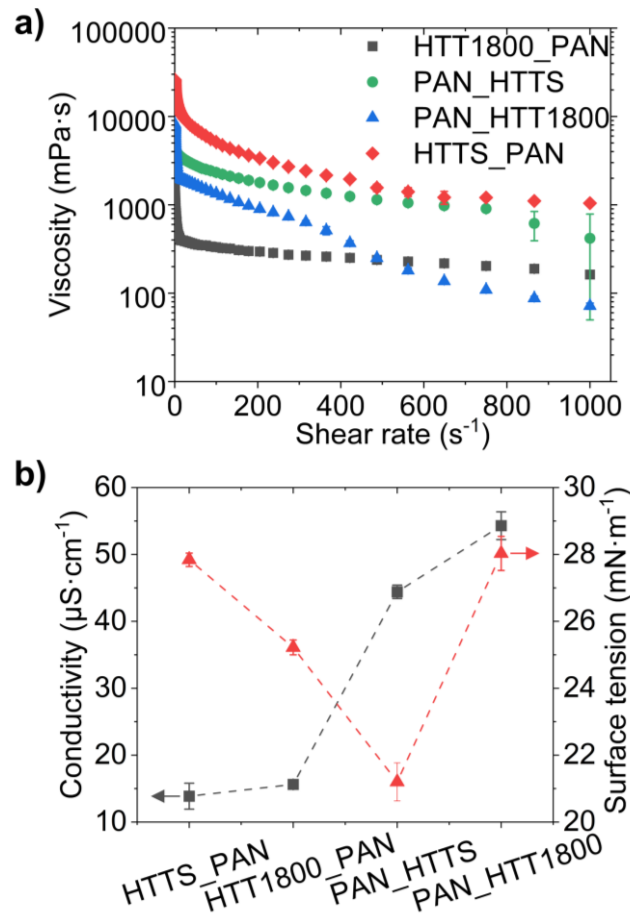
SEM was used to observe the morphology of the electrospun mat with an acceleration voltage of 3 kV and magnification of $\times 3000$ s (Gemini Sigma 300 VP, Zeiss, Germany). The samples were previously sputter-coated with gold (thickness of 280 Å) (Sputter Coater 108auto, Cressington, England). The fiber diameter was evaluated from four different SEM images measuring randomly 100 fibers of each sample with open-source ImageJ software. Normalized IR-spectra were collected using an attenuated total reflection (ATR) sampling unit (Tensor 27, Bruker Corporation, USA). Spectra were min-max normalized for comparison to overcome the confounding effect of varying sample thickness on the band intensity. Carbon structure was analyzed through Raman spectroscopy with 532 nm wavelength laser (Senterra II, Bruker, USA) and X-ray powder diffraction (XRD) using flat-sample transmission geometry with monochromatic CuK α radiation ($\lambda = 1.5418$ Å, 40 mA, and 40 kV) (D8 Advance, Bruker AXS, Germany). The Raman curves were fitted using Lorentzian function and Origin 2021b software. The I_D/I_G and $I_D/I_{D'}$ ratios were calculated based on the height of each peak after curve fitting. The crystallite size (L_a) was determined according to the TK-correlation [19]. Solid-state ^{29}Si -nuclear magnetic resonance (NMR) spectra were recorded using 4 mm Bruker probes ($B_0 = 7.05$ T, $\nu_0(^{29}\text{Si}) = 59.66$ MHz) and spinning frequency of 10 kHz (Bruker AVANCE II 300, Bruker Corporation, USA). The ^{29}Si -NMR spectra were [0,1] normalized for comparison. X-ray photoelectron spectroscopy (XPS) was conducted using Al K α^+ ion beam with an energy of 1486.6 eV and a spot size of 400 μm (Thermo Scientific, Chanhassen, USA). Surface

contamination was removed by surface sputtering with argon at 3.0 keV for 2 min. The mat density was determined by helium pycnometry (AccuPyc II 1340, Micromeritics, USA). The surface area was determined via krypton adsorption using Brunauer-Emmett-Teller theory (ASAP 2010, Micromeritics, USA). Thermal gravimetric analysis (TGA) and differential scanning calorimetry (DSC) were performed heating from 20 to 1000 °C (5 °C·min⁻¹) in a flowing nitrogen atmosphere (~5 mg of sample) (STA 449 F5 Jupiter, Netzsch GmbH, Germany). For thermo-oxidation tests, the same procedure was employed with synthetic air as the carrier gas. The performance of the fiber mats was also evaluated by static oxidation at 600 °C for 1 h (5 °C·min⁻¹) in an industrial furnace.

5.3 RESULTS AND DISCUSSION

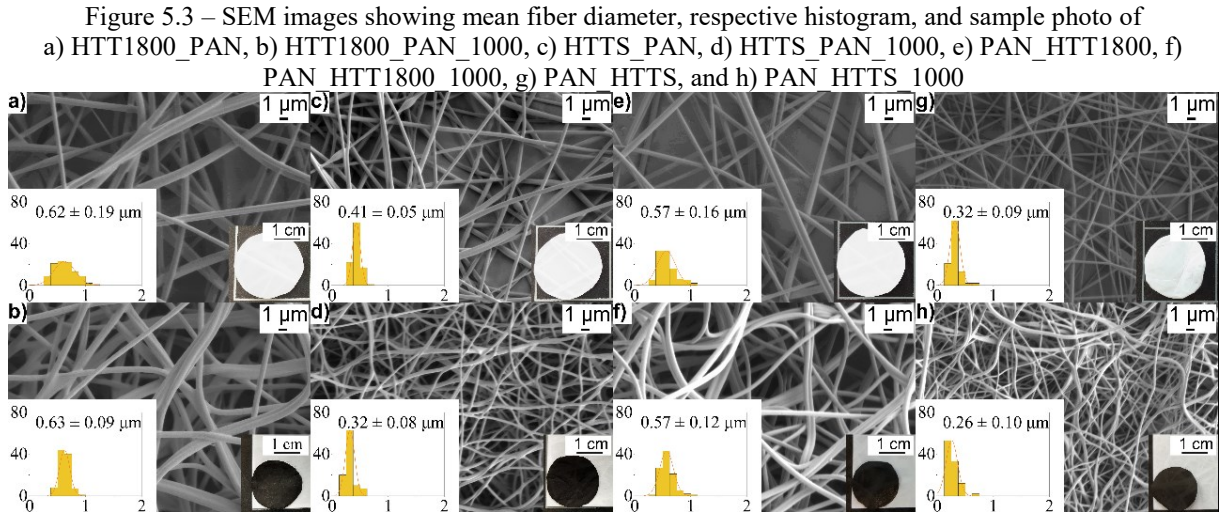
Pseudoplastic behavior was observed with the silazane/PAN solutions whose viscosity decreased under shear rate (Figure 5.2a). As expected, the solutions containing polysilazane (HTTS) resulted in higher viscosities compared to the solutions containing oligosilazane (HTT1800) due to the higher molecular weight resulting from the intermolecular condensation of the oligosilazane rings and chains after selective crosslinking [23]. Despite the higher molecular weight of PAN, the HTTS_PAN solution resulted in the highest viscosity due to the higher polymer concentration of 17.5 wt.% required for the solution to be electrospun. In contrast, the viscosity of PAN_HTT1800 is higher than HTT1800_PAN at a low shear rate, suggesting that the oligomer has a small contribution to the solution viscosity due to very low molecular weight. From approximately 400 s⁻¹, most PAN molecules in PAN_HTT1800 solution are aligned due to the more linear entanglement of this polymer, further lowering the viscosity. The HTT1800_PAN solution has a higher concentration of oligosilazane which is composed of a mixture of cyclic and/or linear units with complex structures and low molecular weight [8], making it difficult to align the molecular chains at a high shear rate. The surface tension and conductivity of the solutions varied from 28.03 to 21.20 mN·m⁻¹ and 13.87 to 54.30 μS·cm⁻¹, respectively (Figure 5.2b). Solutions of PAN_HTT1800 and PAN_HTTS showed a greater ability to conduct electric current coming from PAN, which has a higher ability to conduct electrons in solution than silazane. The presence of silazane decreased the surface tension of the solution when compared to pure DMF (35 mN·m⁻¹ at 20 °C) [24]. Nevertheless, the solutions showed no noteworthy difference in surface tension and these values are very similar to pure solutions of silazane and PAN [22].

Figure 5.2 – a) Viscosity as a function of shear rate and b) conductivity and surface tension of the solutions



After electrospinning, ultrathin fibers ranging from 0.32 μm to 0.62 μm were obtained (Figure 5.3). The solutions containing polysilazane resulted in more uniform fibers (lower dispersion) when compared to the solutions containing oligosilazane. No relationship was observed between fiber diameter and conductivity or surface tension of solutions. The electrospinning of silazane solutions blended with PAN was therefore mainly dependent on rheological properties. Normally higher solution viscosity increases the relaxation time and hinders the elongation of the jets, increasing fiber diameter, however, the results observed here are related to the entanglement of the molecular chains with different conformations. During electrospinning, the HTT1800 precursor might interact with PAN by intercalating among the polymeric chains and thus impeding the translational movements and stretching capacity. The oligomer has a smaller structure when compared to polysilazane, therefore, a higher quantity of oligosilazane molecules was necessary to entangle the PAN chains, increasing fiber diameter by 51% for HTT1800_PAN and 78% for PAN_HTTPT1800 when compared respectively to the

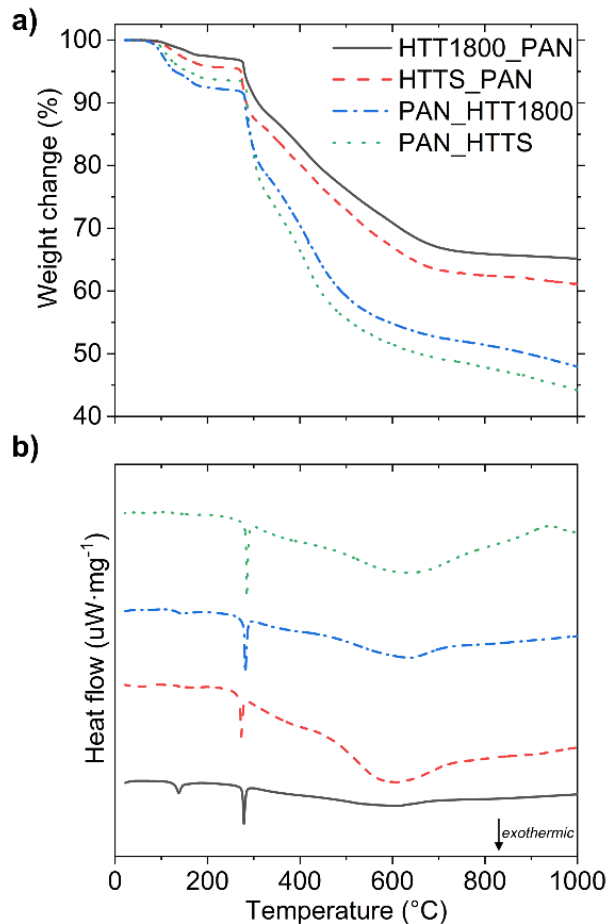
HTTS_PAN and PAN_HTTS, i.e. polysilazane promoted the stretchability of fibers during electrospinning due to more homogeneous molecular chain.



After pyrolysis, the ceramic fibers derived from polysilazane shrunk in diameter size by 22% (HTTS_PAN_1000) and 19% (PAN_HTTS_1000) (Figure 5.3). In contrast, the ceramic fibers derived from the oligomer did not change in fiber size. The final product yield are 65% (HTT1800_PAN_1000), 61% (HTTS_PAN_1000), 48% (PAN_HTT18000_1000), and 44% (PAN_HTTS_1000) (Figure 5.4a). The largest weight change occurred between ~200-400 °C associated with the loss of oligomers by degradation of organic substituents for silazane and the release of mainly methane, other volatile hydrocarbons, volatile silicon-containing products, hydrogen, and small quantities of ammonia for both precursors. The crosslinking reactions to form the ceramic materials may occur between Si-H groups from the silazane with N-functionalities from PAN leading to new Si-N bonds and preventing the release of nitrogen derived from PAN [25,26]. Therefore, the mass loss was lower with fibers containing HTT1800, as more Si-H groups were available to react with PAN. This effect was related to the reaction between silazane and PAN, which can produce a percolation network preventing PAN chains from evaporation. During carbonization and cyclization of PAN, dehydrogenation occurred and aromatic structures were obtained [27]. Between 400-1000 °C, the main products released from PAN are hydrogen, cyanide, ammonia, and nitrogen [28]. The precursors have two main exothermic peaks at 250-300 °C and 500-700 °C, which correspond respectively to the cyclization and decomposition of PAN (Figure 5.4b). The smaller peak at ~600 °C observed for HTT1800_PAN suggests the greater reaction between functional groups of these two precursors. The small exothermic peak at ~125 °C is attributed to the

polymerization initiated by DCP, mainly for HTT1800_PAN sample containing Si-H and vinyl groups via vinyl polymerization and hydrosilylation reactions. Another possible mass loss in this range (~ 125 °C) is the boiling of some DMF adhered to the fibers.

Figure 5.4 – Curves of a) TGA and b) DSC of as-spun fiber mats pyrolyzed in nitrogen atmosphere



To further understand the influence of polysilazane structure on polymer to ceramic transformation, Fourier transform infrared spectroscopy (FTIR) analyses were conducted. The expected absorption bands were in general agreement with the literature (Figure 5.5a and Figure 5.5b) [21,23,29,30]. The spectra of as-spun samples exhibited bands at ~ 3390 and ~ 1150 cm^{-1} from respectively N-H stretching [$\nu_s(\text{NH})$] and N-H bending [$\delta_s(\text{NH})$] (Figure 5.5a). The symmetric C-H stretching at ~ 2950 cm^{-1} [$\nu_s(\text{CH}_3)$] and the symmetric C-H deformation band at ~ 1450 and 1250 cm^{-1} [$\delta_s(\text{CH}_3)$] were also identified. The band at ~ 2100 cm^{-1} was assigned to the symmetric Si-H stretching [$\nu_s(\text{SiH})$]. The vinyl group, Si-C, and Si-N bending bands were determined between 750 - 950 cm^{-1} . The $\text{C}\equiv\text{N}$ stretching band derived from PAN was identified at ~ 2245 cm^{-1} . The conversion of polymer to ceramic at 1000 °C was confirmed by the

disappearance of the N-H and Si-H absorption bands as well as methyl and vinyl groups (Figure 5.5b). Likewise, conversion of PAN to ladder structure carbon was observed by the disappearance of the C≡N absorption band. The wide peak between 700 and 1200 cm^{-1} in pyrolyzed samples is attributed to the formation of SiCN structure derived from the inorganic polymer [$\delta_s(\text{SiC})$ and $\delta_s(\text{SiN})$], while the band at $\sim 1544 \text{ cm}^{-1}$ is attributed to C=C and C=N bands [$\nu_s(\text{C}=\text{C})$ and $\nu_s(\text{C}=\text{N})$]. Characteristic peaks at $\sim 442 \text{ cm}^{-1}$ and $\sim 1060 \text{ cm}^{-1}$ for Si-O stretching [$\delta_s(\text{Si-O})$] were observed mainly for HTT1800-derived samples, which is attributed to oxygen incorporation during the experiments [25,31,32]. A significant difference in peak relative to Si-C and Si-N bands was not observed for HTT1800- and HTTS-derived samples. However, the peak related to C=N and C=C absorption bands is 5.5 times higher in area for HTT1800_PAN_1000, suggesting that oligosilazane promoted carbon cyclization (Table 5.2). The carbon structure was further evaluated through XRD and Raman analyses.

Figure 5.5 – a) FTIR-ATR spectra of as-spun samples, b) FTIR-ATR spectra of pyrolyzed samples, c) XRD patterns, and d) Raman spectra

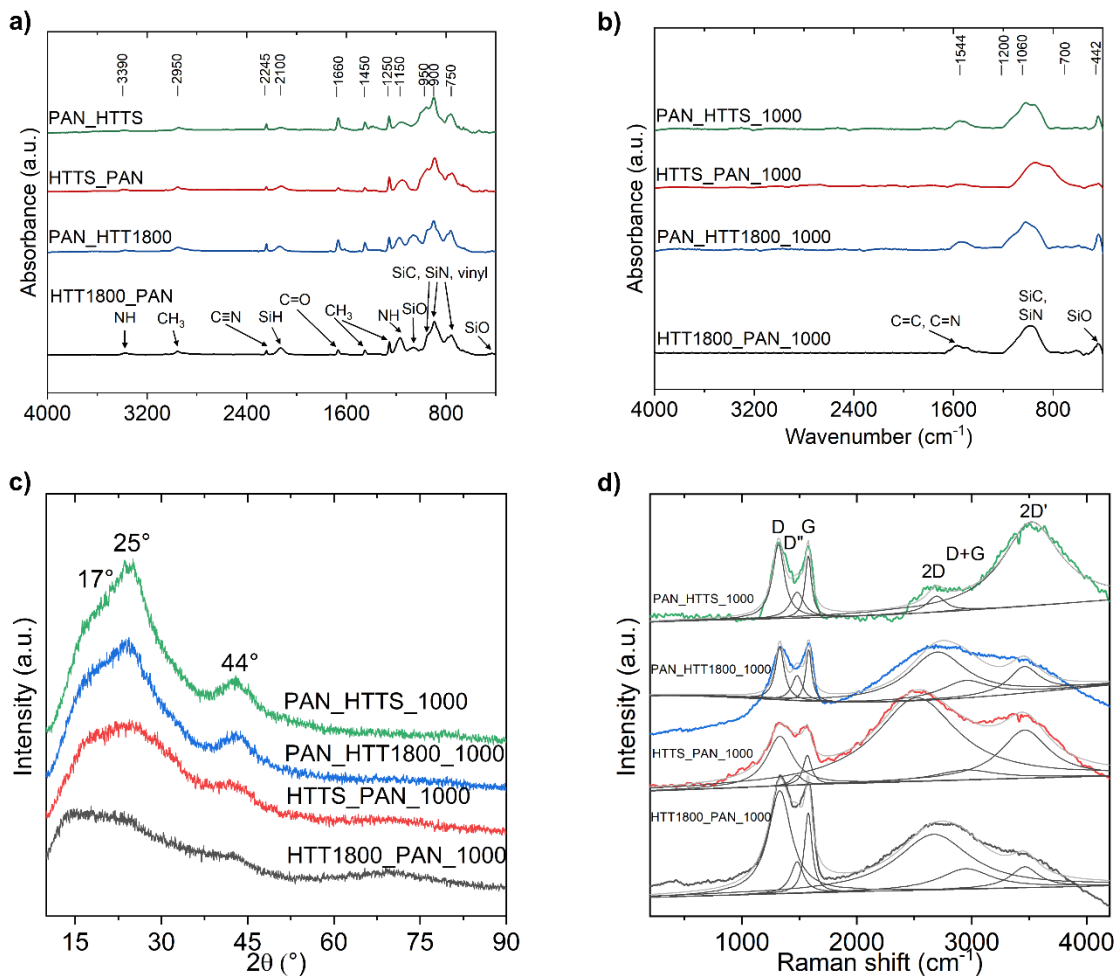


Table 5.2 – Absorption bands and respectively height intensity according to FTIR-ATR spectra of C-rich SiCN fiber mats

Sample	Mode			Ceramic phase/carbon phase ratio
	$\nu_s(\text{Si-O-Si})$	$\delta_s(\text{Si-C})$ and $\delta_s(\text{Si-N})$	$\nu_s(\text{C=C})$ and $\nu_s(\text{C=N})$	
HTT1800_PAN_1000	$\sim 444 \text{ cm}^{-1}$	$\sim 982 \text{ cm}^{-1}$	$\sim 1543 \text{ cm}^{-1}$	5.04
HTTS_PAN_1000	$\sim 447 \text{ cm}^{-1}$	$\sim 941 \text{ cm}^{-1}$	$\sim 1553 \text{ cm}^{-1}$	27.81
PAN_HTT1800_1000	$\sim 440 \text{ cm}^{-1}$	$\sim 1016 \text{ cm}^{-1}$	$\sim 1530 \text{ cm}^{-1}$	5.49
PAN_HTTS_1000	$\sim 442 \text{ cm}^{-1}$	$\sim 1018 \text{ cm}^{-1}$	$\sim 1548 \text{ cm}^{-1}$	5.00

Broad diffraction peaks displayed in the XRD patterns are indexed to free carbon ascribed to (0 1 0) plane of graphite (peak at 17°), (0 0 2) lattice of typical graphite (peak at 25°) and (1 0 0) plane from arbitrary diffraction related to graphene sheets (peak at 44°) [33–35]. According to XRD patterns, the C-rich SiCN samples are composed of an amorphous structure since diffraction peaks showed a diffuse scattering state, and no crystalline peaks were observed (Figure 5.5c). The two small peaks observed at 25° in PAN_HTTS_1000 sample are probably from some noise during the measurement, since the material is expected to be amorphous. Following XRD results, Raman spectroscopy also indicated the existence of a free amorphous carbon phase (Figure 5.5d). The characteristic carbon vibrations appeared in all spectra: the D band at $\sim 1326 \text{ cm}^{-1}$, the D'' band at $\sim 1458 \text{ cm}^{-1}$ and the G band at $\sim 1575 \text{ cm}^{-1}$. The D peak results from disorder and defect-induced vibration modes of graphene layers in the carbon phase, linked to the breathing motion of sp^2 -rings, the D'' peak arises from amorphous carbon, and the G mode from an in-plane bond stretching of sp^2 -hybridized carbon atoms [36,37]. For samples containing a higher content of silazane, the D-band is the strongest band revealing the presence of a disordered graphitic. In addition, 2D, D + G and 2D' bands appeared in the second-order Raman spectra at respectively around 2645 cm^{-1} , 2947 cm^{-1} and 3475 cm^{-1} , which are related to overtones and combinations of the known lattice vibration modes [19]. The results indicated that both defective amorphous carbon and ordered crystalline carbon existed in the C-rich SiCN. The presence of the G band in the Raman spectra but the absence of a characteristic graphitic layer peak in the XRD patterns indicated that each of the graphene carbon layers was embedded into the amorphous SiCN phase and amorphous carbon region [38]. The comparative indication of the peak intensities showed that the samples containing oligosilazane presented a higher amount of carbon. The I_D/I_G ratios were very similar for all samples and the lateral cluster sizes (L_a) ranged from 2.97 to 4.84 nm, indicating the nanostructured nature of the ceramics (Table 5.3) [39]. The $I_D/I_{D''}$ values increased when polysilazane was used, indicating a beginning of an ongoing graphitization process resulting in

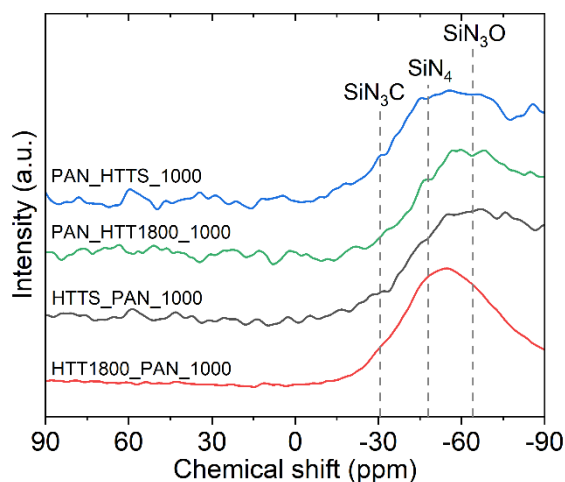
a higher degree of organization. Thus, Raman showed that the samples contain a free disordered carbon phase which tends to order with the addition of polysilazane.

Table 5.3 – Raman features of C-rich SiCN fiber mats

Sample	I _D /I _G	L _a (nm)	I _D /I _{D''}	D intensity (a.u.)	D'' intensity (a.u.)	G intensity (a.u.)
HTT1800_PAN_1000	1.29	3.85	3.26	1330	1481	1578
HTTS_PAN_1000	1.67	2.97	4.91	1330	1481	1570
PAN_HTT1800_1000	1.02	4.84	2.09	1330	1481	1582
PAN_HTTS_1000	1.20	4.14	2.86	1319	1481	1578

To evaluate the molecular structure of the obtained C-rich SiCN, ²⁹Si-NMR was conducted (Figure 5.6). Broad resonances dominated at -48 ppm assigned to silicon bonds in SiN₄ [25]. The formation of SiN₃C environments is more intense in HTT1800_PAN_1000. The possibility of the existence of a small amount of other mixed bonding environments, such as SiC₄ and SiC₂N₂, cannot be ruled out. As mentioned before, the pyrolysis between silazane and PAN led to the formation of additional Si-N bonding, which favored the formation of SiN₄ sites [25,40]. This finding is strong evidence that a hybrid structure instead of a simple mixture of compounds was obtained. The ²⁹Si-NMR spectra showed a -65 ppm peak assigned to SiN₃O environments [41].

Figure 5.6 – Solid-state ²⁹Si-NMR of samples heat-treated at 1000 °C in nitrogen atmosphere



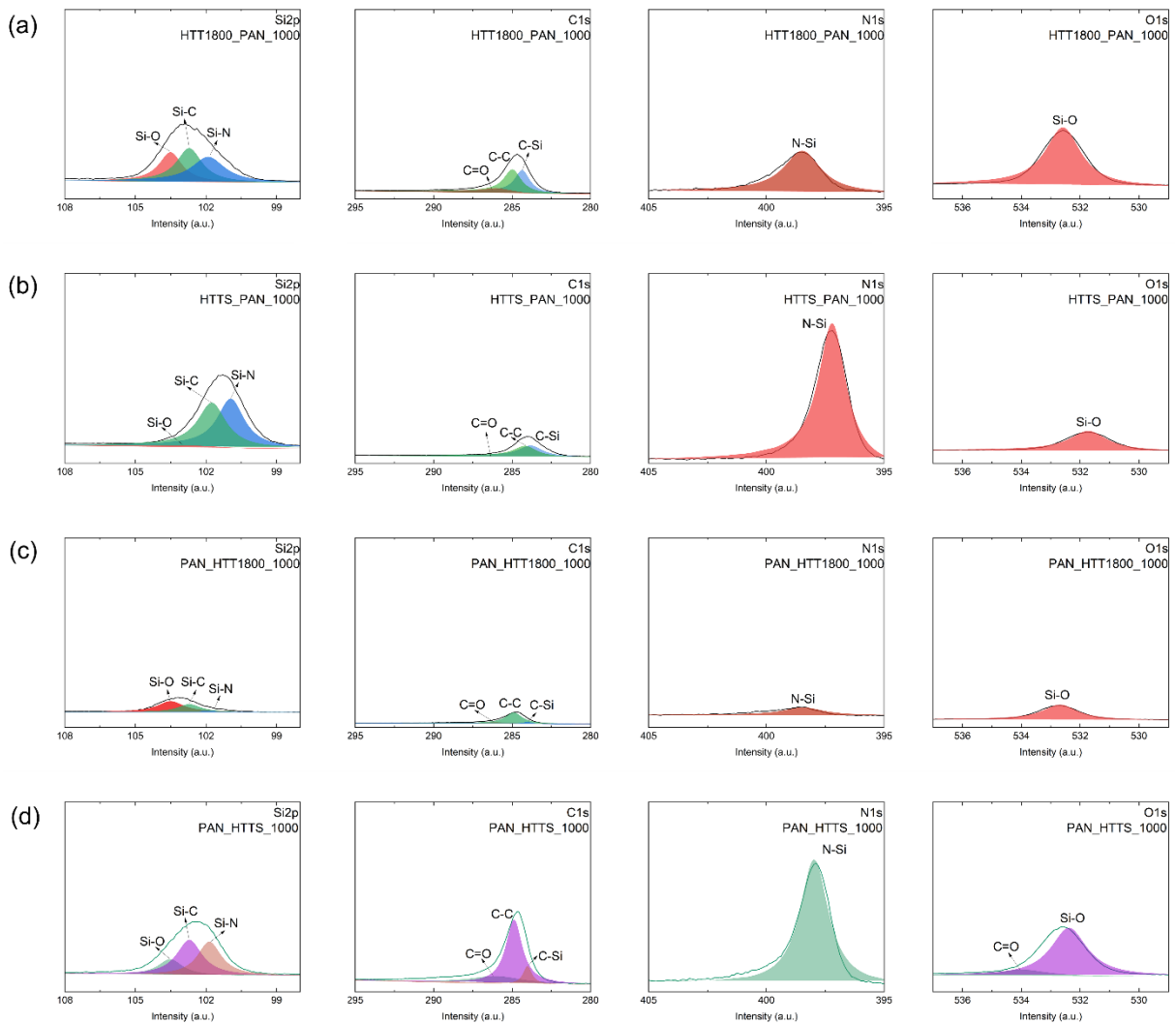
XPS can measure elemental composition as well as the chemical and electronic state of the atoms within a material. According to the molecular composition determined by XPS, all the electrospun mats manufactured here are definitively C-rich PDCs (Table 5.4). A greater

oxygen uptake occurred with samples derived from oligosilazane due to the greater amount of active sites to react with oxygen, following the results detected by FTIR-ATR and ^{29}Si -NMR measurements. The higher content of free carbon was obtained with oligosilazane samples due to the more reactive structure with PAN, confirming TGA/DSC and Raman results. Furthermore, XPS analysis suggested that a higher content of Si is obtained in samples with polysilazane. High-resolution XPS spectra under the Si 2p band indicated the presence of Si-N (101.9 eV), Si-C (102.7 eV), and Si-O (103.5 eV) peaks [42,43]; under C 1s band with C-Si (284.0 eV), C-C (284.9 eV), and C=O (286.0 eV) peaks; under N 1s band with N-Si (397.3 eV) and N-C (400.4 eV) peaks [44,45]; and under O 1s band with O-Si (532.4 eV) and C=O (534.0 eV) peaks (Figure 5.7) [46]. The Si 2p XPS spectra are in good agreement with the ^{29}Si -NMR results, in which different silicon environments were observed. The N 1s XPS spectrum suggests a higher concentration of N-Si chemical bonds in HTTS_PAN_1000 than in HTT1800_PAN_1000. The increased amount of carbon in the fiber mats derived from oligosilazane led to higher intensity of the C-C peak.

Table 5.4 – Elemental compositions of C-rich SiCN fiber mats according to XPS analyses

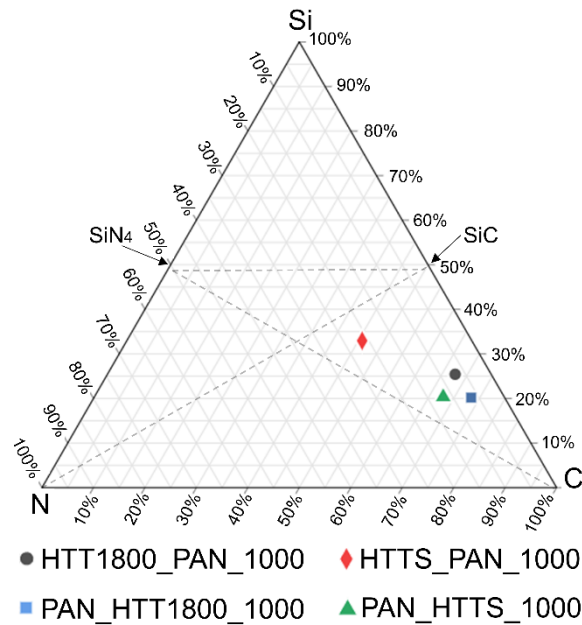
Sample	Composition (at. %)			
	Si	C	N	O
HTT1800_PAN_1000	19.6	52.1	5.4	22.9
HTTS_PAN_1000	28.6	39.7	18.5	13.2
PAN_HTT1800_1000	15.2	55.2	4.9	24.7
PAN_HTTS_1000	16.3	54.3	9.5	19.9

Figure 5.7 – High-resolution XPS spectra of the (a) HTT1800_PAN_1000, (b) HTTS_PAN_1000, (c) PAN_HTT1800_1000 and (d) PAN_HTTTS_1000 fiber mats



The elemental composition is also displayed in the ternary SiCN diagram with the molar compositions of the pyrolyzed samples (Figure 5.8). All the samples tended to lie inside the triangle of thermodynamically stable phases SiC, SiN₄, and carbon except for PAN_HTTTS_1000, which could be considered mostly as carbon (the XPS analysis of this sample is currently being repeated). The selective crosslinking of oligosilazane allowed for tailoring Si-N and Si-C content in the fiber mats as it is closer to the tie-line between SiN₄ and SiC. By electrospinning oligosilazane and PAN, the resulting ceramic compositions tend to have more free carbon in their structure.

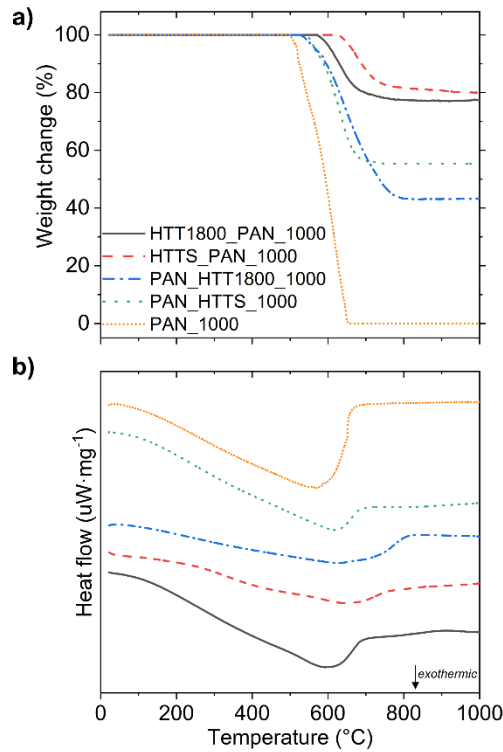
Figure 5.8 – Ternary SiCN phase diagram of C-rich SiCN fiber mats. Hydrogen and oxygen were neglected



TGA and DSC measurements were performed in flowing synthetic air to ascertain the thermo-oxidative resistance of the fiber mats (Figure 5.10). For comparison, carbon fiber mats were produced from PAN under similar conditions. An increase in thermo-oxidative resistance was observed with HTTS_PAN_1000 (ca. 627 °C), PAN_HTT1800_1000 (ca. 546 °C), HTT1800_PAN_1000 (ca. 572 °C) and PAN_HTT1800_1000 (ca. 528 °C) when compared to carbon fiber mats (ca. 500 °C). This oxidation temperature of carbon was also reported in another work [25]. If there were no interaction between polysilazane and PAN, the weight change at 600 °C should be equal to 78% instead of the measured 100% (HTTS_PAN_1000) and 61% instead of the measured 87% (PAN_HTT1800_1000). This fact was also observed elsewhere with polyureasilazane and PAN electrospun fibers [47]. At respectively 600 °C and 700 °C in air, carbon fibers dip-coated with polysilazane showed a weight loss of 2% and 17% [13], while the C-rich SiCN fibers of the present work showed a weight loss of 0 and 12%. Introducing the free carbon phase sacrificed the high-temperature thermal stability of SiCN. At 1000 °C, the samples derived from polysilazane and PAN showed a lower weight loss: 80% for HTTS_PAN_1000, 77% for HTT1800_PAN_1000, 55% for PAN_HTT1800_1000, and 43% for PAN_HTT1800_1000. The weight change is due to the formation of non-volatile oxides and the evolution of CO and N₂ as observed in DSC analysis [48]. The thermo-oxidative resistance of HTTS_PAN_1000 fiber mat is mainly attributed to the chemical composition, molecular structure, and homogeneously distributed free carbon phase within the SiCN matrix. The carbon

phase is protected by the SiCN ceramic due to the formation of passivation layers, which reduced the oxygen permeation and hindered carbon oxidation. In PAN_HTTS_1000, the high quantity of carbon decreased the thermo-oxidation resistance because the amount of ceramic phase is too small to protect the material completely from oxidation.

Figure 5.9 – Curves of a) TGA and b) DSC of C-rich SiCN fiber mats for thermo-oxidation resistance evaluation (heating rate: $5\text{ }^{\circ}\text{C}\cdot\text{min}^{-1}$; atmosphere: synthetic air)



In the case of SiCN ceramics, the parabolic oxidation rates strongly depend on the content of segregated carbon present within the microstructure. Generally, the thermal stability of PDCs and their exceptional crystallization resistance are due to the kinetic stabilization generated by free carbon and the thermodynamical stability when compared to their crystalline binary counterparts [49]. Free carbon acts as a diffusion barrier hindering or retarding the formation of crystalline phases [50]. Nevertheless, the samples prepared here showed an excess of free carbon in the fibers' microstructure, which limited the thermo-oxidative resistance of C-rich SiCN. Under this condition, oxygen can percolate through the SiCN matrix, leading to a catastrophic loss of thermo-oxidation resistance when compared to SiCN. Thus, ceramics with high free carbon content oxidize consequently faster. The high free carbon content in PAN_HTT1800_1000 and PAN_HTTS_1000 reduced the thermo-oxidative resistance due to

the exposition of free carbon directly to oxidation, which is the main drawback in high-temperature applications of carbonaceous materials.

Recently, C-rich SiCN derived from *in situ* radical polymerization of acrylonitrile with HTT1800 using initiators with similar concentrations of this work has experienced oxidation from about 800 °C (60 wt.% of silazane) and 650 °C (70 wt.% of acrylonitrile) [25]. The hybrid polymer fibers were produced by wet spinning with a diameter of 200 μm i.e. 62,400% higher compared to HTTS_PAN_1000 fibers of this work. The higher thermo-oxidative resistance of hybrid polymer can be associated with a better phase distribution resulting from *in situ* reaction between the polymers, but also to lower specific surface in comparison to electrospun fibers. Possible phase separation during electrospinning (solvent evaporation) due to the high molecular mass of PAN cannot be ruled out. However, the low solubilization of the hybrid polymer in solvent limits its shaping in electrospinning.

After furnace oxidative testing up to 600 °C, SEM analyses showed that the fibers remained almost unchanged and no signs of pores or cracks due to oxidation reactions were noticed (Figure 5.10). However, fiber size reduction, change in sample color, reduction in sample weight, and high brittleness were observed for HTT1800_PAN_1000, PAN_HTT1800_1000, and PAN_HTTS_1000 samples. In contrast, the HTTS_PAN_1000 sample showed to be intact and with a similar fiber diameter, indicating its potentiality as C-rich SiCN catalyst support for applications requiring thermo-oxidative resistance up to 600 °C. XPS analyses showed an increase in oxygen content for oxidized HTTS_PAN_1000 (Figure 5.11). When the amount of segregated carbon is relatively low, the SiCN is a continuous phase, and during the oxidation process, a dense and continuous SiO₂ scale is formed on the surface of the SiCN phase protecting further oxidation of both free carbon and SiCN phases. The carbothermal reduction of SiO₂ from free carbon in the structure started at 600 °C with the release of carbon oxides and nitrogen. Nevertheless, the formation of a double Si₂N₂O/SiO₂ layer in the C-rich SiCN acted as an additional diffusion barrier, which could improve oxidation protection [25,51]. The silicon phase also improved the oxidation resistance of ZrB₂-ZrC-SiC fibers up to 587 °C [52].

Figure 5.10 – SEM images containing respective histogram, mean fiber diameter, and sample photo after thermo-oxidation test at 600 °C for 1 h of a) HTT1800_PAN_1000, b) HTTS_PAN_1000, c) PAN HTT1800_1000, and d) PAN HTTS_1000

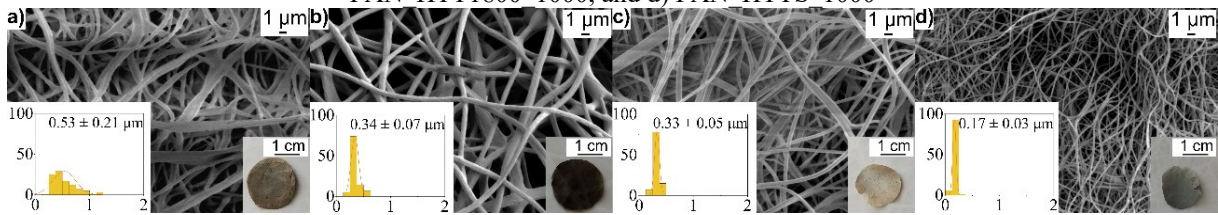
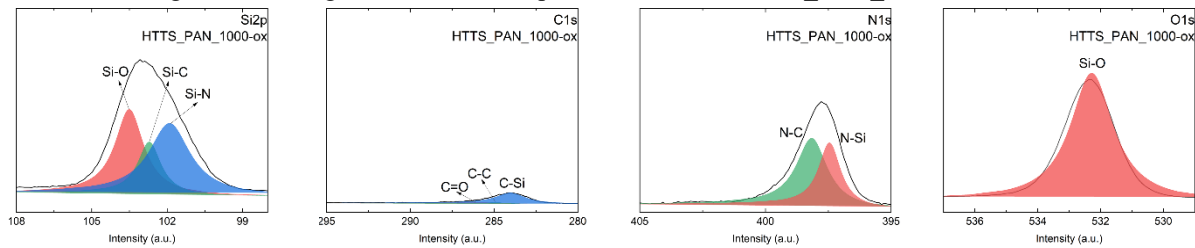


Figure 5.11 – High-resolution XPS spectra of oxidized HTTS_PAN_1000 fiber mats



In this work, C-rich SiCN fiber mat derived from polysilazane/PAN was developed with thermo-oxidation resistance up to 600°C, expanding the application of PDCs. The results suggested that SiCN and free carbon are highly dispersed within the fibers and that this material has the advantages of hybrid material with the potential application as catalyst support in high-temperature and oxidative environments. The surface area varied between 2.7-6.1 m²·g⁻¹ with 4.9 m²·g⁻¹ for HTTS_PAN_1000 fiber mat. Despite that PDCs present low bulk density, the electrospun PDCs from the present work showed even lower density (~1.8-2.1 g·cm⁻³) with a reduction of 18% for HTTS_PAN_1000 when compared to bulk SiCN pyrolyzed at 1000 °C [53] and 6.6% for HTTS_PAN_1000 when compared to SiCN matrix [54], suggesting the application of C-rich SiCN as a lightweight material.

5.4 CONCLUSIONS

The selective crosslinking of oligosilazane was evaluated here to investigate the thermo-oxidative resistance of C-rich SiCN fiber mats. The following conclusions and remarks can be made.

- The viscosity of solutions containing polysilazane and blending with an organic polymer influenced the material processing to improve the features of electrospun mats namely decreasing the fiber diameter and density.

○ The pyrolysis up to 1000 °C caused the growth of SiCN, SiN₄ and free carbon phases converting silazane/PAN into amorphous covalent ceramics. The incorporation and dispersion of high excess free carbon content were governed by the initial conformation of oligosilazane. Selective crosslinking of silazane before electrospinning led to a higher degree of carbon order. The oxygen contamination is evident, especially for oligosilazane-derived fibers as a consequence of the higher content of moisture-sensitive Si-H groups.

○ The chemical composition, the molecular structure, and the homogeneity of carbon phase within the SiCN matrix achievable in polysilazane-derived ceramic favored high-temperature oxidation, whereas oligosilazane ceramics promoted some decomposition at 600 °C. When using oligosilazane, the phase separation reduced the protective effect provided by the oxidation-resistant SiCN phase due to the formation of increased unprotected free carbon regions.

This work demonstrated the advantage of PDCs that can be conveniently adjusted by manipulating the molecular conformation of the precursor, which allows for designing ceramics with tailor-made properties. The strategy of electrospinning preceramic and organic precursors followed by pyrolysis would be an interesting alternative to designing PDCs with a controlled amount of free carbon. Due to its high-temperature stability and oxidation resistance, the C-rich SiCN produced here can be used as catalyst supports.

5.5 ACKNOWLEDGMENTS

This study was financed in part by the Coordenação de Aperfeiçoamento de Pessoal de Nível Superior - Brasil (CAPES) - Finance Code 001. The authors thank CAPES and Deutscher Akademischer Austauschdienst (DAAD) for supporting this work within the project PROBRAL (Grant n° 88887.368756/2019-00).

5.6 AUTHORS' CONTRIBUTIONS

The paper is mainly based on the work of the first author and author of this thesis Heloisa Ramlow. This work was conducted in collaboration with the group of Ceramic Precursors (University of Bayreuth, Germany). The precise contributions of each author are listed below (Table 5.5).

Table 5.5 – Authors' contributions to Chapter 5

Author	Contribution
Ramlow, H.	Conceptualized the work, wrote the manuscript
Ribeiro, L. F. B.	Gave conceptual and scientific advice, helped in the scientific evaluation and editing of the manuscript
Motz, G.	Gave conceptual and scientific advice, helped in the scientific evaluation and editing of the manuscript
Machado, R.	Gave conceptual and scientific advice, helped in the scientific evaluation and editing of the manuscript

5.7 REFERENCES

- [1] Y. Zhang, Y. Zhao, Q. Chen, Y. Hou, Q. Zhang, L. Cheng, L. Zheng, Flexible SiC-CNTs hybrid fiber mats for tunable and broadband microwave absorption, *Ceram. Int.* 47 (2021) 8123–8132. <https://doi.org/10.1016/j.ceramint.2020.11.167>.
- [2] R. Riedel, G. Mera, R. Hauser, A. Klönczynski, Silicon-based polymer-derived ceramics: synthesis properties and applications - a review, *J. Ceram. Soc. Japan.* 114 (2006) 425–444.
- [3] R. Schierholz, D. Kröger, H. Weinrich, M. Gehring, H. Tempel, H. Kungl, J. Mayer, R.-A. Eichel, The carbonization of polyacrylonitrile-derived electrospun carbon nanofibers studied by in situ transmission electron microscopy, *RSC Adv.* 9 (2019) 6267–6277. <https://doi.org/10.1039/C8RA10491C>.
- [4] K. Ge, L. Ye, W. Han, Y. Han, C. Xu, T. Zhao, Si(B)CN-doped carbon nanofibers with excellent oxidation resistance, *Mater. Lett.* 112 (2013) 124–128. <https://doi.org/10.1016/j.matlet.2013.08.122>.
- [5] Y. Iwamoto, G. Motz, E. Ionescu, S. Bernard, Preceramic polymers as precursors of advanced ceramics: the polymer-derived ceramics (PDCs) route, in: *Ref. Modul. Mater. Sci. Mater. Eng.*, Elsevier, 2020. <https://doi.org/10.1016/B978-0-12-803581-8.12080-6>.
- [6] A. Lale, M. Schmidt, M.D. Mallmann, A.V.A. Bezerra, E.D. Acosta, R.A.F. Machado, U.B. Demirci, S. Bernard, Polymer-derived ceramics with engineered mesoporosity: from design to application in catalysis, *Surf. Coatings Technol.* 350 (2018) 569–586. <https://doi.org/10.1016/j.surfcoat.2018.07.061>.
- [7] T. Ohji, M. Singh, eds., *Engineered Ceramics*, John Wiley & Sons, Inc., Hoboken, NJ, USA, 2016. <https://doi.org/10.1002/9781119100430>.
- [8] A. Viard, P. Miele, S. Bernard, Polymer-derived ceramics route toward SiCN and SiBCN fibers: from chemistry of polycarbosilazanes to the design and characterization of ceramic fibers, *J. Ceram. Soc. Japan.* 124 (2016) 967–980. <https://doi.org/10.2109/jcersj2.16124>.
- [9] Q. Tian, N. Wu, B. Wang, Y. Wang, Fabrication of hollow SiC ultrafine fibers by single-nozzle electrospinning for high-temperature thermal insulation application, *Mater. Lett.* 239 (2019) 109–112. <https://doi.org/10.1016/j.matlet.2018.12.077>.
- [10] R. Riedel, I.-W. Chen, *Ceramics Science and Technology Volume 4: Applications*, Wiley-VCH Verlag GmbH & Co. KGaA, Weinheim, 2013.

- <https://doi.org/10.1002/9783527631971>.
- [11] G. Mera, A. Tamayo, H. Nguyen, S. Sen, R. Riedel, Nanodomain structure of carbon-rich silicon carbonitride polymer-derived ceramics, *J. Am. Ceram. Soc.* 93 (2010) 1169–1175. <https://doi.org/10.1111/j.1551-2916.2009.03558.x>.
- [12] Z. Ren, S. Bin Mujib, G. Singh, High-temperature properties and applications of Si-based polymer-derived ceramics: a review, *Materials (Basel)*. 14 (2021) 614. <https://doi.org/10.3390/ma14030614>.
- [13] M.A. Shayed, R.D. Hund, C. Cherif, Polysilazane-based heat- and oxidation-resistant coatings on carbon fibers, *J. Appl. Polym. Sci.* 124 (2012) 2022–2029. <https://doi.org/10.1002/app.35228>.
- [14] P. Colombo, G. Mera, R. Riedel, G.D. Sorarù, Polymer-derived ceramics: 40 years of research and innovation in advanced ceramics, *J. Am. Ceram. Soc.* 93 (2010) 1805–1837. <https://doi.org/10.1002/9783527631971.ch07>.
- [15] G. Mera, E. Ionescu, Silicon-containing preceramic polymers, in: H.F. Mark (Ed.), *Encycl. Polym. Sci. Technol.*, John Wiley & Sons, Inc., Hoboken, NJ, USA, 2013. <https://doi.org/10.1002/0471440264.pst591>.
- [16] G. Mera, M. Gallei, S. Bernard, E. Ionescu, Ceramic nanocomposites from tailor-made preceramic polymers, *Nanomaterials*. 5 (2015) 468–540. <https://doi.org/10.3390/nano5020468>.
- [17] O. Flores, R.K. Bordia, D. Nestler, W. Krenkel, G. Motz, Ceramic fibers based on SiC and SiCN systems: current research, development, and commercial status, *Adv. Eng. Mater.* 16 (2014) 621–636. <https://doi.org/10.1002/adem.201400069>.
- [18] X. Long, C. Shao, J. Wang, Continuous SiCN fibers with interfacial SiC_xN_y phase as structural materials for electromagnetic absorbing applications, *ACS Appl. Mater. Interfaces*. 11 (2019) 22885–22894. <https://doi.org/10.1021/acsami.9b06819>.
- [19] Q. Wen, Z. Yu, R. Riedel, The fate and role of in situ formed carbon in polymer-derived ceramics, *Prog. Mater. Sci.* 109 (2020) 100623. <https://doi.org/10.1016/j.pmatsci.2019.100623>.
- [20] K. Bawane, D. Erb, K. Lu, Carbon content and pyrolysis atmosphere effects on phase development in SiOC systems, *J. Eur. Ceram. Soc.* 39 (2019) 2846–2854. <https://doi.org/10.1016/j.jeurceramsoc.2019.03.032>.
- [21] O. Flores, T. Schmalz, W. Krenkel, L. Heymann, G. Motz, Selective cross-linking of oligosilazanes to tailored meltable polysilazanes for the processing of ceramic SiCN fibres, *J. Mater. Chem. A*. 1 (2013) 15406–15415. <https://doi.org/10.1039/c3ta13254d>.
- [22] H. Ramlow, C. Marangoni, G. Motz, R.A.F. Machado, Statistical optimization of polysilazane-derived ceramic: Electrospinning with and without organic polymer as a spinning aid for manufacturing thinner fibers, *Chem. Eng. J. Adv.* 9 (2022) 100220. <https://doi.org/10.1016/j.cej.2021.100220>.
- [23] R. Chavez, E. Ionescu, C. Balan, C. Fasel, R. Riedel, Effect of ambient atmosphere on crosslinking of polysilazanes, *J. Appl. Polym. Sci.* 119 (2010) 794–802. <https://doi.org/10.1002/app>.
- [24] I.M. Smallwood, *Handbook of organic solvent properties*, Arnold, London, 1996. <https://doi.org/10.3390/cryst7090256>.
- [25] L.F.B. Ribeiro, O. Flores, P. Furtat, C. Gervais, R. Kempe, R.A.F. Machado, G. Motz, A novel PAN/silazane hybrid polymer for processing of carbon-based fibres with extraordinary oxidation resistance, *J. Mater. Chem. A*. 5 (2017) 720–729. <https://doi.org/10.1039/c6ta09293d>.
- [26] W. Dang, J. Liu, X. Wang, K. Yan, A. Zhang, J. Yang, L. Chen, J. Liang, Structural transformation of polyacrylonitrile (PAN) fibers during rapid thermal pretreatment in

- nitrogen atmosphere, *Polymers* (Basel). 12 (2020). <https://doi.org/10.3390/polym12010063>.
- [27] M.T. Jafari, M. Saraji, M. Kermani, Sol-gel electrospinning preparation of hybrid carbon silica nanofibers for extracting organophosphorus pesticides prior to analyzing them by gas chromatography-ion mobility spectrometry, *J. Chromatogr. A.* 1558 (2018) 1–13. <https://doi.org/10.1016/j.chroma.2018.05.014>.
- [28] S.M. Saufi, A.F. Ismail, Development and characterization of polyacrylonitrile (PAN) based carbon hollow fiber membrane, *Songklanakarin J. Sci. Technol.* 24 (2002) 843–854. <http://eprints.utm.my/141/>.
- [29] Y. Feng, S. Dou, Y. Wei, Y. Zhang, X. Song, X. Li, V.S. Battaglia, Preparation and capacity-fading investigation of polymer-derived silicon carbonitride anode for lithium-ion battery, *ACS Omega.* 2 (2017) 8075–8085. <https://doi.org/10.1021/acsomega.7b01462>.
- [30] L. Zhang, Z. Liu, Y. Dai, R. Jin, TG-FTIR study of degradation mechanism and pyrolysis products of high molecular polyacrylonitrile with different oxidation degree, *Asian J. Chem.* 25 (2013) 8797–8802. <https://doi.org/10.14233/ajchem.2013.15711>.
- [31] G. Motz, T. Schmalz, S. Trassl, R. Kempe, Oxidation behavior of SiCN Materials, in: S. Bernard (Ed.), *Des. Process. Prop. Ceram. Mater. from Pre-ceramic Precursors*, Hauppauge USA: Nova Science Publishers Inc., New York, 2011: pp. 15–35.
- [32] E. Bernardo, L. Fiocco, G. Parciannello, E. Storti, P. Colombo, Advanced ceramics from pre-ceramic polymers modified at the nano-scale: A review, *Materials* (Basel). 7 (2014) 1927–1956. <https://doi.org/10.3390/ma7031927>.
- [33] S.W. Choi, J.R. Kim, S.M. Jo, W.S. Lee, Y.-R. Kim, Electrochemical and spectroscopic properties of electrospun PAN-based fibrous polymer electrolytes, *J. Electrochem. Soc.* 152 (2005) A989. <https://doi.org/10.1149/1.1887166>.
- [34] S.A. Smith, B.P. Williams, Y.L. Joo, Effect of polymer and ceramic morphology on the material and electrochemical properties of electrospun PAN/polymer derived ceramic composite nano fiber membranes for lithium ion battery separators, *J. Memb. Sci.* 526 (2017) 315–322. <https://doi.org/10.1016/j.memsci.2016.12.052>.
- [35] Y.S. Kim, Y.L. Joo, Y.J. Kwark, Highly stable silicon-carbon-nitrogen composite anodes from silsesquiazane for rechargeable lithium-ion battery, *J. Mater. Sci. Technol.* 32 (2016) 195–199. <https://doi.org/10.1016/j.jmst.2015.12.019>.
- [36] M. Graczyk-Zajac, C. Fasel, R. Riedel, Polymer-derived-SiCN ceramic/graphite composite as anode material with enhanced rate capability for lithium ion batteries, *J. Power Sources.* 196 (2011) 6412–6418. <https://doi.org/10.1016/j.jpowsour.2011.03.076>.
- [37] M. Wilamowska, V.S. Pradeep, M. Graczyk-Zajac, R. Riedel, G.D. Sorarù, Tailoring of SiOC composition as a way to better performing anodes for Li-ion batteries, *Solid State Ionics.* 260 (2014) 94–100. <https://doi.org/10.1016/j.ssi.2014.03.021>.
- [38] C. Chandra, J. Kim, Silicon oxycarbide produced from silicone oil for high-performance anode material in sodium ion batteries, *Chem. Eng. J.* 338 (2018) 126–136. <https://doi.org/10.1016/j.cej.2018.01.032>.
- [39] E. Ionescu, G. Mera, R. Riedel, Polymer-derived ceramics: materials design towards applications at ultrahigh-temperatures and in extreme environments, in: I.M. Low, Y. Sakka, C.F. Hu (Eds.), *MAX Phases Ultra-High Temp. Ceram. Extrem. Environ.*, IGI Global, 2013: pp. 1–649. <https://doi.org/10.4018/978-1-4666-2982-0>.
- [40] S. Traßl, D. Suttor, G. Motz, E. Rössler, G. Ziegler, Structural characterisation of silicon carbonitride ceramics derived from polymeric precursors, *J. Eur. Ceram. Soc.* 20 (2000) 215–225. [https://doi.org/10.1016/s0955-2219\(99\)00142-9](https://doi.org/10.1016/s0955-2219(99)00142-9).
- [41] S. Kohn, W. Hoffbauer, M. Jansen, R. Franke, S. Bender, Evidence for the formation of

- SiON glasses, *J. Non. Cryst. Solids*. 224 (1998) 232–243. [https://doi.org/10.1016/S0022-3093\(97\)00467-5](https://doi.org/10.1016/S0022-3093(97)00467-5).
- [42] L. David, R. Bhandavat, U. Barrera, G. Singh, Silicon oxycarbide glass-graphene composite paper electrode for long-cycle lithium-ion batteries, *Nat. Commun.* 7 (2016) 10998. <https://doi.org/10.1038/ncomms10998>.
- [43] Y. Feng, N. Feng, Y. Wei, Y. Bai, Preparation and improved electrochemical performance of SiCN-graphene composite derived from poly(silylcarbodiimide) as Li-ion battery anode, *J. Mater. Chem. A*. 2 (2014) 4168–4177. <https://doi.org/10.1039/c3ta14441k>.
- [44] M.A. Abass, A.A. Syed, C. Gervais, G. Singh, Synthesis and electrochemical performance of a polymer-derived silicon oxycarbide/boron nitride nanotube composite, *RSC Adv.* 7 (2017) 21576–21584. <https://doi.org/10.1039/c7ra01545c>.
- [45] X. Guo, J. Lu, J. Liu, C. Liu, Y. Tong, J. Li, H. Sun, H. Peng, S. Wu, Y. Feng, H. Gong, Enhanced electromagnetic wave absorption properties of PDCs-SiCN(Ni) fibers by in-situ formed CNTs and Ni₂Si, *Ceram. Int.* 48 (2022) 20495–20505. <https://doi.org/10.1016/j.ceramint.2022.04.012>.
- [46] S. Bin Mujib, F. Ribot, C. Gervais, G. Singh, Self-supporting carbon-rich SiOC ceramic electrodes for lithium-ion batteries and aqueous supercapacitors, *RSC Adv.* 11 (2021) 35440–35454. <https://doi.org/10.1039/d1ra05968h>.
- [47] P. Lu, Q. Huang, A. Mukherjee, Y. Lo Hsieh, SiCO-doped carbon fibers with unique dual superhydrophilicity/superoleophilicity and ductile and capacitance properties, *ACS Appl. Mater. Interfaces*. 2 (2010) 3738–3744. <https://doi.org/10.1021/am100918x>.
- [48] G. Chollon, Oxidation behaviour of polymer-derived ceramics:, in: P. Colombo, R. Riedel, G.D. Soraru, H.-J. Kleebe (Eds.), *Polym. Deriv. Ceram. From Nano-Structure To Applications*, DEStech Publications, 2016: pp. 292–308.
- [49] E. Ionescu, H.J. Kleebe, R. Riedel, Silicon-containing polymer-derived ceramic nanocomposites (PDC-NCs): preparative approaches and properties, *Chem. Soc. Rev.* 41 (2012) 5032–5052. <https://doi.org/10.1039/c2cs15319j>.
- [50] G. Mera, A. Navrotsky, S. Sen, H.J. Kleebe, R. Riedel, Polymer-derived SiCN and SiOC ceramics-structure and energetics at the nanoscale, *J. Mater. Chem. A*. 1 (2013) 3826–3836. <https://doi.org/10.1039/c2ta00727d>.
- [51] A. Viard, H. Kurz, A. Lale, L. Heymann, B. Weber, S. Bernard, M. Knauer, G. Motz, Superparamagnetic silicon carbonitride ceramic fibers through in situ generation of iron silicide nanoparticles during pyrolysis of an iron-modified polysilazane, *Appl. Mater. Interfaces*. 13 (2021) 8745–8753. <https://doi.org/10.1021/acsami.0c20885>.
- [52] Z. Xu, F. Li, Y. Wang, K. Zhao, Y. Tang, Microstructure and oxidation resistance of ZrB₂-ZrC-SiC composite nanofibers fabricated via electrospinning combined with carbothermal reduction, *Ceram. Int.* 47 (2021) 20740–20744. <https://doi.org/10.1016/j.ceramint.2021.03.317>.
- [53] Y. Li, Y. Yua, H. San, Y. Chen, D. Guo, X. Wu, Full dense SiCN ceramics derived from polysilazane, *Adv. Mater. Res.* 631–632 (2013) 303–305. <https://doi.org/10.4028/www.scientific.net/AMR.631-632.303>.
- [54] B. Mainzer, C. Lin, R. Jemmali, M. Frieß, R. Riedel, D. Koch, Characterization and application of a novel low viscosity polysilazane for the manufacture of C- and SiC-fiber reinforced SiCN ceramic matrix composites by PIP process, *J. Eur. Ceram. Soc.* 39 (2019) 212–221. <https://doi.org/10.1016/j.jeurceramsoc.2018.09.042>.

6 LIGHTWEIGHT AND FLEXIBLE NANOSTRUCTURED C/SiCN NANOFIBER MAT FOR ELECTROMAGNETIC REFLECTION SHIELDING OF 5G C-BAND FREQUENCIES⁴

Conventional metal-based materials are the reflection-dominant shielding materials to block EM radiation due to remarkable electric conductivity, however, they show heavyweight. Carbon materials are well-known as lightweight materials, but their poor impedance matching between material surface and EM waves limits their application to shielding. Here, lightweight and flexible C/SiCN nanofiber mats derived from PAN/polysilazane were manufactured through electrospinning and PDC route using different pyrolysis temperatures. Thermal analysis suggested that SiCN positively interacted with PAN by increasing the ceramic yield. The carbon matrix containing SiCN nanodomains was confirmed through FTIR and EDS. Fibers ranging from 150-250 nm were observed through SEM. XRD and Raman showed the nanostructured carbon phase as a disordered graphitic lattice with some degree of carbon order. Using the four-point method, C/SiCN mats showed a tunable electrical conductivity from 0.0028 S cm^{-1} to 0.0120 S cm^{-1} . The C/SiCN nanofiber mats significantly enhanced the reflection shielding effectiveness compared to pure carbon. Particularly, PAN:HTTS mat pyrolyzed at $800 \text{ }^\circ\text{C}$ exhibited a $RL < -10 \text{ dB}$ in the 5G C-band (90% of EM shielding). The absorption coefficient was $A(\omega) = 0.68$ with a reflection shielding effectiveness $SE_R = 10.42 \text{ dB}$. If the bandwidth is defined as the frequency range where $S_{11} < -10 \text{ dB}$, then the bandwidth of PAN:HTTS pyrolyzed at $800 \text{ }^\circ\text{C}$ would be approximately 4 GHz. Additionally, the impedance was modulated by adding SiCN to the carbon matrix and evaluated by the voltage standing-wave ratio ($VSWR = 1.94:1$ for PAN:HTTS pyrolyzed at $800 \text{ }^\circ\text{C}$ with the best impedance matching). This energy dissipation was attributed to the appropriate electrical conductivity, a high degree of carbon disorder, and the presence of a heterogeneous nanostructure forming interfacial polarization.

6.1 INTRODUCTION

The C-band refers to the EM field operating in a mid-band spectrum frequency (3.7-4 GHz) and is considered the global frequency for 5G worldwide due to more bandwidth with

⁴Based on a paper to be submitted for publication.

higher system capacity at higher data speeds. With the latest significant progress in technologies, severe EM field problems have received extensive research [1]. The EM field shielding can be achieved by reflection, with electrically conductive materials, and absorption, which is highly dependent on the magnetic and dielectric nature of the material [2]. Conventional metal-based materials with remarkable electric conductivity have high reflection loss, enabling them as representative reflection-dominant shielding materials to block electromagnetic radiation. However, metal-based materials show heavyweight, limiting their application.

Electrospinning has been used as a facile manufacturing technique to produce lightweight, ultrathin, and flexible fiber mats for EM field shielding [3,4]. Carbon fiber mats are important among communication devices and EM field shielding materials over a wide range of frequencies. However, the high relative permittivity and very high electrical conductivity of pure carbon fibers render them poor impedance matching [5–7]. High conductivity can cause more impedance mismatch and dielectric loss of the EM field [8]. Usually, carbon fibers are modified to meet the requirements of microwave (frequencies ranging from 300 MHz to 300 GHz) shielding materials in commercial microwave devices (frequencies ranging from 0.5 GHz to 40 GHz) by modulating the characteristic impedance [9]. However, the performance of carbon fibers at frequencies ranging from 0.1–4.5 GHz has been based on only some works [10,11].

Emerging nanomaterials can be used effectively for EM field shielding. Combining materials with hierarchical porous structure and multiphase nanostructured materials could reduce density, enhance attenuation capacity and satisfy impedance matching [12]. PAN is the most widely investigated precursor for carbon fibers with good spinnability and simple thermal treatment [6]. For carbon materials, the dielectric loss capacity is mainly affected by thickness, defects, surface functionalization, and heteroatomic doping, which must be properly adjusted to achieve impedance matching. PDCs using carbon fillers have been reported as potential materials for EM field shielding [14–16]. These are usually bulk/monolith materials produced by cold/warm pressing. Also, it is difficult to ensure the homogeneous dispersion of carbon nanomaterials, such as CNTs, in preceramic polymers. The preceramic precursor and carbon precursor can be shaped by electrospinning and together be converted to a C/SiCN nanocomposite by high-temperature treatment producing a more lightweight, flexible and porous material. Materials with nanosized porosity, nanosized, conductive/semi-conductive secondary material, and insulating matrix are preferred for EM shielding [17]. The pyrolysis

temperature of precursors has been identified as an essential factor in developing the desired nanostructure and controlling the dielectric behavior/conductivity [18]. The heat-treatment temperature and the designing of a complex nanostructure necessary to create more interfaces and scattering the EM field to broaden the frequency band provide valuable development of new shielding materials [19]. For instance, adding polysilazane-derived SiCN to PVDF exhibited superior EM shielding frequency from 0.1 Hz to 1 MHz [20]. Considering the tunable electrical conductivity and dielectric permittivity of carbon [21,22], the EM shielding performance of C/SiCN mats would be considerably improved compared with its constituents individually.

This work aims to investigate the effectiveness of EM reflection shielding in the 5G C-band of C/SiCN flexible electrospun mats pyrolyzed at different temperatures. The direct current (DC) conductivity properties of the fiber mats were also tested. Compared to the literature [23,24], the main advantage presented in this work is the development of a lightweight and flexible nanofiber mat using the precursor approach to produce a conductive carbon matrix with semiconductive SiCN nanodomains, and the low-cost electrospinning technique to produce a porous material. When using SiCN, usually magnetic loss is introduced by adding metallic compounds, which in turn can result in heavyweight and limit advanced applications. The lightweight and flexible C/SiCN nanofiber mat could find applications in the military and aerospace industry that require EM shielding of 5G C-band frequencies, which is fundamental for communication security.

6.2 EXPERIMENTAL

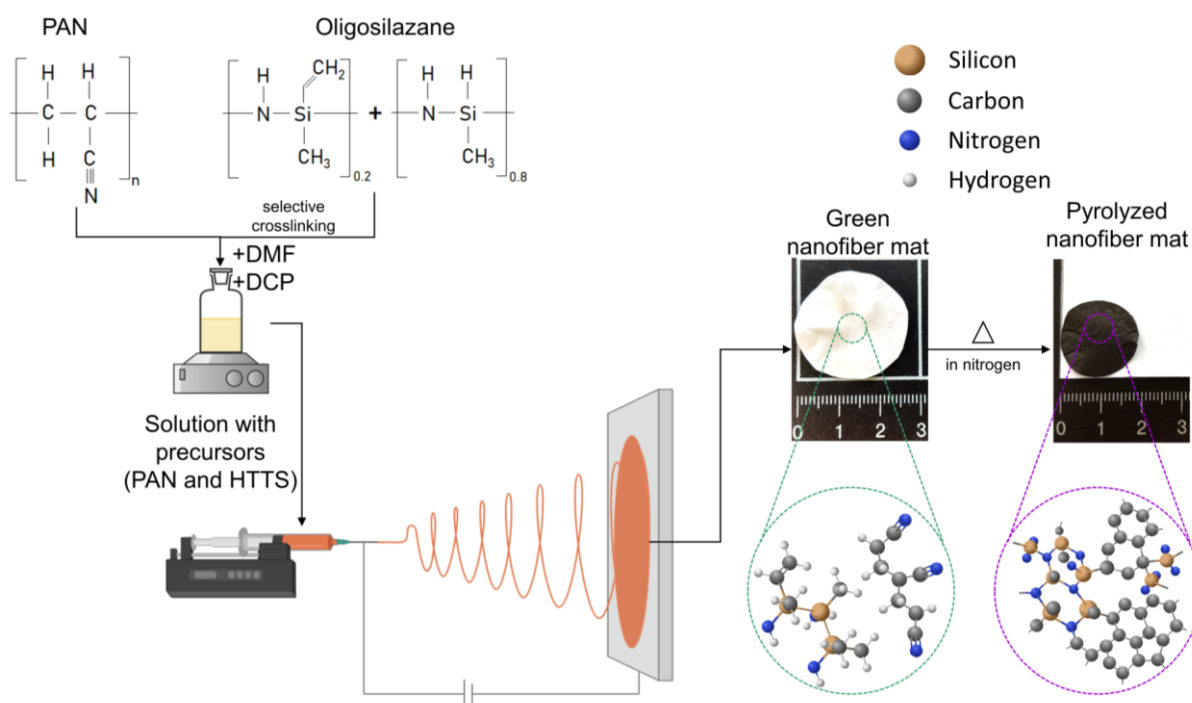
For the carbon mats, a solution containing 1 g PAN in 9.53 ml DMF was prepared, stirred for 3 h at 100 °C and stirred for more 9 h at room temperature (PAN samples). For the PAN/HTTS samples, 0.889 g PAN was first solubilized in 9.25 ml DMF at 100 °C for 3h. After this time, 0.381 g HTTS [25] and 0.0305 g DCP were added to the solution and further stirred for 12 h at room temperature (PAN:HTTS 7:3 wt.%). Well-dissolved polymer solutions after the preparation were obtained with a light yellow-colored PAN solution. The color gradually became darker and intensified with the addition of polysilazane.

The electrospinning was conducted in a lab-scale electrospinning device. The solution was transferred into a syringe with a 21 gauge needle (needle diameter of 0.8 mm), and the

distance between the needle tip and collector was set to 23.5 cm. The applied voltage was 21 kV, and the feed rate of the precursor solution was kept at $\sim 0.2\text{--}0.8\text{ mL min}^{-1}$.

The electrospun mats, PAN and PAN/HTTS samples, were then pyrolyzed in a programmed tube furnace in nitrogen atmosphere at a heating rate of $5\text{ }^{\circ}\text{C min}^{-1}$ up to 800, 1000 and 1200°C . The samples were kept at the defined pyrolysis temperature for 1 h and allowed to cool to room temperature. Sample labels are defined by the polymer system used followed by the pyrolysis temperature employed. The mean thickness of the fiber mats was about 0.04 mm after electrospinning for about 3 h. The major parts of the setup are illustrated in Figure 6.1.

Figure 6.1 – Fabrication of C/SiCN nanofiber mats via precursor approach and electrospinning technique



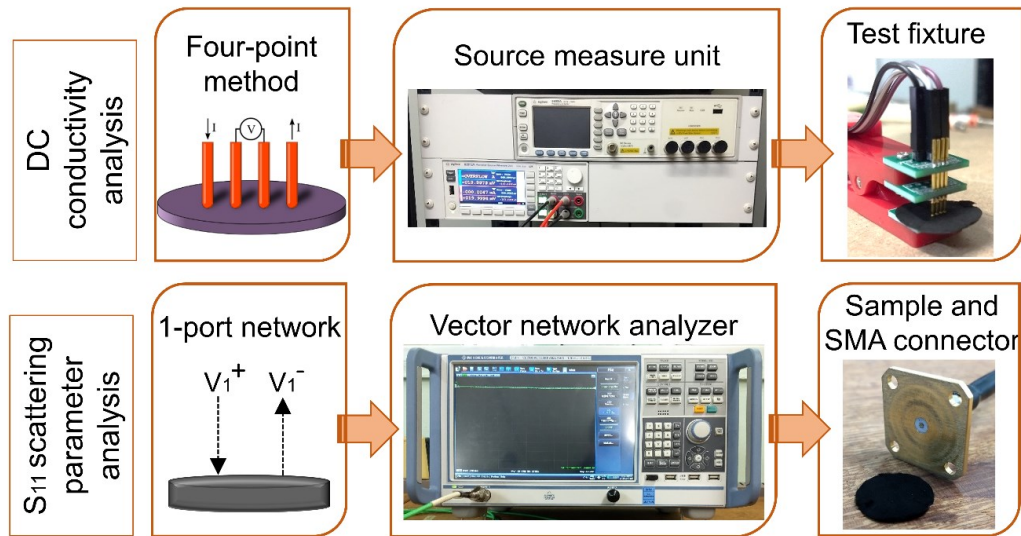
The oscillatory shear rheology of the solutions was investigated with an MCR 702 rotational rheometer (Anton Paar, Austria) in a parallel plate configuration [26]. Surface tension measurements were conducted through the hanging-drop method ($\sim 4\text{ }\mu\text{L}$ each drop) using a DSA25E drop shape analyzer (Krüss, Germany). The conductivity of the solutions was measured by a conductivitymeter SevenCompact S230-Basic (Mettler Toledo, EUA) at room temperature. Three measurements were acquired to calculate the average value.

TGA and DSC of the electrospun samples were performed with STA 449 F5 Jupiter equipment (Netzsch, Germany) with $\sim 5\text{ mg}$ of sample heating from 20 to $1200\text{ }^{\circ}\text{C}$ at a heating rate of $5^{\circ}\text{C min}^{-1}$ in nitrogen atmosphere.

The Zeiss Gemini Sigma 300 VP (Zeiss, Germany) SEM was used to examine the golden-sputtered electrospun samples, and fiber diameter was evaluated from four different SEM images measuring randomly 100 fibers of each sample with open-source ImageJ software. The carbon and silicon content were measured with energy-dispersive X-ray spectroscopy (EDS) Octane Elect EDS System EDAX (Ametek, USA). The IR transmissivity of the fibers was tested on a FTIR Tensor 27 equipped with an ATR sampling unit (Bruker, USA). The carbon structure was analyzed by Raman spectroscopy and XRD. XRD was carried out using a flat-sample transmission geometry using monochromatic CuK α radiation ($\lambda = 1.5418 \text{ \AA}$, 40 mA, and 40 kV) with D8 Advance (Bruker AXS, Germany). The Raman curves obtained at 532 nm with Senterra II (Bruker, USA) were fitted using the Lorentz function with Origin 2022 software (adjusted $R^2 \geq 0.88$). The I_D/I_G and $I_D/I_{D'}$ ratios were calculated based on the height intensity of each peak after curve fitting. The porosity of the nanofiber mats was estimated using the apparent density and the true density was determined with helium pycnometer (AccuPyc II 1340, Micromeritics, USA) [27].

The DC electrical conductivity of the nonwoven mats was examined using a B2912A precision source measure unit (SMU) (Keysight, USA) via the conventional four-probe method. The average results obtained from at least three measurements were reported. The voltage was measured by fixing the current according to each sample. This current was swept from -0.0001 A to 0.001 A for PAN:HTTS pyrolyzed at 800 °C and 1000 °C samples, and -0.009 A to 0.0009 A for PAN:HTTS pyrolyzed at 1200 °C. The current was swept from -10 A to 10 A for all three PAN samples. The measurement was acquired with a quiet time of 0.0005 s and a total scan time between 4 s and 5 s. The data were then subjected to each sample's correction factors according to its boundary conditions [28]. The geometric factor was considered for the calculation, while porosity was not considered due to the complexity of the calculations.

The EM reflection loss was characterized using a ZNB4 1-port VNA (Rohde & Schwarz, Germany) in the range of 100 MHz to 4.5 GHz. The calibration without a metal panel was first conducted, followed by the sample measurement. The S_{11} scattering parameter was measured, which represents the response to incident radiation from port 1, along with any subsequent signals emitted via internal reflections caused by the impedance match of the material concerning free space [29]. The diagram of DC electrical conductivity and S_{11} scattering parameter analyses is illustrated (Figure 6.2).

Figure 6.2 – Diagram of DC electrical conductivity and S_{11} scattering parameter analyses.

The S_{11} scattering parameter is the amplitudes ratio of the incident (V_1^+) and reflected (V_1^-) voltage waves. If $S_{11}=0$, then all the power is reflected from the material and nothing is radiated or absorbed. Equation 6.1 shows the calculation of S_{11} , where Γ_{11} is the reflection coefficient [30]. Since VNA was first calibrated without the sample and the analyzer is configured in 1-port, $V_2^+ = 0$.

$$S_{11} = \left. \frac{V_1^-}{V_1^+} \right|_{V_2^+=0} = \Gamma_{11} \quad (6.1)$$

The return loss ($RL = -S_{11}$, frequently presented with the negative value in materials engineering) is the attenuation of the reflected signal compared to the input signal and is expressed in terms of impedance where $Z_{in}(\omega)$ is the load impedance and Z_0 is the source impedance as shown by Equation 6.2 [31].

$$RL_{dB}(\omega) = 20 \log_{10} \left| \frac{Z_{in}(\omega) - Z_0}{Z_{in}(\omega) + Z_0} \right| \quad (6.2)$$

The VSWR represents the degree to which the impedance of a load matches the characteristic impedance of a transmission line carrying electromagnetic frequency signals. A matched load would mean a VSWR of 1:1 implying no reflected wave. An infinite VSWR represents complete reflection with all the incident power reflected toward the source. An EM

wave in a transmission line is partly reflected when the line is terminated with an impedance unequal to its characteristic impedance. The VSWR was calculated according to Equation 6.3.

$$VSWR = \frac{1+\Gamma_{11}}{1-\Gamma_{11}} \quad (6.3)$$

The equation for shielding effectiveness (SE) is related to the scattering parameters as given by Equation 6.4 with $SE_T(\omega)$, $SE_R(\omega)$, and $SE_A(\omega)$ representing total shielding effectiveness, reflection shielding effectiveness, and absorption shielding effectiveness, respectively [32].

$$SE_T(\omega) = SE_R(\omega) + SE_A(\omega) \quad (6.4)$$

The $SE_R(\omega)$ was calculated using S_{11} parameter as shown by Equation 6.5.

$$SE_{RdB}(\omega) = 10\log_{10} \left(\frac{1}{1-|S_{11}(\omega)|^2} \right) \quad (6.5)$$

The absorption coefficient is expressed by Equation 6.6, where $R(\omega)$ and $T(\omega)$ are the reflection and transmission coefficients respectively. VNA was first calibrated without the sample, so there was no electromagnetic transmission during the measurement i.e. $T(\omega)=0$, and the absorption coefficient was determined.

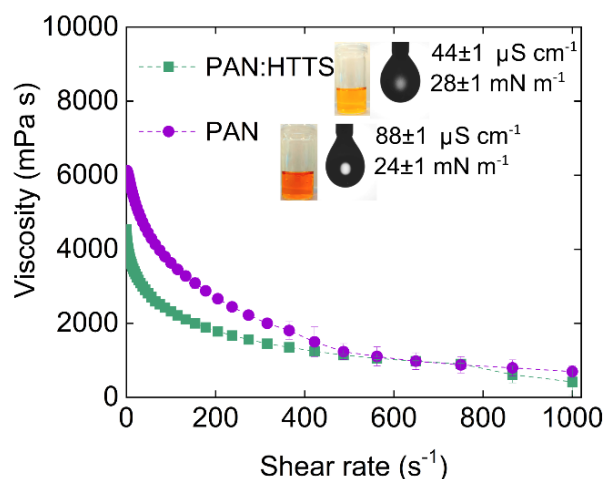
$$A(\omega) = 1 - R(\omega) - T(\omega) \quad (6.6)$$

6.3 RESULTS AND DISCUSSION

Despite electrospinning is a well-established technique for producing organic fibers, investigations on solutions containing preceramic polymers are very limited. It is well-known that fiber morphology depends on polymer and solvent properties beyond process parameters and environmental conditions. Therefore, both solutions were characterized to establish the properties in which it is possible to electrospun and to investigate the influence of adding preceramic polymer to PAN. Oscillatory rheology was used to establish the flow properties of the precursor solutions related to the electrospinning process, which can be considered an

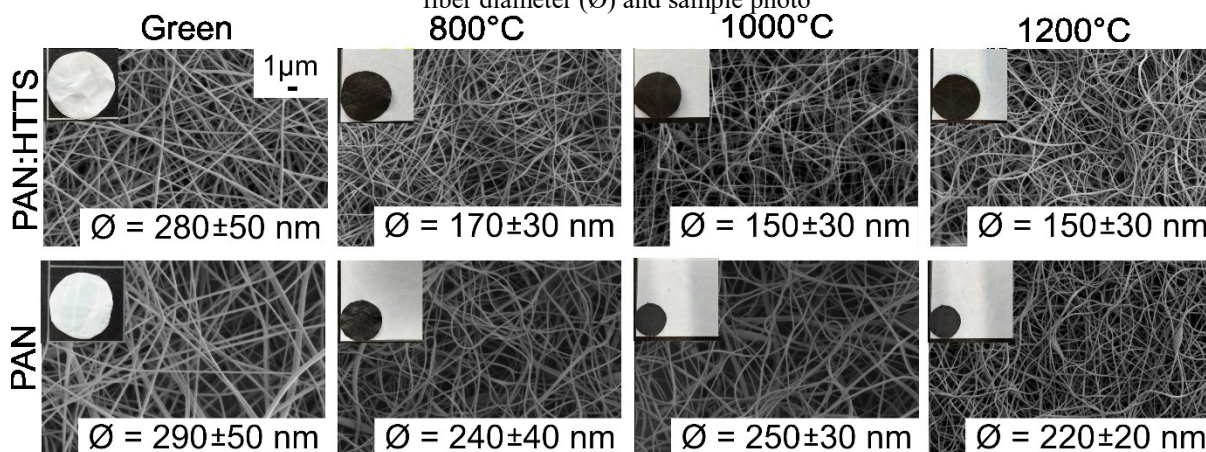
extrusion process with a medium to high shear rate ($10\text{-}1000\text{ s}^{-1}$). Both PAN:HTTS and PAN solutions showed pseudoplastic properties with shear-thinning in which the more shear stress is applied, the more freely the solution flows (Figure 6.3). Under low shear rates, the PAN solution showed a higher viscosity compared to that of PAN:HTTS solution and the rheological behaviors were very similar under high shear rates. Although PAN:HTTS has a higher polymer concentration, the viscosity decreased for a low shear rate, probably because of the low-molecular-weight of polysilazane facilitating the mobility of the molecular chains.

Figure 6.3 – Properties of PAN:HTTS (7:3 wt.% and 13 wt.% polymer concentration) and PAN solutions (10 wt.% polymer concentration). The viscosity is presented according to shear rate, solution appearance, respective electrical conductivity (in $\mu\text{S cm}^{-1}$), and surface tension (in mN m^{-1})



The electrical conductivity of the solutions was tested before electrospinning. Compared to PAN:HTTS, the PAN solution showed a greater ability to conduct electrical current (inset of Figure 6.3). However, this difference is not expressive. The surface tension of both solutions was very similar around 26 mN m^{-1} . The values of viscosity, electrical conductivity and surface tension of the solutions are within the expected ranges [26]. A pseudoplastic behavior was obtained for PAN and PAN:HTTS solutions, which was a key property for producing seamless fibers in electrospinning. Similar properties of the solutions resulted in fiber diameters of $\sim 280\text{-}290\text{ nm}$ for both samples (Figure 6.4). Since the solutions of both systems had similar characteristics for electrospinning, no significant change in green fiber diameter was noticed. After pyrolysis, the mats had different fiber diameters related to the carbonization of PAN and polymer-to-ceramic conversion of polysilazane.

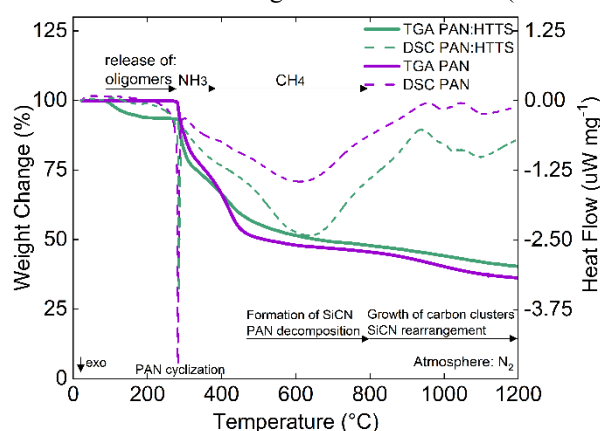
Figure 6.4 – As-spun and pyrolyzed electrospun PAN:HTTS (7:3 wt.%) and PAN mats with corresponding mean fiber diameter (\varnothing) and sample photo



The samples showed similar weight changes, however after pyrolysis, the PAN:HTTS-derived samples presented thinner diameters attributed to the denser ceramic phase than the carbon phase, leading to greater shrinkage during pyrolysis. The polymer to ceramic transformation involved the elimination of organic groups and the rearrangement of carbon atoms from PAN and polysilazane (generally those attached to the Si/N structure). Thermal analysis (Figure 6.5) showed the different pyrolysis stages of carbon and polysilazane. At 200-400 °C the carbonization of PAN occurred and cyclized carbon structures were formed with the release of mainly HCN, NH₃, CH₄, and H₂ [33]. The exothermic peak observed in the DSC curve was due to the uncontrolled thermal polymerization of the nitrile group with the release of the heat of polymerization [34]. Denitrogenation occurred as the temperature increased, transforming carbon ribbons into thin, sheet-like structures and bonding adjacent sheets, which contain numerous vacancy imperfections and were folded to enclose voids, forming graphite-like structures or turbostratic carbon. The basic structural units (BSUs) of carbon consisted of stacked conductive turbostratic or graphite layers. From 800-1200 °C, carbon clusters grew via edge-to-edge linkage of BSUs. At 1200° C, PAN showed only 36% weight retention, with a decomposition beginning at ~280°C and more than 45% evaporating above 800°C. For PAN:HTTS sample, the first weight change at low temperature (< 200 °C) was probably a loss of low-molecular-weight oligomers that were volatilizing. First, hydrosilylation and dehydrocoupling reactions occurred between ~100-400 °C for polysilazane forming Si-C, Si-N, and Si-Si bonds. At ~300 °C, transamination began with the formation of Si-N bonds [25,35]. PAN:HTTS exhibited weight retention of 48% at 800 °C and 40% at 1200 °C. This weight retention suggested that the ceramic positively interacted with PAN by enhancing the thermal stability of the polymer network. The enhanced thermal stability of PAN:HTTS was also

observed through a shift of the DSC peaks to higher temperatures. In fact, at temperatures above 200 °C, the Si-H group can react with PAN, indicating a crosslinking between both precursors, which was also observed elsewhere with a hybrid polymer made up of acrylonitrile and oligosilazane [36]. Within the matrix of polysilazane-derived SiCN, tetrahedral coordinated Si atoms are bonded to either N or C or a mixture of C and N (that is, SiC_xN_y), forming SiC_4 , SiN_4 , or SiC_xN_y units, while graphene-like sp^2 -carbon is located at the boundary of tetrahedral nanodomains of silicon.

Figure 6.5 – TGA and DSC thermograms of PAN:HTTS (7:3 wt.%) and PAN



FTIR-ATR spectra in Figure 6.6 show the carbonization of PAN and the polymer-to-ceramic transformation of polysilazane at different temperatures. The expected absorption bands were observed (Table 6.1). The spectra of as-spun samples exhibited bands corresponding to N-H, C-H, Si-H, vinyl group, Si-C, and Si-N for the polysilazane-containing samples and $\text{C}\equiv\text{N}$ and $\text{C}=\text{O}$ for PAN. The conversion of polymer to ceramic at 800 °C was confirmed by the absence of the N-H and Si-H absorption bands, and the absence of methyl and vinyl groups. On the carbonized PAN fibers, the nitrile band was not observed, suggesting the cyclization of the structure. The wide peak, between 800 and 1260 cm^{-1} , is attributed to the formation of SiCN structure in the carbon matrix, while the band at $\sim 1540 \text{ cm}^{-1}$ is attributed to C=C and C=N bands.

Figure 6.6 – FTIR-ATR spectra of as-spun and pyrolyzed (a) PAN:HTTS and (b) PAN samples

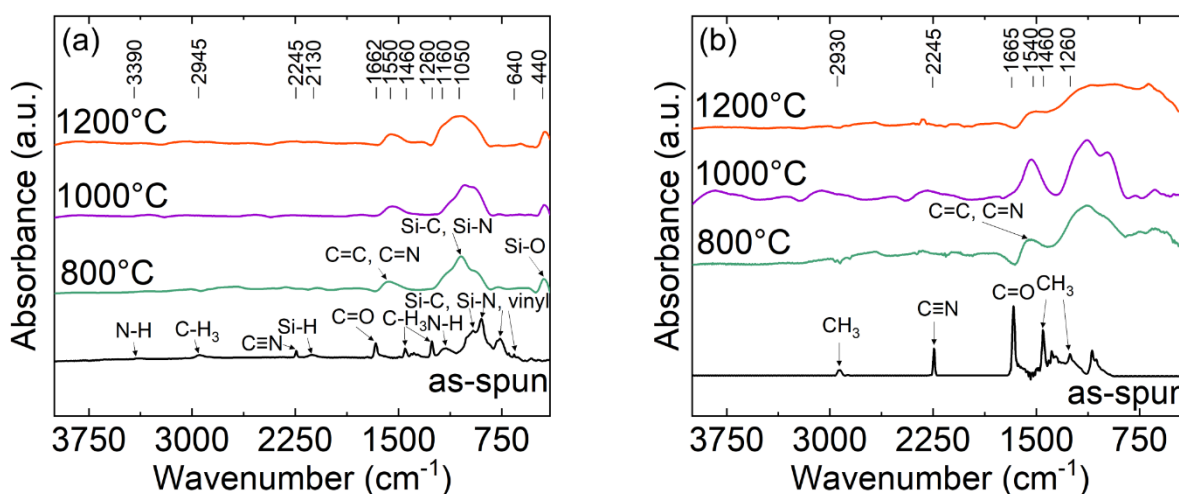
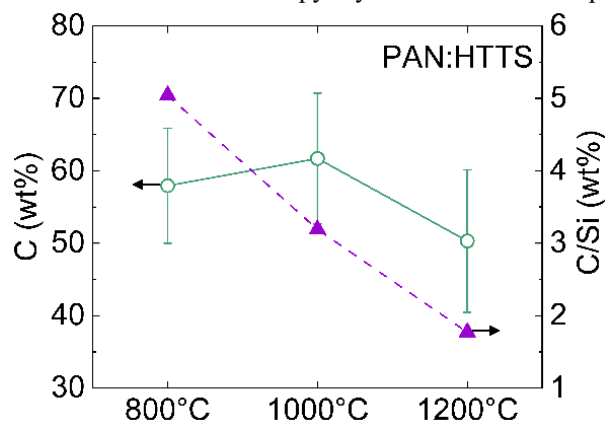


Table 6.1 – FTIR peak assignments of as-spun and pyrolyzed PAN:HTTS and PAN samples

Wavenumber (cm ⁻¹)	Group	Ref.
~3390	$\nu_s(\text{NH})$	[37,38]
~2930	$\nu_s(\text{CH}_3)$	[25,39]
~2245	$\delta_s(\text{C}\equiv\text{N})$	[40,41]
~2130	$\nu_s(\text{SiH})$	[42,43]
~1666	$\nu_s(\text{C}=\text{O})$	[40,41]
~1260 and ~1460	$\delta_s(\text{CH}_3)$	[25,39]
~1160	$\delta_s(\text{NH})$	[25,42]
~640-1074	vinyl group, $\delta_s(\text{Si-C})$ and $\delta_s(\text{Si-N})$	[44,45]
~1540	$\delta_s(\text{C}=\text{C})$ and $\delta_s(\text{C}=\text{N})$	[40,46]
~440 and 1060	$\delta_s(\text{Si-O})$	[45,47]

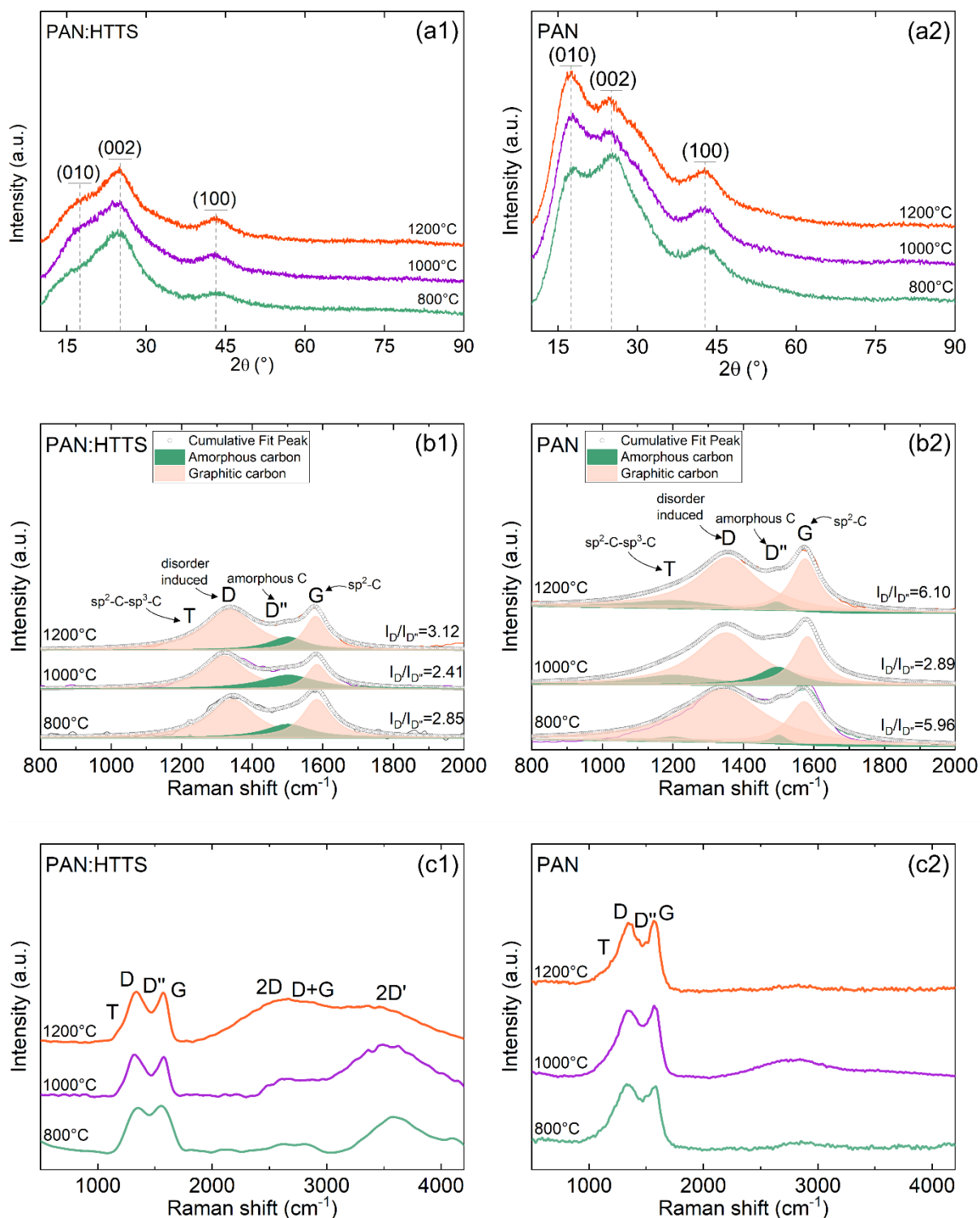
Figure 6.7 shows the weight content of C and C/Si ratio for pyrolyzed PAN:HTTS samples based on EDS results. In PAN:HTTS, the weight content of carbon remained stable between 50.3-61.7 wt% as shown by the error range. This is attributed to carbon coming mainly from the carbonization of PAN and also from the organic backbone structures of HTTS (methyl and vinyl groups), thus preserving the carbon content in the material. The carbonization of PAN leads to the evolution of higher-order structures with pure C=C bonds which are very infra-red inactive [48]. Therefore, XRD and Raman analyses were conducted hereafter to evaluate the carbon nanostructure.

Figure 6.7 – Weight content of C and C/Si ratio for pyrolyzed PAN:HTTS samples based on EDS results



The XRD patterns of the electrospun mats (Figure 6.8a1 and Figure 6.8a2) exhibit peaks at 17° , 25° and 43° corresponding respectively to (0 1 0) plane of graphite ($d = 0.53$ nm), (0 0 2) lattice of typical graphite ($d = 0.34$ nm) and (1 0 0) plane from arbitrary diffraction related to graphene sheets ($d = 0.17$ nm), which is in accordance with the literature [49–51]. The peak at 25° is the (0 0 2) carbon Bragg peak, which gives information about the amount of single, bilayer and trilayer graphene sheets arranged at arbitrary angles [52]. The (0 0 2) peak became weaker for pyrolyzed PAN:HTTS samples, suggesting that the carbon is predominantly of amorphous and disordered nature. This indicated that the inclusion of polysilazane disrupted the crystalline structure and enhanced the amorphousness of carbon as also observed by Smith *et al.* [38]. The 25° peak shows a more pronounced decrease in intensity than the 43° peak with the addition of polysilazane; thus, the preceramic interfered more with the layer stacking than the lateral extent of the layers. With higher pyrolysis temperature, only the peak centered at 17° increased remarkably for PAN-derived samples due to the evolution of graphite.

Figure 6.8 – (a) XRD spectra, (b) first-order Raman spectra and (c) second-order Raman spectra of PAN:HTTS and PAN pyrolyzed at different temperatures



Typical carbon signals in the first-order Raman spectra were identified as disorder-induced D-band at $\sim 1342\text{ cm}^{-1}$ and the G-band at $\sim 1579\text{ cm}^{-1}$ due to in-plane bond stretching of sp² carbon (Figure 6.8b1 and Figure 6.8b2) [53]. The so-called minor bands were included

to improve the quality of the fitting curves. The T-band at $\sim 1206\text{ cm}^{-1}$ corresponds to sp^2 - sp^3 bonds of $\delta_s(\text{C-C})$ and $\delta_s(\text{C=C})$ vibrations of polyene-like structures, and D''-band at $\sim 1499\text{ cm}^{-1}$ corresponds to amorphous carbon contained in the samples [54,55]. The intensities of D- and G-bands were similar for all samples, revealing a disordered graphitic lattice and some degree of carbon order. In contrast to XRD, Raman peak positions and intensities remained almost unchanged after each thermal treatment, suggesting that neither a lateral growth nor a pronounced ordering process of the existing carbon domains occurs from 800 °C to 1200 °C. The ratio of D- and G-bands amplitudes (I_D/I_G) is often used to indirectly reflect the degree of graphitization of carbon materials. The similar intensity ratios of D- and G-bands ($I_D/I_G \approx 1.13$) for increasing temperature indicated a stable size of sp^2 domains and defects in the graphitic lattice. Nevertheless, with increasing pyrolysis temperature, the D- and G-bands got more narrow and distinct due to a decreasing number of intrinsic defect sites, the disappearance of residual C-H bonds, and the vanishing of dangling bonds [56]. According to the Tuinstra-Koenig-correlation theoretically acceptable to estimate the size of carbon clusters along the sixfold ring plane ($L_a > 2.2\text{ nm}$ when $\lambda = 514.5\text{ nm}$) [54], the lateral crystallite size L_a is ~ 3.7 - 5.1 nm for the samples prepared here indicating the nanostructured nature of the materials (Table 6.2). Additionally, the $I_D/I_{D''}$ values increased from 800 °C to 1200 °C, suggesting a higher degree of carbon organization.

Different bands were identified in the second-order Raman spectra of PAN:HTTS-derived samples, including 2D (or G'), D + G, and 2D' respectively at $\sim 2559\text{ cm}^{-1}$, 2783 cm^{-1} , and 3540 cm^{-1} attributed to overtones and combinations of the known lattice vibration modes (Figure 6.8c1 and Figure 6.8c2). Accordingly, the 2D-band is an overtone of the D-band usually found in defect-free graphite samples [54]. The more intense 2D-band identified in the spectra of PAN:HTTS/1200 °C is associated with a higher ordering of the graphene sheets in terms of stacking of the layers along the axis [52,57]. In contrast, the 2D-band of PAN:HTTS pyrolyzed at 800 °C and 1000 °C is less pronounced indicating a random graphene sheet distribution. In parallel, the G-band width of PAN:HTTS/1200 °C is diminished, implying that the carbon ordering increases with increasing pyrolysis temperature (Table 6.2) [57,58]. XRD- and Raman measurements confirmed the presence of carbon as a mixture of disordered carbon, nanocrystalline graphite, and graphene sheets. The presence of the ceramic consisting of Si mixed bond tetrahedral with C and N along with carbon could be confirmed based on the FTIR data presented here and previous work on similar systems [42,44].

Table 6.2 – Raman peak assignments with corresponding full width at half maximum (FWHM) of pyrolyzed PAN:HTTS and PAN samples

Sample	Pyrolysis temperature (°C)	T-band intensity (cm ⁻¹)	D-band intensity (cm ⁻¹)	FWHM _D (cm ⁻¹)	D''-band intensity (cm ⁻¹)	G-band intensity (cm ⁻¹)	FWHM _G (cm ⁻¹)	L _a of graphite (nm)
PAN:HTTS	800	1223	1342	161	1501	1583	99	4.9
	1000	-	1320	146	1502	1584	71	3.7
	1200	-	1336	179	1501	1579	78	4.1
PAN	800	1201	1343	272	1501	1573	113	4.1
	1000	1201	1351	217	1497	1581	92	4.6
	1200	1201	1357	209	1494	1575	95	5.1

Figure 6.9 shows the absorption coefficient $A(\omega)$, reflection shielding effectiveness SER, and the reflection loss RL highlighted in the 5G C-band of PAN:HTTS and PAN pyrolyzed at different temperatures. In the 5G C-band, the $A(\omega)$ was about 0.68, 0.17, and 0.35 for PAN:HTTS pyrolyzed respectively at 800 °C, 1000 °C, and 1200 °C; in contrast, 0.07, 0.10, and 0.11 for PAN pyrolyzed respectively at 800 °C, 1000 °C, and 1200 °C (Figure 6.9a and Figure 6.9b). Therefore, the introduction of defects with the SiCN ceramic constructs small nanodomains in the carbon matrix that significantly enhanced the absorption mechanism. Compared to carbon fibers, the SiCN-containing samples had a higher reflection shielding effectiveness (Figure 6.9c and Figure 6.9d) i.e. lower reflection loss, (Figure 6.9e and Figure 6.9f). Carbon nanofiber mats radiate virtually nothing since S_{11} i.e. RL is close to 0, so almost all the power was reflected. The non-effective dissipation of EM field of pyrolyzed PAN samples was mainly caused by the uncoordinated EM parameters and impedance mismatch [59,60].

Figure 6.9 – Electromagnetic characterization of PAN:HTTS and PAN pyrolyzed at different temperatures highlighted in the 5G C-band. (a) absorption coefficient $A(\omega)$, (b) reflection shielding effectiveness SE_R , and (c) reflection loss RL . The photo inset shows the flexibility of the PAN:HTTS/800 °C sample. The flexibility of the mats was very similar, i.e. the addition of SiCN into the carbon did not change the flexibility because it is present in a low content and is well distributed throughout the carbon matrix

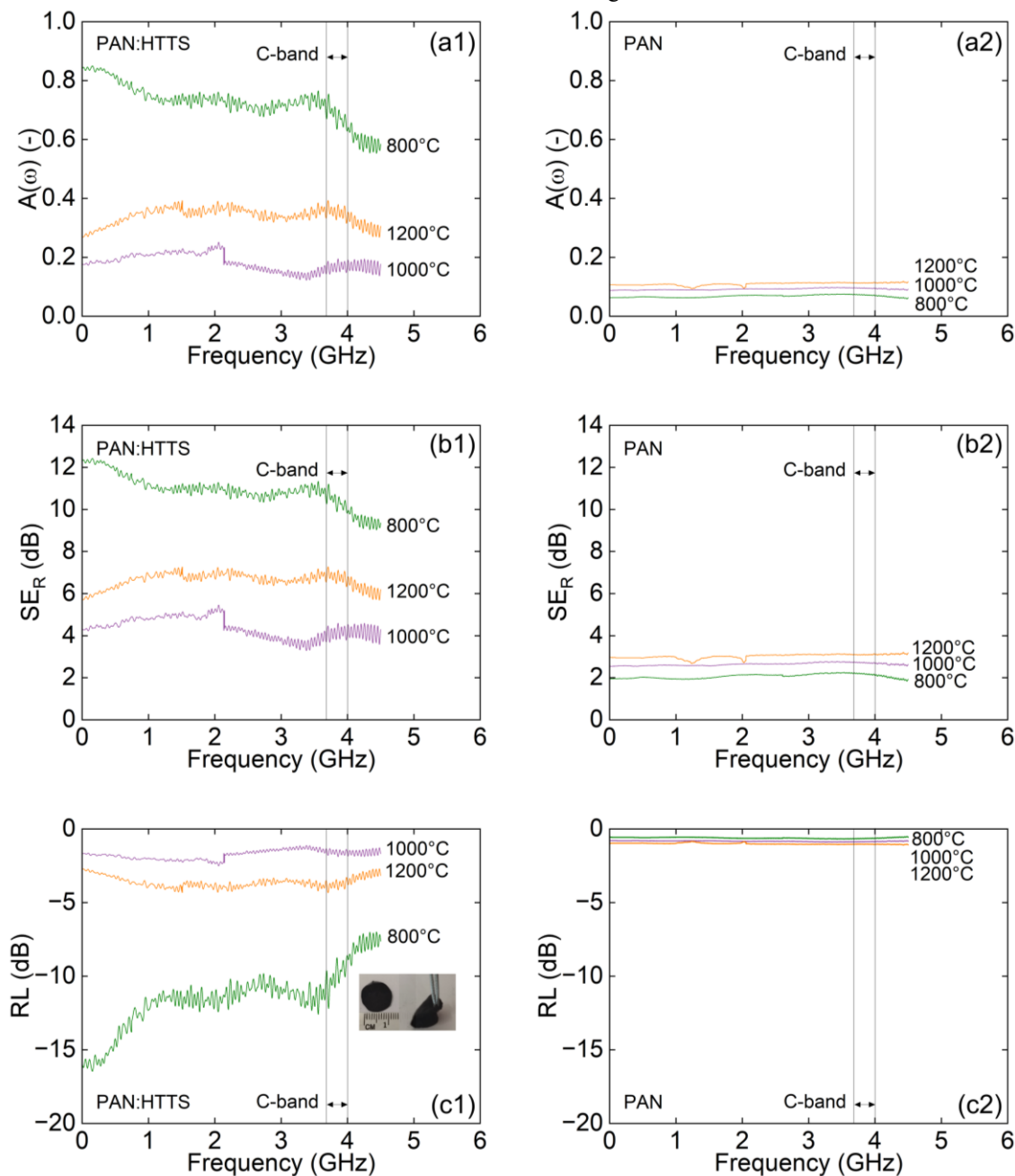
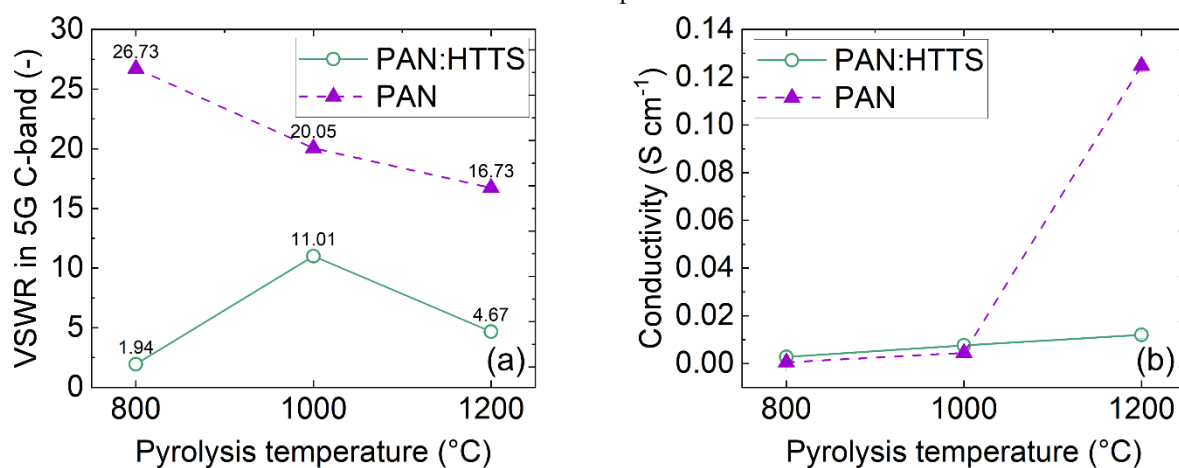


Figure 6.10a shows the VSWR in the 5G C-band of PAN:HTTS and PAN pyrolyzed at different temperatures. When SiCN nanodomains are scattered in the carbon matrix, the VSWR is drastically reduced compared to that of pure carbon relating to a lower impedance mismatch. Specifically, the PAN:HTTS nanofiber mat pyrolyzed at 800 °C is approximately 1.94 in the 5G C-band, which means approximately 11% reflected energy. For PAN:HTTS

nanofiber mats pyrolyzed at 1000 °C and 1200 °C, the RL > -5 dB and the impedance was also mismatched. The acceptable level of mismatch depends on the application. In materials engineering and EM shielding, a good general agreement is RL < -10 dB (VSWR \approx 2), and the PAN:HTTS nanofiber mat pyrolyzed at 800 °C showed a lower level of impedance mismatch. If the bandwidth is defined as the frequency range where S₁₁ is to be less than -10 dB, then the bandwidth of PAN:HTTS pyrolyzed at 800 °C would be roughly 4 GHz. Figure 6.10b shows the DC electrical conductivity of PAN:HTTS and PAN pyrolyzed at different temperatures. For PAN-derived materials, the higher DC electrical conductivity with an increase in pyrolysis temperature translated into a lower impedance mismatch. In contrast, the impedance matching of PAN:HTTS-derived materials depended not only on DC electrical conductivity provided by carbon but also on the dielectric properties i.e. permittivity of SiCN.

Figure 6.10 – (a) VSWR in 5G C-band and (b) DC electrical conductivity of PAN:HTTS and PAN pyrolyzed at different temperatures



The pyrolyzed samples derived from PAN:HTTS and PAN showed a medium DC electrical conductivity, suggesting that carbon is a primary active substance and SiCN acts as a material to modify the conductivity. The conductivity of PAN:HTTS samples pyrolyzed at 800 °C, 1000 °C, or 1200 °C is respectively 0.0028 ± 0.0008 S cm⁻¹, 0.0076 ± 0.0009 S cm⁻¹, and 0.0120 ± 0.0016 S cm⁻¹, which follows the literature about PDC containing high-content of carbon [61]. Likewise, PAN samples are 0.0005 ± 0.00003 S cm⁻¹, 0.0045 ± 0.0001 S cm⁻¹, and 0.1248 ± 0.0027 S cm⁻¹, which is in accordance with the literature on electrospun carbon fibers [62]. For 800 °C and 1000 °C, the conductivity is similar. It is supposed that at 800 °C and 1000 °C, the oriented BSUs are isolated due to heteroatoms (mainly hydrogen) and the voids between them, forming loosely lapped graphene sheet structures and limiting the DC electrical

conductivity. In this case, the electrical conductivity could result from a hopping process occurring between these more-or-less complete-and-interconnected cages of carbon. However, the conductivity increased sharply for PAN pyrolyzed at 1200 °C due to carbon concentration and structural evolution [63]. In the composition of the fibers, amorphous carbon and amorphous SiCN are semiconductors, whereas turbostratic carbon and graphite have significantly higher conductivity [64]. This explains the lower conductivity of PAN:HTTS/1200 °C sample due to the presence of SiCN. These results agree with XRD and Raman results, i.e., the addition of polysilazane and adjustment of pyrolysis temperature varied the defect level and graphitization degree, directly influencing the DC electrical conductivity. Here, graphite provided good electrical conductivity and conduction loss, while amorphous carbon was used as a defect-rich region to provide polarization loss [65].

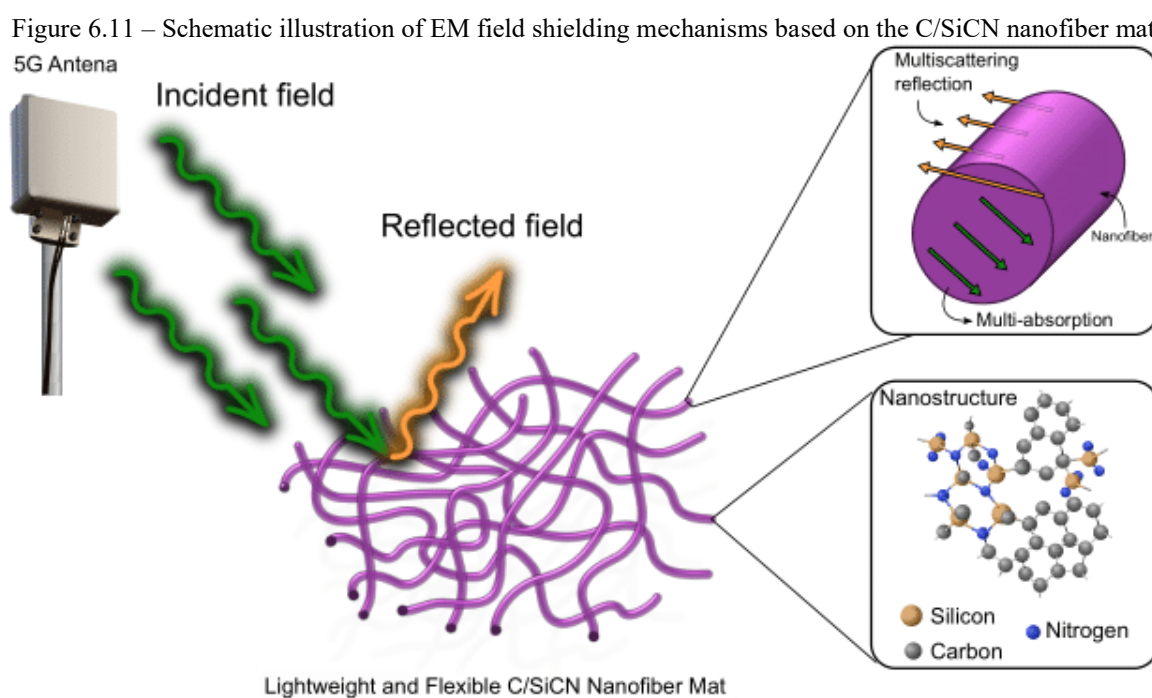
The PAN:HTTS/800°C showed a reflection loss of about -10 dB in the 5G C-band, which is comparable to SiCN pyrolyzed at 1200 °C with a reflection loss of about -10 dB in the same frequency range [66]. The reflection loss of PAN:HTTS/1000°C and PAN:HTTS/1200°C was around -2 dB and -4 dB, respectively. The enhancement in the EM field shielding performance of PAN:HTTS/800 °C is attributed to three points: (1) appropriate electrical conductivity, (2) high degree of carbon disorder, and (3) heterojunction structures due to the accumulation of charges at the interfaces as well as the formation of dipoles on carbon and SiCN [67]. The higher pyrolysis temperature contributed to the EM shielding of SiBCN with higher permittivity and dielectric loss [68]. However, due to the abundant amount of carbon present in the samples prepared in this work, the evolution of carbon with higher pyrolysis temperature decreased the heterojunction interfaces, decreasing EM shielding ability. Moreover, the increased dipole polarization caused by defects of carbon and SiCN contributed to EM shielding performance. The abundance of dangling Si bonds for the 800 °C sample as compared to the 1000 °C specimen resulted in higher reflection loss in a broad bandwidth. Voids or gaps exist at the interface of SiCN and free carbon as the result of bonding mismatches, contributing to EM field shielding. The DC electrical conductivity of 0.0028 S cm⁻¹ for PAN:HTTS/800 °C was similar to polycarbonate/polypropylene nanomaterials with dispersed multiwall carbon nanotubes (MWCNT), which showed a conductivity of 0.03 S cm⁻¹ with a reflection loss of -7 dB in 5G C-band [69]. Likewise, MWCNT/graphene foam with a conductivity of 1 S cm⁻¹ showed a reflection loss in C-band of -10 dB for lower thermal treatment [70]. Polyaniline film was found to have a conductivity of 5300 S cm⁻¹ with a reflection loss of -9 dB in higher frequency [71]. In another work, the incorporation of SiC into

spherical graphite-AlN contributed to a slightly decreasing electrical conductivity and enhanced polarization relaxation [72]. The electromagnetic shielding effectiveness of graphene-based composite film with a conductivity of 1720 S cm^{-1} was attributed to conduction loss and multiple reflections caused by the special structure of the material [73].

The proposed mechanisms of the C/SiCN nanofiber mats are represented in Figure 6.11. The dielectric loss contains conductivity loss and polarization loss [74]. The multiple polarization relaxation processes are due to (1) interfacial polarization originating from interfaces between carbon and SiCN causing differences in conductivity and permittivity and accumulating space charges, (2) dipole polarization from defects and vacancies of carbon mainly observed in PAN:HTTS/800°C samples according to XRD and Raman results. In the literature, it is reported that the interfacial Si-C and N-C bonds of SiCN PDCs are destroyed with concomitant hydrogen loss upon increasing the pyrolysis temperature from 800 °C to 1100 °C [75]. Hence, PAN:HTTS/800°C can simultaneously improve the polarization and conductivity loss. The interfacial polarization mechanism existing between complex nanostructural interfaces resulting in charge unbalance is believed to be responsible for the high reflection loss values observed with PAN:HTTS/800°C sample. Besides the intrinsic electric dipole polarization of Si-C-N, interface loss including charge accumulation, interface polarization, dielectric dissipation, and resonance relaxation contributed to EM absorption [7,76].

The structure of the SiCN material is amorphous 3D networks consisting of nano-clusters and free dangling bonds of silicon and carbon [77]. The introduction of SiCN in the carbon matrix may generate structural defects, which form interfacial and dipole polarization and carrier channels under the action of an external electromagnetic field, and then promote the shielding performance of the fibers under broad electromagnetic bandwidth [78]. Specifically, the PAN:HTTS/800°C was a suitable EM shielding material due to its wide bandgap, tunable electrical conductivity, and dielectric properties. The thin, flexible PAN:HTTS/800°C mat prepared here has a continuous conductive network and an abundant porous structure with a porosity of ~80%, achieving interior scattering and multi-reflection among fibers with a low density of about 1.83 g cm^{-3} [79]. Likewise, graphene foams with lower annealing temperatures showed more substantial shielding peaks at low frequencies (2-4 GHz) [60]. The return loss lower than -10 dB in the 5G C-band frequencies indicated that the carbon/SiCN pyrolyzed at 800 °C can dissipate more than 90% of the EM field achieving a balance between impedance matching and EM field attenuation. The multiscale in nano- and micro design of the materials

enabled the optimization of impedance matching, larger heterointerfaces for inducing polarization loss, extra conduction networks for enhancing conduction loss and increased low-dimensional structural units for promoting geometrical effects, thus improving the EM field absorption capacity.



6.4 CONCLUSIONS

Simultaneously integrating polymer-derived ceramic into carbonaceous material by engineering the nanostructure of the material is a promising method to achieve excellent EM shielding performance. The adjustment of pyrolysis temperature and addition of polysilazane varied the defect level and graphitization degree of PAN at the nanoscale. The DC electrical conductivity and reflection shielding properties of PAN:HTTS materials were tuned by controlling the defects, morphology, and structure with the pyrolysis temperature. The introduction of a Si-based ceramic in carbon may generate structural defects, which form interfacial and dipole polarization and carrier channels under the action of the external EM field. Appropriate electrical conductivity, high degree of carbon disorder, and presence of heterojunction structures played a crucial role in the EM field shielding performance of lightweight and flexible C/SiCN nanofiber mat pyrolyzed at 800°C, which could be employed as a novel material for low-frequency EM shielding. In conclusion, this work showed that defect

engineering (dopants and atom vacancies) in carbon-based materials is an exciting research direction for the development of EM shielding nanomaterials. Our findings might shed insight on the design of novel carbon-based materials with strong reflection loss, wide absorption frequency range, and thin thickness for applications in the military and aerospace industry requiring EM shielding of the 5G C-band frequencies, which is fundamental for communication security.

6.5 ACKNOWLEDGMENTS

This study was financed in part by the Coordenação de Aperfeiçoamento de Pessoal de Nível Superior - Brasil (CAPES) - Finance Code 001. The authors thank CAPES and Deutscher Akademischer Austauschdienst (DAAD) for supporting this work within the project PROBRAL (Grant n° 88887.368756/2019-00) and Conselho Nacional de Desenvolvimento Científico e Tecnológico - CNPq (Grant n° 442149/2018-2).

6.6 AUTHORS' CONTRIBUTIONS

The paper is mainly based on the work of the first author and author of this thesis Heloisa Ramlow. This work was conducted in collaboration with the Electromagnetism and Electromagnetic Compatibility Laboratory and the Laboratory of Electrical Materials (Federal University of Santa Catarina). The precise contributions of each author are listed below (Table 6.3).

Table 6.3 – Authors' contributions to Chapter 6

Author	Contribution
Ramlow, H.	Conceptualized the work, wrote the manuscript
Souza, G. B.	Gave conceptual and scientific advice, helped in the scientific evaluation and editing of the manuscript
Fonseca, M. P.	Gave conceptual and scientific advice, helped in the scientific evaluation and editing of the manuscript
Raizer, A.	Gave conceptual and scientific advice, helped in the scientific evaluation and editing of the manuscript
Rambo, C. R.	Gave conceptual and scientific advice, helped in the scientific evaluation and editing of the manuscript
Machado, R.	Gave conceptual and scientific advice, helped in the scientific evaluation and editing of the manuscript

6.7 REFERENCES

- [1] X. Zeng, E. Li, G. Xia, N. Xie, Z.-Y. Shen, M. Moskovits, R. Yu, Silica-based ceramics toward electromagnetic microwave absorption, *J. Eur. Ceram. Soc.* 41 (2021) 7381–7403. <https://doi.org/10.1016/j.jeurceramsoc.2021.08.009>.
- [2] R. Kumar, S. Sahoo, E. Joanni, R.K. Singh, W.K. Tan, K.K. Kar, A. Matsuda, Recent progress on carbon-based composite materials for microwave electromagnetic interference shielding, *Carbon* N. Y. 177 (2021) 304–331. <https://doi.org/10.1016/j.carbon.2021.02.091>.
- [3] Y. Cheng, W. Zhu, X. Lu, C. Wang, Recent progress of electrospun nanofibrous materials for electromagnetic interference shielding, *Compos. Commun.* 27 (2021) 100823. <https://doi.org/10.1016/j.coco.2021.100823>.
- [4] H. Guo, Y. Chen, Y. Li, W. Zhou, W. Xu, L. Pang, X. Fan, S. Jiang, Electrospun fibrous materials and their applications for electromagnetic interference shielding: A review, *Compos. Part A Appl. Sci. Manuf.* 143 (2021) 106309. <https://doi.org/10.1016/j.compositesa.2021.106309>.
- [5] S. Naghdi, B. Jaleh, M. Eslamipanah, A. Moradi, M. Abdollahi, N. Einali, K.Y. Rhee, Graphene family, and their hybrid structures for electromagnetic interference shielding applications: Recent trends and prospects, *J. Alloys Compd.* 900 (2022) 163176. <https://doi.org/10.1016/j.jallcom.2021.163176>.
- [6] D. Gunwant, A. Vedrtam, Microwave absorbing properties of carbon fiber based materials: A review and prospective, *J. Alloys Compd.* 881 (2021) 160572. <https://doi.org/10.1016/j.jallcom.2021.160572>.
- [7] Z. Wu, K. Pei, L. Xing, X. Yu, W. You, R. Che, Enhanced microwave absorption performance from magnetic coupling of magnetic nanoparticles suspended within hierarchically tubular composite, *Adv. Funct. Mater.* 29 (2019) 1–10. <https://doi.org/10.1002/adfm.201901448>.

- [8] F. Zhang, P. Ren, Z. Guo, J. Wang, Z. Chen, Z. Zong, J. Hu, Y. Jin, F. Ren, Asymmetric multilayered MXene-AgNWs/cellulose nanofiber composite films with antibacterial properties for high-efficiency electromagnetic interference shielding, *J. Mater. Sci. Technol.* 129 (2022) 181–189. <https://doi.org/10.1016/j.jmst.2022.04.039>.
- [9] Z. Chu, H. Cheng, W. Xie, L. Sun, Effects of diameter and hollow structure on the microwave absorption properties of short carbon fibers, *Ceram. Int.* 38 (2012) 4867–4873. <https://doi.org/10.1016/j.ceramint.2012.02.077>.
- [10] X. Zuo, P. Xu, C. Zhang, M. Li, X. Jiang, X. Yue, Porous magnetic carbon nanofibers (P-CNF/Fe) for low-frequency electromagnetic wave absorption synthesized by electrospinning, *Ceram. Int.* 45 (2019) 4474–4481. <https://doi.org/10.1016/j.ceramint.2018.11.127>.
- [11] P. Yin, L. Zhang, J. Wang, X. Feng, J. Dai, Y. Tang, Facile preparation of cotton-derived carbon fibers loaded with hollow Fe₃O₄ and CoFe NPs for significant low-frequency electromagnetic absorption, *Powder Technol.* 380 (2021) 134–142. <https://doi.org/10.1016/j.powtec.2020.11.044>.
- [12] F. Ren, J. Xue, X. Liu, L. Cheng, In situ construction of CNWs/SiC-NWs hybrid network reinforced SiCN with excellent electromagnetic wave absorption properties in X band, *Carbon N. Y.* 168 (2020) 278–289. <https://doi.org/10.1016/j.carbon.2020.06.081>.
- [13] Z. Wu, H.W. Cheng, C. Jin, B. Yang, C. Xu, K. Pei, H. Zhang, Z. Yang, R. Che, Dimensional design and core-shell engineering of nanomaterials for electromagnetic wave absorption, *Adv. Mater.* 34 (2022) 1–30. <https://doi.org/10.1002/adma.202107538>.
- [14] X. Liu, Z. Yu, R. Ishikawa, L. Chen, X. Liu, X. Yin, Y. Ikuhara, R. Riedel, Single-source-precursor derived RGO/CNTs-SiCN ceramic nanocomposite with ultra-high electromagnetic shielding effectiveness, *Acta Mater.* 130 (2017) 83–93. <https://doi.org/10.1016/j.actamat.2017.03.031>.
- [15] Y. Song, L. He, X. Zhang, F. Liu, N. Tian, Y. Tang, J. Kong, Highly efficient electromagnetic wave absorbing metal-free and carbon-rich ceramics derived from hyperbranched polycarbosilazanes, *J. Phys. Chem. C.* 121 (2017) 24774–24785. <https://doi.org/10.1021/acs.jpcc.7b07646>.
- [16] S. Wang, H. Gong, Y. Zhang, M.Z. Ashfaq, Microwave absorption properties of polymer-derived SiCN(CNTs) composite ceramics, *Ceram. Int.* 47 (2021) 1294–1302. <https://doi.org/10.1016/j.ceramint.2020.08.250>.
- [17] W. Duan, X. Yin, Q. Li, L. Schlier, P. Greil, N. Travitzky, A review of absorption properties in silicon-based polymer derived ceramics, *J. Eur. Ceram. Soc.* 36 (2016) 3681–3689. <https://doi.org/10.1016/j.jeurceramsoc.2016.02.002>.
- [18] E.W. Awini, S. Sridar, A.B. Kousaalya, S.S.L. Vendra, E. Koroleva, A. Filimonov, S. Vakhrushev, R. Kumar, Low frequency dielectric behavior and AC conductivity of polymer derived SiC(O)/HfC_xN_{1-x} ceramic nanocomposites, *Mater. Chem. Phys.* 260 (2021) 124122. <https://doi.org/10.1016/j.matchemphys.2020.124122>.
- [19] Z. Jia, D. Lan, K. Lin, M. Qin, K. Kou, G. Wu, H. Wu, Progress in low-frequency microwave absorbing materials, *J. Mater. Sci. Mater. Electron.* 29 (2018) 17122–17136. <https://doi.org/10.1007/s10854-018-9909-z>.
- [20] D. Sun, S. Huang, Y. Gao, B. Ma, Y. Wang, PVDF composites with spherical polymer-derived SiCN ceramic particles have significantly enhanced low-frequency dielectric constants, *J. Alloys Compd.* 783 (2019) 256–262. <https://doi.org/10.1016/j.jallcom.2018.12.323>.
- [21] C. Wang, V. Murugadoss, J. Kong, Z. He, X. Mai, Q. Shao, Y. Chen, L. Guo, C. Liu, S. Angaiyah, Z. Guo, Overview of carbon nanostructures and nanocomposites for electromagnetic wave shielding, *Carbon N. Y.* 140 (2018) 696–733.

- <https://doi.org/10.1016/j.carbon.2018.09.006>.
- [22] X. Liang, W. Liu, Y. Cheng, J. Lv, S. Dai, D. Tang, B. Zhang, G. Ji, Review: Recent process in the design of carbon-based nanostructures with optimized electromagnetic properties, *J. Alloys Compd.* 749 (2018) 887–899. <https://doi.org/10.1016/j.jallcom.2018.03.344>.
- [23] Y. Feng, X. Guo, H. Gong, Y. Zhang, X. Lin, Enhanced electromagnetic microwave absorption of Fe/C/SiCN composite ceramics targeting in integrated structure and function, *Ceram. Int.* 47 (2021) 3842–3852. <https://doi.org/10.1016/j.ceramint.2020.09.244>.
- [24] J.-M. Zhao, W.-X. An, D.-A. Li, X. Yang, Synthesis and microwave absorption properties of SiC–carbon fibers composite in S and C band, *Synth. Met.* 161 (2011) 2144–2148. <https://doi.org/10.1016/j.synthmet.2011.08.016>.
- [25] O. Flores, T. Schmalz, W. Krenkel, L. Heymann, G. Motz, Selective cross-linking of oligosilazanes to tailored meltable polysilazanes for the processing of ceramic SiCN fibres, *J. Mater. Chem. A* 1 (2013) 15406–15415. <https://doi.org/10.1039/c3ta13254d>.
- [26] H. Ramlow, C. Marangoni, G. Motz, R.A.F. Machado, Statistical optimization of polysilazane-derived ceramic: Electrospinning with and without organic polymer as a spinning aid for manufacturing thinner fibers, *Chem. Eng. J. Adv.* 9 (2022) 100220. <https://doi.org/10.1016/j.cej.2021.100220>.
- [27] L.F.B. Ribeiro, R.S. Cunha, A. de Noni, R.A.F. Machado, G. Motz, S.Y.G. González, Flexible and porous nonwoven SiCN ceramic material via electrospinning of an optimized silazane solution, *Adv. Eng. Mater.* 2100321 (2021) 1–7. <https://doi.org/10.1002/adem.202100321>.
- [28] D.K. Schroder, *Semiconductor material and device characterization*, 3rd ed., John Wiley & Sons, Inc., Hoboken, New Jersey, 2006.
- [29] M. Green, X. Chen, Recent progress of nanomaterials for microwave absorption, *J. Mater.* 5 (2019) 503–541. <https://doi.org/10.1016/j.jmat.2019.07.003>.
- [30] C.R. Paul, *Introduction to Electromagnetic Compatibility*, Second Edi, A John Wiley & Sons, New Jersey, 2006.
- [31] Y. Naito, K. Suetake, Application of ferrite to electromagnetic wave absorber and its characteristics, *IEEE Trans. Microw. Theory Tech.* 19 (1971) 65–72. <https://doi.org/10.1109/TMTT.1971.1127446>.
- [32] M.H. Al-Saleh, W.H. Saadeh, U. Sundararaj, EMI shielding effectiveness of carbon based nanostructured polymeric materials: A comparative study, *Carbon N. Y.* 60 (2013) 146–156. <https://doi.org/10.1016/j.carbon.2013.04.008>.
- [33] M.T. Jafari, M. Saraji, M. Kermani, Sol-gel electrospinning preparation of hybrid carbon silica nanofibers for extracting organophosphorus pesticides prior to analyzing them by gas chromatography-ion mobility spectrometry, *J. Chromatogr. A* 1558 (2018) 1–13. <https://doi.org/10.1016/j.chroma.2018.05.014>.
- [34] F. Agend, N. Naderi, R. Fareghi-Alamdari, Fabrication and electrical characterization of electrospun polyacrylonitrile-derived carbon nanofibers, *J. Appl. Polym. Sci.* 106 (2007) 255–259. <https://doi.org/10.1002/app.26476>.
- [35] E. Ionescu, Polymer-derived ceramics, in: R. Riedel, I.-W. Chen (Eds.), *Ceram. Sci. Technol. Vol. 3 Synth. Process.*, Wiley-VCH Verlag GmbH & Co. KGaA, 2011: p. 554.
- [36] L.F.B. Ribeiro, O. Flores, P. Furtat, C. Gervais, R. Kempe, R.A.F. Machado, G. Motz, A novel PAN/silazane hybrid polymer for processing of carbon-based fibres with extraordinary oxidation resistance, *J. Mater. Chem. A* 5 (2017) 720–729. <https://doi.org/10.1039/c6ta09293d>.
- [37] G. Xu, J. Xu, H. Su, X. Liu, H. Zhao, H. Feng, Two-dimensional (2D) nanoporous

- membranes with sub-nanopores in reverse osmosis desalination: latest developments and future directions, *Desalination*. 451 (2019) 18–34. <https://doi.org/10.1016/j.desal.2017.09.024>.
- [38] S.A. Smith, J.H. Park, B.P. Williams, Y.L. Joo, Polymer/ceramic co-continuous nanofiber membranes via room-curable organopolysilazane for improved lithium-ion battery performance, *J. Mater. Sci.* 52 (2017) 3657–3669. <https://doi.org/10.1007/s10853-016-0574-4>.
- [39] A. Tolosa, B. Krüner, N. Jäckel, M. Aslan, C. Vakifahmetoglu, V. Presser, Electrospinning and electrospaying of silicon oxycarbide-derived nanoporous carbon for supercapacitor electrodes, *J. Power Sources*. 313 (2016) 178–188. <https://doi.org/10.1016/j.jpowsour.2016.02.077>.
- [40] W. Dang, J. Liu, X. Wang, K. Yan, A. Zhang, J. Yang, L. Chen, J. Liang, Structural transformation of polyacrylonitrile (PAN) fibers during rapid thermal pretreatment in nitrogen atmosphere, *Polymers (Basel)*. 12 (2020) 1–12. <https://doi.org/10.3390/polym12010063>.
- [41] P. Lu, Q. Huang, A. Mukherjee, Y. Lo Hsieh, SiCO-doped carbon fibers with unique dual superhydrophilicity/superoleophilicity and ductile and capacitance properties, *ACS Appl. Mater. Interfaces*. 2 (2010) 3738–3744. <https://doi.org/10.1021/am100918x>.
- [42] P. Furtat, M. Lenz-Leite, E. Ionescu, R.A.F. MacHado, G. Motz, Synthesis of fluorine-modified polysilazanes: Via Si-H bond activation and their application as protective hydrophobic coatings, *J. Mater. Chem. A*. 5 (2017) 25509–25521. <https://doi.org/10.1039/c7ta07687h>.
- [43] Q. Zhang, D. Jia, Z. Yang, X. Duan, Q. Chen, Y. Zhou, Synthesis of novel cobalt-containing polysilazane nanofibers with fluorescence by electrospinning, *Polymers (Basel)*. 8 (2016) 1–13. <https://doi.org/10.3390/polym8100350>.
- [44] F. Xiao, H. Sun, J. Li, X. Guo, H. Zhang, J. Lu, Z. Pan, J. Xu, Electrospinning preparation and electromagnetic wave absorption properties of SiCN fibers, *Ceram. Int.* 46 (2020) 12773–12781. <https://doi.org/10.1016/j.ceramint.2020.02.046>.
- [45] A. Tolosa, M. Widmaier, B. Krüner, J.M. Griffin, V. Presser, Continuous silicon oxycarbide fiber mats with tin nanoparticles as a high capacity anode for lithium-ion batteries, *Sustain. Energy Fuels*. 2 (2018) 215–228. <https://doi.org/10.1039/c7se00431a>.
- [46] Y. Liu, X. Lin, H. Gong, Y. Zhang, Y. Feng, J. Mao, B. Xie, Electromagnetic properties and microwave absorption performances of nickel-doped SiCN ceramics pyrolyzed at different temperatures, *J. Alloys Compd.* 771 (2019) 356–363. <https://doi.org/10.1016/j.jallcom.2018.08.283>.
- [47] S. Bin Mujib, R. Cuccato, S. Mukherjee, G. Franchin, P. Colombo, G. Singh, Electrospun SiOC ceramic fiber mats as freestanding electrodes for electrochemical energy storage applications, *Ceram. Int.* 46 (2020) 3565–3573. <https://doi.org/10.1016/j.ceramint.2019.10.074>.
- [48] N. Hameed, J. Sharp, S. Nunna, C. Creighton, K. Magniez, P. Jyotishkumar, N. V. Salim, B. Fox, Structural transformation of polyacrylonitrile fibers during stabilization and low temperature carbonization, *Polym. Degrad. Stab.* 128 (2016) 39–45. <https://doi.org/10.1016/j.polymdegradstab.2016.02.029>.
- [49] S.W. Choi, J.R. Kim, S.M. Jo, W.S. Lee, Y.-R. Kim, Electrochemical and spectroscopic properties of electrospun PAN-based fibrous polymer electrolytes, *J. Electrochem. Soc.* 152 (2005) A989. <https://doi.org/10.1149/1.1887166>.
- [50] S.A. Smith, B.P. Williams, Y.L. Joo, Effect of polymer and ceramic morphology on the material and electrochemical properties of electrospun PAN/polymer derived ceramic composite nano fiber membranes for lithium ion battery separators, *J. Memb. Sci.* 526

- (2017) 315–322. <https://doi.org/10.1016/j.memsci.2016.12.052>.
- [51] Y.S. Kim, Y.L. Joo, Y.J. Kwark, Highly stable silicon-carbon-nitrogen composite anodes from silsesquiazane for rechargeable lithium-ion battery, *J. Mater. Sci. Technol.* 32 (2016) 195–199. <https://doi.org/10.1016/j.jmst.2015.12.019>.
- [52] M. Wilamowska, M. Graczyk-Zajac, R. Riedel, Composite materials based on polymer-derived SiCN ceramic and disordered hard carbons as anodes for lithium-ion batteries, *J. Power Sources.* 244 (2013) 80–86. <https://doi.org/10.1016/j.jpowsour.2013.03.137>.
- [53] V.S. Pradeep, M. Graczyk-Zajac, R. Riedel, G.D. Soraru, New insights in to the lithium storage mechanism in Polymer derived SiOC anode materials, *Electrochim. Acta.* 119 (2014) 78–85. <https://doi.org/10.1016/j.electacta.2013.12.037>.
- [54] Q. Wen, Z. Yu, R. Riedel, The fate and role of in situ formed carbon in polymer-derived ceramics, *Prog. Mater. Sci.* 109 (2020) 100623. <https://doi.org/10.1016/j.pmatsci.2019.100623>.
- [55] L.M. Reinold, M. Graczyk-Zajac, Y. Gao, G. Mera, R. Riedel, Carbon-rich SiCN ceramics as high capacity/high stability anode material for lithium-ion batteries, *J. Power Sources.* 236 (2013) 224–229. <https://doi.org/10.1016/j.jpowsour.2013.02.046>.
- [56] J. Kaspar, M. Graczyk-Zajac, R. Riedel, Lithium insertion into carbon-rich SiOC ceramics: Influence of pyrolysis temperature on electrochemical properties, *J. Power Sources.* 244 (2013) 450–455. <https://doi.org/10.1016/j.jpowsour.2012.11.086>.
- [57] M. Graczyk-Zajac, C. Fasel, R. Riedel, Polymer-derived-SiCN ceramic/graphite composite as anode material with enhanced rate capability for lithium ion batteries, *J. Power Sources.* 196 (2011) 6412–6418. <https://doi.org/10.1016/j.jpowsour.2011.03.076>.
- [58] M. Wilamowska, V.S. Pradeep, M. Graczyk-Zajac, R. Riedel, G.D. Soraru, Tailoring of SiOC composition as a way to better performing anodes for Li-ion batteries, *Solid State Ionics.* 260 (2014) 94–100. <https://doi.org/10.1016/j.ssi.2014.03.021>.
- [59] S. Wang, M.Z. Ashfaq, D. Qi, X. Yue, H. Gong, Electromagnetic wave absorption properties of polymer-derived magnetic carbon-rich SiCN-based composite ceramics, *Ceram. Int.* 48 (2022) 4986–4998. <https://doi.org/10.1016/j.ceramint.2021.11.036>.
- [60] Y. Zhao, Y. Zhang, C. Yang, L. Cheng, Ultralight and flexible SiC nanoparticle-decorated carbon nanofiber mats for broad-band microwave absorption, *Carbon N. Y.* 171 (2021) 474–483. <https://doi.org/10.1016/j.carbon.2020.09.040>.
- [61] X. Zhang, Z. Wang, L. Xu, K. Zuraiqi, T. Daeneke, Z. Yao, D.C. Qi, A. Zavabeti, Liquid metal derived MOF functionalized nanoarrays with ultra-wideband electromagnetic absorption, *J. Colloid Interface Sci.* 606 (2022) 1852–1865. <https://doi.org/10.1016/j.jcis.2021.08.143>.
- [62] X. Guo, Y. Feng, X. Lin, Y. Liu, H. Gong, Y. Zhang, The dielectric and microwave absorption properties of polymer-derived SiCN ceramics, *J. Eur. Ceram. Soc.* 38 (2018) 1327–1333. <https://doi.org/10.1016/j.jeurceramsoc.2017.10.031>.
- [63] B. Quan, X. Liang, G. Ji, Y. Cheng, W. Liu, J. Ma, Y. Zhang, D. Li, G. Xu, Dielectric polarization in electromagnetic wave absorption: Review and perspective, *J. Alloys Compd.* 728 (2017) 1065–1075. <https://doi.org/10.1016/j.jallcom.2017.09.082>.
- [64] K. Ge, L. Ye, W. Han, Y. Han, C. Xu, T. Zhao, Si(B)CN-doped carbon nanofibers with excellent oxidation resistance, *Mater. Lett.* 112 (2013) 124–128. <https://doi.org/10.1016/j.matlet.2013.08.122>.
- [65] M.A. Poothanari, J. Abraham, N. Kalarikkal, S. Thomas, Excellent Electromagnetic Interference Shielding and High Electrical Conductivity of Compatibilized Polycarbonate/Polypropylene Carbon Nanotube Blend Nanocomposites, *Ind. Eng. Chem. Res.* 57 (2018) 4287–4297. <https://doi.org/10.1021/acs.iecr.7b05406>.
- [66] H. Chen, Z. Huang, Y. Huang, Y. Zhang, Z. Ge, B. Qin, Z. Liu, Q. Shi, P. Xiao, Y. Yang,

- T. Zhang, Y. Chen, Synergistically assembled MWCNT/graphene foam with highly efficient microwave absorption in both C and X bands, *Carbon* N. Y. 124 (2017) 506–514. <https://doi.org/10.1016/j.carbon.2017.09.007>.
- [67] F. Fang, Y.-Q. Li, H.-M. Xiao, N. Hu, S.-Y. Fu, Layer-structured silver nanowire/polyaniline composite film as a high performance X-band EMI shielding material, *J. Mater. Chem. C* 4 (2016) 4193–4203. <https://doi.org/10.1039/C5TC04406E>.
- [68] X. Fang, L. Pan, J. Yao, S. Yin, Y. Wang, Q. Li, J. Yang, Controllable dielectric properties and strong electromagnetic wave absorption properties of SiC/spherical graphite-AlN microwave-attenuating composite ceramics, *Ceram. Int.* 47 (2021) 22636–22645. <https://doi.org/10.1016/j.ceramint.2021.04.277>.
- [69] L. Zhang, Y. Chen, Q. Liu, W. Deng, Y. Yue, F. Meng, Ultrathin flexible electrospun carbon nanofibers reinforced graphene microgasbags films with three-dimensional conductive network toward synergetic enhanced electromagnetic interference shielding, *J. Mater. Sci. Technol.* 111 (2022) 57–65. <https://doi.org/10.1016/j.jmst.2021.08.090>.
- [70] J. Cheng, H. Zhang, Y. Xiong, L. Gao, B. Wen, H. Raza, H. Wang, G. Zheng, D. Zhang, H. Zhang, Construction of multiple interfaces and dielectric/magnetic heterostructures in electromagnetic wave absorbers with enhanced absorption performance: A review, *J. Mater.* 7 (2021) 1233–1263. <https://doi.org/10.1016/j.jmat.2021.02.017>.
- [71] S. Widgeon, G. Mera, Y. Gao, E. Stoyanov, S. Sen, A. Navrotsky, R. Riedel, Nanostructure and energetics of carbon-rich SiCN ceramics derived from polysilylcarbodiimides: Role of the nanodomain interfaces, *Chem. Mater.* 24 (2012) 1181–1191. <https://doi.org/10.1021/cm2038238>.
- [72] Q. Liu, Q. Cao, H. Bi, C. Liang, K. Yuan, W. She, Y. Yang, R. Che, CoNi@SiO₂@TiO₂ and CoNi@Air@TiO₂ Microspheres with Strong Wideband Microwave Absorption, *Adv. Mater.* 28 (2016) 486–490. <https://doi.org/10.1002/adma.201503149>.
- [73] F. Dalcanale, J. Grossenbacher, G. Blugan, M.R. Gullo, A. Lauria, J. Brugger, H. Tevaearai, T. Graule, M. Niederberger, J. Kuebler, Influence of carbon enrichment on electrical conductivity and processing of polycarbosilane derived ceramic for MEMS applications, *J. Eur. Ceram. Soc.* 34 (2014) 3559–3570. <https://doi.org/10.1016/j.jeurceramsoc.2014.06.002>.
- [74] W. Li, M. Li, K.R. Adair, X. Sun, Y. Yu, Carbon nanofiber-based nanostructures for lithium-ion and sodium-ion batteries, *J. Mater. Chem. A* 5 (2017) 13882–13906. <https://doi.org/10.1039/C7TA02153D>.
- [75] C. Haluschka, C. Engel, R. Riedel, Silicon carbonitride ceramics derived from polysilazanes Part II. Investigation of electrical properties, *J. Eur. Ceram. Soc.* 20 (2000) 1365–1374. [https://doi.org/10.1016/S0955-2219\(00\)00009-1](https://doi.org/10.1016/S0955-2219(00)00009-1).
- [76] J. Cordelair, P. Greil, Electrical conductivity measurements as a microprobe for structure transitions in polysiloxane derived Si-O-C ceramics, *J. Eur. Ceram. Soc.* 20 (2000) 1947–1957. [https://doi.org/10.1016/S0955-2219\(00\)00068-6](https://doi.org/10.1016/S0955-2219(00)00068-6).
- [77] Y. Feng, G.-X. Du, X.-J. Zhao, E.-C. Yang, Preparation and electrochemical performance of SiCN–CNTs composite anode material for lithium ion batteries, *J. Appl. Electrochem.* 41 (2011) 999–1002. <https://doi.org/10.1007/s10800-011-0322-z>.
- [78] B. Du, C. He, J. Qian, M. Cai, X. Wang, A. Shui, Electromagnetic wave absorbing properties of glucose-derived carbon-rich SiOC ceramics annealed at different temperatures, *J. Am. Ceram. Soc.* 102 (2019) 7015–7025. <https://doi.org/10.1111/jace.16549>.
- [79] Y. Bai, F. Qin, Y. Lu, Lightweight Ni/CNT decorated melamine sponge with sensitive strain sensing performance for ultrahigh electromagnetic absorption in both GHz and THz bands, *Chem. Eng. J.* 429 (2022) 132393.

<https://doi.org/10.1016/j.cej.2021.132393>.

7 LIGHTWEIGHT SiCN/C FIBERS FOR MICROWAVE ABSORPTION AND ELECTROMAGNETIC FIELD SHIELDING IN K_u-BAND⁵

SiCN ceramics have been increasingly researched as electromagnetic field (EMF) absorbing materials for application in harsh environments, but studies on the role of carbon in SiCN ceramics for excellent EMF absorbing properties are still lacking. Here, SiCN fibers containing *in-situ* generated nanosized carbon structures (SiCN/C) were prepared by electrospinning polysilazane and polyacrylonitrile with subsequent pyrolysis in nitrogen atmosphere. The phases and microstructures of SiCN and SiCN/C fibers were characterized and their influences on EMF shielding properties in K_u-band (12.4-18 GHz) were investigated using 2-port VNA rectangular waveguide aperture and Nicolson-Ross-Weir (NRW) method. At 16.9 GHz, the SiCN/C fibers showed higher relative complex electrical permittivity ($\epsilon' = 5.8$ and $\epsilon'' = 2.1$) compared to SiCN ($\epsilon' = 3.2$ and $\epsilon'' = 0.15$). The EMF absorption was increased by ~179% with the addition of carbon in the SiCN matrix. Computational simulations clarified the better features of SiCN/C in electromagnetic shielding compared to SiCN. The favorable microwave absorption ability was ascribed to three aspects including enhanced conduction loss derived from the conductivity of free carbon, dipole and interfacial polarization loss generated by defects, and multiple reflection loss enhanced by a hierarchical network from the electrospun fibers. Moreover, the addition of carbon precursor represented a weight decrease of 17% for SiCN/C fibers compared to SiCN fibers. This research will afford an alternative solution for the manufacturing of SiCN/C fibers with EMF absorption properties that can be used as lightweight materials for stealth applications under harsh environments or also for electromagnetic absorber materials used in electromagnetic compatibility and immunity test applications.

7.1 INTRODUCTION

With the accelerated development in electronic and information technology devices, research on materials that can attenuate EMF interference has received a lot of effort [1,2]. Among the Si-based PDCs, SiCN ceramics have attracted considerable attention in the last few decades due to their higher temperature and oxidation stability compared respectively to SiCO and SiC ceramics [3–5]. There are at present two strategies adopted to improve the EMF

⁵Based on a paper to be submitted for publication.

shielding capabilities of PDC materials: combining dielectric and magnetic components or designing their microstructures [6]. Some progress of polysilazane-derived ceramics as EMF absorbing materials include SiCN [7–9], SiCN/Co [10], SiCN/Fe [11,12], SiCN/Ni [13], SiCN/reduced graphene oxide [14], SiC/graphitic carbon/SiCN [15], SiCN/CNTs [15], and PVDF/SiCN particles [16]. The manufacturing of SiCN fibers could broaden their application as lightweight materials with higher surface area for stealth applications under harsh environments.

The manufacturing of SiCN fibers could broaden their application as lightweight materials with higher surface area for stealth applications under harsh environments. Most of the published research is focused on SiC fibers [17–22], while studies on polysilazane-derived SiCN fibers with EMF absorption properties are scarce. Moreover, the magnetic loss is usually introduced in SiCN fibers by adding ferric and nickel compounds [23–27], which in turn can result in high weight density, easy corrosion, difficult treatment, and high cost [28]. The effects of carbon on SiCN fibers remain to be addressed to provide a new way to design high-efficiency EMF absorbers.

Although there are many contributions in the literature of studies exploring materials applied to electromagnetic field shielding, there is a limitation of the method itself that will only work in practical situations if the conditions are replicated. The insertion of the metal panel in the measurement setup allows some simplifications in Maxwell's equations [29], thus leading to analytical calculations that are easy to implement but of little practical use. In such cases, computer simulation studies are best suited to evaluate the material's behavior in more real-life situations using the measured characteristics.

This work aims to investigate the microwave absorption and EMF shielding of SiCN/C electrospun fibers. Combining electrospinning and the PDC route, SiCN fibers containing in-situ generated nanosized carbon structures were prepared and tested for microwave absorption and EMF shielding in K_u-band (12.4-18 GHz). For comparison, SiCN fibers were also manufactured. Polysilazane was used as the precursor of SiCN and PAN was added to the solution to improve the electrospinnability of the preceramic polymer and also as a carbon source. The fibers were investigated according to their relative complex electrical permittivity, total shielding effectiveness (SE) absorption, and reflection loss, and the improved performance of SiCN/C fibers was related to the material microstructure.

7.2 EXPERIMENTAL

The solutions were prepared by dissolving polysilazane, PAN, and 3 wt.% DCP in DMF, which were further electrospun in inert atmosphere. The precursor mats were pyrolyzed in a tube furnace from 20 °C to 1200 °C with a heating rate of 5 °C min⁻¹ for 1 h in nitrogen atmosphere. The details of solutions and electrospinning for the manufacturing of SiCN and SiCN/C fiber mats are presented (Table 7.1). After pyrolysis, the mats were macerated to obtain SiCN and SiCN/C fibers.

Table 7.1 – Details of solution characteristics and operating conditions of electrospinning for manufacturing SiCN and SiCN/C fibers

Name	Solution characteristics		Operating conditions of electrospinning		
	Polymer concentration in DMF (wt.%)	PAN concentration (wt.%)	Voltage (kV)	Feed rate (ml h ⁻¹)	Tip-to-collector-distance (cm)
SiCN	60	0	27	1	19.5
SiCN/C	17.5	40	21	0.8	23.5

The thermal stability of the as-spun fibers was measured with TGA equipment (STA 449 F5 Jupiter, Netzsch GmbH, Germany). The IR transmissivity of the fibers was tested on FTIR equipped with an ATR unit (Tensor 27, Bruker, USA). The morphology of the fibers was characterized by transmission electron microscopy (TEM) with an acceleration voltage of 80 kV (JEM-1011, JEOL, Germany). The elemental composition was analyzed with EDS (Octane Elect EDS System EDAX, Ametek, USA). The density of the fibers was determined by helium pycnometry (AccuPyc II 1340, Micromeritics, USA). The surface area was determined via krypton adsorption using Brunauer-Emmett-Teller theory (ASAP 2010, Micromeritics, USA). The carbon structure phases were identified through XRD (D8 Advance, Bruker, USA) using monochromatic CuK α radiation ($\lambda = 1.5418 \text{ \AA}$, 40 mA and 40 kV) and Raman spectroscopy with a 532 nm wavelength laser (Senterra II, Bruker, USA). The Raman curves were shaped according to Lorentzian fitting (adjusted $R^2 \geq 0.9$) and the crystallite size (L_a) was determined according to the Tuinstra-Koenig-correlation [30]. The I_D/I_G and $I_D/I_{D'}$ ratios were calculated based on the height of each peak after curve fitting. The phases present in the SiCN fibers were evaluated by solid-state ²⁹Si-NMR (Bruker AVANCE II 300, Bruker, USA) and the spectra were [0,1] normalized for comparison.

The SiCN and SiCN/C fibers were mixed with silicone (5 wt.% fibers) and molded into rectangular samples (10.16-22.86 mm) with different thicknesses ranging from 2 mm to 4.5 mm (Figure 7.1). Silicone is an insulating material that is transparent to the electromagnetic field. The scattering parameters (S-parameters) and reflection losses were collected in a vector network analyzer (VNA) (N5230C-PNA-L, Agilent Technologies, USA) employing the rectangular waveguide propagation setup in K_u -band (Figure 7.2).

Figure 7.1 – Schematic diagram of preparing SiCN and SiCN/C samples to be tested for microwave absorption and EMF shielding

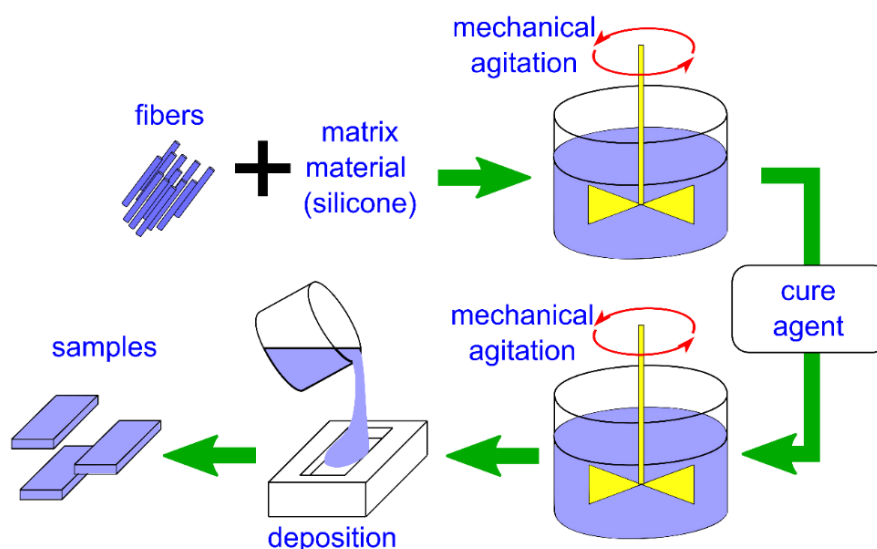
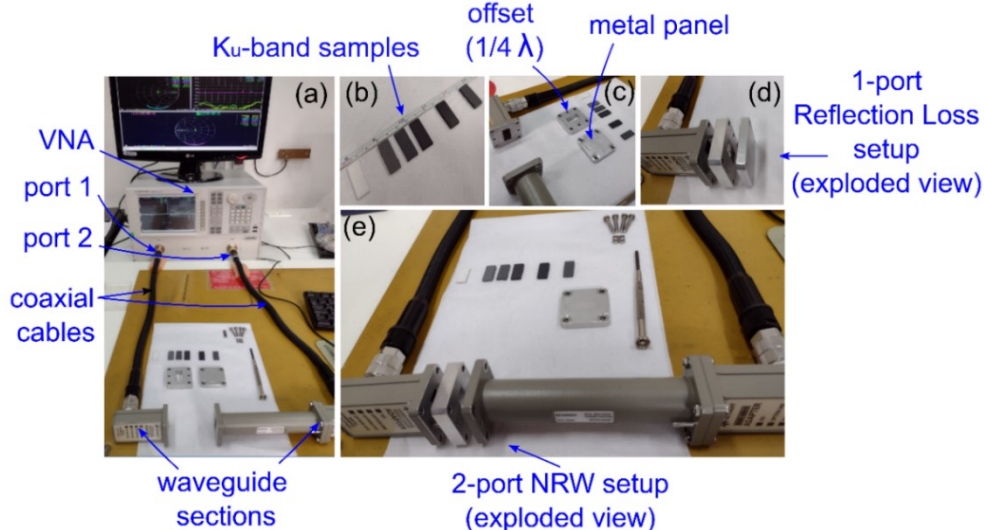


Figure 7.2 – Images of the N5230C-PNA-L VNA and accessories for electromagnetic measurements in K_u -band guided wave testing. (a) Equipment overview, (b) picture of samples, (c) picture of the coaxial cable connected at the coaxial to waveguide transition. Two metal panels are shown, the offset plate, which is cast in rectangular form with the dimensions for guided K_u -band testing (10.16 mm high by 22.86 mm wide) and the metal panel, (d) exploded view of the experimental setup for reflection loss testing, and (e) exploded view of the setup applied for NRW testing.



The transmission/reflection measurement techniques evaluated through a rectangular waveguide is a non-resonant method using a 2-port measurement, which has a radiation/sensing area much greater than that of a coaxial probe [31]. Based on the S-parameters measurements, the NRW method was used to calculate the relative complex permittivity and electrical loss tangent. The VNA equipment was calibrated according to the transmission reflection-line method provided by the equipment supplier. The impedance matching condition of the instrument ports was defined with a reference value set at 50 Ω . The equations related to data conversion are available in the supplementary material of this work. To diminish the influence of possible air gap spaces and to mitigate positioning misalignment influence, three samples for each measurement were prepared and the corresponding errors are reported. The reflection losses were obtained using the 1-port reflection loss setup, commonly used in the literature for both rectangular and coaxial waveguide cross-sections.

Computational electromagnetic calculations were developed using FEKO® software (Altair, USA) based on the materials' properties obtained experimentally. Introductory electromagnetic scattering calculations in free space including the radar cross-section (RCS) study were computed [32]. The complex electrical permittivity (ϵ) in a dispersive, homogeneous, and isotropic material medium is expressed (Equation 7.1),

$$\epsilon(\omega) = \epsilon_0 \epsilon_r(\omega) = \epsilon_0 [\epsilon_r'(\omega) - j\epsilon_r''(\omega)] = \epsilon_0 \epsilon_r'(\omega) [1 - j \tan(\delta_e(\omega))] \quad (7.1)$$

where ϵ_0 is the electric permittivity in vacuum, ϵ_r is the relative complex electrical permittivity, ϵ_r' and ϵ_r'' are respectively the real and imaginary parts of the relative complex electrical permittivity. The electrical tangent loss term, $\tan[\delta_e(\omega)] = \epsilon_r''(\omega)/\epsilon_r'(\omega)$, directly relates the imaginary and real components of the permittivity and measures the inherent dissipation energy due to electrical losses. The term $\omega = 2\pi f$ is the angular frequency ($\text{rad}\cdot\text{s}^{-1}$) with f being the frequency in Hz. The reflection loss considering the slab ended by a conduction plane in dB is given (Equation 7.2), where S_{11} is the scattering parameter obtained from VNA measurements (observed from port 1 of the waveguide), z_{in} is the input impedance, and z_0 is the reference to the impedance load.

$$\text{RL}_{\text{dB}}(\omega) = 20 \log_{10}[S_{11}(\omega)] = 20 \log_{10} \left[\frac{z_{\text{in}}(\omega) - z_0}{z_{\text{in}}(\omega) + z_0} \right] \quad (7.2)$$

The equation for SE related directly to the scattering parameters in dispersive and reciprocal media is given (Equation 7.3)[124],

$$\begin{aligned} SE_{TdB}(\omega) &= 10\log_{10} \left[\frac{1}{1-|S_{11}(\omega)|^2} \right] + 10\log_{10} \left[\frac{1-|S_{11}(\omega)|^2}{|S_{12}(\omega)|^2} \right] \\ SE_{TdB}(\omega) &= SE_{RdB}(\omega) + SE_{AdB}(\omega) \end{aligned} \quad (7.3)$$

where $SE_T(\omega)$, $SE_R(\omega)$, and $SE_A(\omega)$ represent respectively total, reflected, and absorbed shielding effectiveness and the scattering term $S_{12} = S_{21}$ in reciprocal media. The RCS is a far-field parameter employed to characterize the scattering properties of a radar target. For three-dimensional objects, the RCS can be calculated considering the spherical coordinate system (Equation 7.4),

$$\sigma_{RCS}(r, \theta, \phi) = \lim_{r \rightarrow \infty} \left[4\pi r^2 \frac{\vec{S}_e(r, \theta, \phi)}{\vec{S}_i(r, \theta, \phi)} \right] = \lim_{r \rightarrow \infty} \left[4\pi r^2 \frac{|\vec{E}_e(r, \theta, \phi)|^2}{|\vec{E}_i(r, \theta, \phi)|^2} \right] \quad (7.4)$$

where r is the distance between the target object and the observer, $\vec{S}_e(r, \theta, \phi)$ is the scattered power spectral density, $\vec{S}_i(r, \theta, \phi)$ is the incident power spectral density (or the incident Poynting vector), $\vec{E}_e(r, \theta, \phi)$ is the scattered electric field intensity vector, and $\vec{E}_i(r, \theta, \phi)$ is the incident electric field intensity vector. The unit of $\sigma_{RCS}(r, \theta, \phi)$ is m^2 , although the RCS is also commonly presented in dBsm (decibel squared milliwatt) (Equation 7.5),

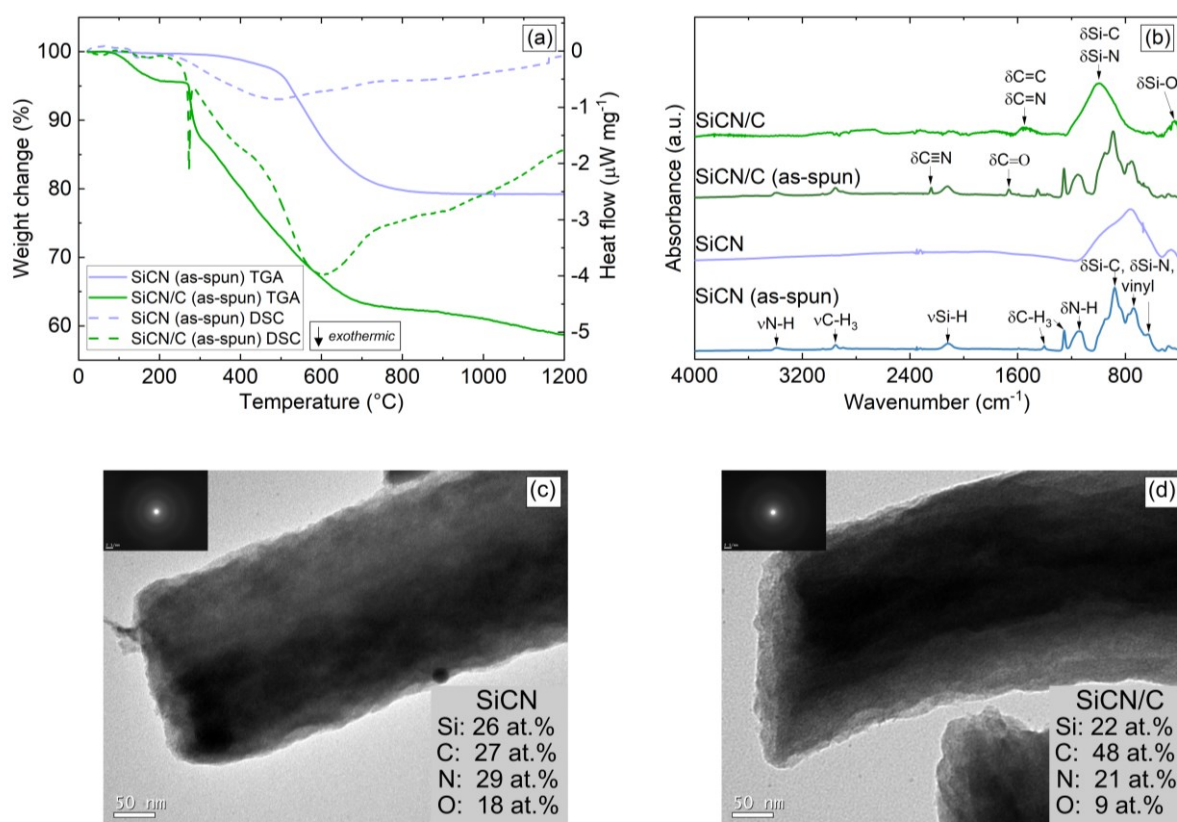
$$\sigma_{RCS_{dBsm}}(r, \theta, \phi) = 10 \log_{10}[\sigma_{RCS}(r, \theta, \phi)] \quad (7.5)$$

7.3 RESULTS AND DISCUSSION

After electrospinning, the polymer fiber mats were pyrolyzed and SiCN and SiCN/C fibers were manufactured. Figure 7.3(a) shows that during pyrolysis, the polysilazane and PAN suffered respectively crosslinking/ceramization and carbonization with mass loss. The TGA curves mainly included two parts: the first part is $\sim 200-500^\circ\text{C}$ corresponding to cyclization of PAN and the removal of organic side groups of the preceramic polymer, and the second part is $\sim 500-800^\circ\text{C}$ owing to pyrolysis of polysilazane and decomposition of PAN. At 1200°C , the final ceramic yield of SiCN and SiCN/C was 79% and 59%. The addition of PAN reduced the

final material yield with the largest weight change occurring between ~ 200 - 600°C associated with the self-crosslinking process that occurred between Si-H groups from the polysilazane with N-functionalities from PAN, the cyclization and decomposition of PAN (at 273°C and 609°C according to DSC curve), and the escape of hydrogen [33,34]. After the cyclization of PAN, it is supposed that aromatic structures are obtained, forming carbon domains inside the SiCN matrix. For the SiCN sample, the largest weight change occurred between ~ 500 - 650°C , as also observed by the broad peak in the DSC curve, when the preceramic changed to amorphous SiCN ceramic characterized by degradation of organic substituents and release of volatile hydrocarbons, volatile silicon products, hydrogen, and small quantities of ammonia [35]. The ceramization was also observed for the SiCN/C sample in this temperature range (~ 500 - 650°C). The initial weight change is attributed to the loss of low-molecular-weight oligomers from polysilazane and DMF volatilization that did not evaporate during electrospinning and adhered to the fibers.

Figure 7.3 – (a) Curves of TGA and DSC, (b) FTIR-ATR spectra, and TEM images with respective SAED and elemental composition according to EDS results of (c) SiCN and (d) SiCN/C fibers



The polymer-to-ceramic transformation and carbonization were confirmed through FTIR-ATR spectra (Figure 7.3(b)). The wide peak observed between ~ 770 - 1058 cm^{-1} was attributed to the formation of SiCN structure derived from the polysilazane [36]. For SiCN/C fibers, the band at $\sim 1550\text{ cm}^{-1}$ was ascribed to C=C and C=N derived from PAN [34,37]. The appearance of the peak $\sim 446\text{ cm}^{-1}$ was assigned to the formation of Si-O caused probably by the reaction of polysilazane to oxygen contamination during solution preparation [38,39]. According to a previous work of the authors, electrospun fibers in the range of 500-1500 nm are produced [40]. After macerating, very thin fibers with a diameter up to 242 nm were obtained according to TEM images exhibited in Figure 7.3(c) and Figure 7.3(d). The corresponding selected area electron diffraction (SAED) patterns exhibited a diffuse ring characteristic for an amorphous material. The fibers can be considered lightweight materials with 2.58 ± 0.08 and $2.14 \pm 0.04\text{ g cm}^{-3}$ respectively for SiCN and SiCN/C. The addition of carbon precursor represented a weight decrease of 17% for SiCN/C fibers compared to SiCN fibers. Furthermore, the surface area was increased by 84%, which was determined as $2.66\text{ m}^2\text{ g}^{-1}$ and $4.91\text{ m}^2\text{ g}^{-1}$ respectively for SiCN and SiCN/C. EDS results indicated the presence of SiCN with some oxygen contamination, as already suggested by FTIR-ATR analyses. The addition of carbon precursor reduced the silicon and nitrogen contents, however, the carbon amount was increased. As expected, the SiCN/C showed a higher carbon content with 48 at.% compared to 27 at.% of SiCN fibers.

According to Figure 7.4, the ^{29}Si -NMR spectra displayed five peaks at chemical shifts of -14, -19, -31, -48, and -65 ppm corresponding respectively to SiN_2C_2 , SiC_4 , SiN_3C , SiN_4 , and SiN_3O units. In contrast to SiCN which is composed of different silicon environments due to a lower amount of carbon, SiCN/C fibers showed a preferential formation of amorphous SiN_4 environments due to the additional formation of Si-N bonding resulting from the reaction between polysilazane and PAN as discussed previously.

The XRD peaks of SiCN and SiCN/C fibers showed diffuse scattering indicating an amorphous material (Figure 7.5a), which is in accordance with TEM results. The XRD pattern of SiCN/C displayed two peaks at $\sim 24^\circ$ and $\sim 43^\circ$ which correspond respectively to the reflections of the (0 0 2) and (1 0 0) peaks related to carbon segregations within the SiCN microstructure [41]. According to Bragg's equation, the signal at 24° corresponds to the interlayer distance of graphite with some carbon phase composed of graphitic carbon [42]. The peak at 43° originated from arbitrary diffraction related to graphene sheets, a characteristic of amorphous and disordered carbons [43]. The XRD pattern of SiCN showed a very weak signal

at 24° , indicating that no noticeable amount of graphitic carbon was formed. Moreover, the diffraction peaks are broad, also suggesting a more amorphous structure than SiCN/C fibers, which corresponds with the SiCN structure in previous research [44–46]. In SiCN/C, the graphite peak at $\sim 24^\circ$ covered the amorphous peak of SiCN material. Since the intensity of the graphitic signal is not sharp, the free carbon phase is predominantly composed of a mixture of disordered carbon, nano-crystalline graphite, and graphene sheets.

Figure 7.4 – Solid-state Si-NMR of SiCN and SiCN/C fibers

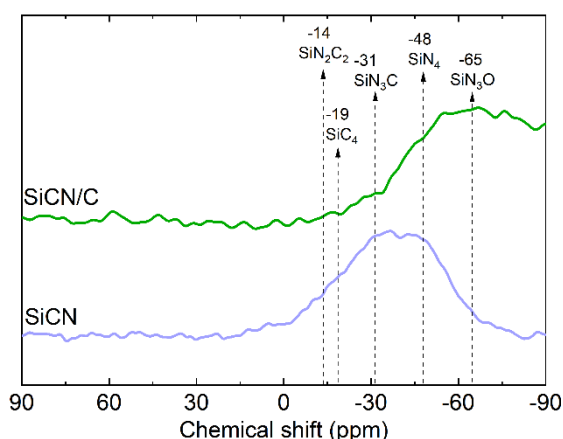
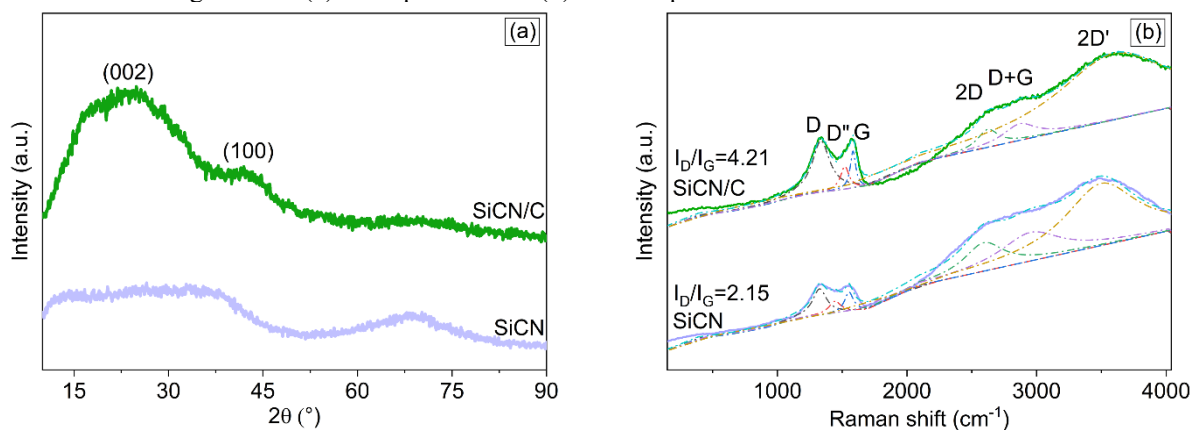


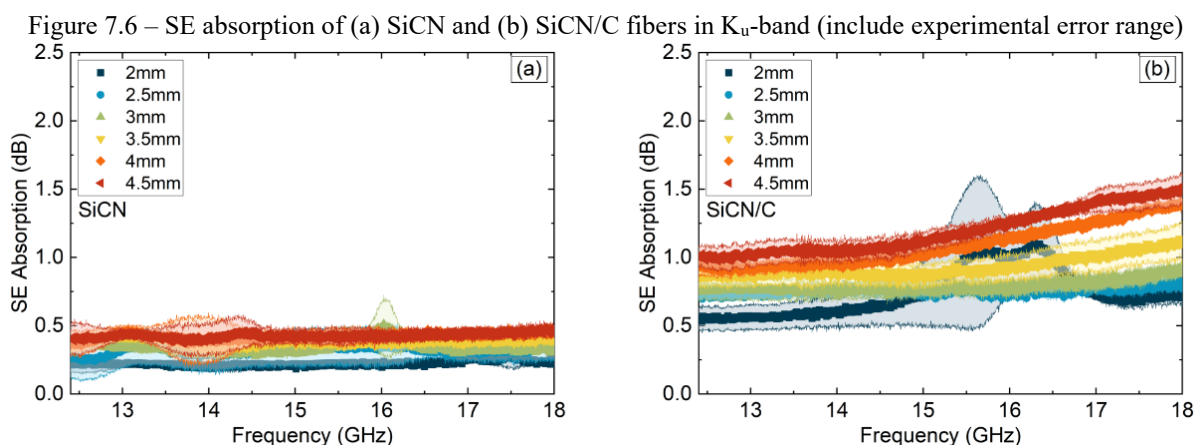
Figure 7.5 – (a) XRD patterns and (b) Raman spectra of SiCN and SiCN/C fibers



In the Raman spectra of the fibers, some bands were identified including the D-band ($\sim 1330\text{ cm}^{-1}$, representing carbon defects and disorder), D'-band ($\sim 1482\text{ cm}^{-1}$, representing amorphous carbon) and G-band ($\sim 1568\text{ cm}^{-1}$, representing the graphitic structure), along with another two second-order bands corresponding to the 2D- ($\sim 2700\text{ cm}^{-1}$ representing the degree of organization of the graphene layers), D+G ($\sim 2945\text{ cm}^{-1}$ representing the disturbed graphitic structures) and 2D'-bands ($\sim 3460\text{ cm}^{-1}$ representing the disordered graphitic lattice) (Figure 7.5b) [42,47]. These indicated that both defective amorphous and ordered carbon existed in the

fibers. The existence of segregated free carbon is outlined by the presence of more intense D- and G-bands in the Raman spectra of SiCN/C. These were also identified in SiCN to a lesser extent due to free carbon forming from methyl and vinyl groups present in polysilazane. The intensity ratio of the D- to the G-band (I_D/I_G) was respectively 1.35 and 1.38 for SiCN and SiCN/C. The low values of I_D/I_G indicated that the graphitization degree of carbon was low and the degree of the disordered amorphous state of carbon is high, which is consistent with the XRD data. Another work also reported that the thermal evolution of disordered carbon into higher organized derivatives is slowed down with the addition of graphite to oligosilazane [48]. According to the TK-correlation, the crystallite size was calculated as 3.67 nm and 3.58 nm respectively for SiCN and SiCN/C indicating the nanostructured nature of the ceramics. This indicated that the SiCN/C fibers have a lower degree of microstructural order compared to SiCN fibers [49]. This was also observed with the increase of D-band width with the addition of carbon precursor (from 134 cm^{-1} to 166 cm^{-1}). Additionally, the I_D/I_D' ratios were similar i.e. 2.17 for SiCN and 2.23 for SiCN/C, suggesting carbon amorphousness at the edge and the surface of graphitic crystallites [30].

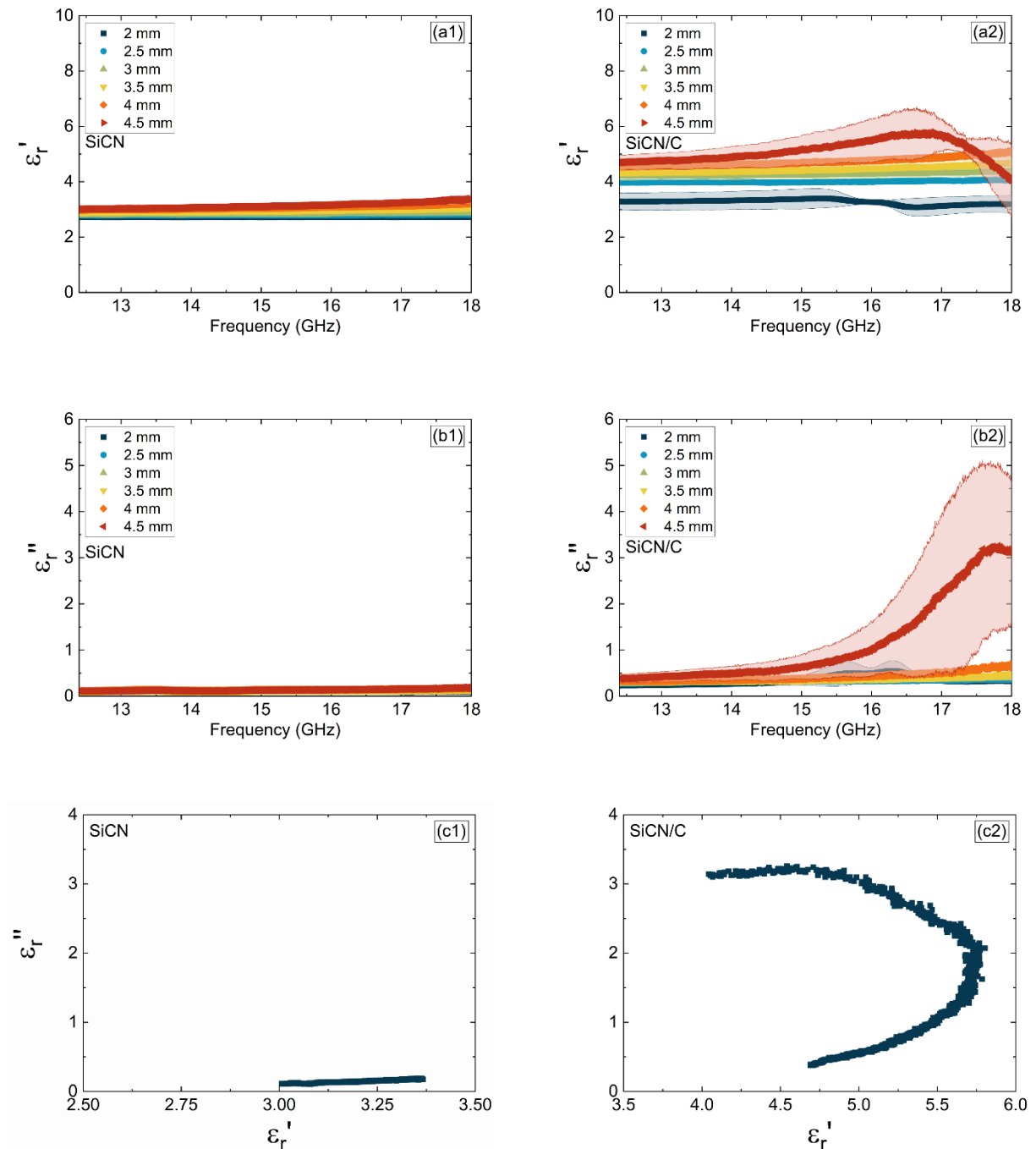
The EMF shielding mechanisms of a conductive shielding material include reflection, absorption, and multiple reflections. Multiple reflections are the reflections between the internal surfaces of the shielding material. The absorption of EMF radiation is how matter, typically electrons bound in atoms, takes up a photon's energy and so transforms electromagnetic energy into internal energy. The SiCN/C fibers increased the microwave absorption in the whole K_u -band compared to SiCN fibers (Figure 7.6). With a 4.5 mm thickness, the SE absorption of the SiCN/C fibers ranged from 1 dB to 1.5 dB, while the SiCN fibers ranged from 0.41 dB to 0.47 dB. This represents an increase of about 179% in microwave absorption of SiCN/C compared to SiCN fibers.



The EMF shielding of a material is highly dependent on its relative complex electrical permittivity ($\epsilon_r = \epsilon_r' - j\epsilon_r''$) and relative complex magnetic permeability ($\mu_r = \mu_r' - j\mu_r''$). Since magnetic shielding is not present in the fibers, the values of the real and imaginary part of permeability are approximately 1 and 0 respectively [50]. Therefore, the EMF shielding performance of the fibers is mainly determined by the permittivity. According to the Debye theory, the real part of the permittivity ($\epsilon' = \epsilon_0\epsilon_r'$) is related to dielectric storage and the imaginary part of the electrical permittivity ($\epsilon'' = \epsilon_0\epsilon_r''$) represents the dielectric loss [51]. The presence of free carbon in SiCN/C fibers enhanced the permittivity of fibers when compared to SiCN fibers, mainly for dielectric storage (Figure 7.7a and Figure 7.7b). The ϵ_r' and ϵ_r'' values of SiCN fibers remained constant at respectively ~ 3 and ~ 0.13 over frequency and sample thickness. On the other hand, the ϵ_r' values of SiCN/C fibers increased with the thickness from 3.38 (2 mm) to 5.15 (4.5 mm) at 15 GHz. Similarly, the ϵ_r'' values of SiCN/C fibers also increased with the thickness with a maximum value of 3.26 (4.5 mm). The ϵ_r'' curve of SiCN/C fibers with 4.5 mm showed a broad error, however, the curve follows the trend observed in SE absorption, confirming that the mean values are correct and the broad error is attributed to a limitation of the NRW method [52].

The losses of a microwave absorber come mainly from dielectric loss and magnetic loss mechanisms. The dielectric loss is derived from the hysteresis effect which occurs due to the electrical polarization and conduction processes in the presence of alternating electromagnetic fields. Upon increasing the EM frequency, the polarizability cannot be maintained and some corresponding hysteresis phenomena occur during this process, called polarization relaxation [53]. Thus, the plot of ϵ_r' versus ϵ_r'' would be a single semicircle, denoted as the Cole-Cole semicircle corresponding to one Debye relaxation process [54]. The dielectric loss is associated with both conductive loss dependent on electrical conductivity, and polarization loss originating from the ionic, electronic, dipole, and interfacial polarizations [28]. Since ionic and electronic polarizations occur at much higher frequencies (10^3 - 10^6 GHz) [6,56], dipole and interfacial polarization influenced the electrical permittivity.

Figure 7.7 – (a) Real (ϵ_r'), (b) imaginary (ϵ_r'') components of the complex permittivity obtained experimentally by the NRW method (include experimental error range) and (c) Cole-Cole curves of SiCN and SiCN/C fibers (4.5 mm) in the K_v-band frequency range

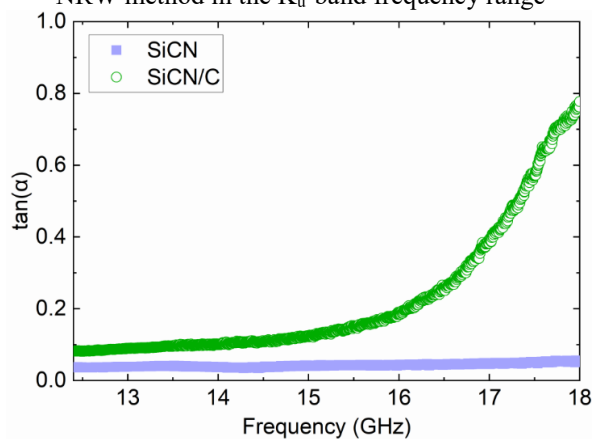


The polarization loss and conduction loss promoted the dielectric loss together. Under the action of the external alternating electric field, the SiCN/C fibers generated an induced current due to the formation of a continuous conductive network, which converts the EMF energy into heat energy by conduction loss mechanism. No semicircle was identified for SiCN (Figure 7.7c1), however, the SiCN/C had one Cole-Cole complete semicircle (Figure 7.7c2),

indicating that there is one polarization center. The defect density in the carbon structure present in SiCN/C fibers restricted the transmission of free electrons, leading to asymmetric charge distribution, which induced dipole and interfacial polarization due to lower crystallite size under the electromagnetic field [17,18,56,57]. Recently, the Cole-Cole plot also indicated that carbon nanofibers-SiBCN ceramics showed strong polarization capability due to the defect-rich structure of carbon [59]. The free carbon as a class of high conductive phase determined fibers' conductivity, which has an important influence on impedance matching. Carbon transformed part of electromagnetic field energy into heat energy through dipole orientation polarization occurring at carbon defects and consuming electromagnetic energy. Since Si_xN_y is transparent to electromagnetism, its incorporation increased interfaces and enhanced impedance matching of SiCN/C fibers [53]. Multiple reflection loss resulting from a hierarchical network built by the fibers also enhanced the loss mechanisms.

The $\tan(\alpha)$ values provided a measure of EMF energy lost compared with total EMF energy stored. The higher $\tan(\alpha)$ values in the SiCN/C fibers indicated that more electromagnetic energy is consumed suggesting better EMF dissipation ability than SiCN fibers (Figure 7.8).

Figure 7.8 – Tangent of electrical losses of SiCN and SiCN/C fibers (4.5 mm) obtained experimentally by the NRW method in the K_u-band frequency range

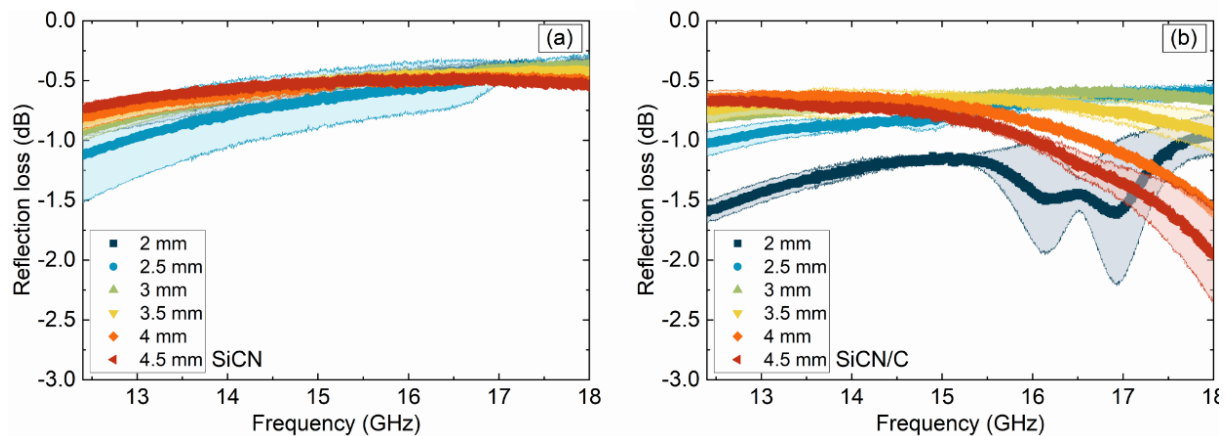


The reflection loss was calculated from the permittivity and samples' thickness to evaluate the EMF shielding of absorbers. A minimum reflection loss of -1.97 dB is observed for SiCN/C fibers with a thickness of 4.5 mm at 18 GHz (Figure 7.9). Furthermore, the SiCN/C fibers with a thickness of 2 mm showed a broad EMF shielding bandwidth with a reflection loss ranging from -0.96 dB to -1.6 dB. In contrast, SiCN fibers showed a minimum reflection loss of -1.13 dB at 12.4 GHz. The SiCN/C is thus a promising candidate as an EMF shielding

material, due to the electrically conductive phase (graphite carbon) scattered in an amorphous SiCN matrix. Free carbon in polymer-derived SiCN played a dominating role in the improved dielectric properties, which is in accordance with the literature [7]. The conductive network formed by the free carbon dispersed in the SiCN matrix provided a transmission channel for electrons, which significantly improved the attenuation of electromagnetic waves. Moreover, the addition of carbon precursor in the ceramic introduced more defects into the material, which increased the distribution of dipoles and enhanced the dipole polarization under the electromagnetic field.

Regarding the dielectric behavior, the SiCN/C achieved both the enhancement of the polarization effect and the introduction of conduction loss. Firstly, the combination of SiCN and carbon enabled the material with improved polarization loss, which is ascribed to the dipole and interfacial polarization caused by the residual bonds and defects in free carbon. Secondly, the introduction of carbon provided conduction loss. Thirdly, the interlaced network created by the fibers provided platforms for multiple scattering of the incident electromagnetic field, which increased the transmission process within the material.

Figure 7.9 – Reflection loss of (a) SiCN and (b) SiCN/C fibers in K_u-band (include experimental error range)



In the literature, the reflection loss properties are normally calculated according to the metal backup panel model (see the 1-port reflection loss setup in Figure 7.2(d)) to predict the EMF shielding for an idealized measurement with masked effects, i.e. reflection loss as a combined effect of material, thickness, and geometry. The metal backplane allows the total reflection of the EMF incident into the material which passes through the multiple reflections, absorption and loss inside the material. This phenomenon implies in the EMF phase destructive cancelation at some specific frequency and finally, the vanishing value of the input reflection

coefficient occurs. Thus, a kind of ‘destructive interferometric EMF effect’ can be seen inside the material from the point of view of the input reflection coefficient. This effect does not necessarily depend on the absorbent characteristics of the material but on the ability to engineer the actual real component of electrical permittivity to cause a null value at the input reflection coefficient at some specific frequency in a given thickness of a slab material media. Such an analogous effect is referred to as the quarter-wavelength transformer that is popular in transmission line design. It is important to highlight that the quarter-wavelength transformer approach can also be applied for multilayer slab material media including loss and lossless dielectric materials [59].

The high reflection losses commonly reported in the literature are thus the outcome of an approach of theoretical analysis with narrow practical applications. The evaluation of reflection loss with a metal panel is valid for scientific purposes, but will not work in most practical applications unless one replicates the same conditions including the metal panel that promotes the total reflection of the electromagnetic waves, which in turn is limited and impractical for example in applications that consider the reduction of the total weight of the system. A numerical simulation study is hereafter performed to fill this gap and contribute to the literature for new discussions on ceramic fibers applied to EMF shielding.

The free space scattering radiation performance of an object describes how energy is scattered when an object is exposed to a plane wave electromagnetic incident field [32]. One approach to verify it is based on scattered RCS analysis that is related to the electromagnetic scattering reflected from some particular object (see the supplementary information for details). The three-dimensional (3D half sphere) RCS simulated results using experimental electromagnetic properties from SiCN/C were calculated assuming the frequencies of $f = 12.4$ GHz, $f = 15.2$ GHz, and $f = 18.0$ GHz (Figure 7.10). At the normal EMF incidence angle, the maximum RCS values obtained were 13.69 dBsm, 15.74 dBsm and 17.12 dBsm at frequency values of $f = 12.4$ GHz, $f = 15.2$ GHz and $f = 18.0$ GHz, respectively. The main RCS lobe amplitude is enhanced when the electromagnetic wave frequency increases as well the number of lateral RCS side lobes also increase due to the increments in the frequency of the wave excitation.

Figure 7.10 – Computational results of RCS scattering study in free space. a) Numerical computation of the far-field spectral diagram of radiation scattering RCS from SiCN/C at the frequency of 12.4 GHz, b) 15.2 GHz, and c) 18.0 GHz. d) Computational setup illustration for the far-field spectral diagram of radiation scattering

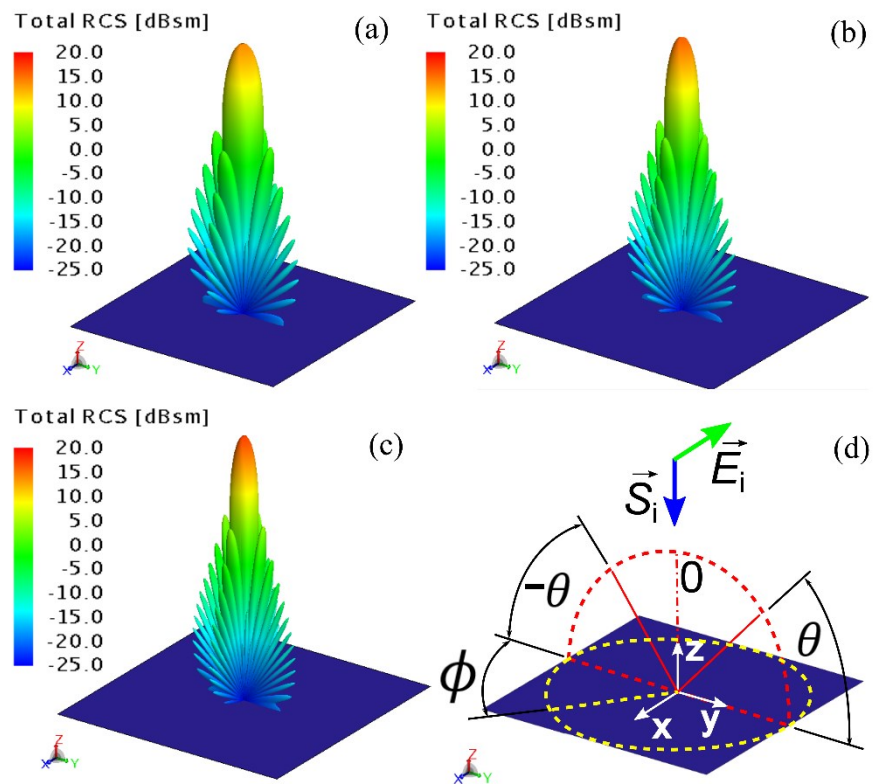
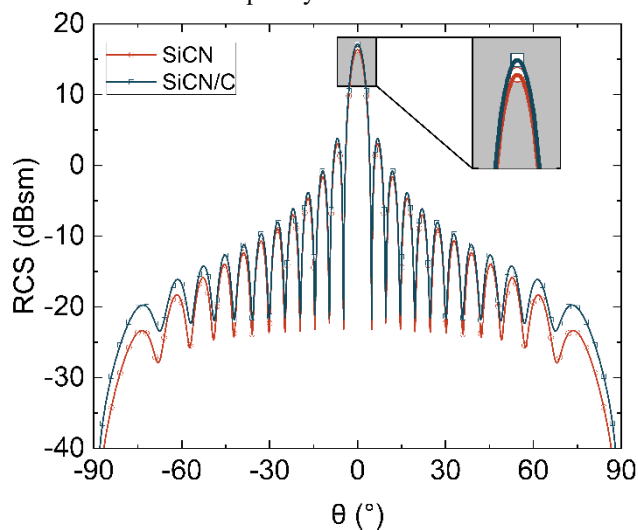


Figure 7.10(d) shows the simulated target applied to the computational scattering study. The computational target was defined with a thickness of 4.5 mm and 200 mm of side length. In the picture, the green arrow represents its polarization vector direction (i.e. the incident electric intensity field vector \vec{E}_i) defined in $-x$ axis direction, whereas its amplitude value was set as unitary. The blue arrow represents the direction of the electromagnetic wave propagation (i.e. the incident Poynting vector, \vec{S}_i) as normal orientation ($-z$ axis direction) assuming the x - y target plane. The free space electromagnetic scattering of SiCN/C defined with arbitrary frequency ($f = 18.0$ GHz) showed better features when compared to SiCN simulations at the same frequency (Figure 7.11). Because the propagation of the incident wave is normal to the surface, the maximum amplitudes are expected to be normal since the computational body is flat. The maximum RCS values are 16.34 dBsm for SiCN and 17.12 dBsm for SiCN/C. The highest RCS value obtained for SiCN/C is associated with the highest values of the electrical loss tangent (Figure 7.8), which in turn can be associated with the highest values obtained in the imaginary component of electrical permittivity (Figure 7.7(b2)) in $f = 18$ GHz.

Figure 7.11 – Radiation diagram according to observation angle (θ) from -90° to 90° of SiCN and SiCN/C at the frequency of 18 GHz



Nanomaterials based on electrically conducting percolative networks consisting of carbon secondary phase dispersed within a PDC matrix are attractive for applications operating in harsh conditions such as high temperatures and corrosive environments [60]. Under the joint action of the above mechanisms, the SiCN/C fibers showed potential as lightweight microwave absorbers and EMF shielders for stealth applications under harsh environments.

7.4 CONCLUSIONS

The SiCN/C fibers showed to be promising for microwave absorption and EMF shielding. The 2-port VNA rectangular waveguide aperture and NRW method were effective to determine the electromagnetic properties of the materials prepared here. The absorption and complex permittivity of SiCN/C fibers was improved compared to SiCN fibers by simply adjusting the carbon content through the PDC route. The enhancement of electromagnetic properties of SiCN/C fibers was attributed to the dipole and interfacial polarization caused by residual bonds and defects in free carbon, conduction loss provided by conductive carbon, and multiple reflection loss from a hierarchical network of electrospun fibers. The SiCN/C fibers are potential to be used as lightweight materials for stealth applications under harsh environments. Additionally, SiCN/C fibers present potential characteristics for electromagnetic absorber materials used in electromagnetic compatibility and immunity test applications, which are essential tools for the development of next-generation of electromagnetic devices, for automotive, aerospace and space applications.

7.5 ACKNOWLEDGEMENTS

This study was financed in part by the Coordenação de Aperfeiçoamento de Pessoal de Nível Superior - Brasil (CAPES) - Finance Code 001. The authors thank CAPES and Deutscher Akademischer Austauschdienst (DAAD) for supporting this work within the project PROBRAL (Grant nº 88887.368756/2019-00). The authors thank Altair® for the availability of the Altair software package.

7.6 AUTHORS' CONTRIBUTIONS

The paper is mainly based on the work of the first author and author of this thesis Heloisa Ramlow. This work was conducted in collaboration with the Sensors and Materials Laboratory (National Institute for Space Research, Brazil). The precise contributions of each author are listed below (Table 7.2).

Table 7.2 – Authors' contributions to Chapter 7

Author	Contribution
Ramlow, H.	Conceptualized the work, wrote the manuscript
Lutiani, L.	Helped in the scientific evaluation, editing the manuscript and performing the simulation
Marangoni, C.	Gave conceptual and scientific advice, helped in the scientific evaluation and editing of the manuscript
Baldan, M. R.	Gave conceptual and scientific advice, helped in the scientific evaluation and editing of the manuscript
Machado, R.	Gave conceptual and scientific advice, helped in the scientific evaluation and editing of the manuscript

7.7 REFERENCES

- [1] D.D.L. Chung, Materials for electromagnetic interference shielding, *Mater. Chem. Phys.* 255 (2020) 123587. <https://doi.org/10.1016/j.matchemphys.2020.123587>.
- [2] J. Cheng, H. Zhang, Y. Xiong, L. Gao, B. Wen, H. Raza, H. Wang, G. Zheng, D. Zhang, H. Zhang, Construction of multiple interfaces and dielectric/magnetic heterostructures in electromagnetic wave absorbers with enhanced absorption performance: A review, *J. Mater.* 7 (2021) 1233–1263. <https://doi.org/10.1016/j.jmat.2021.02.017>.

- [3] O. Flores, R.K. Bordia, D. Nestler, W. Krenkel, G. Motz, Ceramic fibers based on SiC and SiCN systems: current research, development, and commercial status, *Adv. Eng. Mater.* 16 (2014) 621–636. <https://doi.org/10.1002/adem.201400069>.
- [4] P. Colombo, G. Mera, R. Riedel, G.D. Sorarù, Polymer-derived ceramics: 40 years of research and innovation in advanced ceramics, *J. Am. Ceram. Soc.* 93 (2010) 1805–1837. <https://doi.org/10.1002/9783527631971.ch07>.
- [5] R. Riedel, G. Mera, R. Hauser, A. Kloneczynski, Silicon-based polymer-derived ceramics: synthesis properties and applications - a review, *J. Ceram. Soc. Japan.* 114 (2006) 425–444.
- [6] B. Wang, Q. Wu, Y. Fu, T. Liu, A review on carbon/magnetic metal composites for microwave absorption, *J. Mater. Sci. Technol.* 86 (2021) 91–109. <https://doi.org/10.1016/j.jmst.2020.12.078>.
- [7] X. Li, Y. Wang, Complex impedance study on polymer-derived amorphous silicon carbonitride, *Ceram. Int.* 43 (2017) 13560–13564. <https://doi.org/10.1016/j.ceramint.2017.07.062>.
- [8] X. Long, C. Shao, J. Wang, Continuous SiCN fibers with interfacial SiC_xN_y phase as structural materials for electromagnetic absorbing applications, *ACS Appl. Mater. Interfaces.* 11 (2019) 22885–22894. <https://doi.org/10.1021/acsami.9b06819>.
- [9] W. Zhao, G. Shao, M. Jiang, B. Zhao, H. Wang, D. Chen, H. Xu, X. Li, R. Zhang, L. An, Ultralight polymer-derived ceramic aerogels with wide bandwidth and effective electromagnetic absorption properties, *J. Eur. Ceram. Soc.* 37 (2017) 3973–3980. <https://doi.org/10.1016/j.jeurceramsoc.2017.04.068>.
- [10] G. Shao, J. Liang, W. Zhao, B. Zhao, W. Liu, H. Wang, B. Fan, H. Xu, H. Lu, Y. Wang, R. Zhang, Co decorated polymer-derived SiCN ceramic aerogel composites with ultrabroad microwave absorption performance, *J. Alloys Compd.* 813 (2020) 152007. <https://doi.org/10.1016/j.jallcom.2019.152007>.
- [11] X. Guo, Y. Feng, H. Sun, Q. Hu, Novel electromagnetic metamaterial: Polymer-derived SiCN(Fe) ceramics, *Ceram. Int.* 46 (2020) 27634–27640. <https://doi.org/10.1016/j.ceramint.2020.07.258>.
- [12] Y. Feng, X. Guo, H. Gong, Y. Zhang, X. Lin, Enhanced electromagnetic microwave absorption of Fe/C/SiCN composite ceramics targeting in integrated structure and function, *Ceram. Int.* 47 (2021) 3842–3852. <https://doi.org/10.1016/j.ceramint.2020.09.244>.
- [13] Y. Liu, Y. Feng, H. Gong, Y. Zhang, X. Lin, B. Xie, J. Mao, Microwave absorbing performance of polymer-derived SiCN (Ni) ceramics prepared from different nickel sources, *J. Alloys Compd.* 749 (2018) 620–627. <https://doi.org/10.1016/j.jallcom.2018.03.346>.
- [14] X. Liu, Z. Yu, R. Ishikawa, L. Chen, X. Yin, Y. Ikuhara, R. Riedel, Single-source-precursor synthesis and electromagnetic properties of novel RGO-SiCN ceramic nanocomposites, *J. Mater. Chem. C.* 5 (2017) 7950–7960. <https://doi.org/10.1039/c7tc00395a>.
- [15] X. Liu, H. Xu, G. Liu, W. Duan, Y. Zhang, X. Fan, R. Riedel, Electromagnetic shielding performance of SiC/graphitic carbon-SiCN porous ceramic nanocomposites derived from catalyst assisted single-source-precursors, *J. Eur. Ceram. Soc.* 41 (2021) 4806–4814. <https://doi.org/10.1016/j.jeurceramsoc.2021.03.026>.
- [16] D. Sun, S. Huang, Y. Gao, B. Ma, Y. Wang, PVDF composites with spherical polymer-derived SiCN ceramic particles have significantly enhanced low-frequency dielectric constants, *J. Alloys Compd.* 783 (2019) 256–262. <https://doi.org/10.1016/j.jallcom.2018.12.323>.

- [17] Y. Huo, K. Zhao, Z. Xu, F. Li, X. Zhao, Q. Meng, C. Tang, Y. Tang, Ultralight and superelastic polyvinyl alcohol/SiC nanofiber/reduced graphene oxide hybrid foams with excellent thermal insulation and microwave absorption properties, *Ceram. Int.* 47 (2021) 25986–25996. <https://doi.org/10.1016/j.ceramint.2021.06.004>.
- [18] X. Li, J. Wei, B. Chen, Y. Wang, C. Jiang, H. Zhang, M. Qiao, Effective electromagnetic wave absorption and photoluminescence performances of flexible SiC nanowires membrane, *Ceram. Int.* 47 (2021) 17615–17626. <https://doi.org/10.1016/j.ceramint.2021.03.080>.
- [19] Y. Huo, Y. Tan, K. Zhao, Z. Lu, L. Zhong, Y. Tang, Enhanced electromagnetic wave absorption properties of Ni magnetic coating-functionalized SiC/C nanofibers synthesized by electrospinning and magnetron sputtering technology, *Chem. Phys. Lett.* 763 (2021) 138230. <https://doi.org/10.1016/j.cplett.2020.138230>.
- [20] Y. Hou, L. Cheng, Y. Zhang, X. Du, Y. Zhao, Z. Yang, High temperature electromagnetic interference shielding of lightweight and flexible ZrC/SiC nanofiber mats, *Chem. Eng. J.* 404 (2021) 126521. <https://doi.org/10.1016/j.cej.2020.126521>.
- [21] Y. Zhang, Y. Zhao, Q. Chen, Y. Hou, Q. Zhang, L. Cheng, L. Zheng, Flexible SiC-CNTs hybrid fiber mats for tunable and broadband microwave absorption, *Ceram. Int.* 47 (2021) 8123–8132. <https://doi.org/10.1016/j.ceramint.2020.11.167>.
- [22] Y. Huo, K. Zhao, Z. Xu, Y. Tang, Electrospinning synthesis of SiC/Carbon hybrid nanofibers with satisfactory electromagnetic wave absorption performance, *J. Alloys Compd.* 815 (2020) 152458. <https://doi.org/10.1016/j.jallcom.2019.152458>.
- [23] Y. Feng, X. Guo, J. Lu, J. Liu, G. Wang, H. Gong, Enhanced electromagnetic wave absorption performance of SiCN(Fe) fibers by in-situ generated Fe₃Si and CNTs, *Ceram. Int.* 47 (2021) 19582–19594. <https://doi.org/10.1016/j.ceramint.2021.03.296>.
- [24] X. Guo, F. Xiao, J. Li, H. Zhang, Q. Hu, G. Li, H. Sun, Fe-doped SiCN composite fibers for electromagnetic waves absorption, *Ceram. Int.* 47 (2021) 1184–1190. <https://doi.org/10.1016/j.ceramint.2020.08.236>.
- [25] X. Guo, J. Lu, J. Liu, C. Liu, Y. Tong, J. Li, H. Sun, H. Peng, S. Wu, Y. Feng, H. Gong, Enhanced electromagnetic wave absorption properties of PDCs-SiCN(Ni) fibers by in-situ formed CNTs and Ni₂Si, *Ceram. Int.* (2022). <https://doi.org/10.1016/j.ceramint.2022.04.012>.
- [26] J. Lu, Y. Feng, J. Liu, C. Liu, Y. Tong, S. Wu, H. Sun, H. Gong, X. Guo, Improved electromagnetic wave absorbing performance of PDCs-SiCN(Ni) fibers with different nickel content, *Ceram. Int.* 48 (2022) 23578–23589. <https://doi.org/10.1016/j.ceramint.2022.05.006>.
- [27] S. Wang, H. Gong, M.Z. Ashfaq, D. Qi, P. Xu, X. Yue, Tailoring microwave absorption bandwidth of SiCN based composite ceramic fibers by tuning the embedding ratio of Ni₃Si, *Ceram. Int.* (2022). <https://doi.org/10.1016/j.ceramint.2022.05.294>.
- [28] Y. Cheng, W. Zhu, X. Lu, C. Wang, Recent progress of electrospun nanofibrous materials for electromagnetic interference shielding, *Compos. Commun.* 27 (2021) 100823. <https://doi.org/10.1016/j.coco.2021.100823>.
- [29] Y. Naito, K. Suetake, Application of ferrite to electromagnetic wave absorber and its characteristics, *IEEE Trans. Microw. Theory Tech.* 19 (1971) 65–72. <https://doi.org/10.1109/TMTT.1971.1127446>.
- [30] Q. Wen, Z. Yu, R. Riedel, The fate and role of in situ formed carbon in polymer-derived ceramics, *Prog. Mater. Sci.* 109 (2020) 100623. <https://doi.org/10.1016/j.pmatsci.2019.100623>.
- [31] K.Y. You, Materials characterization using microwave waveguide system, in: *Microw. Syst. Appl.*, InTech, 2017: pp. 341–358. <https://doi.org/10.5772/66230>.

- [32] H. Ramlow, L.L. da Silva, B.H.K. Lopes, M.R. Baldan, R.A.F. Machado, SiCN fibers as advanced materials for electromagnetic shielding in X-band: experiments and computational modelling and simulation, *Comput. Aided Process Eng.* 1 (2022) 199–204. <https://doi.org/10.1016/B978-0-323-95879-0.50034-5>.
- [33] L.F.B. Ribeiro, O. Flores, P. Furtat, C. Gervais, R. Kempe, R.A.F. Machado, G. Motz, A novel PAN/silazane hybrid polymer for processing of carbon-based fibres with extraordinary oxidation resistance, *J. Mater. Chem. A.* 5 (2017) 720–729. <https://doi.org/10.1039/c6ta09293d>.
- [34] W. Dang, J. Liu, X. Wang, K. Yan, A. Zhang, J. Yang, L. Chen, J. Liang, Structural transformation of polyacrylonitrile (PAN) fibers during rapid thermal pretreatment in nitrogen atmosphere, *Polymers (Basel)*. 12 (2020) 1–12. <https://doi.org/10.3390/polym12010063>.
- [35] O. Flores, T. Schmalz, W. Krenkel, L. Heymann, G. Motz, Selective cross-linking of oligosilazanes to tailored meltable polysilazanes for the processing of ceramic SiCN fibres, *J. Mater. Chem. A.* 1 (2013) 15406–15415. <https://doi.org/10.1039/c3ta13254d>.
- [36] Y. Feng, S. Dou, Y. Wei, Y. Zhang, X. Song, X. Li, V.S. Battaglia, Preparation and capacity-fading investigation of polymer-derived silicon carbonitride anode for lithium-ion battery, *ACS Omega*. 2 (2017) 8075–8085. <https://doi.org/10.1021/acsomega.7b01462>.
- [37] Y. Liu, X. Lin, H. Gong, Y. Zhang, Y. Feng, J. Mao, B. Xie, Electromagnetic properties and microwave absorption performances of nickel-doped SiCN ceramics pyrolyzed at different temperatures, *J. Alloys Compd.* 771 (2019) 356–363. <https://doi.org/10.1016/j.jallcom.2018.08.283>.
- [38] S. Bin Mujib, R. Cuccato, S. Mukherjee, G. Franchin, P. Colombo, G. Singh, Electrospun SiOC ceramic fiber mats as freestanding electrodes for electrochemical energy storage applications, *Ceram. Int.* 46 (2020) 3565–3573. <https://doi.org/10.1016/j.ceramint.2019.10.074>.
- [39] A. Tolosa, M. Widmaier, B. Krüner, J.M. Griffin, V. Presser, Continuous silicon oxycarbide fiber mats with tin nanoparticles as a high capacity anode for lithium-ion batteries, *Sustain. Energy Fuels*. 2 (2018) 215–228. <https://doi.org/10.1039/c7se00431a>.
- [40] H. Ramlow, C. Marangoni, G. Motz, R.A.F. Machado, Statistical optimization of polysilazane-derived ceramic: Electrospinning with and without organic polymer as a spinning aid for manufacturing thinner fibers, *Chem. Eng. J. Adv.* 9 (2022) 100220. <https://doi.org/10.1016/j.cej.2021.100220>.
- [41] J. Marie, J. Bourret, P.M. Geffroy, A. Smith, V. Chaleix, T. Chartier, Eco-friendly alumina suspensions for tape-casting process, *J. Eur. Ceram. Soc.* 37 (2017) 5239–5248. <https://doi.org/10.1016/j.jeurceramsoc.2017.04.033>.
- [42] M. Wilamowska, M. Graczyk-Zajac, R. Riedel, Composite materials based on polymer-derived SiCN ceramic and disordered hard carbons as anodes for lithium-ion batteries, *J. Power Sources*. 244 (2013) 80–86. <https://doi.org/10.1016/j.jpowsour.2013.03.137>.
- [43] Y.S. Kim, Y.L. Joo, Y.J. Kwark, Highly stable silicon-carbon-nitrogen composite anodes from silsesquiazane for rechargeable lithium-ion battery, *J. Mater. Sci. Technol.* 32 (2016) 195–199. <https://doi.org/10.1016/j.jmst.2015.12.019>.
- [44] Y. Hishinuma, T. Ogihara, Preparation of silica glass films on the surface of polypropylene microporous membrane separators by dip coating with polysilazane and their application in lithium-ion batteries, *J. Ceram. Soc. Japan*. 124 (2016) 480–483. <https://doi.org/10.2109/jcersj2.15306>.
- [45] J. Zhang, C. Xu, Z. Liu, W. Wang, X. Xin, L. Shen, X. Zhou, J. Zhou, Q. Huang, Enhanced rate capability of polymer-derived SiCN anode material for electrochemical

- storage of lithium with 3-D carbon nanotube network dispersed in nanoscale, *J. Nanosci. Nanotechnol.* 15 (2015) 3067–3075. <https://doi.org/10.1166/jnn.2015.9690>.
- [46] Y. Feng, N. Feng, Y. Wei, Y. Bai, Preparation and improved electrochemical performance of SiCN-graphene composite derived from poly(silylcarbodiimide) as Li-ion battery anode, *J. Mater. Chem. A.* 2 (2014) 4168–4177. <https://doi.org/10.1039/c3ta14441k>.
- [47] A. Sadezky, H. Muckenhuber, H. Grothe, R. Niessner, U. Pöschl, Raman microspectroscopy of soot and related carbonaceous materials: Spectral analysis and structural information, *Carbon N. Y.* 43 (2005) 1731–1742. <https://doi.org/10.1016/j.carbon.2005.02.018>.
- [48] M. Graczyk-Zajac, C. Fasel, R. Riedel, Polymer-derived-SiCN ceramic/graphite composite as anode material with enhanced rate capability for lithium ion batteries, *J. Power Sources.* 196 (2011) 6412–6418. <https://doi.org/10.1016/j.jpowsour.2011.03.076>.
- [49] X. Xi, D.D.L. Chung, Colossal electric permittivity discovered in polyacrylonitrile (PAN) based carbon fiber, with comparison of PAN-based and pitch-based carbon fibers, *Carbon N. Y.* 145 (2019) 734–739. <https://doi.org/10.1016/j.carbon.2019.01.069>.
- [50] L. Kong, S. Luo, G. Zhang, H. Xu, T. Wang, J. Huang, X. Fan, Interfacial polarization dominant CNTs/PyC hollow microspheres as a lightweight electromagnetic wave absorbing material, *Carbon N. Y.* 193 (2022) 216–229. <https://doi.org/10.1016/j.carbon.2022.03.016>.
- [51] X. Chen, Y. Wu, W. Gu, M. Zhou, S. Tang, J. Cao, Z. Zou, G. Ji, Research progress on nanostructure design and composition regulation of carbon spheres for the microwave absorption, *Carbon N. Y.* 189 (2022) 617–633. <https://doi.org/10.1016/j.carbon.2021.12.100>.
- [52] S. Arslanagić, T. V. Hansen, N.A. Mortensen, A.H. Gregersen, O. Sigmund, R.W. Ziolkowski, O. Breinbjerg, A review of the scattering-parameter extraction method with clarification of ambiguity issues in relation to metamaterial homogenization, *IEEE Antennas Propag. Mag.* 55 (2013) 91–106. <https://doi.org/10.1109/MAP.2013.6529320>.
- [53] B. Quan, X. Liang, G. Ji, Y. Cheng, W. Liu, J. Ma, Y. Zhang, D. Li, G. Xu, Dielectric polarization in electromagnetic wave absorption: Review and perspective, *J. Alloys Compd.* 728 (2017) 1065–1075. <https://doi.org/10.1016/j.jallcom.2017.09.082>.
- [54] N. Liu, Y. Dou, X. Zhang, L. Yu, X. Yan, Design of porous FeNi-carbon nanosheets by a double-effect synergistic strategy for electromagnetic wave absorption, *Carbon N. Y.* 190 (2022) 125–135. <https://doi.org/10.1016/j.carbon.2022.01.007>.
- [55] V. Shukla, Review of electromagnetic interference shielding materials fabricated by iron ingredients, *Nanoscale Adv.* 1 (2019) 1640–1671. <https://doi.org/10.1039/c9na00108e>.
- [56] F. Xiao, H. Sun, J. Li, X. Guo, H. Zhang, J. Lu, Z. Pan, J. Xu, Electrospinning preparation and electromagnetic wave absorption properties of SiCN fibers, *Ceram. Int.* 46 (2020) 12773–12781. <https://doi.org/10.1016/j.ceramint.2020.02.046>.
- [57] Z. Shen, J. Chen, B. Li, G. Li, Z. Zhang, X. Hou, Recent progress in SiC nanowires as electromagnetic microwaves absorbing materials, *J. Alloys Compd.* 815 (2020) 152388. <https://doi.org/10.1016/j.jallcom.2019.152388>.
- [58] H. Liu, Y. Zhang, X. Liu, W. Duan, M. Li, Q. Zhou, S. Li, G. Wang, G. Han, Additive manufacturing of nanocellulose/polyborosilazane derived CNFs-SiBCN ceramic metamaterials for ultra-broadband electromagnetic absorption, *Chem. Eng. J.* 433 (2022) 133743. <https://doi.org/10.1016/j.cej.2021.133743>.
- [59] C.A. Balanis, *Advanced Engineering Electromagnetics*, 2nd ed., John Wiley & Sons, Danvers, 2012.
- [60] C.L. Cramer, E. Ionescu, M. Graczyk-Zajac, A.T. Nelson, Y. Katoh, J.J. Haslam, L.

Wondraczek, T.G. Aguirre, S. LeBlanc, H. Wang, M. Masoudi, E. Tegeler, R. Riedel, P. Colombo, M. Minary-Jolandan, Additive manufacturing of ceramic materials for energy applications: Road map and opportunities, *J. Eur. Ceram. Soc.* 42 (2022) 3049–3088. <https://doi.org/10.1016/j.jeurceramsoc.2022.01.058>.

8 ELECTROCHEMICAL PERFORMANCE OF SiCN FIBER MAT ELECTRODES FOR LITHIUM-ION BATTERY: ELECTROSPINNING POLYSILAZANE IN AIR OR PROTECTIVE ATMOSPHERE⁶

Electrodes prepared through electrospinning and PDC route have been researched lately, however, investigations on polysilazane-derived SiCN are still scarce. This study describes the electrospinning in air or protective atmosphere (nitrogen) for the manufacturing of polysilazane/polyacrylonitrile fiber mats. After pyrolysis, SiCN containing *in-situ* synthesized carbon (SiCN-C) was tested as LIB electrodes. Electron microscopy showed that fibers electrospun in nitrogen are found to be thinner than samples manufactured by conventional electrospinning performed in air due to the slower solidification of the flying jet. XPS analyses confirmed that fibers electrospun in air incorporated a great oxygen content during shaping. The highest charge capacity of 773 mA h g⁻¹ at 50 mA g⁻¹ was recovered for SiCN-C electrospun in air. Oxygen increased the capacity due to its high character to attract Li⁺ ions, but SiCN-C electrospun in air suffered voltage hysteresis. Contrariwise, the SiCN-C electrospun in nitrogen demonstrated stable cycling with a charge capacity of 299 mA h g⁻¹ due to enhanced free carbon content. This capacity was higher than SiCN and carbon electrodes processed under similar conditions. Improved performance of SiCN-C is attributed to synergetic effects between SiCN (a pathway for Li⁺ transfer) and carbon (improved electronic conductivity and more active sites for Li⁺ ions). After 100 cycles, the SiCN-C electrode electrospun in nitrogen atmosphere exhibited up to 98% of the initial capacity once it returned to lower current cycling showing improved cycling stability and significantly lower capacity losses. These findings make electrospinning very promising for the highly controlled production of SiCN fiber mat electrodes.

8.1 INTRODUCTION

Efficient utilization of future electronic devices will require increased storage capacities, long-term safety, and stability of rechargeable batteries. Among various rechargeable batteries technologies, the LIB continues to dominate mainly because of consistent specific energies of approximately 120 W h kg⁻¹, low reduction potentials, and the small ionic

⁶Based on a paper to be submitted for publication.

size of a Li^+ ion (0.76 Å) which facilitates smooth intercalation and fast electrochemical kinetics [1].

Recent studies have investigated silicon-based covalent ceramics (such as SiCO and SiCN) prepared via the PDC process as potential electrode materials for LIB because of favorable electrochemical properties [2], such as reversible accommodation of Li^+ ions in a potential range of 0-2.5 V with high electrochemical capacities up to 900 mAh g^{-1} (despite that low capacities are also reported) and Coulombic efficiencies over 99% [3]. Particularly, PDCs with excess carbon such as C-rich SiCN have been shown to improve the electrochemical performance as LIB anode significantly due to sufficient nanocarbon clusters and free dangling bonds of silicon and carbon, which are active sites for the intercalating/de-intercalating of Li^+ ions, and the presence of nanoholes or nanochannels in the SiCN network, which improve electrochemical dynamic properties [4–9]. Although Dahn *et al.* filed a patent in 1996 for polysilazane-derived SiCN electrodes for LIBs [10], minimal research has been conducted compared to the application of SiCO in LIBs.

Silicon-based PDCs are generally poor conductors of electronic/ionic current and the electrode preparation often requires the incorporation of conducting agents and binders on a metal current collector, thereby increasing the weight of the energy storage device [11]. However, future electrochemical energy storage devices must be lightweight to accommodate advances in wearable, flexible electronics [12]. Moreover, the addition of a conductive agent (considered a non-active phase for Li-ion storage) masks the real electrochemical performance of the electrode material [13]. Engineering electrode structures to enhance their ionic and electronic conductivity can significantly improve the electrochemical properties [14] and as a result, electrodes that are free of binder, conducting agents, and current collectors are desirable. For example, free-standing fiber electrodes are advantageous due to their higher overall gravimetric energy density [15–17].

Non-woven fiber mats prepared via electrospinning and the PDC process have recently been considered electrode materials [18–22]. Electrospinning creates freestanding fiber mats that may be used as binder-free working electrodes. Since initial research published in 2007 [23,24], some progress has been made regarding PDC fiber mats shaped through electrospinning, but additional research is required, such as investigating the influence of the electrospinning atmosphere on PDC composition, especially for oxygen-sensitive polysilazanes typically electrospun in air [25–28]. Additional studies are required to understand the effect of

nitrogen and oxygen and the structure-property relationship of SiCN on Li⁺ ions' electrochemical energy storage to design effective polymer-derived SiCN fiber mat electrodes.

This work aims to investigate the electrochemical performance of SiCN fiber mats electrospun in air or protected nitrogen atmosphere and applied as LIB electrodes. Solutions containing polysilazane as the preceramic polymer and PAN as the carbon source were shaped via electrospinning performed in air or in nitrogen (inert atmosphere). After pyrolysis, SiCN fiber mats with *in situ* synthesized carbon derived from PAN were manufactured, and a single material was obtained. To the best of our knowledge, this is the first known report that proposes SiCN electrospun fiber mats as electrodes for LIBs. The results of this work will provide a reference for designing the optimal composition of PDC-based fiber mat electrodes manufactured via the electrospinning process. Here we show that the atmosphere of the electrospinning process may influence the fiber mats regarding their morphology as demonstrated by electron microscopy, and composition as confirmed through XPS analysis. The fiber mats shaped in air showed a high electrochemical capacity as LIB electrodes due to the oxygen incorporation during electrospinning. Nevertheless, the fiber mats shaped in nitrogen showed excellent electrochemical stability and recovery of the initial reversible capacity after fast-cycling attributed to their high content of free carbon.

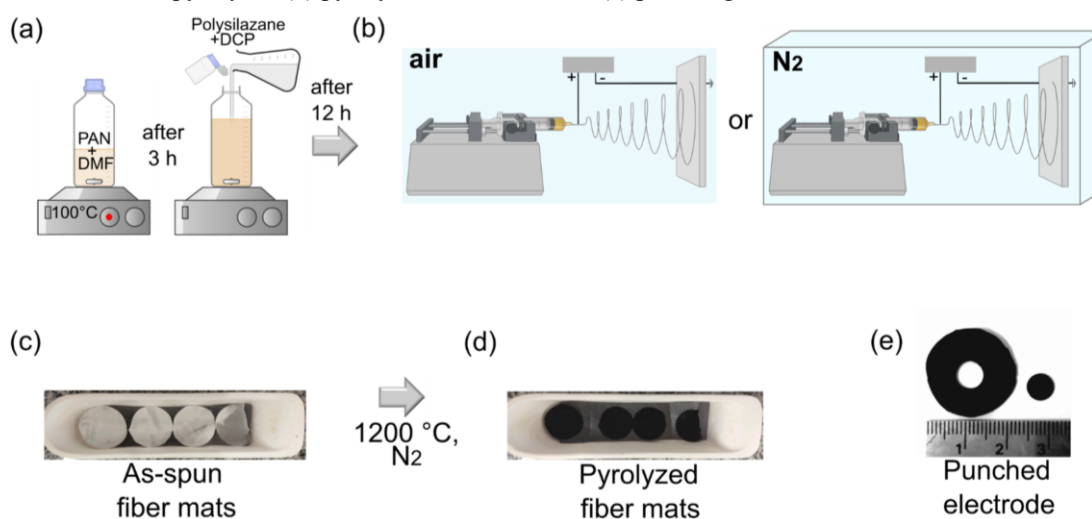
8.2 EXPERIMENTAL

Solutions containing different amounts of HTTS and PAN were prepared (Table 8.1 and Figure 8.1a). The solution was placed in a syringe coupled with a 21 G metallic needle clamped to a high-voltage power supply that applied approximately 24 kV and was fixed approximately 23.5 cm from the collector. The sample was extruded at a flow rate of approximately 0.9 mL h⁻¹ controlled by a pump. The polymer solutions were electrospun in two different devices: one device was in air with a relative humidity of approximately 60%, and the other device was inside a glove box with a protective atmosphere (i.e. nitrogen atmosphere) (Figure 8.1b). As-spun mats were prepared for pyrolysis (Figure 8.1c), placed in a tubular furnace, and heated up to 1200 °C for 1 h with a heating rate of 5 °C min⁻¹ in a nitrogen atmosphere. Ceramic fiber mats were obtained (Figure 8.1d). For comparison, SiCN (electrospun in inert atmosphere) and carbon (electrospun in air) fiber mats were also manufactured under similar conditions.

Table 8.1 – Denomination of the samples investigated in this work

Sample name	Polymer concentration in solution for electrospinning (wt.%)	Polysilazane: PAN concentration (wt.%)	Electrospinning atmosphere
SiCN-40C-a	17.5	60:40	Air
SiCN-40C-i	17.5	60:40	Inert (nitrogen)
SiCN-70C-a	13	30:70	Air
SiCN-70C-i	13	30:70	Inert (nitrogen)

Figure 8.1 – Schematic diagram of the experimental process of this work including (a) precursor solution preparation, (b) electrospinning in air or protective atmosphere (nitrogen), (c) preparation of as-spun fiber mats for pyrolysis, (d) pyrolyzed fiber mats, and (e) punching of fiber mat electrode



Using EVO MA10 SEM (Zeiss, Germany) with an acceleration voltage of 5 kV, the fiber diameter was evaluated from four SEM images that randomly measured 100 fibers of each sample using open-source ImageJ software. XPS was performed to analyze the composition of the electrospun mats. The XPS spectra were obtained with a Thermo Scientific Al $K\alpha^+$ ion beam with an energy of 1486.6 eV and a spot size of 400 μm (Chanhassen, USA). Surface contamination of the ceramic fiber mats was removed via surface sputtering with argon at 3.0 keV for 2 min.

The electrospun mats were used as freestanding electrodes in LIB half-cells, in which a lithium metal electrode (14.3 mm diameter and 75 μm thick) was utilized as both the counter and reference electrode. This configuration provides a stable reference potential with a large specific capacity, affording a very large reservoir of capacity so that the reactions at the working electrode are not limited by the capacity available at the counter electrode [31]. A disk electrode with an approximate diameter of 6.35 mm was punched out from the pyrolyzed mat and used as the working electrode (Figure 8.1e). The electrolyte solution was a mixture of 1 M lithium

hexafluorophosphate (LiPF_6) in 1:1 dimethyl carbonate:ethylene carbonate vol% (Sigma Aldrich, USA). A glass fiber separator (19 mm diameter, 25 μm thick) separated the two electrodes as they were pre-soaked with the electrolyte. The batteries were assembled in LIR-2032 coin cells in a glove box filled with argon 99.9% and tested using a multichannel BT 2000 Arbin test unit (College Station, USA) between 10 mV and 2.5 V vs. Li/Li^+ . The cells were subjected to symmetric cycling at current densities of 50, 100, 200, 400, 600, and 800 mA g^{-1} for 10 cycles each followed by a current density of 50 mA g^{-1} for 40 cycles. The capacity was represented in mAh g^{-1} considering the anode mass, and the Coulombic efficiency (%) was calculated as the ratio of discharge capacity after full charge and charge capacity of the same cycle.

8.3 RESULTS AND DISCUSSION

SEM images of the pyrolyzed samples showed the morphology of the resulting SiCN fiber mats after electrospinning and polymer to ceramic transformation. The fiber diameter was 937 ± 235 nm for SiCN-40C-a, 153 ± 20 nm for SiCN-40C-i, 833 ± 237 nm for SiCN-70C-a, and 150 ± 26 nm for SiCN-70C-i (Figure 8.2). The fibers electrospun in nitrogen atmosphere had a much thinner diameter (approx. 83%) when compared to the fibers electrospun in air, attributed to the influence of 60% relative humidity in the air. Despite that electrospinning is a very fast process, the influence of air moisture is not limited. The presence of water molecules in the air discharges the electrospinning jet due to molecular polarization; the jet is less vigorously subjected to whipping instabilities and less elongated. For a system composed of hydrophobic PAN, the high humidity in the air led to early solidification resulting in thicker diameters and the suppression of bead-on-string morphologies. The fibers electrospun in a protective atmosphere were uniform and smoother than fibers obtained by electrospinning performed in air, as also reported in a previous study that investigated the electrospinning of organic fibers [29]. However, the presence of solvent molecules inside the electrospinning chamber delayed the solidification of the fibers due to some solvent absorption into the jet and polymer plasticizing, and, consequently, favoring the apparition of bead-on-string fibers. The histogram of the fiber diameter was better normally distributed compared to the histogram of fiber diameter electrospun in the air, which showed some fiber diameter difference. This was not observed with polysilazane-derived SiCN fibers, which showed a homogeneous morphology when electrospun in nitrogen atmosphere attributed to the high polymer concentration hindering

further jet elongation (Figure 8.3a). In contrast, carbon fibers electrospun in air also showed some irregularities due to the high moisture content in the air during electrospinning (Figure 8.3b).

Figure 8.2 – SEM images, respective fiber diameter (Φ) and histogram of pyrolyzed fiber mats electrospun in air (SiCN-40C-a and SiCN-70C-a) or protective atmosphere (SiCN-40C-i and SiCN-70C-i)

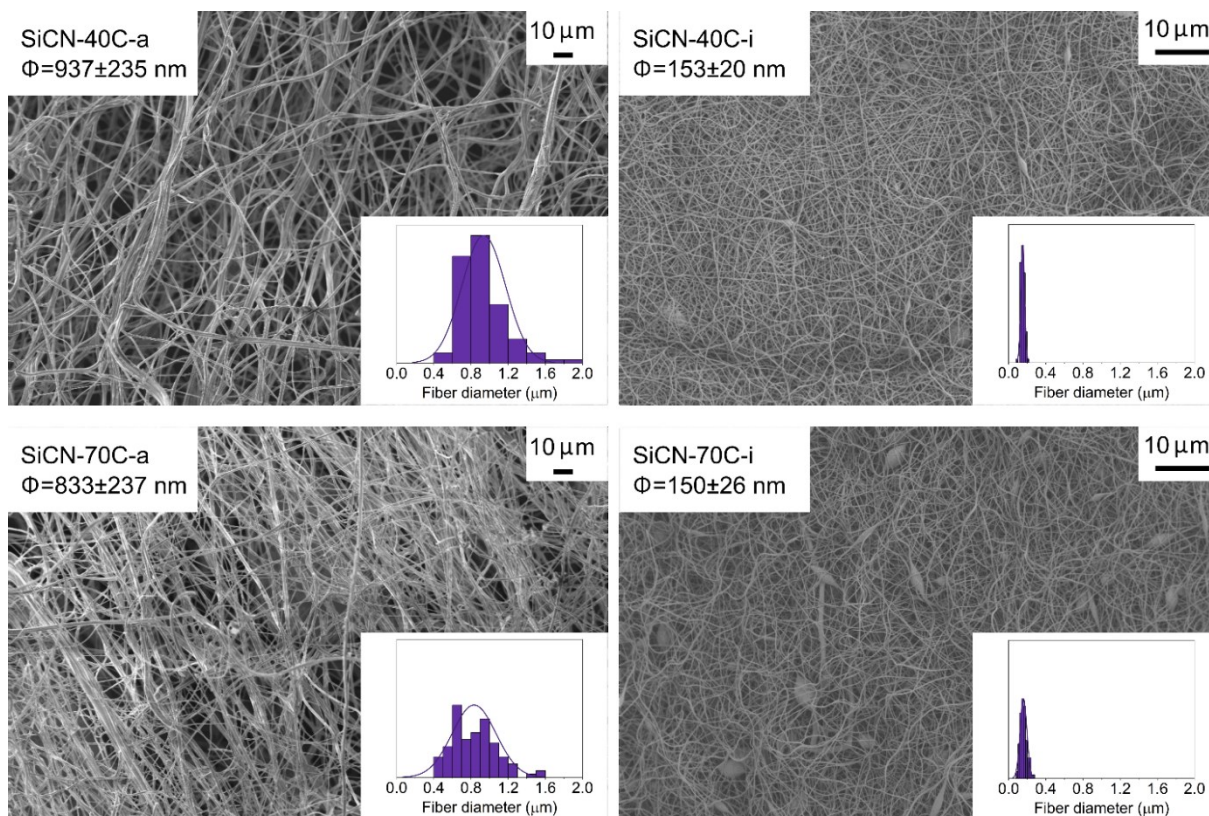
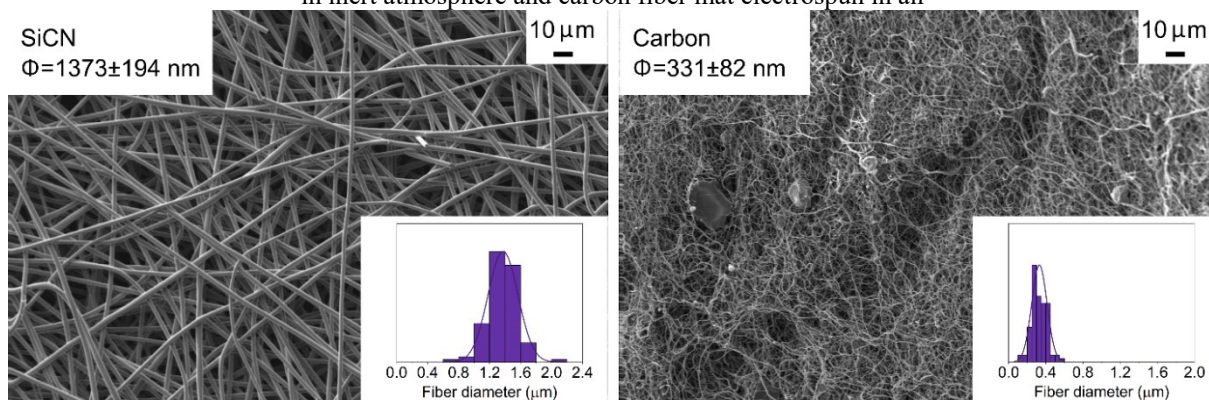
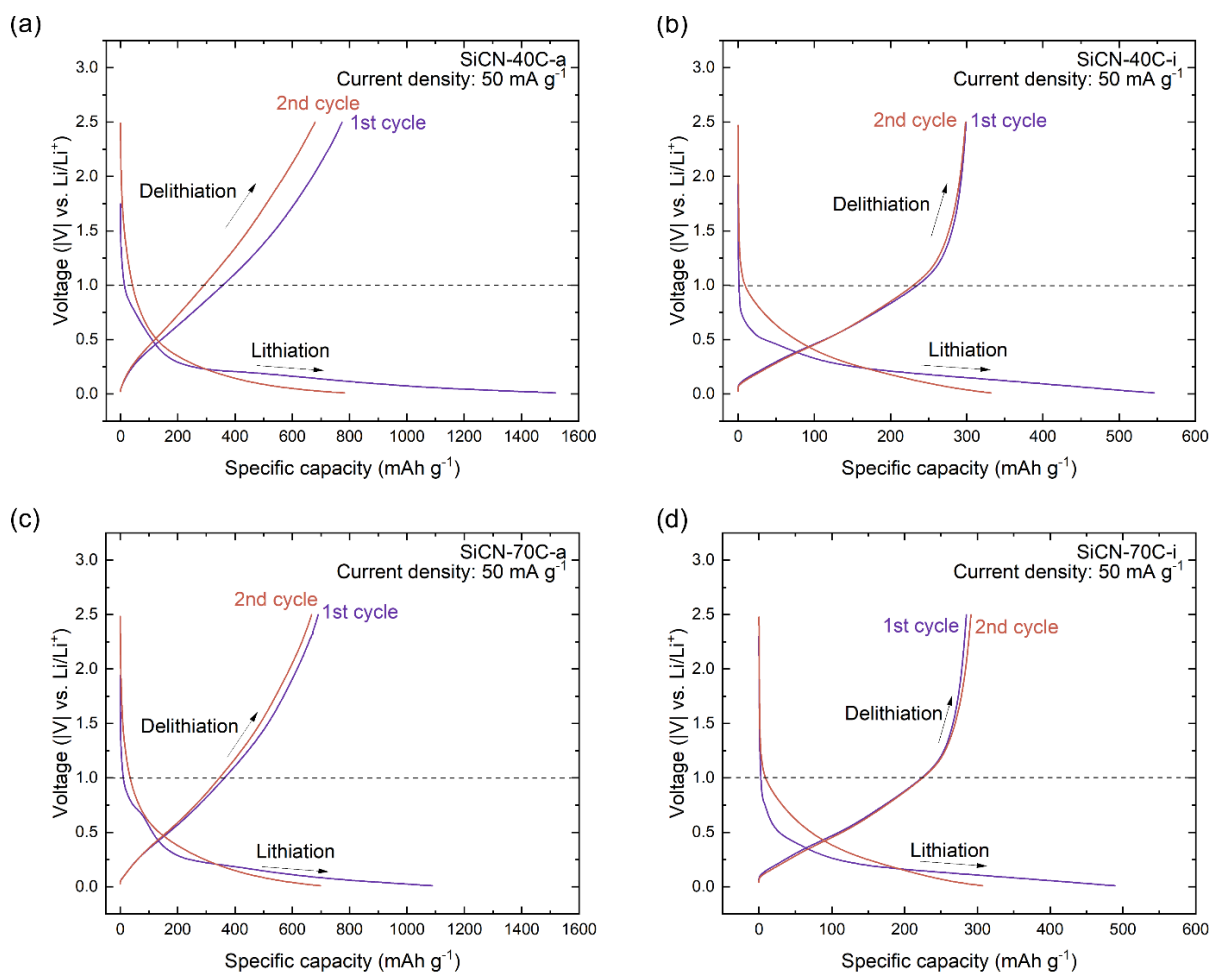


Figure 8.3 – SEM images, respective fiber diameter (Φ) and histogram of pyrolyzed SiCN fiber mat electrospun in inert atmosphere and carbon fiber mat electrospun in air



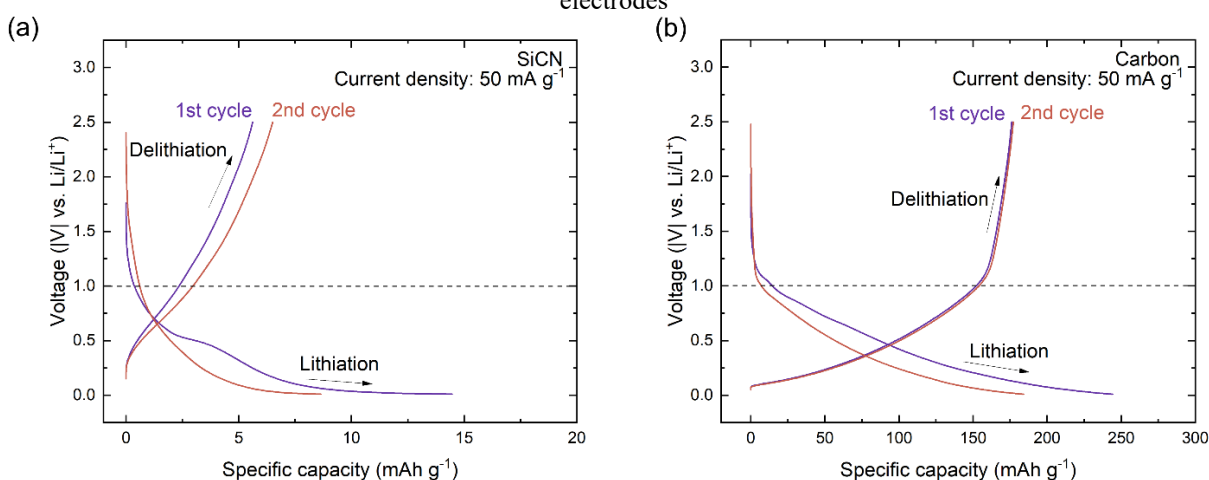
Later, the as-prepared polymer-derived SiCN fiber mats were used as the working electrodes in LIBs coin cell in half-cell configuration. The porous structure and microstructure provided by the electrospinning and PDC approach allowed the liquid electrolyte to fully penetrate the electrode thereby providing a shorter path for solvated ions to be transported onto the surface of the fibers [11]. The voltage plots of the first and second cycles at a current density of 50 mA g^{-1} are presented (Figure 8.4). Ideally, the discharge/charge curves should be identical in opposite directions, but the voltage profiles showed that the first cycle had experienced irreversible capacity decay primarily for the mats electrospun in air since the increased voltage is needed for the discharge of the same capacity. Irreversibility in these materials typically occurs because of the formation of poorly reversible structures of solvated lithium (e.g. Li_2O_3 due to the presence of oxygen) and solid electrolyte interphase (SEI) formation related to the surface area [30–32].

Figure 8.4 – Voltage profiles with 1st and 2nd charge-discharge cycles of the (a-d) SiCN-40C-a, SiCN-40C-i, SiCN-70C-a, and SiCN-70C-i fiber mat electrodes



Different charge-discharge profiles were observed for fiber mat electrodes depending on the electrospinning atmosphere in which they were processed. For example, a pronounced voltage hysteresis was detected for SiCN-40C-a and SiCN-70C-a samples, with a higher voltage being required for Li^+ extraction than for Li^+ insertion due to electrochemical polarization arising from the internal resistance of the electrode materials [33]. Despite the low current, pronounced voltage hysteresis of up to 2.5 V was observed for the electrospinning conducted in air, which results in low energy efficiency. However, for the electrospinning conducted in a protective atmosphere, the voltage hysteresis of SiCN-40C-i and SiCN-70C-i was suppressed and the major part of the charge was recovered at a potential below 1 V. This is most likely due to the existence of different potential states for Li-ion insertion [31,34]. For SiCO electrodes, which have structures similar to SiCN, voltage hysteresis was attributed to a difference in the electrochemical potential of the Li^+ ions at the SiCO-electrolyte interface, and the electrochemical potential of the Li^+ ions within the electrolyte that is in equilibrium with the lithium metal counter electrode [35]. The voltage profile of the SiCN electrode also exhibited some voltage hysteresis (Figure 8.5a) as contrasted with the carbon electrode (Figure 8.5b), which did not show significant hysteresis due to its structural uniformity during Li-ion charging and discharging [34,36]. The fiber mats electrospun in air showed a higher capacity compared to fiber mats electrospun in a protective atmosphere due to the higher content of oxygen as explained hereafter.

Figure 8.5 – Voltage profiles with 1st and 2nd charge-discharge cycles of the (a) SiCN and (b) carbon fiber mat electrodes



Despite that XPS is a surface analysis, the fibers prepared here are ultrathin materials and, therefore this technique can be considered as appropriate for the identification and quantification of the elements present in the fiber as has been conducted in other studies on

ultrathin PDC fibers [20, 37]. The XPS survey scan (Figure 8.6) confirmed the presence of silicon, carbon, nitrogen, and oxygen in SiCN fiber mat materials. XPS spectra of the electrospun fiber mats also clearly showed distinct Si 2p, C 1s, N 1s, and O 1s peaks according to the electrospinning atmosphere. The XPS elemental composition for various specimens is summarized (Table 8.2). High-resolution XPS spectra show the bonding of the pyrolyzed fiber mats after the curve fitting of peaks (Figure 8.7). Spectra under the Si 2p band indicated the presence of Si-N (101.9 eV), Si-C (102.7 eV), and Si-O (103.5 eV) peaks [11,38]. In addition, C-Si (284.0 eV), C-C (284.9 eV), and C=O (286.0 eV) peaks were observed in the C 1s band and N-Si (398.1 eV) in the N 1s band [39]. The increased amount of carbon in the fiber mats electrospun in the protective atmosphere leads to higher intensity of the C-C peak, suggesting an increased possibility of a free carbon phase. Indeed, PAN-derived carbon fibers showed mostly the presence of sp^2 -carbon (84.13 at%) (Figure 8.8b). The O 1s band was fitted with two peaks at 532.4 eV and 534.0 eV corresponding to O-Si and C=O, respectively [3]. The fiber mats electrospun in air showed a significant increase in oxygen content (i.e., 45.61 at% and 12.60 at% for SiCN-40C-a and SiCN-40C-i, respectively; 31.14 at% and 19.91 at% for SiCN-70C-a and SiCN-70C-i, respectively). Oxygen replaced nitrogen in the SiCN structure, particularly nitrogen present on the fiber surface after electrospinning in air, since the surface atoms are more easily detected by XPS analysis. However, it is here highlighted that the fiber core when electrospun in air can be different from the fiber surface and oxygen was probably concentrated only on the fiber surface. The increased amount of oxygen in samples electrospun in air (more than 30 at%), correlated to a decreased amount of carbon. During pyrolysis at 1200 °C, the reaction of oxygen with carbon formed evaporable CO, which subsequently reduced the carbon content in the SiCN fibers electrospun in air. Additionally, the irreversible capacity and voltage hysteresis observed in the voltage profiles of the SiCN-C electrodes electrospun in air (Figure 8.4) may be due to the high oxygen content present in these samples [40].

Figure 8.6 – XPS spectra of the fiber mat electrodes

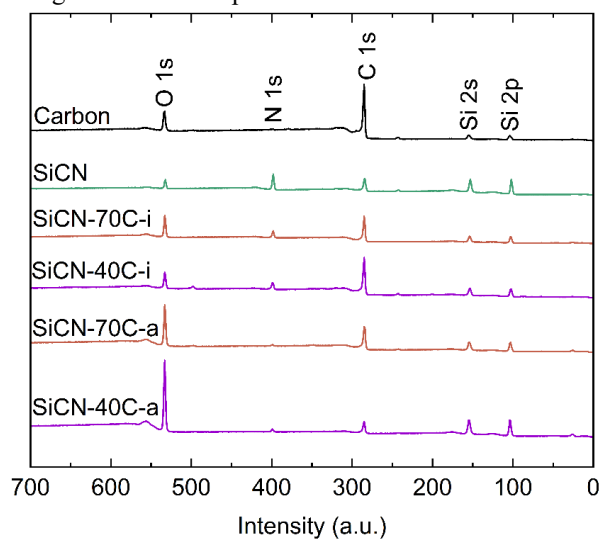


Table 8.2 – Elemental composition by XPS analyses

Sample	Element composition (at.%)			
	Si	C	N	O
SiCN-40C-a	28.85	22.32	3.22	45.61
SiCN-40C-i	14.70	64.11	8.59	12.60
SiCN-70C-a	19.11	47.27	2.48	31.14
SiCN-70C-i	16.24	54.32	9.53	19.91
SiCN	33.42	34.99	21.56	10.03
Carbon	-	84.13	1.37	14.5

Figure 8.7 – High-resolution XPS spectra of the (a) SiCN-40C-a, (b) SiCN-40C-i, (c) SiCN-70C-a, and (d) SiCN-70C-i fiber mats

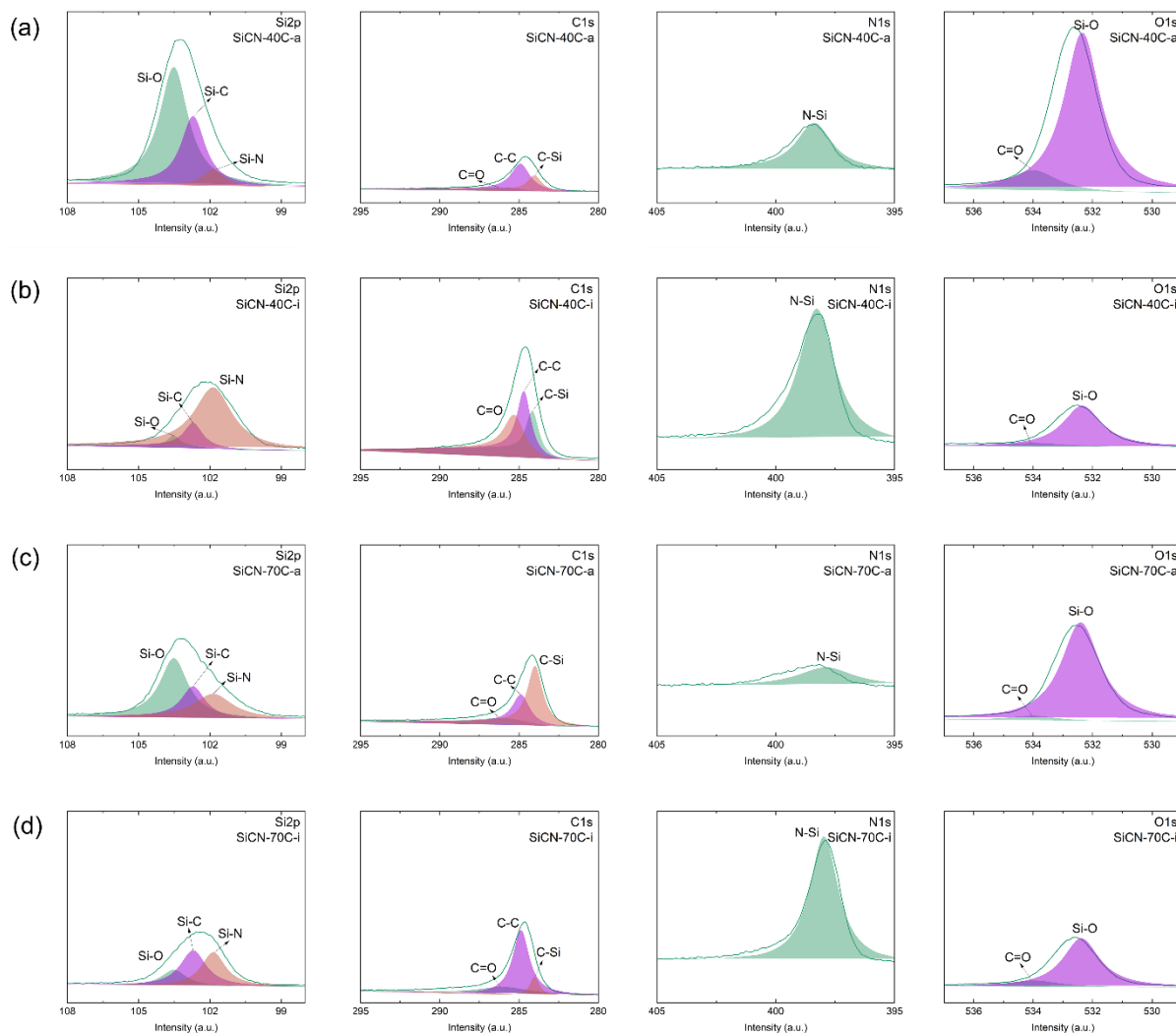
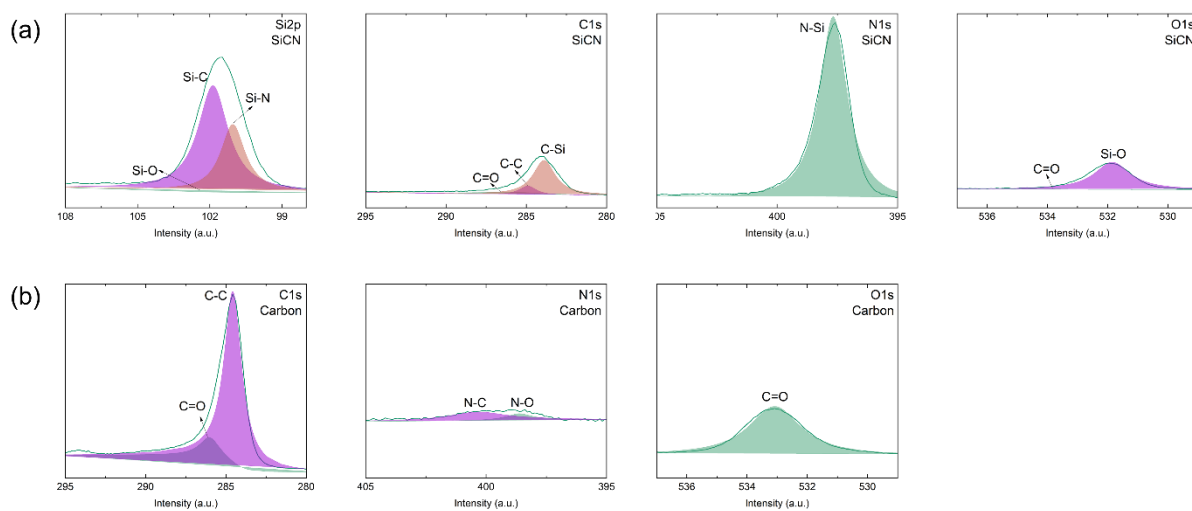


Figure 8.8 – High-resolution XPS spectra of the (a) SiCN and (b) carbon fiber mats



For SiCN-40C-a, SiCN-40C-i, SiCN-70C-a, and SiCN-70C-i fiber mats, an initial charge of 773 mAh g⁻¹, 299 mAh g⁻¹, 690 mAh g⁻¹, and 285 mAh g⁻¹ was obtained with Coulombic efficiency of 51%, 55%, 63%, and 58%, respectively (Table 8.3). The electronegativity values of oxygen and nitrogen are 3.5 and 3.0, respectively. The SiCN-40C-a and SiCN-70C-a electrodes showed increased levels of oxygen coming from the air during electrospinning since silicon more readily reacts with electronegative oxygen than nitrogen. High lithiation capacities observed here for SiCN-40C-a and SiCN-70C-a are due to the increased attraction of Li⁺ by oxygen in the Si-C-O network because of the pronounced ionic character of Si-O bonds with high electron density on the oxygen atom. A previous study has shown that when oxygen is replaced by nitrogen (e.g., high N/O ratio in SiCNO), the ceramic becomes less attractive for Li⁺ ions due to the more covalent character of Si-N bonds and lower electron density on the nitrogen atom resulting in less capture of Li⁺ in the ceramic matrix [41], as confirmed by the decreased electrochemical performance of the LIB electrodes in the current study. Similarly, the high capacity of C-rich SiCN prepared in air has been previously attributed to the presence of high content of disordered carbon and the presence of oxygen in the SiCN phase [6]. Here, when oxygen was introduced to the SiCN system and the O/N ratio was 14.2 and 12.6 respectively for SiCN-40C-a and SiCN-70C-a, the reversible capacity of the anodes was increased and initial capacities higher than 600 mA h g⁻¹ were obtained [42]. The O/N ratio of SiCN-40C-i and SiCN-70C-i was respectively 1.5 and 2.1.

Table 8.3 – Charge and discharge capacities with respective Coulombic efficiency of 1st and 2nd cycles of fiber mat electrodes

Sample	Cycle index	Charge capacity (mAh g ⁻¹)	Discharge capacity (mAh g ⁻¹)	Coulombic efficiency (%)
SiCN-40C-a	1	773	1519	51
	2	679	782	87
SiCN-40C-i	1	299	546	55
	2	298	332	90
SiCN-70C-a	1	690	1088	63
	2	667	698	96
SiCN-70C-i	1	285	489	58
	2	291	307	95
SiCN	1	6	14	39
	2	7	9	75
Carbon	1	176	244	72
	2	177	184	96

Previous research focused more on SiCO fiber mat electrodes than SiCN systems for LIBs. For example, polysiloxane-derived SiCO electrodes shaped through electrospinning have shown a first-cycle charge capacity ranging from 400 to 924 mA h g⁻¹ [3,18,21,22,43]. In another work, a SiCN/graphite ceramic composite was fabricated by pyrolyzing a mixture of commercial-grade graphite powder (75 wt%) with a crosslinked polysilazane (25 wt%). This material had a charge capacity of 266 mA h g⁻¹ and Coulombic efficiency of 62% [31], which is very similar to the SiCN-70C-i electrode prepared in this work (285 mAh g⁻¹ and 58%).

In terms of Li⁺ insertion/extraction, the materials exhibited higher capacity than that of the sum of components SiCN and carbon. Free carbon domains in the SiCN-C materials, derived from PAN and some amount from polysilazane, are supposed to be active sites for Li⁺ insertion [44], while the amorphous structure of SiCN provides a pathway for Li⁺ transfer, resulting in a synergistic effect of the SiCN-C electrodes. It is supposed that Li⁺ insertion is firstly absorbed in the nanovoid sites, and then it is accommodated by the Si-C-N tetrahedral units, free carbon, and topological defects at the edge of or within the segregated carbon network [45]. Moreover, as already mentioned, the nano-holes or nano-channels in the SiCN network provide many smooth Li⁺ transfer channels, which improved the electrochemical dynamic properties.

For SiCN-C samples, the free carbon phase played likely a dominant role in bringing 1st cycle irreversible capacities due to Li⁺ capturing in some pores and voids between carbon layers [41]. The relationship between the charge capacity and the carbon content is observed through diminishing 1st cycle irreversible capacity with higher carbon precursor content (Table 8.3). Carbon electrodes such as graphite have a low theoretical capacity of 372 mAh g⁻¹ [46], as also observed for the carbon electrode prepared here with a charge capacity of 176 mAh g⁻¹ in the 1st cycle. Thus, a certain equilibrium between the ceramic and carbon has to be maintained to achieve high capacity and stable performance concerning continuous Li⁺ insertion/extraction. The SiCN anode showed very low charge capacities (6 mAh g⁻¹) with Coulombic efficiency lower than 80% due to its low electrical conductivity resulting from low free carbon content (C-C) (Figure 8.8a), which is in accordance with the literature [47,48]. Thus, it is supposed that the major portion of the electrochemical capacity in SiCN is due to reversible Li⁺ adsorption in the disordered carbon phase through intercalation and not the conventional alloying reaction with Si, which involves the breakage/distortion of Si-Si bonds to generate new Si-Li bonds. The alloying occurring in Si-based anodes may result in material delamination, particle cracking, recurrent dynamic creation of SEI layers, and ineffective electron transfer [49],

however, these drawbacks are not expected to occur with the SiCN-C anodes prepared here. The charge capacity in 1st cycle of SiCN electrodes is usually based on electrodes prepared through the screen-printing method with values of 313 mA h g⁻¹ for 3D-CNT SiCN [48], 447 mA h g⁻¹ for C-rich SiCN [8], and 900 mA h g⁻¹ for NaOH-treated SiCN [50]. These values are higher than observed in the present work, however, the elimination of conducting agents, collector, binder, and solvents obtained with free-standing mats could provide positive environmental impacts and cost reduction.

In the second cycle, the electrodes showed a Coulombic efficiency of 87% (SiCN-40C-a), 90% (SiCN-40C-i), 96% (SiCN-70C-a), and 95% (SiCN-70C-i). The lower Coulombic efficiency observed for SiCN-40C-a is attributed to lithium reacting with oxygen present in their structure generating Li₂O₃, as mentioned previously, and also to lower free carbon content. For SiCN-70C-a and SiCN-70C-i, the efficiency was very similar due to the high carbon content present in these samples.

Differential capacity plots (Figure 8.9), showed Li⁺ ions diffusing in or out of the SiCN-C electrodes at a given voltage with distinct regions: a sharp cathodic peak around 0.02–0.15 V, corresponding to Li⁺ insertion into disordered carbon [5,11,46,51]; a sharp cathodic peak at 0.2 V, reflecting SiOC/SiO_x lithiation since this is observed for SiCN-40C-a and SiCN-70C-a containing high oxygen content [52,53]; and a broad cathodic peak at 0.7–0.8 V, indicating the availability of multiple Li-ion intercalation phases in the ceramic materials and SEI formation [54]. The broad anodic region at 0.07–0.95 V is ascribed to the interaction between Li⁺ and the Si-N and Si-O network [55]. Moreover, the materials electrospun in nitrogen, (i.e., SiCN-40C-i and SiCN-70C-i), demonstrated a broad cathodic peak at 0.42–0.5 V due to the lithiation and delithiation of Li⁺ in the amorphous SiCN structure (Figure 8.9b and Figure 8.9d), since it was also observed in the SiCN electrode (Figure 8.10a). Various peaks ranging from 0.67 to 1.07 V were also observed in the carbon fiber mat (Figure 8.10b), due to the decomposition of the electrolyte and SEI formation [56,57]. The oxidation peak at 0.1 V observed in the carbon electrode, not observed in the SiCN-C electrodes, corresponds to Li⁺ deintercalation from graphitic carbon [58]. In the second cycle, no peak was found in the profile of the SiCN-C electrodes, suggesting that no new phases were formed toward lithium intercalation and that a stable SEI was formed.

Figure 8.9 – Differential capacity (Q) and V (voltage) curves of the (a-d) SiCN-40C-a, SiCN-40C-i, SiCN-70C-a, and SiCN-70C-i electrodes

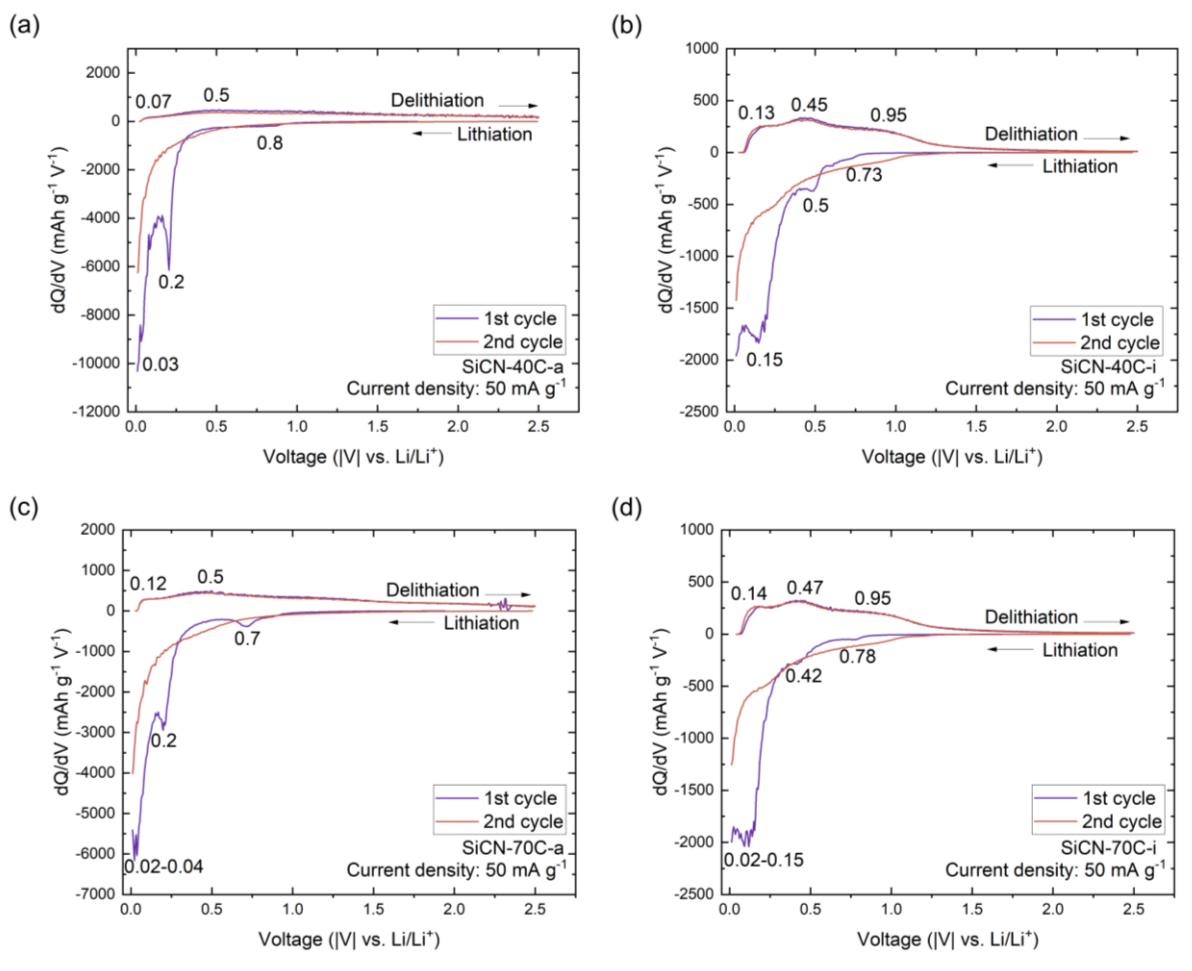
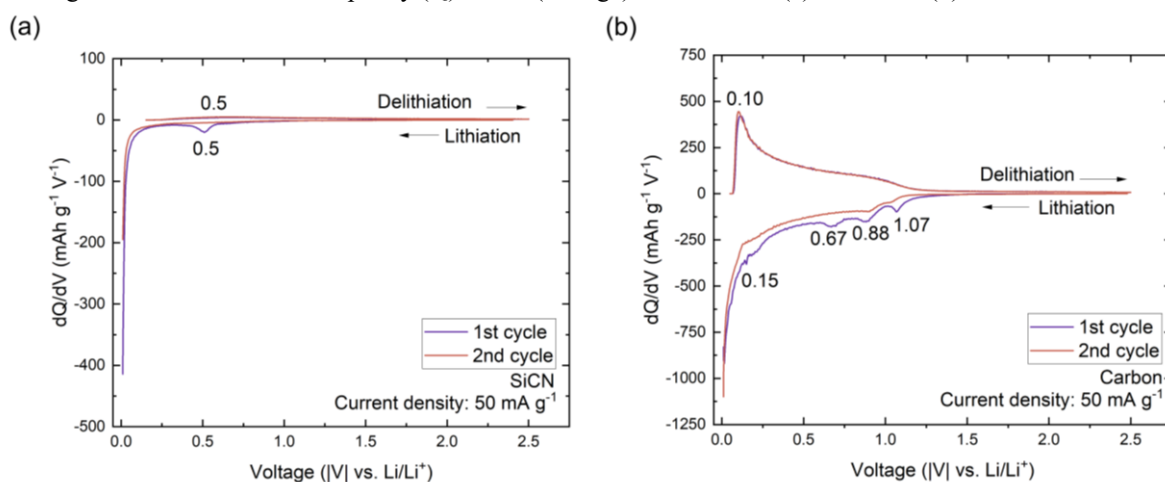


Figure 8.10 – Differential capacity (Q) and V (voltage) curves of the (a) SiCN and (b) carbon electrodes

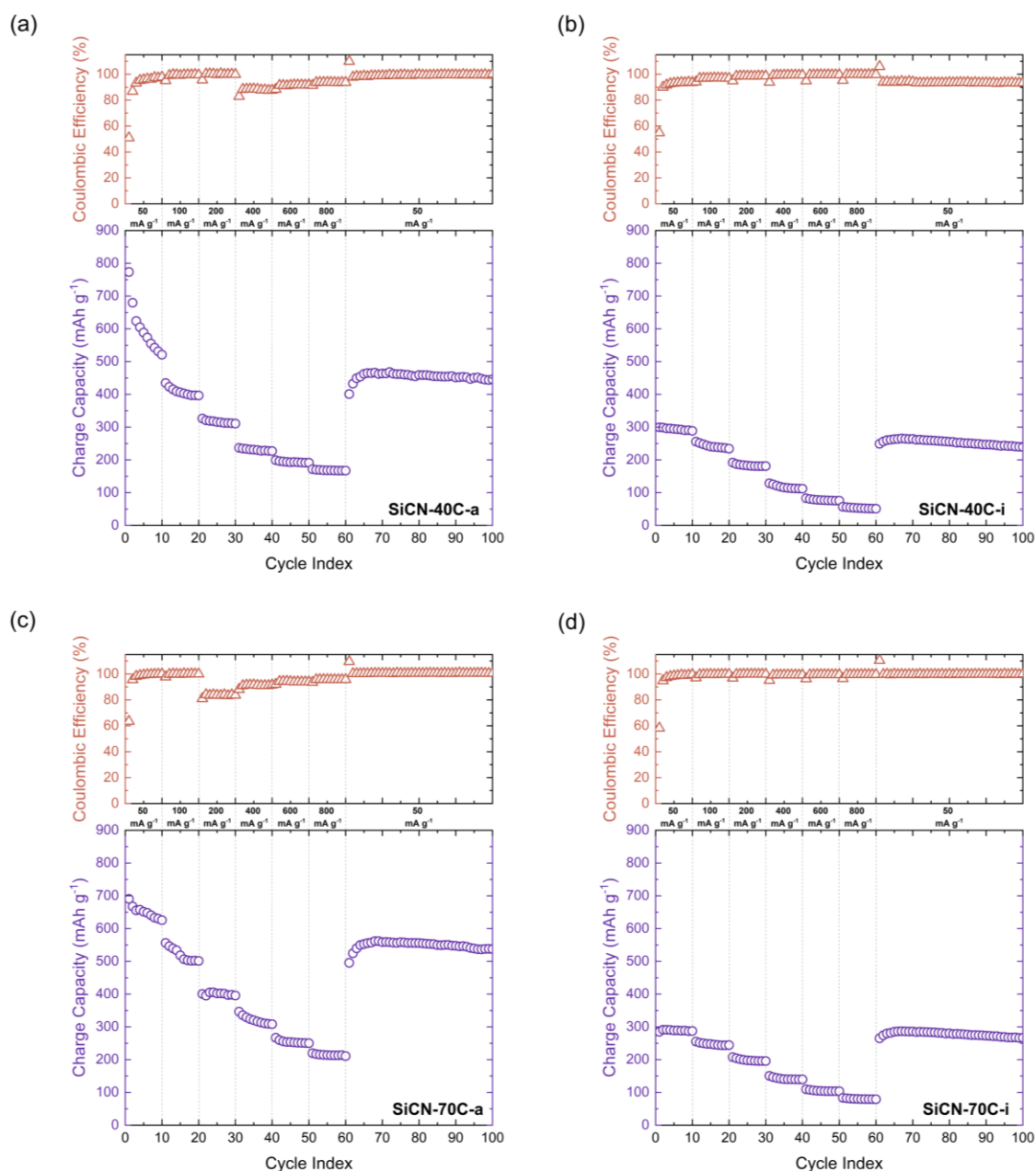


This study also tested the long-term stability and rate capability of the SiCN-C fiber mats as electrode materials for LIBs. The charge capacities of the samples were tested at

different current densities (Figure 8.11). When tested for cycling stability after 10 cycles at 50 mA g^{-1} , the SiCN-40C-a electrode showed decreased performance, and the charge capacity dropped to 521 mA h g^{-1} with Coulombic efficiency of 98% compared to the SiCN-70C-a electrode with 629 mA h g^{-1} and Coulombic efficiency of 100%. In contrast, the samples electrospun in nitrogen showed similar capacities (i.e., 289 mA h g^{-1} and Coulombic efficiency of 94% for SiCN-40C-i; 288 mA h g^{-1} and Coulombic efficiency of 100% for SiCN-70C-a). These results demonstrate the influence of the Si-O network on the cycling stability of the PDC electrodes. Compared to fiber mats electrospun in protective atmosphere, the SiCN-40C-a and SiCN-70C-a electrodes showed a high capacity loss in the initial cycles due to excessive oxygen, which is considered a source of high irreversible capacity and significant voltage hysteresis [30]. Furthermore, the Coulombic efficiency of SiCN-70C-i was greater than SiCN-40C-a due to the increased free carbon content.

Increasing the current rate decreased the capacity of the SiCN-C electrodes, although most of their original capacity could be regained when the current density decreased back to 50 mA g^{-1} , proving that the materials have sufficient capacity recovery capabilities. Once the electrodes returned to lower current cycling, SiCN-40C-a, SiCN-40C-i, SiCN-70C-a, and SiCN-70C-i exhibited respectively 85%, 90%, 86%, and 98% of the initial capacity. Recovery of the initial reversible capacity after fast cycling showed that the materials were not damaged under the conditions of fast charge/discharge rates.

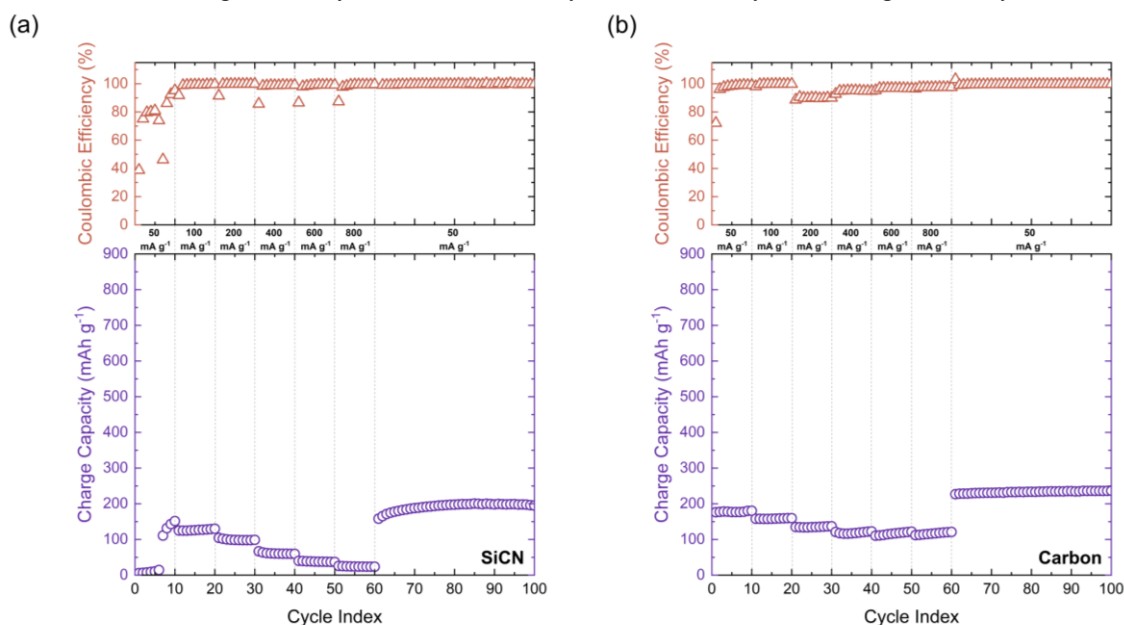
Figure 8.11 – Long-term stability and rate capability data of the SiCN-C for 100 cycles at different current densities. The cells were subjected to symmetric cycling at current densities of 50, 100, 200, 400, 600, and 800 mA g⁻¹ for 10 cycles each followed by a current density of 50 mA g⁻¹ for 40 cycles



The SiCN electrode showed a capacity increase during the initial 10 cycles due to a structural reorganization (i.e., microstructure opening of the material during lithium intercalation/extraction to form new conducting paths) (Figure 8.12a). However, the Coulombic efficiency decreased to 46% after seven cycles, meaning that more lithium ions were trapped, but not discharged by the SiCN matrix. After 10 cycles, the capacity of the SiCN electrode remained steady with no capacity decay because the active materials became stable and electrochemically reversible. There are two models proposed in the literature to explain the

lithium storage mechanism in polymer-derived SiCO ceramics: mixed Si-C-O tetrahedra as active sites for Li^+ storage [59]; and interstitial spaces or edges between the graphene layers as the primary storing sites, the Si-O-C phase and the micropores [60]. Since the SiCN has a similar structure to the SiCO, the reversible capacity measured during the first discharge has been ascribed to the low content of free carbon (C-C) as presented in the XPS spectrum. Additionally, the carbon electrode exhibited steady capacity, but with low charge capacities at various current densities (Figure 8.12b), which is in accordance with the literature on carbon-based anodes [49].

Figure 8.12 – Long-term stability and rate capability data of the SiCN and carbon for 100 cycles at different current densities. The cells were subjected to symmetric cycling at current densities of 50, 100, 200, 400, 600, and 800 mA g^{-1} for 10 cycles each followed by a current density of 50 mA g^{-1} for 40 cycles



Of all the samples in this study, the SiCN-70C-a anode exhibited the highest performance, delivering the highest capacity of about 518, 402, 320, 254, and 214 mA h g^{-1} at each of the applied current densities of 100, 200, 400, 600, and 800 mA g^{-1} , respectively. Carbon and oxygen contents in the SiCN-70C-a fiber mat provided additional Li-ion storage sites and improved the electrochemical properties of SiCN as already explained before. After 100 cycles, the SiCN-70C-a fiber mat electrode recovered most of the capacity with 538 mA h g^{-1} at 50 mA g^{-1} . This value is comparable to or even higher than SiCO fiber mat electrodes (e.g., 281 mA h g^{-1} after 100 cycles at 35 mA g^{-1} [15], 500 mA h g^{-1} after 10 cycles at 50 mA g^{-1} [22], 543 mA h g^{-1} after 200 cycles at 50 mA g^{-1} [18], and 669 mA h g^{-1} after 80 cycles at 50 mA g^{-1}

[43]). Compared to SiCN electrodes prepared through the screen printing method, the SiCN-70C-a electrode showed higher charge capacity, (e.g., 326 mA h g⁻¹ at 100 mA g⁻¹ after 30 cycles for 3D-CNT SiCN [48], 458 mA h g⁻¹ at 20 mA g⁻¹ after 134 cycles for C-rich SiCN [9], and 534 mA h g⁻¹ at 72 mA g⁻¹ after 100 cycles for C-rich SiCN [8]). Despite the irreversible capacity and voltage hysteresis, the SiCN-70C-a demonstrated attractive values of recovered capacity and outstanding cyclability for 100 cycles even at high current rates, making this material a promising anode material for energy devices.

In summary, we have demonstrated the manufacturing of SiCN-C freestanding fiber mats as stable and durable battery electrodes. The synergistic effect of the SiCN-C electrodes enhanced the electrochemical performance of LIBs, and the SiCN provided a pathway for Li⁺ transfer, while free carbon improved electronic conductivity and the availability of active sites for Li⁺. Nevertheless, a certain equilibrium between SiCN and carbon must be maintained to achieve high capacity and stable performance for continuous Li⁺ insertion/extraction. In addition, the electrospinning atmosphere influenced the composition of the fiber mats. Electrospinning in air increase oxygen content in the polysilazane-derived SiCN, generating thus SiCNO ceramics. The SiCN-C-a fiber mat electrodes exhibited higher capacities at different current densities due to oxygen attracting the Li-ions to the materials. However, a correlation was observed between both the irreversible capacity and voltage hysteresis with the oxygen content of the SiCN-C electrodes shaped in air. The SiCN-C-i electrodes electrospun in protective atmosphere demonstrated improved cycling stability and significantly lower losses with increasing cycling current rates, which may be attributed to the presence of free carbon. These findings support electrospinning for the highly controlled production of SiCN fiber mat electrodes and even for other advanced applications and will prompt further research on PDC fibers.

8.4 CONCLUSIONS

This study explored the influence of the electrospinning atmosphere conducted in air or a protective atmosphere on SiCN fiber mats applied as LIB electrodes. Electron microscopy characterization revealed the morphology of smoother, more uniform, and thinner fibers when polysilazane was electrospun in nitrogen. In addition, various compositions in the SiCN-C fiber mats were obtained, as confirmed through XPS analysis. The SiCN-C materials showed promising electrochemical results for capacity and stability when compared to SiCN and carbon

electrodes processed under similar conditions. The main reasons may be as follows: first, the improvement of capacity is due to the increasing free carbon content in the SiCN materials which are Li^+ ion active sites, and SiCN with smooth transfer channels for Li^+ mobility to attain a high charge current improving the electrochemical dynamic properties. Second, the SiCN fiber mats electrospun in air contained oxygen that is easy to link with Li^+ ions, leading to the high capacity. Third, the improvement of cycle stability is due to the stable mechanical structure of SiCN-C fiber mats without breaking/disintegrating.

The strong dependence of the polymer-derived SiCN materials on their compositions and structures suggests the potential to enhance the electrochemical performance of these materials through molecular design and/or the control of material structure including the electrospinning atmosphere, as demonstrated in this work. The atmosphere in which the polymers are electrospun has a great influence on the morphology and composition of the ceramic fibers. The electrospinning and PDC processes could beneficially impact the preparation of Si-based fiber mat electrodes by controlling carbon, nitrogen, and oxygen content for electrochemical energy storage devices. Therefore, PDCs with enhanced Li-ion storage capacity, long-term safety, and stability may be developed as freestanding and binder-free fiber mats to meet the requirements of LIB electrodes.

8.5 ACKNOWLEDGEMENTS

The authors thank CAPES and Deutscher Akademischer Austauschdienst (DAAD) for supporting this work within the project PROBRAL (Grant n° 88887.368756/2019-00). This study was financed in part by the Coordenação de Aperfeiçoamento de Pessoal de Nível Superior - Brasil (CAPES) - Finance Code 001 and CNPq - Brasil (Grant n° 442149/2018-2). GS thanks for financial support from National Science Foundation (NSF) Partnerships for International Research and Education (PIRE) grant number 1743701. HR thanks Sonjoy Dey for his help with cell assembly. The XPS analysis was performed in part in the Nebraska Nanoscale Facility: National Nanotechnology Coordinated Infrastructure and the Nebraska Center for Materials and Nanoscience (and/or NERCF), which are supported by the National Science Foundation under Award ECCS: 2025298, and the Nebraska Research Initiative.

8.6 AUTHORS' CONTRIBUTIONS

The paper is mainly based on the work of the first author and author of this thesis Heloisa Ramlow. This work was conducted in collaboration with the Nanoscience and Engineering Laboratory (Kansas State University, USA). The precise contributions of each author are listed below (Table 8.4).

Table 8.4 – Authors' contributions to Chapter 8

Author	Contribution
Ramlow, H.	Conceptualized the work, wrote the manuscript
Marangoni, C.	Gave conceptual and scientific advice, helped in the scientific evaluation and editing of the manuscript
Motz, G.	Gave conceptual and scientific advice, helped in the scientific evaluation and editing of the manuscript
Singh, G.	Gave conceptual and scientific advice, helped in the scientific evaluation and editing of the manuscript
Machado, R.	Gave conceptual and scientific advice, helped in the scientific evaluation and editing of the manuscript

8.7 REFERENCES

- [1] S. Mukherjee, S. Bin Mujib, D. Soares, G. Singh, Electrode materials for high-performance sodium-ion batteries, *Materials* (Basel). 12 (2019) 1952. <https://doi.org/10.3390/ma12121952>.
- [2] Q. Wen, Z. Yu, R. Riedel, The fate and role of in situ formed carbon in polymer-derived ceramics, *Prog. Mater. Sci.* 109 (2020) 100623. <https://doi.org/10.1016/j.pmatsci.2019.100623>.
- [3] S. Bin Mujib, F. Ribot, C. Gervais, G. Singh, Self-supporting carbon-rich SiOC ceramic electrodes for lithium-ion batteries and aqueous supercapacitors, *RSC Adv.* 11 (2021) 35440–35454. <https://doi.org/10.1039/d1ra05968h>.
- [4] Y. Feng, G.-X. Du, X.-J. Zhao, E.-C. Yang, Preparation and electrochemical performance of SiCN–CNTs composite anode material for lithium ion batteries, *J. Appl. Electrochem.* 41 (2011) 999–1002. <https://doi.org/10.1007/s10800-011-0322-z>.
- [5] J. Kaspar, G. Mera, A.P. Nowak, M. Graczyk-Zajac, R. Riedel, Electrochemical study of lithium insertion into carbon-rich polymer-derived silicon carbonitride ceramics, *Electrochim. Acta.* 56 (2010) 174–182. <https://doi.org/10.1016/j.electacta.2010.08.103>.
- [6] M. Graczyk-Zajac, G. Mera, J. Kaspar, R. Riedel, Electrochemical studies of carbon-rich polymer-derived SiCN ceramics as anode materials for lithium-ion batteries, *J. Eur. Ceram. Soc.* 30 (2010) 3235–3243. <https://doi.org/10.1016/j.jeurceramsoc.2010.07.010>.

- [7] L.M. Reinold, M. Graczyk-Zajac, Y. Gao, G. Mera, R. Riedel, Carbon-rich SiCN ceramics as high capacity/high stability anode material for lithium-ion batteries, *J. Power Sources*. 236 (2013) 224–229. <https://doi.org/10.1016/j.jpowsour.2013.02.046>.
- [8] M. Storch, D. Vrankovic, M. Graczyk-Zajac, R. Riedel, The influence of pyrolysis temperature on the electrochemical behavior of porous carbon-rich SiCN polymer-derived ceramics, *Solid State Ionics*. 315 (2018) 59–64. <https://doi.org/10.1016/j.ssi.2017.11.032>.
- [9] L.M. Reinold, Y. Yamada, M. Graczyk-Zajac, H. Munakata, K. Kanamura, R. Riedel, The influence of the pyrolysis temperature on the electrochemical behavior of carbon-rich SiCN polymer-derived ceramics as anode materials in lithium-ion batteries, *J. Power Sources*. 282 (2015) 409–415. <https://doi.org/10.1016/j.jpowsour.2015.02.074>.
- [10] J. Dahn, A. Wilson, W. Xing, G. Zank, Electrodes for lithium ion batteries using polysilazanes ceramic with lithium, 1997.
- [11] L. David, R. Bhandavat, U. Barrera, G. Singh, Silicon oxycarbide glass-graphene composite paper electrode for long-cycle lithium-ion batteries, *Nat. Commun.* 7 (2016) 10998. <https://doi.org/10.1038/ncomms10998>.
- [12] S. Bin Mujib, Z. Ren, S. Mukherjee, D.M. Soares, G. Singh, Design, characterization, and application of elemental 2D materials for electrochemical energy storage, sensing, and catalysis, *Mater. Adv.* 1 (2020) 2562–2591. <https://doi.org/10.1039/D0MA00428F>.
- [13] A.A. Hamedani, C.W. Ow-Yang, S. Hayat Soytaş, Silicon nanocrystals-embedded carbon nanofibers from hybrid polyacrylonitrile – TEOS precursor as high-performance lithium-ion battery anodes, *J. Alloys Compd.* 909 (2022) 164734. <https://doi.org/10.1016/j.jallcom.2022.164734>.
- [14] H. Tetik, J. Orangi, G. Yang, K. Zhao, S. Bin Mujib, G. Singh, M. Beidaghi, D. Lin, 3D printed MXene aerogels with truly 3D macrostructure and highly engineered microstructure for enhanced electrical and electrochemical performance, *Adv. Mater.* 34 (2022) 2104980. <https://doi.org/10.1002/adma.202104980>.
- [15] A. Tolosa, M. Widmaier, B. Krüner, J.M. Griffin, V. Presser, Continuous silicon oxycarbide fiber mats with tin nanoparticles as a high capacity anode for lithium-ion batteries, *Sustain. Energy Fuels*. 2 (2018) 215–228. <https://doi.org/10.1039/c7se00431a>.
- [16] E.S. Pampal, E. Stojanovska, B. Simon, A. Kilic, A review of nanofibrous structures in lithium ion batteries, *J. Power Sources*. 300 (2015) 199–215. <https://doi.org/10.1016/j.jpowsour.2015.09.059>.
- [17] M.S. Kolathodi, L. David, M.A. Abass, G. Singh, Polysiloxane-functionalized graphene oxide paper: pyrolysis and performance as a Li-ion battery and supercapacitor electrode, *RSC Adv.* 6 (2016) 74323–74331. <https://doi.org/10.1039/C6RA15746G>.
- [18] M. Ma, H. Wang, X. Li, K. Peng, L. Xiong, X. Du, Free-standing SiOC/nitrogen-doped carbon fibers with highly capacitive Li storage, *J. Eur. Ceram. Soc.* 40 (2020) 5238–5246. <https://doi.org/10.1016/j.ceramint.2020.11.031>.
- [19] S. Dey, S. Bin Mujib, G. Singh, Enhanced Li-ion rate capability and stable efficiency enabled by MoSe₂ nanosheets in polymer-derived silicon oxycarbide fiber electrodes, *Nanomaterials*. 12 (2022) 553. <https://doi.org/10.3390/nano12030553>.
- [20] Q. Chen, D. Jia, B. Liang, Z. Yang, Y. Zhou, D. Li, R. Riedel, T. Zhang, C. Gao, Electrospinning of pure polymer-derived SiBCN nanofibers with high yield, *Ceram. Int.* 47 (2021) 10958–10964. <https://doi.org/10.1016/j.ceramint.2020.12.215>.
- [21] Z. Sang, X. Yan, L. Wen, D. Su, Z. Zhao, Y. Liu, H. Ji, J. Liang, S.X. Dou, A graphene-modified flexible SiOC ceramic cloth for high-performance lithium storage, *Energy Storage Mater.* 25 (2019) 876–884. <https://doi.org/10.1016/j.ensm.2019.11.014>.
- [22] S. Bin Mujib, R. Cuccato, S. Mukherjee, G. Franchin, P. Colombo, G. Singh, Electrospun

- SiOC ceramic fiber mats as freestanding electrodes for electrochemical energy storage applications, *Ceram. Int.* 46 (2020) 3565–3573. <https://doi.org/10.1016/j.ceramint.2019.10.074>.
- [23] S. Sarkar, A. Chunder, W. Fei, L. An, L. Zhai, Superhydrophobic mats of polymer-derived ceramic fibers, *J. Am. Ceram. Soc.* 91 (2008) 2751–2755. <https://doi.org/10.1111/j.1551-2916.2008.02500.x>.
- [24] D.G. Shin, D.H. Riu, H.E. Kim, Web-type silicon carbide fibers prepared by the electrospinning of polycarbosilanes, *J. Ceram. Process. Res.* 9 (2008) 209–214.
- [25] X. Guo, F. Xiao, J. Li, H. Zhang, Q. Hu, G. Li, H. Sun, Y. Feng, X. Guo, J. Lu, J. Liu, G. Wang, H. Gong, Enhanced electromagnetic wave absorption performance of SiCN(Fe) fibers by in-situ generated Fe₃Si and CNTs, *Ceram. Int.* 47 (2021) 19582–19594. <https://doi.org/10.1016/j.ceramint.2021.03.296>.
- [26] X. Guo, F. Xiao, J. Li, H. Zhang, Q. Hu, G. Li, H. Sun, Fe-doped SiCN composite fibers for electromagnetic waves absorption, *Ceram. Int.* 47 (2021) 1184–1190. <https://doi.org/10.1016/j.ceramint.2020.08.236>.
- [27] F. Xiao, H. Sun, J. Li, X. Guo, H. Zhang, J. Lu, Z. Pan, J. Xu, Electrospinning preparation and electromagnetic wave absorption properties of SiCN fibers, *Ceram. Int.* 46 (2020) 12773–12781. <https://doi.org/10.1016/j.ceramint.2020.02.046>.
- [28] Y. Liu, W. Yang, X. He, H. Hou, Tailored synthesis of amorphous SiCNO mesoporous fibers through combining a facile electrospinning process and microwave-assisted pyrolysis, *Ceram. Int.* 45 (2019) 8640–8645. <https://doi.org/10.1016/j.ceramint.2019.01.184>.
- [29] V. Fasano, M. Moffa, A. Camposeo, L. Persano, D. Pisignano, Controlled atmosphere electrospinning of organic nanofibers with improved light emission and waveguiding properties, *Macromolecules.* 48 (2015) 7803–7809. <https://doi.org/10.1021/acs.macromol.5b01377>.
- [30] P. Dibandjo, M. Graczyk-Zajac, R. Riedel, V.S. Pradeep, G.D. Soraru, Lithium insertion into dense and porous carbon-rich polymer-derived SiOC ceramics, *J. Eur. Ceram. Soc.* 32 (2012) 2495–2503. <https://doi.org/10.1016/j.jeurceramsoc.2012.03.010>.
- [31] R. Kolb, C. Fasel, V. Liebau-Kunzmann, R. Riedel, SiCN/C-ceramic composite as anode material for lithium ion batteries, *J. Eur. Ceram. Soc.* 26 (2006) 3903–3908. <https://doi.org/10.1016/j.jeurceramsoc.2006.01.009>.
- [32] L. David, D. Asok, G. Singh, Synthesis and extreme rate capability of Si-Al-C-N functionalized carbon nanotube spray-on coatings as li-ion battery electrode, *ACS Appl. Mater. Interfaces.* 6 (2014) 16056–16064. <https://doi.org/10.1021/am5052729>.
- [33] C. Liu, Z.G. Neale, G. Cao, Understanding electrochemical potentials of cathode materials in rechargeable batteries, *Mater. Today.* 19 (2016) 109–123. <https://doi.org/10.1016/j.mattod.2015.10.009>.
- [34] S. Wang, X. Hu, Y. Dai, Preparation and electrochemical performance of polymer-derived SiBCN-graphene composite as anode material for lithium ion batteries, *Ceram. Int.* 43 (2017) 1210–1216. <https://doi.org/10.1016/j.ceramint.2016.10.065>.
- [35] D. Ahn, R. Raj, Thermodynamic measurements pertaining to the hysteretic intercalation of lithium in polymer-derived silicon oxycarbide, *J. Power Sources.* 195 (2010) 3900–3906. <https://doi.org/10.1016/j.jpowsour.2009.12.116>.
- [36] D. Su, Y.L. Li, Y. Feng, J. Jin, Electrochemical properties of polymer-derived SiCN materials as the anode in lithium ion batteries, *J. Am. Ceram. Soc.* 92 (2009) 2962–2968. <https://doi.org/10.1111/j.1551-2916.2009.03317.x>.
- [37] A. Vashisth, S. Khatri, S.H. Hahn, W. Zhang, A.C.T. Van Duin, M. Naraghi, Mechanical size effects of amorphous polymer-derived ceramics at the nanoscale: Experiments and

- ReaxFF simulations, *Nanoscale*. 11 (2019) 7447–7456. <https://doi.org/10.1039/c9nr00958b>.
- [38] Y. Feng, N. Feng, Y. Wei, Y. Bai, Preparation and improved electrochemical performance of SiCN-graphene composite derived from poly(silylcarbodiimide) as Li-ion battery anode, *J. Mater. Chem. A*. 2 (2014) 4168–4177. <https://doi.org/10.1039/c3ta14441k>.
- [39] M.A. Abass, A.A. Syed, C. Gervais, G. Singh, Synthesis and electrochemical performance of a polymer-derived silicon oxycarbide/boron nitride nanotube composite, *RSC Adv.* 7 (2017) 21576–21584. <https://doi.org/10.1039/c7ra01545c>.
- [40] M. Wilamowska, V.S. Pradeep, M. Graczyk-Zajac, R. Riedel, G.D. Soraru, Tailoring of SiOC composition as a way to better performing anodes for Li-ion batteries, *Solid State Ionics*. 260 (2014) 94–100. <https://doi.org/10.1016/j.ssi.2014.03.021>.
- [41] M. Graczyk-Zajac, L.M. Reinold, J. Kaspar, P.V.W. Sasikumar, G.D. Soraru, R. Riedel, New insights into understanding irreversible and reversible lithium storage within SiOC and SiCN ceramics, *Nanomaterials*. 5 (2014) 233–245. <https://doi.org/10.3390/nano5010233>.
- [42] D. Ahn, R. Raj, Cyclic stability and C-rate performance of amorphous silicon and carbon based anodes for electrochemical storage of lithium, *J. Power Sources*. 196 (2011) 2179–2186. <https://doi.org/10.1016/j.jpowsour.2010.09.086>.
- [43] Y. Li, Y. Hu, Y. Lu, S. Zhang, G. Xu, K. Fu, S. Li, C. Chen, L. Zhou, X. Xia, X. Zhang, One-dimensional SiOC/C composite nanofibers as binder-free anodes for lithium-ion batteries, *J. Power Sources*. 254 (2014) 33–38. <https://doi.org/10.1016/j.jpowsour.2013.12.044>.
- [44] S.H. Baek, L.M. Reinold, M. Graczyk-Zajac, R. Riedel, F. Hammerath, B. Büchner, H.J. Grafe, Lithium dynamics in carbon-rich polymer-derived SiCN ceramics probed by nuclear magnetic resonance, *J. Power Sources*. 253 (2014) 342–348. <https://doi.org/10.1016/j.jpowsour.2013.12.065>.
- [45] H. Sun, K. Zhao, Atomistic origins of high capacity and high structural stability of polymer-derived SiOC anode materials, *ACS Appl. Mater. Interfaces*. 9 (2017) 35001–35009. <https://doi.org/10.1021/acsami.7b10906>.
- [46] Y. Feng, S. Dou, Y. Wei, Y. Zhang, X. Song, X. Li, V.S. Battaglia, Preparation and capacity-fading investigation of polymer-derived silicon carbonitride anode for lithium-ion battery, *ACS Omega*. 2 (2017) 8075–8085. <https://doi.org/10.1021/acsomega.7b01462>.
- [47] M. Wilamowska, M. Graczyk-Zajac, R. Riedel, Composite materials based on polymer-derived SiCN ceramic and disordered hard carbons as anodes for lithium-ion batteries, *J. Power Sources*. 244 (2013) 80–86. <https://doi.org/10.1016/j.jpowsour.2013.03.137>.
- [48] J. Zhang, C. Xu, Z. Liu, W. Wang, X. Xin, L. Shen, X. Zhou, J. Zhou, Q. Huang, Enhanced rate capability of polymer-derived SiCN anode material for electrochemical storage of lithium with 3-D carbon nanotube network dispersed in nanoscale, *J. Nanosci. Nanotechnol.* 15 (2015) 3067–3075. <https://doi.org/10.1166/jnn.2015.9690>.
- [49] P.U. Nzereogu, A.D. Omah, F.I. Ezema, E.I. Iwuoha, A.C. Nwanya, Anode materials for lithium-ion batteries: A review, *Appl. Surf. Sci. Adv.* 9 (2022) 100233. <https://doi.org/10.1016/j.apsadv.2022.100233>.
- [50] Y. Feng, Y. Wei, Z. Jia, Y. Zhang, V. Battaglia, G. Liu, Polymer-derived and sodium hydroxide-treated silicon carbonitride material as anodes for high electrochemical performance Li-ion batteries, *ChemistrySelect*. 1 (2016) 309–317. <https://doi.org/10.1002/slct.201600046>.
- [51] M. Klett, J.A. Gilbert, S.E. Trask, B.J. Polzin, A.N. Jansen, D.W. Dees, D.P. Abraham,

- Electrode behavior RE-visited: monitoring potential windows, capacity loss, and impedance changes in $\text{Li}_{1.03}(\text{Ni}_{0.5}\text{Co}_{0.2}\text{Mn}_{0.3})\text{O}_{2.97}$ /silicon-graphite full cells, *J. Electrochem. Soc.* 163 (2016) A875–A887. <https://doi.org/10.1149/2.0271606jes>.
- [52] I.E. Monje, N. Sanchez-Ramirez, S.H. Santagneli, P.H. Camargo, D. Bélanger, S.B. Schougaard, R.M. Torresi, In situ-formed nitrogen-doped carbon/silicon-based materials as negative electrodes for lithium-ion batteries, *J. Electroanal. Chem.* 901 (2021) 115732. <https://doi.org/10.1016/j.jelechem.2021.115732>.
- [53] P. Lv, H. Zhao, C. Gao, Z. Du, J. Wang, X. Liu, SiO-C dual-phase glass for lithium ion battery anode with high capacity and stable cycling performance, *J. Power Sources.* 274 (2015) 542–550. <https://doi.org/10.1016/j.jpowsour.2014.10.077>.
- [54] L. David, S. Bernard, C. Gervais, P. Miele, G. Singh, Facile synthesis and high rate capability of silicon carbonitride/boron nitride composite with a sheet-like morphology, *J. Phys. Chem. C.* 119 (2015) 2783–2791. <https://doi.org/10.1021/jp508075x>.
- [55] Z. Wu, W. Lv, X. Cheng, J. Gao, Z. Qian, D. Tian, J. Li, W. He, C. Yang, A nanostructured Si/SiOC composite anode with volume-change-buffering microstructure for lithium-ion batteries, *Chem. – A Eur. J.* 25 (2019) 2604–2609. <https://doi.org/10.1002/chem.201805255>.
- [56] B.-S. Lee, S.-B. Son, K.-M. Park, G. Lee, K.H. Oh, S.-H. Lee, W.-R. Yu, Effect of pores in hollow carbon nanofibers on their negative electrode properties for a lithium rechargeable battery, *ACS Appl. Mater. Interfaces.* 4 (2012) 6702–6710. <https://doi.org/10.1021/am301873d>.
- [57] I. Zeferino González, H.-C. Chiu, R. Gauvin, G.P. Demopoulos, Y. Verde-Gómez, Silicon doped carbon nanotubes as high energy anode for lithium-ion batteries, *Mater. Today Commun.* 30 (2022) 103158. <https://doi.org/10.1016/j.mtcomm.2022.103158>.
- [58] R. Bhandavat, G. Singh, Stable and efficient Li-ion battery anodes prepared from polymer-derived silicon oxycarbide-carbon nanotube shell/core composites, *J. Phys. Chem. C.* 117 (2013) 11899–11905. <https://doi.org/10.1021/jp310733b>.
- [59] P.E. Sanchez-Jimenez, R. Raj, Lithium insertion in polymer-derived silicon oxycarbide ceramics, *J. Am. Ceram. Soc.* 93 (2010) 1127–1135. <https://doi.org/10.1111/j.1551-2916.2009.03539.x>.
- [60] H. Fukui, H. Ohsuka, T. Hino, K. Kanamura, A Si-O-C composite anode: high capability and proposed mechanism of lithium storage associated with microstructural characteristics, *ACS Appl. Mater. Interfaces.* 2 (2010) 999–1008. <https://doi.org/10.1021/am100030f>.

9 CONCLUSIONS

The main contributions of this Ph.D. thesis are here highlighted to the scientific community. Hereby, not only the novelty is emphasized but rather why this work should be considered valuable.

The relevance of the literature review presented in Chapter 3 contributed to the core topic of this thesis. Compiling and critically discussing the efforts and gaps in the literature suggested that much more work on electrospun-based PDC fibers is needed, mainly on processing SiCN e-fibers and their application. In addition, this review work will be a reference for the scientific community in discussing the strategies involved in the preparation of preceramic polymers shaped via electrospinning and converted to PDC fibers.

The rheological characterization of precursor solutions conducted in Chapter 4 is critical in producing identical fiber products from run to run of electrospinning. This is a key characterization technique for developing PDC fibers/fiber mats with the desired physical properties and for controlling the manufacturing process to ensure product quality, especially in the case of advanced ceramics. In addition, the electrospinning optimization using a statistical approach was successfully first applied to preceramic polymer solutions. This leads to working more efficiently by reducing errors and avoiding duplicate work. The precise control of fiber diameter during electrospinning is very crucial for many applications.

The versatility of SiCN precursor and electrospinning was successfully explored in Chapter 5. The influence of precursor molecular conformation highlighted the importance of the PDC route for controlling the desired composition/microstructure of the resulting ceramics. The precipitation of *in-situ* formed carbon depended on the molecular structure of the preceramic polymer and significantly affected the composition, microstructural evolution as well as thermo-oxidative resistance of the fiber mats. Even though the thermo-oxidative resistance of SiCN/C (~600 °C) is lower than SiCN (> 1000 °C, not reported in this work), the results will serve as a basis for future work during the choice of precursor to manufacturing advanced ceramics.

The applicability of the fiber mats prepared in this thesis was ultimately evaluated for advanced applications. Manufacturing new materials for electromagnetic field shielding has become increasingly important due to the rapid development of electronic and information technology. Current electromagnetic field shielding materials mainly include metals and their alloy materials, intrinsic conductive polymer materials and carbon materials. Chapter 6

demonstrated that the incorporation of SiCN into carbon improved the electromagnetic reflection loss in comparison to carbon fiber mats by adjusting the pyrolysis temperature. The pyrolysis temperature also influenced the direct current conductivity of the fiber mats, corroborating its effect on the material structure when employing the PDC process. In Chapter 7, further investigation of ceramic fibers that can effectively shield and even absorb the interference of electromagnetic field is a contribution to the literature with great practical significance. Particularly, this is the first work that investigated in deep the role of carbon in electromagnetic field shielding of SiCN fibers.

In Chapter 8, the influence of the electrospinning atmosphere was proven, which will not only be a fundamental work for processing preceramic polymers fibers, but also other compounds that are sensitive to moisture. The atmosphere choice demonstrated the advantages of PDCs by controlling the composition and structure of the material. It is also highlighted that the electrochemical properties of SiCN fiber mats were first investigated in this thesis. Moreover, this work will encourage more research into Si-based PDC fiber mat electrodes.

In summary, this thesis showed that polysilazane-based materials can be prepared by conventional electrospinning using different strategies that are available to be fully explored, i.e. addition of organic precursor, selective crosslinking of oligosilazane and controlling the electrospinning atmosphere, to tailor the final microstructure of the ceramic. The versatility of preceramic polymers and the feasibility of manufacturing advanced ceramic materials via electrospinning with practical applications were here demonstrated. The novelty of this work is the development of SiCN fiber mats/fibers via electrospinning with further advanced applications, since these materials are still little explored in the literature. This thesis is expected not only to fulfill some of the current gaps within the literature but more importantly, expand the universe of possibilities yet to be unraveled in the development of electrospun ceramic fibers from Si-based preceramic polymers.

10 OUTLOOK

In this thesis, the characterization and application of polysilazane-derived SiCN fiber mats shaped via electrospinning were addressed. Despite the advances obtained here, continuous work is needed for progress in the development of electrospun PDCs. Thus, some ideas for future research are suggested hereafter.

The SiCN fiber mats were successfully manufactured via the electrospinning technique and PDC route, however, they were still quite brittle. This brittleness is attributed to the fibers sticking to each other as Griffith's criterion, thus the crosslinking step needs more research to avoid this issue. Adding the fibers in aerogel and hierarchically structured fiber mats (e.g. nanorods, nanotubes and nanowires) are attractive possibilities to produce ceramics with complex structures. In addition, co-electrospinning to produce core-shell fibers and embedding/doping compounds into the fibers are also interesting research topics to bring new functionalities to PDC materials.

Another important aspect is the production velocity of preceramic polymers via electrospinning, which is a pivotal factor in the incorporation of this developing technology into the industry. The productivity of fibers may be enhanced by improving needleless electrospinning and the use multi-jet system, which can be tested on a laboratory scale.

The electromagnetic field shielding of SiCN fiber mats can be improved by tailoring the carbon content or incorporating magnetic compounds in the ceramic. In addition, computational studies are tools for better evaluation of the electromagnetic properties of the PDC fiber mats in applications with geometries of commercial interest. The development of heat-resistant absorbers is a very exciting research topic for applications in the aerospace industry and nuclear reactors industries. In lithium-ion batteries, the synergistic effect of SiCN and carbon in the electrode was demonstrated. However, high and stable charge capacity will be obtained with an optimized concentration between polysilazane and organic polymer before electrospinning and pyrolysis, which still needs to be investigated.

The SiCN fiber mats exhibited potential properties in electromagnetic field shielding and electrochemical energy storage, but other potential applications of electrospun PDCs deserving more research include membranes in harsh environments, gas sensors and photoactive membranes.

CURRICULUM VITAE

Heloisa Ramlow

Curriculum vitae

Surname Ramlow
First name Heloisa
Date/Place of birth July 27th, 1991/Pomerode, Brazil
Nationality Brazilian



Education

03.2018 – 08.2022 Ph.D. student
(expected) Department of Chemical Engineering
Federal University de Santa Catarina
Florianópolis, Brazil

2016 – 2018 Master in Chemical Engineering
Federal University of Santa Catarina
Florianópolis, Brazil

2009 – 2014 Bachelor in Chemical Engineering
University of Blumenau
Blumenau, Brazil

Professional/Research experience

01.2022 – 04.2022 Visiting Ph.D. student
Department of Mechanical and Nuclear Engineering
Kansas State University
Manhattan KS, USA

09.2019 – 09.2020 Visiting Ph.D. student
Department of Ceramic Materials Engineering
Bayreuth University
Bayreuth, Germany

02.2015 – 02.2016 Product analyst
R&D
All4Labels Group
Blumenau, Brazil

CURRICULUM VITAE

Heloisa Ramlow

- 09.2014 – 01.2015** Intern
R&D
All4Labels Group
Blumenau, Brazil
- 04.2013 – 08.2014** Intern
08.2011 – 12.2011 Department of Chemical Engineering
University of Blumenau
Blumenau, Brazil
- 04.2012 – 01.2013** Intern
Department of Process Engineering
Bremen University
Bremen, Germany

Languages

- Portuguese** Native language
English Advanced (level B2)
German Advanced (level C1)

IT knowledge

Ansys ICEM CFD and Ansys FLUENT CFD, AutoCAD, ChemSketch, CorelDRAW, ImageJ, Inkscape, Microsoft Office, OriginLab, Simapro, Statistica, Tableau.

List of publications

Peer-reviewed

From this Ph.D.:

H. Ramlow, L. L. Silva, B. H. K. Lopes, M. R. Baldan, R. A. F. Machado. SiCN fibers as advanced materials for electromagnetic shielding in X-band: experiments and computational modelling and simulation. *Comput. Aided Chem. Eng.* 1 (2022) 199–204. <https://doi.org/10.1016/B978-0-323-95879-0.50034-5>.

H. Ramlow, C. Marangoni, G. Motz, R. A. F. Machado, Statistical optimization of polysilazane-derived ceramic: Electrospinning with and without organic polymer as a spinning aid for manufacturing thinner fibers, *Chem. Eng. J. Adv.* 9 (2022) 100220. <https://doi.org/10.1016/j.ceja.2021.100220>.

K.L. Andrade, **H. Ramlow**, J.F. Floriano, E.D. Acosta, F.L. Faita, R.A.F. Machado, Latex and natural rubber: recent advances for biomedical applications, *Polímeros.* 32 (2022) 1–12. <https://doi.org/10.1590/0104-1428.20210114>.

H. Ramlow, K. L. Andrade, A. P. S. Immich, Smart textiles: an overview of recent progress on chromic textiles, *J. Text. Inst.* 112 (2021) 152–171. <https://doi.org/10.1080/00405000.2020.1785071>.

R. K. M. Ferreira, **H. Ramlow**, C. Marangoni, R. A. F. Machado, A review on the manufacturing techniques of porous hydrophobic ceramic membranes applied to direct contact membrane distillation, *Adv. Appl. Ceram.* 120 (2021) 336–357. <https://doi.org/10.1080/17436753.2021.1981749>.

R. S. Silva, **H. Ramlow**, B. C. Santos, H. B. Madalosso, R. A. F. Machado, C. Marangoni, Membrane distillation: experimental evaluation of Liquid Entry Pressure in commercial membranes with textile dye solutions, *J. Water Process Eng.* 44 (2021) 102339. <https://doi.org/10.1016/j.jwpe.2021.102339>.

R. S. Silva, **H. Ramlow**, C. Cavalcanti, R. C. S. C. Valle, R. A. F. Machado, C. Marangoni, Steady state evaluation with different operating times in the direct contact membrane distillation process applied to water recovery from dyeing

wastewater, *Sep. Purif. Technol.* 230 (2020) 115892. <https://doi.org/10.1016/j.seppur.2019.115892>.

H. Ramlow, R. K. M. Ferreira, C. Marangoni, R. A. F. Machado, Ceramic membranes applied to membrane distillation: a comprehensive review, *Int. J. Appl. Ceram. Technol.* 16 (2019) 2161–2172. <https://doi.org/10.1111/ijac.13301>.
Others:

H. Ramlow, R. A. F. Machado, A. C. K. Bierhalz, C. Marangoni, Direct contact membrane distillation applied to wastewaters from different stages of the textile process, *Chem. Eng. Commun.* 207 (2020) 1062–1073. <https://doi.org/10.1080/00986445.2019.1640683>.

P. Linzmeyer, **H. Ramlow**, O. Souza, N. Sellin, C. Marangoni, Influence of neutralizing agents on the recovery of ethanol from banana pseudostem broth by pervaporation, *Waste and Biomass Valorization.* 11 (2020) 4269–4277. <https://doi.org/10.1007/s12649-019-00773-z>.

H. Ramlow, R. A. F. Machado, A. C. K. Bierhalz, C. Marangoni, Dye synthetic solution treatment by direct contact membrane distillation using commercial membranes, *Environ. Technol.* 41 (2020) 2253–2265. <https://doi.org/10.1080/09593330.2018.1561758>.

H. Ramlow, R. A. F. Machado, A. C. K. Bierhalz, C. Marangoni, Influence of dye class on the comparison of direct contact and vacuum membrane distillation applied to remediation of dyeing wastewater, *J. Environ. Sci. Heal. Part A.* 54 (2019) 1337–1347. <https://doi.org/10.1080/10934529.2019.1647059>.

H. Ramlow, V. H. M. Correa, R. A. F. Machado, A. C. K. Bierhalz, C. Marangoni, Intensification of water reclamation from textile dyeing wastewater using thermal membrane technologies – Performance comparison of vacuum membrane distillation and thermopervaporation, *Chem. Eng. Process. - Process Intensif.* 146 (2019) 107695. <https://doi.org/10.1016/j.cep.2019.107695>.

H. Ramlow, C. Cavalcanti, R. A. F. Machado, A. C. K. Bierhalz, C. Marangoni, Direct contact membrane distillation applied to colored reactive or disperse dye solutions, *Chem. Eng. Technol.* 42 (2019) 1045–1052. <https://doi.org/10.1002/ceat.201800468>.

D. L. Medeiros, F. L. Braghirolli, **H. Ramlow**, G. N. Ferri, A. Kiperstok, Environmental improvement in the printing industry: the case study of self-

adhesive labels, *Environ. Sci. Pollut. Res.* 26 (2019) 13195–13209. <https://doi.org/10.1007/s11356-019-04460-3>.

P. Linzmeyer, **H. Ramlow**, O. Souza, N. Sellin, C. Marangoni, Effects of by-products of fermentation of banana pseudostem on ethanol separation by pervaporation, *Biotechnol. Prog.* 35 (2019) 1–10. <https://doi.org/10.1002/btpr.2830>.

R.F. dos Santos, **H. Ramlow**, N. Dolzan, R. A. F. Machado, C. R. L. de Aguiar, C. Marangoni, Influence of different textile fibers on characterization of dyeing wastewater and final effluent, *Environ. Monit. Assess.* 190 (2018) 693. <https://doi.org/10.1007/s10661-018-7068-6>.

H. Ramlow, R. A. F. Machado, C. Marangoni, Direct contact membrane distillation for textile wastewater treatment: a state of the art review, *Water Sci. Technol.* 76 (2017) 2565–2579. <https://doi.org/10.2166/wst.2017.449>.

Conference presentation/proceedings

From this Ph.D.:

H. Ramlow, L. L. Silva, B. H. K. Lopes, M. R. Baldan, R. A. F. Machado. SiCN fibers as advanced materials for electromagnetic shielding in X-band: experiments and computational modelling and simulation, in: ESCAPE-32, Toulouse, France, 2022.

H. D. Rengel, R. S. Silva, **H. Ramlow**, R.A.F. Machado, C. Marangoni. Influência da limpeza química na reusabilidade de membranas aplicadas no processo de destilação por membranas de águas residuais têxteis, in: I Web Encontro Nacional de Engenharia Química, Diamantina, 2021.

Others:

B. C. Santos, H. B. Madalosso, R. S. Silva, **H. Ramlow**, R.A.F. Machado, C. Marangoni. Influência do tamanho do módulo de folha plana na destilação por membranas, in: II Congresso Brasileiro Interdisciplinar em Ciência e Tecnologia, Diamantina, 2021.

H. Ramlow, K.L. Andrade, C. Marangoni, R.A.F. Machado, Smart polymeric materials applied to industry 4.0: A review on electrochromic textiles, in: PPS 2019 Eur. Reg. Conf. Polym. Process. Soc., Pretoria, 2019.

H. Ramlow, V. H. M. Correa, R. C. S. C. Valle, J. A. B. Valle, A. C. K. Bierhalz, C. Marangoni. Destilação por membrana a vácuo aplicada ao tratamento de águas residuais da indústria têxtil contaminadas com corantes reativos, in: Semana Nacional de Ciência e Tecnologia 2017, Blumenau, 2017.

H. Ramlow, C. Cavalcanti, R. C. S. C. Valle, J. A. B. Valle, A. C. K. Bierhalz, C. Marangoni. Avaliação da destilação por membrana por contato direto utilizando diferentes módulos para tratamento de águas residuais da indústria têxtil, in: Semana Nacional de Ciência e Tecnologia 2017, Blumenau, 2017.

H. Ramlow, V. H. M. Correa, R. C. S. C. Valle, J. A. B. Valle, A. C. K. Bierhalz, C. Marangoni. Destilação por membranas aplicada ao tratamento de águas residuais da indústria têxtil, in: 5º Congresso Científico Têxtil e Moda - Contexmod, São Paulo, 2017.

H. Ramlow, V. H. M. Correa, R. C. S. C. Valle, J. A. B. Valle, A. C. K. Bierhalz, C. Marangoni. Potencialidade da destilação por membranas por contato direto para recuperação de águas residuais têxteis, in: 2º Seminário Nacional de Ciência, Tecnologia e Inovação na Indústria Têxtil, Blumenau, 2017.

H. Ramlow, V. H. M. Correa, C. Marangoni. Comparação do processo de destilação por membranas de contato direto no tratamento de águas residuais têxteis contendo corante vermelho reativo ou disperso, in: 2º Congresso de Engenharia Ambiental do Sul do Brasil, Lages, 2017.

V. H. M. Correa, T. E. Gomes, **H. Ramlow**, C. Marangoni, C. R. L. Aguiar. Adsorventes naturais in natura na remoção do corante azul reativo 222 em solução aquosa, in: 2º Congresso de Engenharia Ambiental do Sul do Brasil, Lages, 2017.

V. H. M. Correa, **H. Ramlow**, R. C. S. C. Valle, A. C. K. Bierhalz, C. Marangoni. Tratamento de águas residuais com corante disperso da indústria têxtil utilizando destilação por membranas, in: Congresso Brasileiro de Engenharia Química em Iniciação Científica - COBEQ-IC 2017, São Carlos, 2017.

H. Ramlow, A. C. Klemz, D. Noriler, H. F. Meier, U. Fritsching, W. Gonçalves. Análise da interação entre chamas em reatores de spray flamejante por técnicas de CFD, in: XX Congresso Brasileiro de Engenharia Química, Florianópolis, 2014.

A. C. Klemz, **H. Ramlow**, D. Noriler, H. F. Meier, U. Fritsching, W. Gonçalves. Análise da atomização giratória em reatores de spray flamejante por técnicas de CFD, in: XX Congresso Brasileiro de Engenharia Química, Florianópolis, 2014.